European School for Advanced Studies
in Reduction of Seismic Risk

Research Report No. ROSE-2005/01

Modelling and Analysis of High-damping Rubber Bearings for the Seismic Protection of Bridges

by

Damian N. Grant
Doctoral Graduate
ROSE School, Pavia, Italy

Gregory L. Fenves
Professor of Civil Engineering
University of California, Berkeley, USA

Ferdinando Auricchio
Professor of Mechanics of Solids
University of Pavia, Italy

ROSE School
Collegio Alessandro Volta
Via Ferrata, 27100, Pavia, Italy

May 2005

prodotto da:
Multimedia Cardano
Via Cardano, 14 - 27100 Pavia, Italy
Tel.: (+39) 0382.539776 - fax: (+39) 0382.306406 - e-mail: multimediacardano@multimediacardano.191.it

distribuito da:
IUSS Press
IUSS, Collegio Giasone del Maino, Via Luino, 4 - 27100 Pavia, Italy
Tel.: (+39) 0382.375841 - fax: (+39) 0382.375899 - email: info@iusspress.it - web: www.iusspress.it

ABSTRACT

High-damping rubber (HDR) bearings are used in seismic isolation applications for buildings and bridges, although no models are currently available for the accurate description of the shear force–deformation response under bidirectional loading. Furthermore, existing state-of-the-practice and research-oriented unidirectional models are unable to describe adequately the strain-stiffening and strain-induced degradation observed in experimental tests of HDR bearings. An accurate bidirectional model that is able to describe HDR bearing response *a priori* is required for analysis and design applications.

For these reasons, a strain rate-independent, phenomenological model is developed which effectively represents the stiffness, damping, and degradation response of HDR bearings. The model decomposes the resisting force vector as the sum of an elastic component in the direction of the displacement vector and a hysteretic force component which evolves based on the current displacement and velocity vectors. The elastic component is obtained from a generalised Mooney–Rivlin strain energy function, and the hysteretic component is described by an approach similar to bounding surface plasticity. Degradation is decomposed into long term ("scragging") and short term ("Mullins' effect") components.

Calibration of the proposed model is carried out over a series of bidirectional test data, using the downhill simplex algorithm to obtain a set of material parameters for the bearing. The model provides a good match of slow strain-rate experimental data using a unique set of material parameters for all tests. A testing protocol and calibration of the model for use in design of structures with HDR bearings are discussed.

The analysis and design of seismically-isolated bridges involves a number of assumptions about the input ground motion, and the distribution of mass, stiffness and damping in the substructure, superstructure and bearings. Existing design procedures provide inconsistent recommendations, particularly for the design of piers. A design methodology that targets performance goals at two levels of seismic hazard is developed, as an extension of existing displacement-based design methods. The design method aims to ensure that pier inelasticity is prevented at a "design" seismic hazard level, and is limited to a specified ductility for

"maximum credible" hazard.

Finally, a number of parametric studies of isolated bridge system response are carried out, using the proposed bearing model to represent isolator response, and simple bridge geometries. Input ground motion is simultaneously applied in two orthogonal directions, and is scaled by a range of scaling factors to assess the effects of bidirectional input and variable seismic intensity on isolated bridge response. It is found that the nonlinear response of HDR bearings reduces the bearing displacement demand at high intensity levels, at the expense of increased force demand in the piers, particularly compared to the response of other bearing types. When nonlinear pier behaviour is considered, this results in a significant ductility demand in piers for ground motions greater than design level intensity. The multiple performance level design approach is also assessed in the parametric studies, and it performs adequately for simple bridge configurations; the method will, however, require modification to account for the effects of superstructure flexibility and more complicated bridge geometries.

ACKNOWLEDGMENTS

The authors would like to thank Nigel Priestley, Andrew Whittaker, Julian Bommer and Rui Pinho, who provided valuable technical advice on various stages of this research.

TABLE OF CONTENTS

LIST OF TABLES

LIST OF FIGURES

1. INTRODUCTION

1.1 SEISMIC ISOLATION

Seismic isolation is a widely used method of protecting both bridges and buildings from the effects of strong ground motion. Flexible isolation bearings are placed between the primary mass of the structure and the source motion, effectively using inertia and lengthened vibration period to limit structural deformation in critical components. In this manner, a building is isolated from its foundations, and the superstructure of a bridge is isolated from the piers.

The main benefits of seismically isolating a structure, either new or existing, are:

1. The addition of flexibility to the system increases the fundamental period, which, for short period structures, will decrease the design forces. However, for long period structures, or ground motions with unusual frequency content, this effect may be negligible, and in extreme cases, design forces may even be higher.
2. Although increased flexibility can lead to larger system displacements, inelastic deformation is confined to the bearing, allowing elastic design of the remainder of the structure. Bearings are relatively easy to maintain, and if necessary, replace, compared to structural elements.
3. Significant seismic energy may be dissipated in the isolators, by hysteretic damping in its components, or through the addition of supplemental dampers to the isolation system. This has the effect of further decreasing the shear forces and limiting the maximum displacement demand on the bearing.
4. The shear forces transmitted to the piers are limited by the amount of force that can be transmitted across the bearing, which, in some cases, allows the isolation device to act as a fuse for the structure.

In new bridge design, and retrofit and repair of existing bridges, isolation devices are generally placed between the piers and the superstructure. Typically, seismic isolation bearings may be used in the place of other bearing types detailed for non-seismic design requirements.

1.2 High-Damping Rubber Bearings

Since the first use of seismic isolation in bridges in the early 1970s, many novel devices have been proposed and implemented for the isolation of structures. High-damping rubber (HDR) bearings are a type of seismic isolator commonly used in bridge and building construction and retrofit. As with other elastomeric isolation devices, HDR bearings are composed of layers of an elastomeric compound, reinforced with steel shims to provide vertical stiffness. The elastomer is typically a filled natural rubber or synthetic rubber to provide energy dissipation under cyclic loading, without the need for additional dampers. The nonlinear stress–strain behaviour of filled or synthetic rubbers used in HDR bearings results in high horizontal stiffness for low shear strains, low stiffness for intermediate strains, and an increasing shear modulus under higher strains. This behaviour has some advantages for earthquake protection, because under service conditions, such as wind or small earthquakes, the stiffness of the bearing is high, and the forces and deformation in the structure are expected to be in the elastic range. In a moderate seismic event, the bearing deforms, thus isolating the structure and providing additional energy dissipation. In an extreme earthquake loading, the strain-stiffening behaviour of the elastomer limits the deformation in the bearing, at the expense of increased force, which helps to reduce the risk of bearing instability.

With respect to the four benefits of seismic isolation discussed in the previous section, HDR bearings provide an efficient source of energy dissipation (benefit 3), and at moderate displacement levels, satisfy the requirements of benefit 1 and 2. However, because the maximum shear force is not well-defined for HDR bearings, the device does not provide an effective fuse across the isolated interface, violating benefit 4. Because of this, at high strains it may not be possible to confine inelastic deformation to the isolator, and piers may experience inelastic demand. Current design guidelines for isolated structures [AASHTO, 1999; Ministry of Public Works, 1998] prohibit the development of pier ductility by prescribing appropriate behaviour factors. One motivation for developing an accurate phenomenological model for HDR bearings is to assess the system response of isolated bridges, and consider the interaction between bearing deformation and inelasticity in piers.

The behaviour of high-damping rubber bearings has been the subject of numerous experimental studies. Extensive tests were carried out on bearings for use in the Foothill Community Law and Justice Center, the first building to be seismically-isolated in the United States [Tarics *et al.*, 1984; Kelly and Çelebi, 1984]. These tests included both prototype and production bearings, and distinguished between the virgin and degraded behaviour characteristics. HDR bearings manufactured by the Bridgestone corporation [Bridgestone Corporation, 1994] have been extensively studied at the Earthquake Engineering Research Center (EERC) in the University of California, Berkeley [Kelly, 1991], and the Argonne National Laboratory, Illinois [Chang and Seidensticker, 1993]. The unidirectional, cyclic force–deformation behaviour of the bearings was studied, and failure mechanisms were characterised. In the late 1990's a joint research project between the Shimizu Corporation,

Japan, and EERC was carried out. This project, which was described in details by Clark *et al.* [1997], included unidirectional component tests of HDR bearings, in addition to shake table tests of a 0.4-scale base-isolated reinforced-concrete building. The component tests included investigations of horizontal and vertical force–deformation behaviour, failure modes, and ageing effects.

The Caltrans Seismic Protective Systems Project [Thompson *et al.*, 2000; Morgan, 2000; Huang, 2002], carried out at the University of California, Berkeley included pseudo-static and dynamic tests on HDR bearings under several different bidirectional load paths. The project aimed to characterise, and to develop predictive models for, the response under earthquake loading. In this thesis, experimental data from the Caltrans Seismic Protective Systems Project is used in the development of a new mathematical model that describes bidirectional response. The testing programme is discussed in more detail in Section 2.1.

1.3 Existing Models for HDR Bearings

The dynamic analysis of structures for seismic assessment and design requires an accurate mathematical model of the isolation bearings. The strongly nonlinear response of HDR bearings has made the development of mathematical models challenging. Unlike other isolation devices, such as lead–rubber (LR) bearings [Tyler and Robinson, 1984; Kelly, 1996] and friction pendulum system (FPS) bearings [Zayas *et al.*, 1987], a bilinear approximation to the force–deformation relationship is not adequate for HDR bearings under unidirectional or bidirectional loading [Huang, 2002]. In addition, laboratory tests [Thompson *et al.*, 2000; Huang, 2002] reveal other characteristics of HDR bearings, including "scragging", Mullins' effect, strain-induced anisotropy, and dependence on load history. Other factors that are difficult to represent are the variation in horizontal stiffness with axial load and temperature, strain-rate dependence and ageing effects.

To enable dynamic analysis of structures with HDR bearings, several mathematical models have been proposed in the literature for unidirectional loading. Models based on an additive decomposition of the total shear force in the bearing into a restoring force and damping force have appeared promising. The damping force may be considered as a hysteretic, rate-independent effect [Kikuchi and Aiken, 1997], or as a viscoelastic dissipation that depends on the strain rate [Hwang *et al.*, 2002]. Tsai *et al.* [2003] recently proposed a model based on a Bouc–Wen [Bouc, 1967] approach, coupled with a linear viscous term. These models, however, require the identification of a large number of material parameters that in some cases have little obvious physical significance, and the models are difficult to extend to bidirectional response. Furthermore, existing models either have no evolution rules to represent degradation under arbitrary loading paths, or the rules are very simple.

The large strain constitutive response of filled elastomers has been extensively studied, including nonlinear elastic, viscoelastic and viscoplastic models. Recent models by Miehe and Keck [2000]

and Haupt and Sedlan [2001] consider all three of these aspects of elastomer behaviour, represented rheologically by a number of appropriately defined springs in parallel. In addition, they consider a damage parameter to represent the degradation of the stress and stiffness under cyclic loading. The "8-chain network model" [Arruda and Boyce, 1993] considers the hyperelastic behaviour of an elastomer to be represented by eight macroscopic polymer chains that stretch from the corners of a rectangular prism to its centre. Subsequent developments, also based on macroscopic interpretations of micromechanical theories, have added rate-dependency [Bergström and Boyce, 1998] and degradation [Chagnon *et al.*, 2002] to the 8-chain model.

Material models of this type may be used in a finite element representation of an individual bearing. Indeed, material level representations may be necessary to investigate local aspects of bearing behaviour, such as cavitation and failure modes. However, continuum models of bearings are not useful for design and analysis of structures with seismic isolation bearings, and phenomenological models of the shear force–deformation relationship for bearings are necessary.

1.4 Desirable Features of a HDR Bearing Model

For the development of a new bidirectional model for use in design and analysis of HDR bearings, a number of desirable features can be identified. Clearly, it is important for a model to be able to capture the nonlinearity of stiffness and damping observed in experimental tests. Models that are calibrated for a certain level of shear strain, such as linear viscoelastic or bilinear models, are inadequate for describing the response to a large range of strain levels in earthquake loading. In the case where an "equivalent viscous damping" is calculated for a certain peak displacement excursion, cycles at lower levels of displacement will typically be overdamped. Although simplicity is important in both analysis and design, accuracy and robustness are paramount.

A model that can represent the coupling of response in two orthogonal directions is also important. Experimental evidence, presented in Section 2.2, shows that loading a bearing in one direction affects the load resisted in an orthogonal direction. The use of two unidirectional models in parallel cannot describe this behaviour, so a model that incorporates coupling between the two directions is required.

The degradation of stiffness and damping must also be included in a model for HDR bearings. Stiffness and damping typically degrade after the first cycle of loading, a phenomenon variously referred to in the literature as "scragging" or "Mullins' effect". Because bearings are typically scragged before use to provide stable hysteretic behaviour, this feature is often ignored in proposed models. However, virgin behaviour is typically recovered over a period of a few years [Thompson *et al.*, 2000], which is well within the design life of a typical structure. Consequently, it is not known in advance if isolation bearings will be in scragged or unscragged state when an earthquake occurs, and it is important that both types of behaviour can be described by the model.

HDR bearings also exhibit some degree of strain-rate dependence [Huang, 2002], and ideally this should be included in a prospective model. Some existing models [Hwang *et al.*, 2002; Tsai *et al.*, 2003] include strain-rate dependence, although different material parameters are used for tests at different strain rates, which suggests that the models cannot describe the dependence *a priori*.

Other features that are desirable in a HDR bearing model, but not essential, are the inclusion of axial load and temperature dependence. For the range of axial loads typical of bridge isolation applications, the variation of HDR bearing behaviour with axial load is expected to be relatively insignificant, provided that the model has been calibrated appropriately. Temperature of a bearing typically increases with cyclic loading, but this change will be taken into account in the degradation and strain rate components of the model. Again, different ambient temperatures can be taken into account with material parameters calibrated at the appropriate temperature.

1.5 Design Guidelines for Isolated Bridges

Most existing design approaches for isolated systems in general [BSSC, 1997], and bridges in particular [AASHTO, 1999], are based on an equivalent linearisation of nonlinear bearing properties. Priestley *et al.* [1996] have also presented a displacement-based design approach for isolated bridges that adopts the equivalent linear approximation for bearing response. In these approaches, an equivalent linear viscoelastic model, defined by its stiffness and fraction of critical damping, is used to approximate the real nonlinear response of the bearing, which greatly simplifies the evaluation of peak demand on the isolators and structural elements. Many authors [e.g. Rosenblueth and Herrera, 1964; Iwan, 1980; Hwang *et al.*, 1994, 1996] have presented combinations of effective stiffness (or equivalently, a period shift) and viscous damping, which are generally functions of bearing properties and maximum deformation, to best approximate the nonlinear response.

For the design of isolation systems for existing bridges, Calvi and Pavese [1998] present an optimisation procedure that is based on varying an assumed superstructure deflected shape to obtain an optimum value for a defined regularity index. The authors propose that the methodology can also be adopted for new bridges, as the converged superstructural deformation will be relatively insensitive to assumed pier and abutment strengths.

Recently, Ryan and Chopra [2004] published a method for estimating the displacement demand for an isolation bearing characterised by bilinear hysteretic behaviour, subjected to a suite of ground motions. The proposed procedure has the advantage that it is able to directly account for bidirectional ground motion, and does not require linearisation of bearing response. By normalising the equation of motion in an appropriate manner, it is shown that the median bearing demand over the suite can be made a function of only the isolation period of the bearing, and its normalised strength. However, with isolation systems for which a bilinear model is less appropriate, such as HDR bearings, the results

of the design method may not be applicable. The method is also difficult to extend to predicting the system response of a pier and an isolator in series, or more complicated bridge geometries.

1.6 System Response Studies of Isolated Bridge Systems

Analytical studies on isolated bridge systems has been directed primarily at the unidirectional response, and for isolation devices that may be characterised by bilinear hysteresis. Kartoum *et al.* [1992] presents such a study for sliding Teflon bearings, with a two-span continuous deck bridge model, incorporating the effects of superstructure and pier flexibility. The analytical work complements an experimental study on the same bearings by Constantinou *et al.* [1992].

Franchin *et al.* [2001] conducted a study on the use of equivalent linearisation for bearing response in isolated bridges. The authors discuss the difficulty in assembling a classical damping matrix when equivalent linear viscoelastic properties have been derived for each of the bearing locations in the structure. They show that the complex mode shapes resulting from such a non-classical damping matrix can be approximated accurately by appropriately defined real mode shapes. They also compare bridge response, in terms of deck, pier and isolator displacement and isolator force, for three linearisation formulae: the model contained in the AASHTO provisions [AASHTO, 1999], and two models due to Hwang and coauthors [Hwang *et al.*, 1994, 1996]. The authors find that the equivalent linearisation procedures give the best results for regular bridges, and poor results for irregular ones. They suggest that codes should limit the use of linearisation to the former type of structure.

Huang [2002] and Mosqueda *et al.* [2004] have conducted bidirectional analytical parametric studies for bridges isolated with LR and FPS bearings, respectively, using data from the Caltrans Protective Systems Project (discussed further in Chapter 2). It is the intention of this study to adapt the conclusions of these references to the bidirectional response of bridges isolated with HDR bearings. In addition, nonlinear pier behaviour is considered, to investigate the interaction of pier and isolator nonlinearity at different levels of seismic hazard.

1.7 Organisation of Thesis

This thesis is an investigation of the bidirectional response of bridges isolated with high-damping rubber bearings. Chapter 2 outlines a series of bidirectional tests that was carried out at the University of California, Berkeley, as part of the Caltrans Seismic Protective Systems Project. This experimental programme has been described previously [Morgan, 2000; Huang *et al.*, 2000], and included bidirectional tests on lead–rubber (LR) bearings, and friction pendulum systems (FPS), in addition to the HDR bearings considered in this thesis. Although effective models have been developed from the bidirectional data for LR [Huang, 2002] and FPS bearings [Mosqueda *et al.*, 2004],

the bidirectional behaviour of HDR bearings has not been adequately described. The observed behaviour of the bearings is discussed in the context of micromechanics in Section 2.3.

In Chapter 3, existing approaches to the modelling of HDR bearings are discussed. In the first part, Section 3.1, several phenomenological models for the unidirectional response are considered. The linearised viscoelastic and bilinear idealisations of bearing behaviour, considered in most existing design guidelines [BSSC, 1997; AASHTO, 1999], are discussed in Section 3.1.1. Following this, promising models by Hwang *et al.* [2002] and Kikuchi and Aiken [1997], based on a decomposition of the total resisting force into an elastic force and damping force, are considered in Sections 3.1.2 and 3.1.3. Finally, a model recently proposed by Tsai *et al.* [2003] is discussed in Section 3.1.4. In each case, advantages and limitations of the existing undirectional modelling approaches are discussed, in addition to the difficulties in adapting these models to bidirectional response.

Although no models have been developed specifically for the bidirectional modelling of HDR bearings, several existing approaches from plasticity theory have been considered in the past. In the second part of Chapter 3, Section 3.2, several approaches from classical plasticity and bounding surface plasticity [Dafalias and Popov, 1975] are presented, and an attempt is made to reconcile model response with HDR bearing behaviour. This chapter also includes a "stiffening surface" model which was developed as an extension of the bounding surface approach, as an attempt to describe the stiffening observed in HDR bearings at high strain levels. As with the existing unidirectional approaches, limitations and advantages of the bidirectional modelling approaches are discussed.

In Chapter 4, a new mathematical model for the bidirectional shear force–displacement response of HDR bearings is developed. The force vector is additively decomposed into two components: a pseudo-elastic resisting force in the direction of the displacement vector, and a hysteretic damping force in the direction of the velocity vector. The latter component evolves within a rate-independent envelope, similar to a bounding surface plasticity approach [Dafalias and Popov, 1975]. Both components are modified by two damage parameters, which take into account the effects of both scragging and Mullins' effect separately. In Section 4.3, a sensitivity study is conducted to assess the effects of changing model parameters. In Section 4.4, the model is extended to describe rate-dependent effects in HDR bearing response, with the addition of a third force term to the original two-component model. As with existing models, the effects of temperature, axial load and ageing can only be included in the proposed model *a priori*, through the determination of appropriate material parameters for the conditions.

The model is calibrated using data from a series of displacement-controlled experiments, in Chapter 5, to obtain a unique set of material parameters for a given bearing. This approach allows a consistent and realistic portrayal of the long and short-term degradation in stiffness and damping with cyclic

loading. Two alternative sets of experimental data are included in the calibration procedure, and a comparison between the results is made. Using the material parameters obtained in each calibration, the predictive power of the model is assessed by considering tests that were not explicitly included in the calibration procedure. The calibration of the model for rate-dependent data, and the sensitivity of the calibration algorithm to the initial parameter set are also discussed. Finally, minimum requirements for an experimental protocol that would allow effective calibration of the model are suggested. This experimental programme would allow practical application of the model beyond a research setting, for any new high-damping rubber bearings that are developed.

In Chapter 6, existing methodologies for the analysis and design of isolated bridges are summarised. Section 6.1 discusses modelling issues for time history analysis, with a particular focus on the four principal elements of the equation of motion: the representation of inertial mass, viscous damping, structural stiffness and input ground motion. In Section 6.2, a number of issues related to the displacement-based design of isolated bridges are considered. The representation of bidirectional seismic demand, and the equivalent linearisation of bearing and, if necessary, pier properties are discussed in Sections 6.2.1 and 6.2.2, respectively, and are placed within the context of direct displacement-based design [Priestley *et al.*, 1996] in Section 6.2.3. Finally, in Section 6.2.4, the existing design framework is extended to allow design for multiple performance levels for different return periods of earthquake hazard. Specifically, the design goals considered are elastic piers and the limitation of bearing displacement at design intensity, and the limitation of pier and bearing displacement demand for higher intensities.

In Chapter 7, a number of parametric studies of simple isolated bridge models are presented. The response of bridges isolated with HDR bearings is compared with other bearing types, assuming both elastic and inelastic pier response. The design methodologies discussed in Chapter 6 are also investigated.

Finally, it should be noted that a mixture of imperial and SI units are used in this thesis. Imperial units are used in Chapters 2–5, which deal with experimental data from the Caltrans Protective Systems Project. The experimental work and data collection were carried out using imperial units, and the results are presented in this form for consistency with other publications from this project. Chapter 7 considers analytical parametric studies in which SI units are used, although the results are presented in a normalised form, and should be generally applicable. The design methods considered in Chapter 6 are independent of the system of units used, provided that it is internally consistent.

2. HIGH-DAMPING RUBBER BEARING BEHAVIOUR

2.1 CALTRANS PROTECTIVE SYSTEMS PROJECT

The Caltrans Protective Systems Project at the University of California, Berkeley included a number of bidirectional experiments to characterise the behaviour of elastomeric and friction bearings. The experimental programme, thoroughly described by Thompson [1998], Morgan [2000] and Huang [2002], included bidirectional tests of bearings under imposed displacement orbits, and dynamic tests using scaled earthquake records. Most tests of HDR bearings were conducted on low-modulus, high-damping Bridgestone KL301 bearings, illustrated in Fig. 2.1. Although the behaviour of the bearing is dependent on the compound, these bearings can be considered typical of those commonly used in the construction of seismically-isolated bridges. The thickness of rubber in the bearing (t_r) is 1.8 in. (45mm). The unidirectional behavior of these bearings has been studied extensively [Clark *et al.*, 1997], and one objective of the experimental programme was to improve knowledge about the bidirectional behaviour.

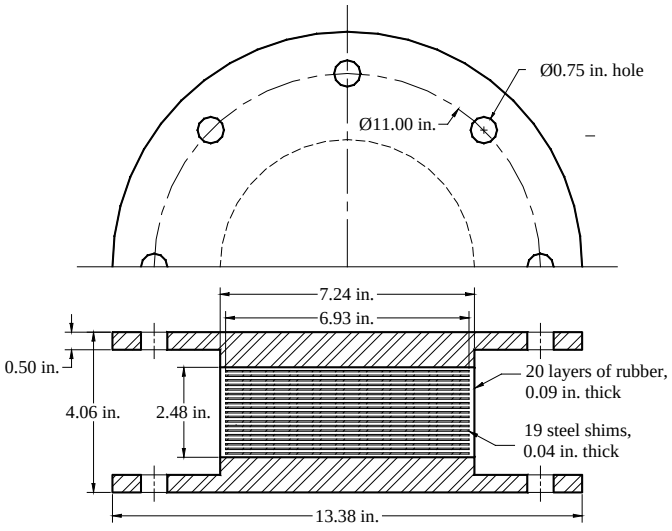

Figure 2.1. Bridgestone KL301 high-damping rubber bearing used for experimental programme.

The earthquake simulator at the Pacific Earthquake Engineering Research (PEER) Center was used for both displacement-controlled and dynamic tests on the bearings. For the displacement-controlled tests, a rigid block was supported by four bearings on the platform, and the block was held in place by horizontal struts reacting against abutments. The simulator platform was subjected to bidirectional displacement orbits at varying levels of maximum strain and at a slow rate (approximately 0.01 Hz). The four orbits illustrated in Fig. 2.2 were selected to investigate the force–deformation behaviour of the bearings, including the effects of scragging, Mullins' effect and path-history dependence. To investigate the effects of strain-rate, orbit 4 was also run at an increased strain-rate of 0.5 Hz.

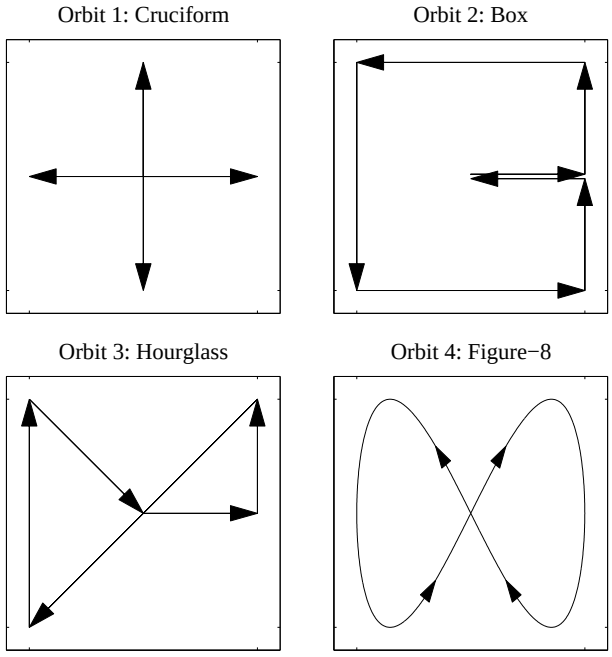

Figure 2.2. Orbits for bidirectional displacement-controlled tests of seismic isolation bearings.

2.2 Displacement-Controlled Experimental Data

To illustrate several important aspects about the bidirectional behaviour of HDR bearings, Figs. 2.3 and 2.4, show the experimental shear force–deformation relationship for the cruciform (orbit 1) and box (orbit 2) displacement orbits, respectively. In each case, the results from moderate ($\gamma = 100\%$) and high ($\gamma = 250\%$) shear strain tests are shown. The test numbers cited in the figures refer to the order within the entire series, listed in Table 2.1, which will be important when history effects are considered.

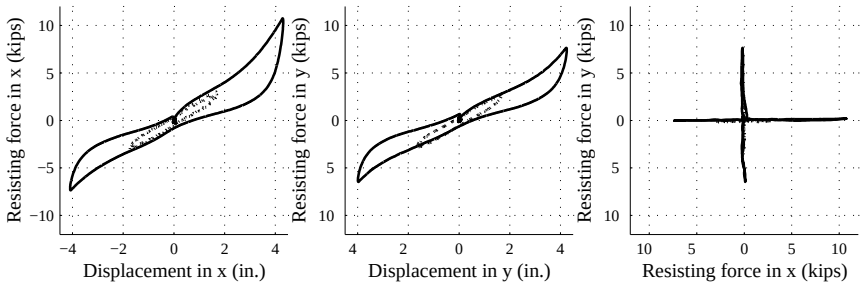

Figure 2.3. Experimental results for cruciform orbit 1: tests 2 (solid line) and 4 (dashed line), $\gamma_x = \gamma_y = 250\%$ and $\gamma_x = \gamma_y = 100\%$, respectively.

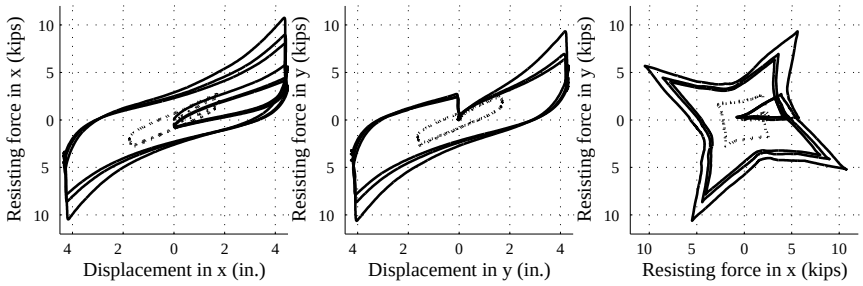

Figure 2.4. Experimental results box orbit 2: tests 24 (solid line) and 12 (dashed line), $\gamma_x = \gamma_y = 250\%$ and $\gamma_x = \gamma_y = 100\%$, respectively.

The cruciform tests (orbit 1) are useful for assessing the unidirectional response of the bearing in two orthogonal directions, and to determine if there is interaction between them. From the first part of Fig. 2.3 it is clear that the stiffness decreases up to a strain level of 100% to 125%, but then the stiffness increases at larger strains. This stiffening behaviour is also apparent in the reversed cycle in the x-direction, and for subsequent loading in the y-direction. Comparing the peak shear forces in each half cycle, however, degradation of the bearing stiffness can be observed. In the x-direction, the peak shear force is approximately 10.5 kips (47 kN) on the first half cycle, and 7.5 kips (33 kN) in the reverse direction; in the y-direction, the corresponding forces are 7.5 kips (33 kN) and 6.5 kips (29 kN), respectively. This type of degradation of filled rubbers was studied extensively by Mullins [1969], and is referred to as "Mullins' effect" or "scragging".

For developing a new bidirectional model, the interaction between scragging in each direction is of interest. From the results in Fig. 2.3, it can be observed that loading in one direction appears to scrag the bearing in the orthogonal direction. However, Thompson *et al.* [2000] have suggested that this interaction between directions could be dependent on the compound.

If a scragged bearing is retested after some time, it is found that a portion of the degradation is

Table 2.1. Displacement-controlled tests of HDR bearings

Test	Orbit	Rate (Hz)	$\gamma_x(\%)^a$	$\gamma_y(\%)^b$	Test log
(1)	1	0.01	25	25	980514182504
(2)	1	0.01	250	250	980514185709
(3)	1	0.01	25	25	980515135923
(4)	1	0.01	100	100	908515143353
(5)	1	0.01	200	200	980515145330
(6)	2	0.01	25	25	980515152024
(7)	3	0.01	25	25	980515153657
(8)	4	0.01	25	25	980515160926
(9)	2	0.01	25	100	980515161626
(10)	3	0.01	25	100	980515162423
(11)	4	0.01	25	100	980515163026
(13)	3	0.01	100	100	980515171130
(14)	4	0.01	100	100	980515172315
(15)	4	0.50	100	100	980515174937
(16)	2	0.01	100	200	980515180155
(17)	3	0.01	100	200	980515181019
(18)	4	0.01	100	200	980515181927
(19)	4	0.50	100	200	980515184130
(20)	2	0.01	200	200	980515184556
(21)	3	0.01	200	200	980515185801
(22)	4	0.01	200	200	980515190354
(23)	2	0.50	200	200	980515191558
(24)	2	0.01	250	250	980515192119
(25)	3	0.01	250	250	980515193319
(26)	4	0.01	250	250	980515194014
(27)	1	0.01	25	25	980515195509
(28)	1	0.01	250	250	980515200229

[a] Maximum shear strain in x-direction

[b] Maximum shear strain in y-direction

recovered over a period of a few days, whereas full recovery occurs over a period of a few years [Thompson *et al.*, 2000]. Although the distinction is not discussed consistently in the literature, Clark *et al.* [1997] referred to the short-term and long-term degradation as Mullins' effect and scragging, respectively. The consideration of the recovery of virgin bearing properties is important for the development of a model capable of predicting HDR bearing behaviour over a range of service conditions.

The box orbit tests demonstrate the behaviour of HDR bearings when subjected to loading in orthogonal directions simultaneously. From Fig. 2.4, the degradation of stiffness between successive cycles is apparent. It can also be noted that increasing the displacement in one direction while keeping the displacement in the orthogonal direction fixed affects the shear force in both directions. This experimental observation means that bidirectional motion is coupled and that two independent unidirectional models will not accurately describe the bidirectional behaviour. Finally, the force vector with components F_x and F_y pointing from the origin to the force point, can be observed in the third part of Fig. 2.4. The force vector is clearly not in the same direction as the displacement vector for all parts of the displacement orbit. For example, when the shear strain is 250% in each direction, in the first cycle of loading, the displacement vector will be oriented at 45° to the x-axis, while the force vector is approximately $\{ 6 \;\; 9 \}^T$ kips. The implication of this observation is that a mathematical model in which the force vector is expressed solely as a function of the current displacement vector will not be able to describe adequately the bidirectional response of HDR bearings. The orientation of the force vector will be considered in more detail in the development of the bidirectional model in Chapter 4.

2.3 Micromechanical Explanation of Observed Behaviour

The experimental behaviour described in the previous section can be explained in terms of the micromechanics of high-damping rubber materials. The stiffening and degradation of high-damping rubber bearings, and the strain-rate dependence (discussed further in Sections 4.4 and 5.3) may be related to the interaction between the rubber matrix and filler particles, and how this interaction evolves with strain and time. In this section, the micromechanical behaviour of filled rubber is summarised briefly, and related to the macroscopic observations from the previous section; more information may be found in other references on high-damping rubber behaviour [Govindjee and Simo, 1991; Clark *et al.*, 1997; Morgan, 2000].

At the microscopic level, vulcanised natural rubbers are composed of a matrix of randomly-oriented polymer chains. Under small strain loading and unloading, the chains are untangled and re-tangled in an essentially linear elastic manner. At higher strain levels, the links become fully straightened, and subsequent loading leads to strain crystallisation, which is reversible on unloading. The macroscopic result of this process is an increase in stiffness and energy dissipation relative to the low strain behaviour.

Although not discussed in Section 2.2, the tests conducted at higher strain rates in the test programme (test numbers 15, 19 and 23) confirmed the well-known rate-dependence of both filled and unfilled natural rubbers [e.g. Govindjee and Simo, 1992; Bergström and Boyce, 1998; Thompson *et al.*, 2000]. This rate-dependence may be related to the presence of inactive chain segments in the polymer lattice, as shown in Fig. 2.5 [Bergström and Boyce, 1998]. When the network is strained at a sufficiently fast

rate, the free chain segment (the black line in Fig. 2.5) is stretched along with the rest of the polymer matrix. In the deformed configuration, the loop A–B–C undergoes Brownian motion, and tends to return to a relaxed equilibrium state over time. This implies that the macroscopic force carried by the elastomer is a function of how much the network is allowed to relax during loading, and therefore the rate at which the strain is applied.

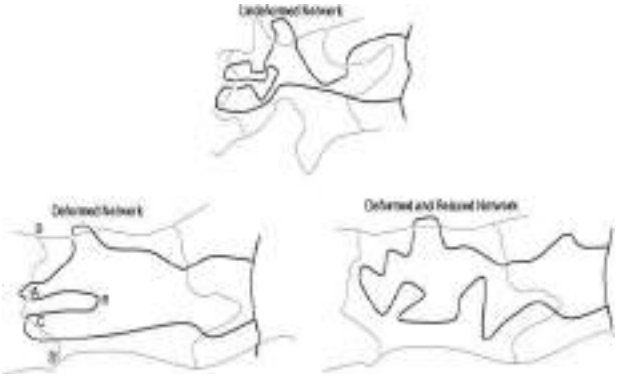

Figure 2.5. Relaxation of inactive chain segments in a perfect network (from [Bergström and Boyce, 1998]).

The addition of filler materials, such as carbon black or oil resins, to the rubber compound does not change the micromechanical behaviour of the polymer chains. The filler particles, however, obstruct the chains from untangling fully and lead to stress concentrations in parts of the rubber matrix. For this reason, the stiffness of the compound is higher than the unfilled rubber, and strain crystallises at lower strain levels. Traditionally, this process has been used to enhance the abrasion resistance, tear strength and tensile strength of natural rubbers [Govindjee and Simo, 1992], although in earthquake engineering applications the increased energy dissipation at moderate strain levels is of most interest. The change in macroscopic material properties is a function of the size and surface area, in addition to the total volumetric ratio, of filler particles added [Clark *et al.*, 1997].

Adding fillers to provide enhanced stiffness and energy dissipation has the side effect of introducing stiffness degradation under cyclic loading. According to Clark *et al.* [1997], two distinct mechanisms are responsible for this degradation, and they may be distinguished by their rate of recovery. The semi-permanent stiffness reduction that occurs primarily in the first cycle to a given strain level is referred to as "scragging", and the recoverable reduction in stiffness that occurs under subsequent cyclic loading is "Mullins' effect". This distinction is not followed consistently in the literature, and other references on filled rubber behaviour attribute both effects to the same micromechanical mechanism, with the possibility of multiple relaxation processes acting in parallel [e.g. Govindjee and Simo, 1992]. Experimental evidence that unscragged stiffness is recovered over a period of a few

years [Thompson *et al.*, 2000] suggests that the degradation and recovery mechanism may be more complicated than Clark *et al.* [1997] propose. Nevertheless, the distinction between scragging and Mullins' effect is followed in this thesis, and the phenomenological model described in Chapter 4 is defined on this basis.

Clark *et al.* [1997] attribute the scragging effect to the semi-permanent damage of some molecular links in the polymer matrix. The first cycle of loading to a given strain level will exhibit a higher stiffness than subsequent cycles. If the material is loaded to a higher strain amplitude, further degradation of stiffness will be observed, as further polymer chains are broken. The eventual recovery of the original "virgin" or "unscragged" material stiffness may be attributed to the healing of the polymer chains with time.

Govindjee and Simo [1991] report two main micromechanical explanations for Mullins' effect. The first theory, originating with some of the early experimental work on the subject by Mullins and coworkers [Mullins, 1969], is that strain-induced crystallisation and decrystallisation takes place in the polymer chains under cyclic loading. The second theory [e.g. Bueche, 1960] proposes that links between the filler particles and polymer chains are broken under sufficient load. Both theories allow for the recovery of material properties with time – in the first case healing involves a rearrangement of the polymer matrix, while in the second case, the bonds between the filler and polymer are reformed.

As discussed above, it is not clear if the distinction between scragging and Mullins' effect should be made on a molecular level, and it is possible that a combination of the effects discussed above is responsible for the observed degradation of high-damping rubbers under cyclic loading. Indeed, although Clark *et al.* [1997] cite the two theories discussed in the previous paragraph as the possible causes of the Mullins' effect component of degradation, they were originally postulated to explain the total reduction in stiffness, including scragging and Mullins' effect. In fact, typically the first cycle semi-permanent degradation was of more interest in the development of these theories, as it has a larger effect on material properties. Although bearings are typically prescragged to a certain level of displacement before installation, the complete recovery of virgin properties with time suggests that both degradation effects need to be carefully considered in analysis and design.

3. EXISTING PHENOMENOLOGICAL MODELS FOR HIGH-DAMPING RUBBER BEARINGS

3.1 UNIDIRECTIONAL HDR BEARING MODELS

Existing phenomenological models describe HDR bearing behaviour for unidirectional loading. Typically, they express the resisting force of the bearing, F, in terms of the shear displacement, U. In this section, recent approaches to unidirectional modelling are summarised, and advantages and limitations of each model are highlighted.

3.1.1 State-of-the-Practice Modelling: Linear and Bilinear Models

Guidelines for the design of seismic isolation systems are primarily based on a linearised viscoelastic model for bearing behaviour [BSSC, 1997; AASHTO, 1999]. The nonlinear, hysteretic response of a bearing is represented by two parameters: an effective stiffness, K_{eff}, and equivalent viscous damping, ξ_{eff}. This is an idealisation of bearing behaviour, with the same inherent assumptions and limitations as in design approaches that make use of a "substitute structure" approach [Shibata and Sozen, 1976] to represent inelasticity of structural elements. For example, the equivalent stiffness and damping values are both fixed for a certain level of displacement (typically the design peak displacement), and the equivalent viscous damping is fixed for a single natural frequency of the excitation (the fundamental frequency of the bearing). Compared with typical civil engineering materials, however, the assumption of viscous damping holds more validity for elastomers, because some of the observed hysteretic energy dissipation is viscous (though nonlinear) in nature [Kelly, 1998].

In addition to the usual limitations of the substitute structure approach, the behaviour of HDR bearings is particularly difficult to characterise with a linearised viscoelastic model. As discussed in Chapter 2, the virgin bearing properties recover with time, and bearings can be expected to degrade over the course of induced cyclic deformations. Expressions for K_{eff} and ξ_{eff} given by manufacturers are typically calibrated for scragged bearings, and cannot be applied to virgin response.

The above comments notwithstanding, it should be emphasised that the linearised viscoelastic model

is a design tool, and bearing design based on the model can be verified with time history analysis using a more sophisticated model. A bilinear force–displacement model represents the next level of sophistication. Although the bilinear model is not required for time history analyses in design provisions, it forms the basis of the property modification factors concept outlined in the AASHTO Guide Specifications for Seismic Isolation Design [AASHTO, 1999], described in Section 6.2.2. For LR and FPS bearings, the physical interpretation of a bilinear model is more apparent. In the former case, the lead plug dominates the elastic stiffness, and when the lead yields, the post-yield stiffness is essentially the shear stiffness of the rubber. In the latter case, a very high initial stiffness is specified, primarily for computational convenience, and the post-yield stiffness represents the geometrical stiffness of the bearing.

In the case of HDR bearings, the bilinear hysteretic relationship is clearly an idealisation of the actual unidirectional behaviour. It is suggested [BSSC, 1997] that a bilinear hysteretic model (or a smoothed version of a bilinear model) is appropriate, provided that the peak shear strain is less than approximately 150–200%, depending on the rubber compound. Even within these limits, the three parameters used to define the model (for example, initial stiffness K, post-yield stiffness ratio α, and yield force F_y) are displacement dependent, which suggests that an iterative process is required to obtain appropriate values.

The relationship between the bilinear and linearised viscoelastic models is illustrated in Fig. 3.1, using the secant stiffness to characterise the equivalent linearisation. The total restoring force, equal to the elastic (spring) restoring force, F_s, plus the viscous damping force, F_d, is shown in the plots. For the rate-independent bilinear model the viscous force is zero, while for the viscoelastic model, the viscous force is linearly proportional to the velocity. As discussed in the previous section, the equivalent damping for the linearised model is commonly calculated such that the energy dissipated in a cycle *at resonant frequency* is equal to the energy dissipated in hysteresis in the bilinear model [AASHTO, 1999]. More sophisticated approaches for calculating the equivalent damping have also been used, based on optimisation of the peak response [Iwan and Gates, 1979], and on random vibration theory [Hwang *et al.*, 1994, 1996].

As noted by Kelly [1998], one implication of using a bilinear approach for elastomeric bearings is that damping at small to moderate displacements is underestimated. Clark and Kelly [1996] use the experimental observation that energy dissipated in a HDR bearing in one cycle is proportional to a power of displacement close to 1.5 to develop a viscoplastic model. Similarly, Tsai *et al.* [2003] adds a viscous element to a rate-independent hysteretic model to obtain a closer match for small strain response.

The Bouc–Wen model [Bouc, 1967] is also commonly used for elastomeric bearings. The model is particularly useful for stochastic analysis because of its differential equation form [Wen, 1976],

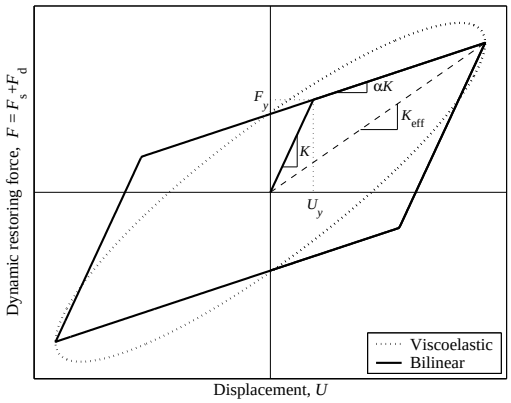

Figure 3.1. Relationship between bilinear and linearised viscoelastic models in terms of dynamic restoring force versus displacement.

and it has also been adapted for bidirectional response by Park *et al.* [1986], and generalised by Casciati [1989]. The Bouc–Wen model, in unidirectional or bidirectional form, may be considered a smoothed form of the classical bilinear model, and in this respect is similar to bounding surface plasticity, introduced for bidirectional loading in Section 3.2.2. Huang [2002] shows that the Bouc–Wen model performs similarly to the bounding surface model, although it violates Drucker's and Ilyushin's plasticity postulates [Lubliner, 1990]. Nevertheless, the Bouc–Wen framework is used as the basis of a unidirectional model recently developed by Tsai *et al.* [2003], which is discussed in Section 3.1.4.

Linear and bilinear models give a simple and convenient description of bearing response for design applications. The equivalent linearisation of bearing and structural properties is discussed further in Section 6.2.2. The strong nonlinearity of HDR bearings, however, and the change of bearing behaviour with cyclic loading suggest that improved models are required for accurate time history analysis of isolated structural systems. Some of these models are discussed in the following sections.

3.1.2 Hwang *et al.* [2002] Model

Several existing mathematical models for HDR bearings express the shear force as the summation of a restoring force and a damping force. The model of Hwang *et al.* [2002], modified from Pan and Yang [1996] to consider the effects of degradation, gives the bearing force, F in the form:

$$F(U,\dot{U}) = K(U,\dot{U},W_D)U + C(U,\dot{U},W_D)\dot{U} \tag{3.1}$$

where U and $\dot{U}$ are the relative displacement and velocity of the bearing, W_D is a history variable representing the work done, and K and C are nonlinear stiffness and damping coefficients, respectively.

The dependence of K and C on $U, \dot{U}$ and W_D is given by:

$$K(U, \dot{U}, W_D) = a_1 + a_2 U^2 + a_3 U^4 + \frac{a_4 \exp(a_9 W_D)}{\cosh^2(a_5 \dot{U})} \tag{3.2}$$

and

$$C(U, \dot{U}, W_D) = \frac{a_6 + a_7 U^2}{\sqrt{a_8^2 + \dot{U}^2}} (1 + \exp(a_{10} W_D)) \tag{3.3}$$

where a_1 to a_{10} are material parameters. Parameters a_1 to a_5 describe the shape of the elastic skeleton, and a_6 to a_8 determine the shape of the hysteresis loop through the nonlinear damping force. Finally, parameters a_9 and a_{10} describe the degradation with work done in cyclic loading, W_D, of the stiffness and damping, respectively.

Figure 3.2(a) illustrates the force–displacement behaviour of the Hwang *et al.* [2002] model, for high-strain level harmonic loading, with typical material parameters, a_1 to a_8. Degradation is neglected in the figure ($a_9 = a_{10} = 0$). The elastic skeleton provides the stiffening behaviour at high strains, and the damping force provides increasing hysteretic area as the strain level increases. The total restoring force from Eq. (3.1) is shown [Hwang *et al.*, 2002] to provide a good match of experimental data from unidirectional harmonic loading tests, when the ten material parameters are calibrated for each experiment.

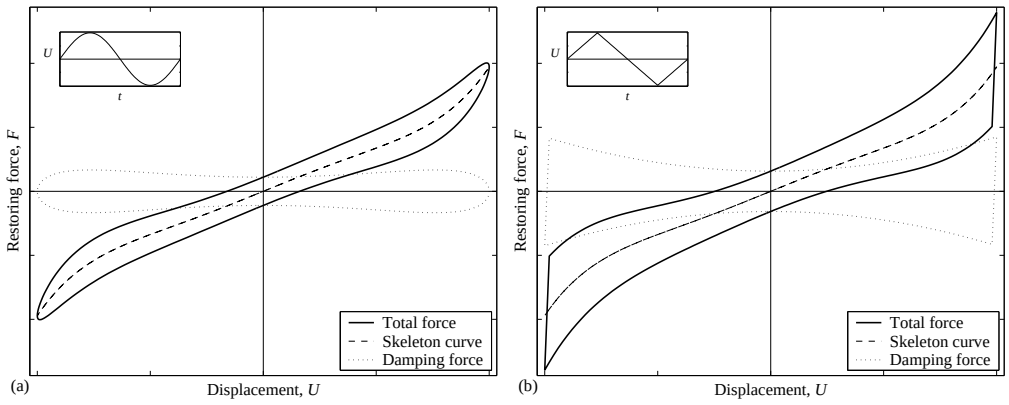

Figure 3.2. Force–displacement hysteresis for Hwang *et al.* [2002] model: total resisting force, F, and elastic (KU) and damping ($C\dot{U}$) components for (a) harmonic displacement history (inset), and (b) 'sawtooth' displacement history (inset).

Although the model provides a good match of experimental data for unidirectional and harmonic loading, a number of shortcomings can be observed. Despite the rate-dependence of Eq. (3.1), a separate parameter identification procedure must be carried out for loading at different strain rates [Hwang *et al.*, 2002], and there can be significant differences between the two sets of material parameters obtained for a single bearing. The velocity term appearing in the expressions for K

and C simply provides a harmonic component out of phase with the displacements, which is only relevant for sinusoidal loading. When applied to 'sawtooth' displacement histories, the velocity is a step function, and the model cannot adequately represent the force–deformation behaviour. Figure 3.2(b) illustrates the hysteretic behaviour under such a displacement history. The elastic skeleton is not changed significantly, but the damping component continues to increase with the square of the displacement, and changes abruptly when the direction of loading reverses. This behaviour is not observed in experimental tests carried out with sawtooth displacement histories, such as those described in Section 2.2, and a smoother transition would be desirable. It could be argued, however, that the sawtooth displacement history can never be recreated exactly in an experimental setting, and a more gradual transition would be observed under an experimental displacement input.

A second shortcoming with the Hwang *et al.* [2002] model is the calibration procedure used to obtain material parameters for a bearing. Although the model describes scragging and Mullins' effects for a given test, a separate parameter identification is performed on subsequent tests of post-scragged behaviour, and the damage parameter is reset to zero. As with the calibration at different strain rates, there are significant changes in material parameters between tests. These changes are not consistent with the damage model used for scragging and Mullins' effect, as even components of the stiffness and damping that do not degrade are changed between calibrations. It would be desirable to calibrate the model over a series of tests, retaining damage variables between tests, to obtain a unique set of material parameters for a given bearing. This approach is discussed further in Chapter 5.

Jankowski [2004] presents another adaptation of the model due to Pan and Yang [1996], which slightly improves the response of the original model under small loading cycles. This model, however, exhibits the same shortcomings as the Hwang *et al.* [2002] model, discussed above.

3.1.3 Kikuchi and Aiken [1997] Model

Kikuchi and Aiken [1997] present a strain-rate independent model, similar to Hwang *et al.* [2002]. The steady-state force–displacement response is given by the following expression:

$$F(U, U_i, F_i, n) = F_1(U) + F_2(U, U_i, F_i, n) + \Delta F(U) \tag{3.4}$$

where F_1 and F_2 describe an elastic skeleton and hysteretic damping force, respectively, and ΔF represents the difference between first cycle response and the subsequent cycles. In addition to Eq. (3.4), a set of hysteresis rules based on Masing's rules [Masing, 1926] is used to characterise the response under a randomly varying displacement history. To describe the hysteretic response, U_i and F_i are the displacement and force at the most recent load reversal, and $n = \text{sgn}(U)$ gives the direction of loading.

The elastic skeleton, F_1, is given by:

$$F_1 = \frac{1}{2}(1-\phi)F_m\{u + \text{sgn}(U)|u|^n\} \tag{3.5}$$

and the hysteretic force, F_2:

$$\begin{aligned} F_2 &= \phi F_m\{1 - 2\exp(-a(1+u)) + b(1+u)\exp(-c(1+u))\}, \qquad \text{for } \dot{U} > 0 \\ F_2 &= -\phi F_m\{1 - 2\exp(-a(1-u)) + b(1-u)\exp(-c(1-u))\}, \qquad \text{for } \dot{U} < 0 \end{aligned} \tag{3.6}$$

where ϕ is the ratio of force at zero displacement to a maximum reference force, F_m, and u is the displacement normalised with respect to a corresponding reference displacement, U_m . The exponent n gives a measure of stiffening in the elastic skeleton. Parameters a, b and c control the shape of the hysteresis loop: a and b are determined by equating the area of the experimental and analytical hysteresis loops, and c is a preselected material constant.

The reference force value, F_m, is determined from the reference displacement U_m from an experimentally-determined, strain-dependent equation involving six parameters. The increment ΔF in Eq. (3.4) is calculated in the same manner, from virgin test data and five parameters. The values of ϕ, the equivalent experimental damping, h_{eq}, and the exponent, n, from Eq. (3.5) are given by two, three and four-parameter equations in terms of the shear strain, respectively. Finally, the value of c, and upper bounds on a and b, account for another three constants to be determined from experiments. Although many of these expressions are of a form commonly reported in laboratory experiments, the task of calibrating 23 material parameters for a new bearing is a demanding requirement for the practical use of the model.

A typical steady-state force–displacement envelope for high strain levels is illustrated in Fig. 3.3. In Fig. 3.3(a), the addition of the first two components, F_1 and F_2 is shown. As with the previously discussed model, the elastic term accounts for the stiffening behaviour, while the hysteretic term provides nonlinear damping. In Fig. 3.3(b), the force envelope for the first and subsequent cycles are shown. The difference between the two curves is equal to the force increment, ΔF, which is only applied on the first cycle. It should be noted that this increment is applied over the whole first cycle in this model, whereas experimental evidence (Section 2.2) suggests that most degradation occurs in the first half cycle. Note also that no further degradation is applied after the first cycle, which is an approximation of actual bearing behaviour.

3.1.4 Tsai *et al.* [2003] Model

Tsai *et al.* [2003] recently proposed a force–displacement model for HDR bearings based on the Bouc–Wen hysteretic model, introduced in Section 3.1.1. A linear viscous term was added to this rate-independent component to more accurately describe small strain response. Although expressions

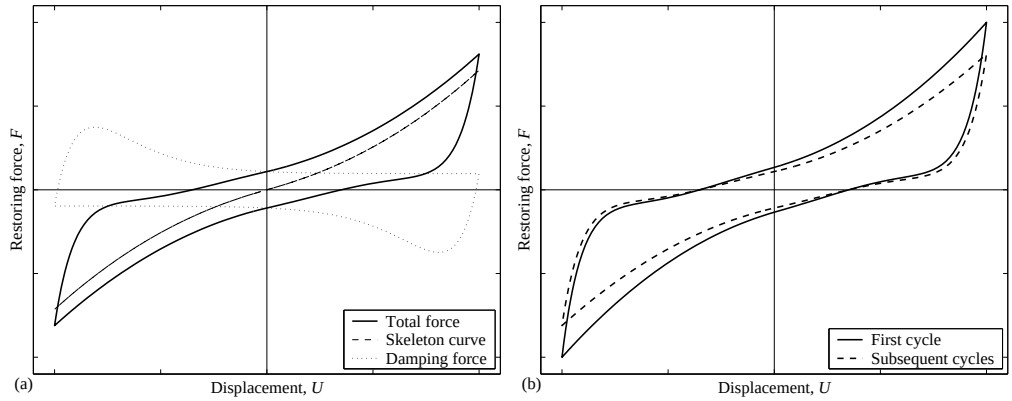

Figure 3.3. Force–displacement hysteresis envelope for Kikuchi and Aiken [1997] model. (a) Total steady-state resisting force, and elastic and damping components, and (b) virgin and scragged response.

are given for the force in two orthogonal directions, the components are uncoupled. As was shown in Section 2.2, two uncoupled unidirectional models are unable to describe the bidirectional response of HDR bearings.

The unidirectional force–displacement response is therefore expressed as:

$$F(U, \dot{U}, Z) = F_s(U, Z) + F_v(\dot{U}) \tag{3.7}$$

where F_s and F_v are the rate-independent hysteretic force, and the rate-dependent viscous force. The latter is given by a linear viscous damping equation, with viscosity coefficient, C:

$$F_v = C\dot{U} \tag{3.8}$$

The former is expressed in incremental form, in terms of a normalised plastic internal variable, $-1 < Z < 1$, which represents the evolution from elastic ($Z = 0$) to fully plastic ($Z = \pm 1$) response. In time discrete form, F_s is given by:

$$F_s = F_{s,n} + D(U - U_n) \tag{3.9}$$

where the subscript n represents quantities at the previous time step, and D is the tangent stiffness. In the standard, smoothed bilinear Bouc–Wen formulation [Bouc, 1967; Wen, 1976], D may be expressed as:

$$D = \alpha K + (1 - \alpha)K[A - (\gamma \text{sgn}(\dot{U}Z) + \xi)Z^2] \tag{3.10}$$

where A, γ and ξ are material constants; recommended values are 1.0, 0.1 and 0.9, respectively [Tsopelas *et al.*, 1994]. The terms K and α are the initial stiffness and plastic stiffness ratio, respectively, and are taken as constant in the original Bouc–Wen model. The evolution of Z is also governed by an incremental equation [Tsai *et al.*, 2003].

The main innovation in the Tsai *et al.* [2003] model is the introduction of strain-dependence to the stiffness terms, $K = K(U)$ and $\alpha = \alpha(U)$ in Eq. (3.10). The authors report that the initial stiffness, $K(U)$, has been calculated experimentally in terms of the maximum shear strain, although the relationship is not provided in the paper. The ratio of tangent stiffness to initial stiffness, $\alpha(U) = K_T(U)/K(U)$, is similarly determined from experimental data for K_{eff}, as a function of displacement. Different values for K_T are given for unloading, based on the envelope shown in Fig. 3.4. The solid line portions are obtained directly from the experimental data, the dashed lines are at constant slope determined by a model parameter, and the dotted line is given by a transition equation between the slopes before and after. The size of the transition region is governed by another material parameter. At each time step, the appropriate values of $K(U)$ and $\alpha(U)$ are substituted into Eq. (3.10), then the force on the bearing is calculated from Eqs. (3.9) and (3.7).

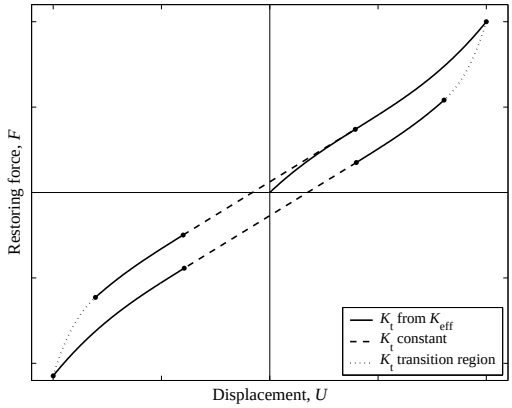

Figure 3.4. Force–displacement hysteresis envelope for Tsai *et al.* [2003] model.

The biggest shortcoming of the Tsai *et al.* [2003] model is that degradation with cyclic loading is not included. Even if a damage parameter were added to the model to describe this degradation, it seems that the original framework would be inadequate for describing virgin response. In particular, the use of a constant tangent slope for the dashed line portion of Fig. 3.4, and the form of the equation for the transition region, shown as a dotted line, does not easily permit the nonlinear damping, increasing with shear strain, observed in experimental tests of virgin response (Section 2.2). It is possible that a modified form of transition slope equation could be introduced to properly account for this nonlinearity in damping, although this would require the introduction of additional material parameters.

It is not clear how the model is calibrated for the series of tests presented in [Tsai *et al.*, 2003]. Although the model describes the behaviour of scragged HDR bearings with different levels of axial

load, strain level and strain rate, it appears that a separate set of material parameters are obtained for each test. For example, the model response is different in two tests for the same strain history and strain rate, but with different axial load. Because the effect of axial load is not accounted for in the mathematical model, it is reasonable to assume that different calibrations have been used for every test. If this is the case, then the ability of the model to capture the strain-rate dependence of a given bearing is questionable, as with the Hwang *et al.* [2002] model, discussed in Section 3.1.2.

Finally, because the equations used for K_{eff} in terms of shear strain are not provided in the reference, it is impossible to judge exactly how many material constants must be calibrated for a given material. However, if the Kikuchi and Aiken [1997] model, discussed in Section 3.1.3 is any indication, six parameters will be required to define the backbone curve of $K_T(U)$ (the solid line in Fig. 3.4), and presumably several more for the initial stiffness, $K(U)$. Additionally, three parameters are required to define the various regions in Fig. 3.4, three more (A, ξ and γ) define the Bouc–Wen evolutionary equation, and one (C) represents the linear viscous damping term. As with the Kikuchi and Aiken [1997] model, it could be argued that many of these parameters are readily available from manufacturer guidelines or are consistently obtained in experimental testing. In any case, a large number of material parameters are required.

3.2 Plasticity-based Approaches to Bidirectional Bearing Modelling

Aside from fully three-dimensional constitutive models applied in a finite element setting [Miehe and Keck, 2000; Haupt and Sedlan, 2001], no phenomenological models have been specifically developed for the bidirectional behaviour of HDR bearings. Huang [2002] has applied bidirectional models based on rate-independent classical and bounding surface plasticity to lead–rubber (LR) bearings, and obtained a good match of experimental data. Huang also calibrated a classical plasticity model for the HDR test data from the Caltrans Protective Systems Project (Chapter 2.1), but did not obtain a good match of the experimental behaviour across the full range of strains. In particular, classical and bounding surface plasticity is unable to capture the strain-stiffening behaviour at high strains, and path dependence of HDR bearings.

Nevertheless, these plasticity-based attempts highlight many of the difficulties in developing bidirectional models for HDR bearings. For this reason, this section contains a summary of these various approaches, primarily adapted from the work of Huang [2002]. In addition, a first attempt at modifying the plasticity models to describe the characteristic strain-stiffening behaviour is presented in Section 3.2.3, through the addition of a 'stiffening surface' model in parallel to the standard bounding surface model.

In the following, the bidirectional force and displacement quantities are expressed in terms of vector

quantities $\mathbf{F}$ and $\mathbf{U}$, given by:

$$\mathbf{F} = \begin{Bmatrix} F_x \\ F_y \end{Bmatrix} \quad ; \qquad \mathbf{U} = \begin{Bmatrix} U_x \\ U_y \end{Bmatrix} \tag{3.11}$$

where the subscripts x and y refer to the components of a quantity in orthogonal directions in the plane of the bearing. The dot product and tensor product of two column vectors are defined, respectively, by:

$$\mathbf{a} \cdot \mathbf{b} = \mathbf{a}^T \mathbf{b} \quad ; \qquad \mathbf{a} \otimes \mathbf{b} = \mathbf{a}\mathbf{b}^T \tag{3.12}$$

where the superscript 'T' represents vector transposition.

In plasticity theory, the displacement vector is additively decomposed into an elastic part, which is recovered upon unloading, and a plastic part, which represents unrecoverable deformation:

$$\mathbf{U} = \mathbf{U}^e + \mathbf{U}^p \tag{3.13}$$

This assumption is used in the models presented in the remainder of this chapter.

3.2.1 Classical Plasticity with Kinematic Hardening

A classical rate-independent plasticity model [Lubliner, 1990] with linear kinematic hardening may be considered a bidirectional generalisation of the bilinear unidirectional model discussed in Section 3.1.1. The time continuous version of the model is discussed below, followed by the time discretisation, solution algorithm, and application to the HDR bearing experimental data.

3.2.1.1 Time continuous model. An isotropic yield function is postulated, which delineates the boundary between elastic and plastic states. With a "back force" $\boldsymbol{\alpha}_y$, and a radius R_y, the yield function is given by:

$$f_y = \|\mathbf{F} - \boldsymbol{\alpha}_y\| - R_y \tag{3.14}$$

The equation $f_y = 0$ then defines a circular yield surface in bidirectional force space. Within this yield surface, the response may be considered linearly isotropic, with the force related to the displacement by a constant stiffness parameter, K_1. In combination with the elastic-plastic decomposition of the displacement vector, Eq. (3.13), the following expression is assumed:

$$\mathbf{F} = K_1 \mathbf{U}^e = K_1(\mathbf{U} - \mathbf{U}^p) \tag{3.15}$$

For many applications, an associative plastic flow rule is both computationally convenient, and gives a good fit of experimental data. Indeed, an associative flow rule has been shown to describe the experimentally observed force vector, for lead–rubber bearings [Huang *et al.*, 2000] and high-damping

rubber bearings at low to moderate strain levels [Huang, 2002]. Associative flow implies that the evolution of the plastic displacement vector is always normal to the yield surface in force space:

$$\dot{\mathbf{U}}^p = \dot{\gamma}\frac{\partial f_y(\mathbf{F}, \boldsymbol{\alpha}_y)}{\partial \mathbf{F}} = \dot{\gamma}\mathbf{n} \tag{3.16}$$

where $\dot{\gamma}$ is the time continuous consistency parameter, and $\mathbf{n}$ is given by:

$$\mathbf{n} = \frac{\partial f_y(\mathbf{F}, \boldsymbol{\alpha}_y)}{\partial \mathbf{F}} = \frac{\mathbf{F} - \boldsymbol{\alpha}_y}{\|\mathbf{F} - \boldsymbol{\alpha}_y\|} \tag{3.17}$$

The consistency parameter, $\dot{\gamma}$, must satisfy the Kuhn–Tucker conditions [Lubliner, 1990]:

$$f_y \leq 0, \qquad \dot{\gamma} f_y = 0, \qquad \dot{\gamma} \geq 0 \tag{3.18}$$

The Kuhn–Tucker conditions of Eq. (3.18) require elastic force states (for which $\dot{\gamma} = 0$) to lie on or inside the yield surface, and plastic force states ($\dot{\gamma} > 0$) to lie on the yield surface. Furthermore, the consistency condition must be satisfied, given by:

$$\dot{\gamma}\dot{f}_y = 0 \tag{3.19}$$

which prohibits the force point from leaving the yield surface during plastic flow.

Finally, a linear kinematic hardening rule is specified, with:

$$\dot{\boldsymbol{\alpha}}_y = K_2\dot{\mathbf{U}}^p = K_2\dot{\gamma}\mathbf{n} \tag{3.20}$$

where K_2 is a constant hardening modulus. Note that in a unidirectional force–displacement history, with elastic stiffness K_1, and second slope αK_1, the hardening modulus is given by:

$$K_2 = K_1\frac{\alpha}{(1-\alpha)} \tag{3.21}$$

3.2.1.2 Integration algorithm. For use of the plasticity model in a discrete time regime, the time continuous rate equations of the previous section must be integrated. The problem may be considered displacement driven, in that the displacement history $\{\mathbf{U}_n, \mathbf{U}_{n+1}\}$ is known over a time step, Δt, and $\mathbf{F}_{n+1}$ is to be determined. A backward Euler implicit integration scheme is used to evaluate the discrete change in model variables over the time step, and calculate $\mathbf{F}_{n+1}$ from Eq. (3.15).

In the following, quantities at time t_n carry a subscript 'n', and, to minimise the appearance of subscripts, quantities at time $t_{n+1} = t_n + \Delta t$ carry no subscript. Furthermore, the discrete consistency parameter is denoted by λ, where:

$$\lambda = \int_{t_n}^{t_{n+1}} \dot{\gamma}\,\mathrm{d}t$$

Using the backward Euler scheme, the plastic displacement rate equation, Eq. (3.16), and the hardening expression, Eq. (3.20), are integrated to obtain:

$$\mathbf{U}^p = \mathbf{U}^p_n + \lambda \mathbf{n} \tag{3.22}$$

and

$$\boldsymbol{\alpha}_y = \boldsymbol{\alpha}_{y,n} + K_2 \lambda \mathbf{n} \tag{3.23}$$

This expression is substituted into Eq. (3.15) to give:

$$\mathbf{F} = K_1(\mathbf{U} - \mathbf{U}^p_n - \lambda \mathbf{n}) \tag{3.24}$$

Finally the Kuhn–Tucker conditions, Eq. (3.18), in their discrete forms are given by:

$$f_y \leq 0, \qquad \lambda f_y = 0, \qquad \lambda \geq 0 \tag{3.25}$$

The time discrete system of equations can be conveniently and efficiently solved using the return mapping algorithm [Simo and Hughes, 1998]. To this end, an elastic trial state at time t_{n+1} is obtained by setting the discrete consistency parameter to zero, effectively freezing plastic flow for the time step. Substituting $\lambda = 0$ into Eqs. (3.14), (3.22), (3.23) and (3.24) the following trial state values (denoted by a 'tr' superscript) are obtained:

$$\begin{cases} \mathbf{U}^{p,tr} = \mathbf{U}^p_n \\ \mathbf{F}^{tr} = K_1(\mathbf{U} - \mathbf{U}^p_n) \\ \boldsymbol{\alpha}^{tr}_y = \boldsymbol{\alpha}_{y,n} \\ f^{tr}_y = \|\mathbf{F}^{tr} - \boldsymbol{\alpha}^{tr}_y\| - R_y \end{cases} \tag{3.26}$$

If $f^{tr}_y \leq 0$, then the Kuhn–Tucker conditions (3.25) are all satisfied by the trial state values given in Eq. (3.26). Therefore, the time step Δt is elastic as assumed, and the correct state at time t_{n+1} is given by Eq. (3.26).

However, if $f^{tr}_y > 0$, then Eq. $(3.25)_1$ is violated for the trial state, and the time step must result in inelastic deformation. For $\lambda \neq 0$, $(3.25)_2$ requires that $f_y = 0$, and Eqs. (3.22), (3.23) and (3.24) give the following plastic state, as functions of the trial state values in Eq. (3.26):

$$\begin{cases} \mathbf{U}^p = \mathbf{U}^{p,tr} + \lambda \mathbf{n} \\ \mathbf{F} = K_1(\mathbf{U} - \mathbf{U}^{p,tr} - \lambda \mathbf{n}) = \mathbf{F}^{tr} - K_1 \lambda \mathbf{n} \\ \boldsymbol{\alpha}_y = \boldsymbol{\alpha}^{tr}_y + K_2 \lambda \mathbf{n} \end{cases} \tag{3.27}$$

Substituting Eq. (3.27) into Eq. (3.17) it can easily be shown that $\mathbf{n} = \mathbf{n}^{tr}$. Therefore, taking the dot product of both sides with $\mathbf{n}$, substituting for R_y from Eq. (3.14), and solving for λ, the following expression for the discrete consistency parameter is obtained:

$$\lambda = \frac{\left\|\mathbf{F}^{tr} - \boldsymbol{\alpha}_y^{tr}\right\| - R_y}{K_1 + K_2} = \frac{f_y^{tr}}{K_1 + K_2} \tag{3.28}$$

The consistency parameter is substituted into Eq. (3.27) to obtain the present state corrected for the plastic deformation.

3.2.1.3 Model application. In this section, the calculated response of a linear kinematic hardening plasticity model is compared with the medium strain behaviour of HDR bearings. Huang [2002] calibrated this model separately for each of the tests referred to in Table 2.1. The nonlinearity of the force–deformation response of HDR bearings meant that the material parameters obtained varied significantly with strain level. In addition, Huang [2002] found that the parameters also varied significantly with the displacement orbit used in the test. This suggests that even if the nonlinearity in the unidirectional force–deformation response could be described by nonlinear hardening equations, a classical plasticity approach is not adequate for modelling the bidirectional response.

The three model parameters obtained in the calibration of Huang for test 12 (orbit 2 with 100% maximum strain in each direction) were: $K_1 = 3.29$ kips/in., $K_2 = 1.68$ kips/in. and $R_y = 1.15$ kips. Different model parameters were used to characterise the bilinear curve in the reference, so these have been converted to the parameters used in the model description above. Using these material parameters, Fig. 3.5 shows a comparison of experimental and model response. The figure suggests that at this moderate strain level, a properly calibrated classical plasticity model can describe approximately the bidirectional coupling in the response. At the point in the displacement orbit when the loading first changes from the x- to the y-direction, the force point follows the circumference of the yield surface until subsequent plastic flow is in the direction of loading. This results in approximately the correct amount of coupling between force components for a well-calibrated classical plasticity model, although the force trajectory of the experimental data is not followed perfectly.

Beyond this strain level, the stiffening and degradation behaviour of HDR bearings cannot be captured by the linear hardening model. Furthermore, even at moderate strains and below, the classical plasticity model must be recalibrated for every strain level and displacement orbit, which is inadequate for structural analysis and design applications. The next sections describe extensions to the classical plasticity framework which address these issues.

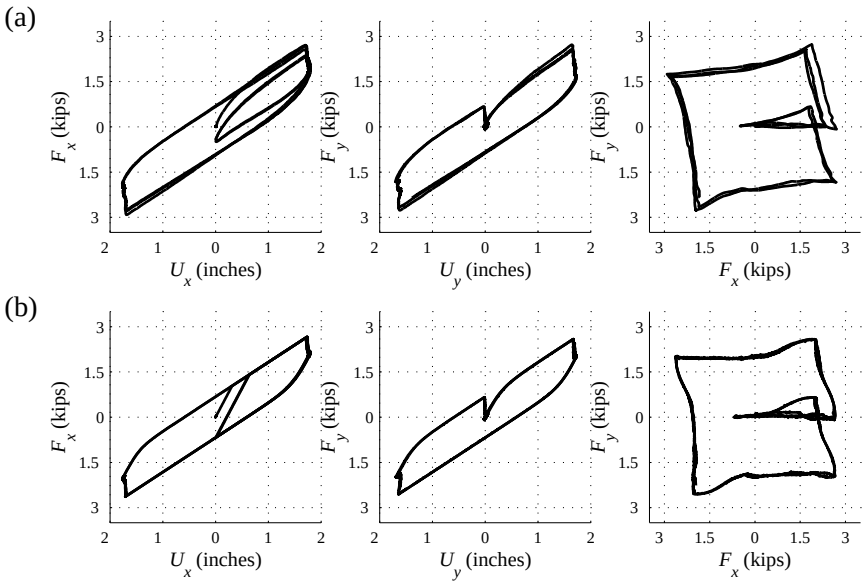

Figure 3.5. (a) Experimental response and (b) classical plasticity model response for test 12: orbit 2, $\gamma_x = \gamma_y = 100\%$, slow strain rate.

3.2.2 Bounding Surface Model

Bounding surface plasticity is a commonly used framework for the development of constitutive models for soils [e.g. Dafalias and Herrmann, 1982] and metals [e.g. Krieg, 1975; Dafalias and Popov, 1975]. Bounding surface model response is characterised by a smooth transition from elastic to plastic behaviour, and, on reloading, the onset of plasticity at a stress level lower than that reached previously. This is more representative of the response of real materials, including HDR bearings at strains less than approximately 150%, than provided by a classical plasticity model with linear kinematic hardening. Bounding surface plasticity may be considered a generalisation of classical plasticity, with a nonlinear kinematic hardening law. More importantly, the bounding surface model does not require recalibration at different strain levels because the inelastic stiffness is strain-dependent.

The main feature of bounding surface plasticity is the postulation of a "bounding surface" in stress (force) space, which delineates the boundary between admissible and inadmissible stress states, in addition to the yield surface of classical plasticity. Although there are many different types of model within the general framework, a common requirement of all bounding surface models is a mapping of the current stress state onto a stress state on the bounding surface, called the "image stress". With this defined, an expression for the plastic modulus at any inelastic stress state within the bounding surface is given as a function of the distance from the current stress to the image stress and the

asymptotic plastic modulus at the image stress. This allows a smooth transition from the elastic stiffness, at the immediate onset of yielding, to a fully plastic stiffness as the stress point moves towards the bounding surface.

Huang [2002] shows that a bounding surface model provides a good description of the unidirectional cyclic behaviour of LR isolation bearings. Furthermore, he presents a bidirectional "improved parallel" model which makes use of a bounding surface backbone for LR bearings, which is described in the following section. In this section, a bidirectional bounding surface model is presented, based on the generalisation of the model by Dafalias [1986], and applied to medium strain HDR bearing response.

3.2.2.1 Time continuous model description. In the bounding surface formulation, elastic behaviour within a yield surface in force space is considered, as with the classical plasticity model (Eqs. (3.14) and (3.15)). Furthermore, a circular bounding surface is also postulated in force space, and is defined by the following expression:

$$f_b = \|\hat{\mathbf{F}} - \boldsymbol{\alpha}_b\| - R_b = 0 \tag{3.29}$$

where $\boldsymbol{\alpha}_b$ and R_b define the centre and radius of the bounding surface, as before. The "image force", $\hat{\mathbf{F}}$, may be defined by an appropriate mapping rule, and represents a mapping of the current force state, $\mathbf{F}$, onto the bounding surface. A homologous mapping rule is commonly used with purely kinematic hardening, which is given by:

$$\hat{\mathbf{F}} = b(\mathbf{F} - \boldsymbol{\alpha}_y) + \boldsymbol{\alpha}_b \tag{3.30}$$

where b is a constant material parameter. By substituting Eq. (3.30) into Eq. (3.29), it can be seen that b represents the ratio of the radii of the two surfaces, R_b/R_y, provided that $f_y = 0$ holds. When $f_y < 0$, either one of the material parameters (R_y, R_b, b) must change, or the image force does not lie on the bounding surface.

Although the image force is only required for inelastic states ($f_y = 0$), it is more consistent to define a mapping rule of the form:

$$\hat{\mathbf{F}} = R_b\mathbf{n} + \boldsymbol{\alpha}_b \tag{3.31}$$

where $\mathbf{n}$ is the outward normal vector to the yield surface at the current force point, and is defined as before (3.17). While Eqs. (3.30) and (3.31) are equivalent for inelastic states, the latter gives an image force which satisfies Eq. (3.29) for $f_y < 0$.

The homologous mapping rule of Eq. (3.31), combined with the assumption of associative flow, allows the following evolutionary expression for the plastic displacement:

$$\dot{\mathbf{U}}^p = \dot{\gamma}\frac{\partial f_b(\hat{\mathbf{F}}, \boldsymbol{\alpha}_b)}{\partial \hat{\mathbf{F}}} = \dot{\gamma}\frac{\partial f_y(\mathbf{F}, \boldsymbol{\alpha}_y)}{\partial \mathbf{F}} = \dot{\gamma}\mathbf{n} \tag{3.32}$$

where $\dot{\gamma}$ is the time continuous consistency parameter, as before. The consistency parameter must satisfy the Kuhn–Tucker conditions, which in bounding surface plasticity are usually defined in terms of the bounding function, f_b. In the current formulation, however, in which purely kinematic hardening is used (defined below), the conditions may be postulated in terms of the yield function, f_y, as stated previously in Eq. (3.18).

The principal advantage of the bounding surface formulation over classical plasticity is in the modelling of hardening, especially for cyclic loading histories. It was postulated in the original presentations of bounding surface plasticity [Dafalias and Popov, 1975; Krieg, 1975] that the plastic modulus at a given force state may be defined as a function of the distance to the bounding surface, and appropriate "plastic internal variables" [Dafalias and Popov, 1976] representing the prior loading history. Dafalias [1986] changed the scalar distance term to a vector connecting the current force and the image force:

$$\boldsymbol{\delta} = \hat{\mathbf{F}} - \mathbf{F} \tag{3.33}$$

The prior loading history is taken into account by the internal variable, $\boldsymbol{\delta}_{in}$, which represents the value of $\boldsymbol{\delta}$ immediately after the last detection of unloading. In this manner, the value of $\boldsymbol{\delta}$ reduces from a value of $\boldsymbol{\delta}_{in}$ to $\mathbf{0}$ on plastic loading and reloading. An unloading condition may be considered in the following form [Dafalias, 1986]:

$$\boldsymbol{\delta}_{in} \cdot \mathbf{n} - \boldsymbol{\delta} \cdot \mathbf{n} < 0 \tag{3.34}$$

which allows for the update of $\boldsymbol{\delta}_{in}$ under general bidirectional loading, even if a sharp change in loading direction does not occur.

Note that the dependence of the plastic modulus on the discontinuous parameter, $\boldsymbol{\delta}_{in}$, results in a non-smooth force–displacement response upon unloading. This is not a problem for general loading histories, but it can lead to difficulties when small perturbations in the loading occur. In this case, a small reversal in load may result in the satisfaction of Eq. (3.34), and the updating of $\boldsymbol{\delta}_{in}$. On reloading in the original direction, the plastic modulus will be defined with respect to the new $\boldsymbol{\delta}_{in}$, and stiffer model response will be observed. This 'overshooting' phenomenon, first recognised by Dafalias [1986], is of particular significance when using experimental displacement histories, which may be influenced by fluctuations in equipment response. Dafalias suggests the use of a threshold of reverse plastic strain (displacement) accumulation before $\boldsymbol{\delta}_{in}$ is updated. This will lead to discontinuity in the plastic modulus as the threshold is exceeded, but should limit the effect of small load perturbations on the model response.

To simplify the current model, a modified version of this proposal is adopted here. Instead of a plastic displacement threshold, a force threshold is used, whereby the update of $\boldsymbol{\delta}_{in}$ occurs only

when both the unloading condition (3.34) and the yield surface equation (3.14) are satisfied[1]. The implication is that small unloading cycles within the elastic range ($f_y < 0$) will not affect subsequent loading, and the model response is less susceptible to small load perturbations. The update of $\boldsymbol{\delta}_{in}$ now occurs with the first onset of plastic flow ($f_y = 0$) in an unloading state (3.34), at which time $\boldsymbol{\delta}_{in}$ is set equal to the current value of $\boldsymbol{\delta}$[2].

With an appropriate definition of $\boldsymbol{\delta}$ and $\boldsymbol{\delta}_{in}$, evolutionary equations for the internal hardening variables of the model may be defined. Adopting a purely kinematic hardening formulation, R_y and $R_b = bR_y$ are taken as constant, and the evolution of the back force terms, $\boldsymbol{\alpha}_y$ and $\boldsymbol{\alpha}_b$, is defined through rate equations. As with many classical plasticity applications, Prager's kinematic hardening rule is adopted for the first of these back force rate terms, whereby $\dot{\boldsymbol{\alpha}}_y$ is defined parallel to the plastic displacement increment:

$$\dot{\boldsymbol{\alpha}}_y = (K_2 + \Delta K_p)\,\dot{\mathbf{U}}^p = (K_2 + \Delta K_p)\,\dot{\gamma}\mathbf{n} \tag{3.35}$$

where K_2 is the asymptotic plastic stiffness of the bearing, and ΔK_p is an appropriately defined scalar function of $\boldsymbol{\delta}$, $\boldsymbol{\delta}_{in}$ and $\mathbf{n}$. For a smooth transition from elastic, to inelastic, to perfectly plastic response, it is required that $\Delta K_p = \infty$ for $\boldsymbol{\delta} = \boldsymbol{\delta}_{in}$ and $\Delta K_p \to 0$ for $\boldsymbol{\delta} \to \mathbf{0}$. A possible function, adapted from Dafalias [1986], is:

$$\Delta K_p = K_3 \left[\frac{\boldsymbol{\delta} \cdot \mathbf{n}}{(\boldsymbol{\delta}_{in} - \boldsymbol{\delta}) \cdot \mathbf{n}} \right] \tag{3.36}$$

where K_3 is a material parameter describing the transition from elastic to fully plastic response, with dimensions of stiffness. The term in square brackets takes values from ∞ to 0, for $\boldsymbol{\delta}$ between $\boldsymbol{\delta}_{in}$ and $\mathbf{0}$.

As shown by Dafalias and Popov [1976], Prager's hardening rule is not appropriate for the evolution of the back force term, $\boldsymbol{\alpha}_b$. It is important for the consistency of the model that convergence of the two surfaces occurs along a unit vector joining the current force point and the image force – i.e. a unit vector in the direction of $\boldsymbol{\delta}$ – and any contact of the surfaces occurs at the current force point. It is required that the yield surface may contact the bounding surface, but may not overlap. Because of the homologous mapping rule used here, for which $\mathbf{n} = \partial f_y/\partial \mathbf{F} = \partial f_b/\partial \hat{\mathbf{F}}$, this condition can only be satisfied if contact is confined to the current force point. Furthermore, on contact, it is required that the two surfaces translate together, such that $\dot{\boldsymbol{\alpha}}_y = \dot{\boldsymbol{\alpha}}_b = K_2\dot{\mathbf{U}}^p$.

[1] The use of the yield surface as a force threshold is in fact equivalent to the plastic displacement threshold, $\dot{\mathbf{U}}^p = 0$, as a nonzero value of $\dot{\mathbf{U}}^p$ implies yielding is occurring.

[2] It is interesting to note that this realisation of $\boldsymbol{\delta}_{in}$ is much closer to the original, uniaxial definition as "the value of δ at the initiation of yielding for each loading process..." [Dafalias and Popov, 1976], while the multiaxial generalisation of this definition in the same paper referred to an update of $\boldsymbol{\delta}_{in}$ "at each stress reversal".

The above conditions can be satisfied by a hardening equation of the following form [Dafalias and Popov, 1976]:

$$\dot{\boldsymbol{\alpha}}_b = \dot{\boldsymbol{\alpha}}_y - M\boldsymbol{\mu} \tag{3.37}$$

where M is an appropriately selected function, which specifies the rate of convergence of the two surfaces along $\boldsymbol{\mu} = \boldsymbol{\delta}/\|\boldsymbol{\delta}\|$.

Based on the general form given by Eq. (3.37), the following expression for $\dot{\boldsymbol{\alpha}}_b$ is considered:

$$\dot{\boldsymbol{\alpha}}_b = \dot{\boldsymbol{\alpha}}_y - \Delta K_p \frac{\dot{\gamma}\boldsymbol{\delta}}{\boldsymbol{\delta}\cdot\mathbf{n}} \tag{3.38}$$

For uniaxial loading, $\boldsymbol{\mu} = \mathbf{n}$, and Eq. (3.38) gives:

$$\dot{\boldsymbol{\alpha}}_b = \dot{\boldsymbol{\alpha}}_y - \Delta K_p \dot{\mathbf{U}}^p = K_2 \dot{\mathbf{U}}^p \tag{3.39}$$

while for more general loading conditions, the following expression results:

$$\dot{\boldsymbol{\alpha}}_b = \left[K_2\mathbf{n} + \Delta K_p \left(\mathbf{n} - \frac{\boldsymbol{\delta}}{\boldsymbol{\delta}\cdot\mathbf{n}} \right) \right] \dot{\gamma} \tag{3.40}$$

The unidirectional response of the bounding surface model is illustrated in Fig. 3.6(a). When force is plotted against plastic displacement, the bounding surface is a pair of straight lines with slope K_2. As the plastic displacement increases, the plastic modulus evolves from initially infinite within the yield surface, to K_2 as the force approaches the bounding surface.

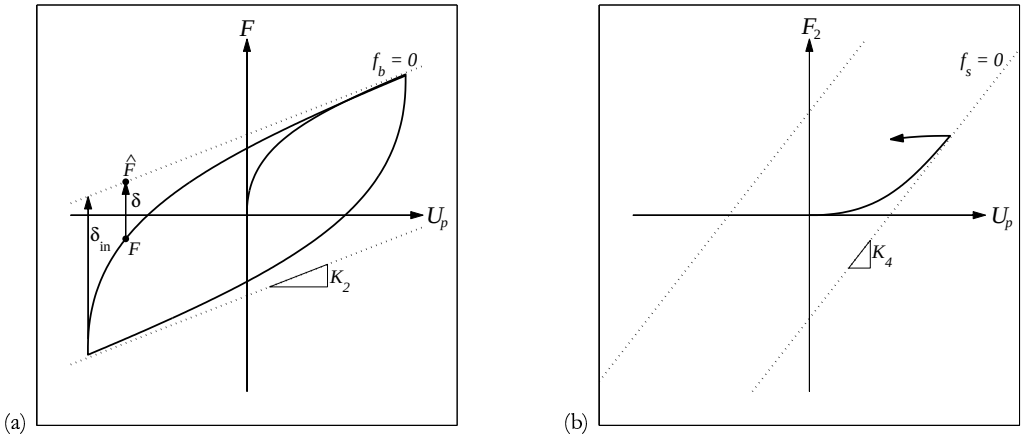

Figure 3.6. Unidirectional response of (a) bounding surface and (b) stiffening surface models.

3.2.2.2 Integration algorithm. As with the classical plasticity model time integration, a backward Euler implicit integration scheme is used to evaluate the discrete change in model variables over the time step. The return mapping algorithm is set up in the same manner as Section 3.2.1, with an additional step added for the unloading check. As before, the elastic trial state at time t_{n+1} is obtained by freezing plastic flow over the time step:

$$\begin{cases} \mathbf{U}^{p,tr} = \mathbf{U}_n^p \\ \mathbf{F}^{tr} = K_1(\mathbf{U} - \mathbf{U}_n^p) \\ \boldsymbol{\alpha}_y^{tr} = \boldsymbol{\alpha}_{y,n} \\ \boldsymbol{\alpha}_b^{tr} = \boldsymbol{\alpha}_{b,n} \\ f_y^{tr} = \|\mathbf{F}^{tr} - \boldsymbol{\alpha}_y^{tr}\| - R_y \end{cases} \tag{3.41}$$

If $f_y^{tr} \leq 0$, then the discrete Kuhn–Tucker conditions (3.25) are all satisfied by the trial state values given in Eq. (3.41). Because the unloading condition is only checked for inelastic time steps, the time step Δt is elastic as assumed, and the correct state is represented by the trial state.

If $f_y^{tr} > 0$, then Eq. $(3.25)_1$ is violated for the trial state, and the time step is inelastic. By hypothesis, inelastic states may satisfy the unloading condition, Eq. (3.34), and this must be checked. The evaluation of the unloading condition will require values of $\mathbf{n}$ and $\boldsymbol{\delta}$ that are consistent with the trial state, Eq. (3.41). From Eq. (3.17):

$$\mathbf{n}^{tr} = \frac{\mathbf{F}^{tr} - \boldsymbol{\alpha}_y^{tr}}{\|\mathbf{F}^{tr} - \boldsymbol{\alpha}_y^{tr}\|} \tag{3.42}$$

The trial image stress may also be directly evaluated from Eq. (3.31); after substituting trial values, the following is obtained:

$$\hat{\mathbf{F}}^{tr} = \boldsymbol{\alpha}_b^{tr} + \mathbf{n}^{tr} R_b \tag{3.43}$$

The trial value of $\boldsymbol{\delta}$ could now be evaluated directly from Eq. (3.33), using the trial values of $\mathbf{F}$ and $\hat{\mathbf{F}}$. However, this definition of $\boldsymbol{\delta}^{tr}$ could lead to some difficulties, particularly for time steps where the yield surface lies close to the bounding surface. In this case, $\mathbf{F}^{tr}$ could lie outside the bounding surface, and $\boldsymbol{\delta}^{tr}$ will point inwards. This change in direction of $\boldsymbol{\delta}$ will lead to the detection of unloading, even though the load is increasing.

An effective solution to this problem can be achieved by defining $\boldsymbol{\delta}^{tr}$ in the following manner:

$$\boldsymbol{\delta}^{tr} = \hat{\mathbf{F}}^{tr} - \mathbf{F}_y^{tr} \tag{3.44}$$

where

$$\mathbf{F}_y^{tr} = \boldsymbol{\alpha}_y^{tr} + \mathbf{n}^{tr} R_y \tag{3.45}$$

In this context, $\mathbf{F}_y^{tr}$ may be thought of as the trial value of $\mathbf{F}$, radially returned to the yield surface such that $f_y(\mathbf{F}_y^{tr}, \boldsymbol{\alpha}_y^{tr}) = 0$. Although the value of $\mathbf{F}$ to be obtained in the plastic correction phase is also obtained by a radial return [Simo and Hughes, 1998], in that case the evolutionary equations for the hardening variables must also be satisfied.

Using this definition of $\boldsymbol{\delta}^{tr}$, and $\mathbf{n}^{tr}$ defined above, Eq. (3.34), in the discrete case, becomes:

$$\boldsymbol{\delta}_{in} \cdot \mathbf{n}^{tr} - \boldsymbol{\delta}^{tr} \cdot \mathbf{n}^{tr} < 0 \tag{3.46}$$

The definition of $\boldsymbol{\delta}^{tr}$ in (3.44) is not used in the plastic correction, so it does not affect the final solution for the inelastic time step. However, it does provide an accurate evaluation of $\boldsymbol{\delta}$ which may be used in the unloading check above. It also coincides with the updated value of $\boldsymbol{\delta}_{in}$ if Eq. (3.46) is satisfied because it represents the value of $\boldsymbol{\delta}$ immediately after yielding takes place within the time step Δt. Therefore, if unloading is detected, the initial value of $\boldsymbol{\delta}$ is reset, using the following expression:

$$\boldsymbol{\delta}_{in} = \boldsymbol{\delta}^{tr} \tag{3.47}$$

If the trial yield function violates the first of the Kuhn–Tucker conditions, Eq. $(3.25)_1$, then the initial assumption that $\lambda = 0$ was incorrect. Backward Euler integration gives the following plastic state, as functions of the trial state values in Eq. (3.41):

$$\begin{cases} \mathbf{U}^p = \mathbf{U}^{p,tr} + \lambda \mathbf{n} \\ \quad \mathbf{F} = K_1(\mathbf{U} - \mathbf{U}^{p,tr} - \lambda \mathbf{n}) = \mathbf{F}^{tr} - K_1 \lambda \mathbf{n} \\ \boldsymbol{\alpha}_y = \boldsymbol{\alpha}_y^{tr} + (K_2 + \Delta K_p)\lambda \mathbf{n} \\ \boldsymbol{\alpha}_b = \boldsymbol{\alpha}_b^{tr} + (K_2 + \Delta K_p)\lambda \mathbf{n} - \Delta K_p \lambda \dfrac{\boldsymbol{\delta}}{\boldsymbol{\delta} \cdot \mathbf{n}} \end{cases} \tag{3.48}$$

Following the same procedure as for classical plasticity, it can again be shown that $\mathbf{n} = \mathbf{n}^{tr}$. Solving Eqs. (3.17) and (3.48) for λ, and substituting for R_y from Eq. (3.14), the following expression for the discrete consistency parameter can be derived:

$$\lambda = \frac{\left\| \mathbf{F}^{tr} - \boldsymbol{\alpha}_y^{tr} \right\| - R_y}{K_1 + K_2 + \Delta K_p} = \frac{f_y^{tr}}{K_1 + K_2 + \Delta K_p} \tag{3.49}$$

This is an implicit expression for λ, as the ΔK_p appearing on the right-hand side of the equation is also a function of $\boldsymbol{\delta}$, and thus λ.

To evaluate $\boldsymbol{\delta}$, and hence ΔK_p and λ, an expression for the image stress for the plastic state must be determined. Equation $(3.48)_4$ is substituted into Eqs. (3.31) and (3.43), to give:

$$\hat{\mathbf{F}} = \hat{\mathbf{F}}^{tr} + (K_2 + \Delta K_p)\lambda \mathbf{n} - \Delta K_p \lambda \frac{\boldsymbol{\delta}}{\boldsymbol{\delta} \cdot \mathbf{n}} \tag{3.50}$$

Starting from the original definition of $\boldsymbol{\delta}$, Eq. (3.33), λ is substituted from Eq. (3.49), and the dot product is taken with $\mathbf{n}$. This gives the following result:

$$\boldsymbol{\delta} \cdot \mathbf{n} = (\hat{\mathbf{F}}^{tr} - \mathbf{F}^{tr}) \cdot \mathbf{n} + f_y^{tr} \left(1 - \frac{\Delta K_p}{K_1 + K_2 + \Delta K_p}\right) \tag{3.51}$$

Finally, the definition of ΔK_p is recalled from Eq. (3.36), which is a function of $\boldsymbol{\delta} \cdot \mathbf{n}$. This system must be solved with the Newton–Raphson algorithm for ΔK_p. To do so, the following residual function is defined:

$$g(\Delta K_p) = K_3 \left[\frac{\boldsymbol{\delta} \cdot \mathbf{n}}{(\boldsymbol{\delta}_{in} - \boldsymbol{\delta}) \cdot \mathbf{n}}\right] - \Delta K_p \tag{3.52}$$

where $\boldsymbol{\delta} \cdot \mathbf{n}$ is obtained from Eq. (3.51), and $\mathbf{n} = \mathbf{n}^{tr}$ applies. The gradient of the residual function, $g(\Delta K_p)$ is also required. After differentiating Eq. (3.52), and some rearranging, the gradient is:

$$g'(\Delta K_p) = -1 - \frac{f_y^{tr} K_3 (K_1 + K_2)(\boldsymbol{\delta}_{in} \cdot \mathbf{n})}{(K_1 + K_2 + \Delta K_p)^2 (\boldsymbol{\delta}_{in} \cdot \mathbf{n} - \boldsymbol{\delta} \cdot \mathbf{n})^2} \tag{3.53}$$

The Newton–Raphson algorithm starts with an initial value of ΔK_p derived from Eq. (3.36) and the trial state (3.41). The $(k+1)^{\text{th}}$ iterate of ΔK_p is obtained from the k^{th} from the following:

$$\Delta K_p^{(k+1)} = \Delta K_p^{(k)} - \left[g'(\Delta K_p^{(k)})\right]^{-1} g\left(\Delta K_p^{(k)}\right) \tag{3.54}$$

and convergence may be considered achieved when the residual function is less than the machine tolerance:

$$g(\Delta K_p) < TOL \tag{3.55}$$

When a converged value of ΔK_p has been reached, the corrected consistency parameter may be evaluated from Eq. (3.49), and, the remainder of the plastic state obtained from Eq. (3.48).

3.2.2.3 Model application. As with the classical plasticity model, the bounding surface model is compared with the medium strain bidirectional response of HDR bearings, using the experimental data from test 12. Model parameters were determined based on the calibrated classical plasticity parameters, and to fit the initial unidirectional backbone of the loading, and are shown in Table 3.1. Note that the bounding surface model is intended to describe model response across a range of strain levels, so it should be calibrated across a series of tests. By just comparing with one test, the advantages over the classical formulation, in which material parameters are strain-dependent, are not so apparent.

The experimental and model response are compared in Fig. 3.7. The unidirectional response of the model in the first excursion of the displacement orbit is described well by the bounding surface model,

Table 3.1. Material parameters for bounding surface model.

K_1	K_2	K_3	R_y	R_b	η
3.29 kip/in	1.3 kip/in	0.35 kip/in	0.7 kip	2.8 kip	1

with a smooth transition from elastic to plastic response. However, the bidirectional response for the remainder of the orbit is poorly-described. For the first change of loading direction, the unloading condition, Eq. (3.46) is satisfied, and the tangent stiffness returns to the elastic stiffness, K_1. This means that while the hardening vector, $\mathbf{n}$, is evolving from the x-direction to the y-direction, the response is too stiff to capture the change in F_x. Consequently, the force trajectory of the first cycle model response is essentially the same shape as the displacement orbit, and the bidirectional coupling of force is not described.

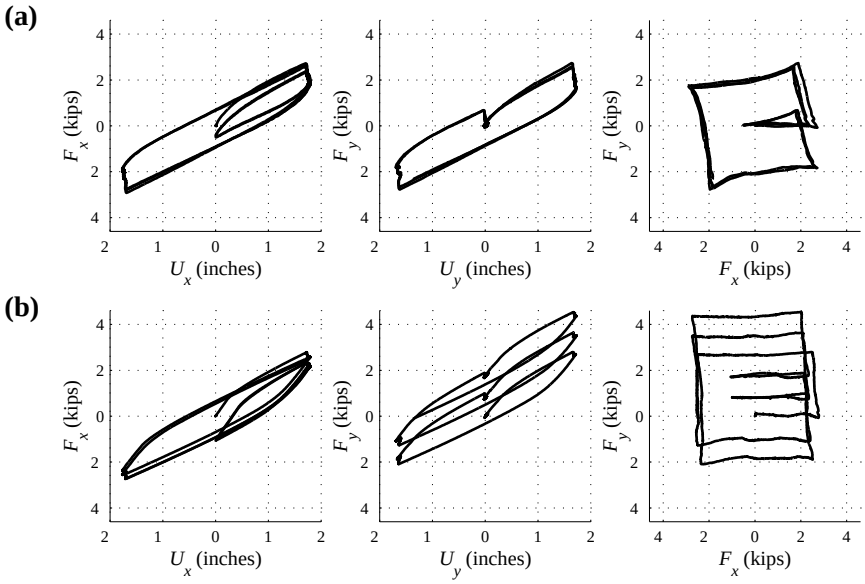

Figure 3.7. (a) Experimental response and (b) bounding surface model response for test 12: orbit 2, $\gamma_x = \gamma_y = 100\%$, slow strain rate.

Several alternative approaches have been adopted to properly describe the force trajectory. Different hardening rules, including Mróz hardening [Mróz, 1967], and a linear combination of Mróz and Prager hardening were examined, although these approaches generally involved greater computational effort, and did not provide a satisfactory description of the experimental response.

The second and third cycles in Fig. 3.7 exhibit another limitation of the bounding surface model.

After the first complete displacement orbit, the force point returns to a position offset from the origin due to accumulation of kinematic hardening. Subsequent cycles continue this ratchetting behaviour, and the force trajectories propagate in the y-direction. The bounding surface model, in this form, does not exhibit stable hysteresis, contrary to the observed experimental response of HDR bearings. For this reason, the bidirectional version of the bounding surface model presented in this section is inappropriate for bidirectional analyses.

Because of these difficulties, Huang [2002] developed an improved model for LR bearings, that could be calibrated for low to medium strain HDR bearing behaviour. The Huang model represents the bidirectional response by a set of classical plasticity models in parallel, calibrated on a bounding surface backbone. The result is a piecewise linear approximation of the bounding surface model in unidirectional loading, which provides a better match of force component coupling in bidirectional loading. Because LR bearings do not exhibit the nonlinearity of stiffness and damping, and degradation with cyclic loading, the approach does not include these considerations, and it may be difficult to extend to high strain HDR bearing behaviour.

3.2.3 Bounding and Stiffening Surfaces Model

The bounding surface model discussed in the previous section accurately describes the smooth transition from elastic to plastic behaviour in a unidirectional loading regime. Although this was not demonstrated in this thesis, the model could also allow the calibration of a unique set of strain-dependent material parameters for unidirectional loading, appropriate for a range of low to medium strain level tests. For higher strains, the stiffening behaviour governs and the bounding surface model cannot capture the unidirectional response.

In this section, an extension to the bounding surface model is presented that represents the nonlinear stiffening backbone of the monotonic loading response of HDR bearings. The limitations of the bounding surface approach for bidirectional loading, highlighted in Fig. 3.7, are not addressed in this section, and the same limitations may be expected to apply here. The model presented below is one of several attempts that were made to extend the bounding surface model for stiffening behaviour, and illustrates some of the difficulties involved in such an approach.

3.2.3.1 Time continuous model description. The stiffening surface model is defined by adding a second force component in parallel to the bounding surface force ($\mathbf{F}_1$), such that the total force is given by:

$$\mathbf{F} = \mathbf{F}_1 + \mathbf{F}_2 \tag{3.56}$$

where $\mathbf{F}_2$ is the stiffening force. This additional force component describes the stiffening of the bearing for high strains. In addition to Eq. (3.56), the elastic force–displacement law holds for the

total force vector, as previously defined in Eq. (3.15).

The first component of force, $\mathbf{F}_1$, is described completely by the bounding surface model discussed in the previous section. In particular, the yield surface and bounding surface in $\mathbf{F}_1$ space are defined by the equations $f_y(\mathbf{F}_1, \boldsymbol{\alpha}_y) = 0$ and $f_b(\hat{\mathbf{F}}, \boldsymbol{\alpha}_b) = 0$, respectively, with the functions defined earlier in Eqs. (3.14) and (3.29). The image force and associative plastic flow rule are as given in Eqs. (3.31) and (3.16), and kinematic hardening of the yield and bounding surfaces is defined by:

$$\dot{\boldsymbol{\alpha}}_y = (K_2 + \Delta K_{p1})\, \dot{\mathbf{U}}^p = (K_2 + \Delta K_{p1})\, \dot{\gamma} \mathbf{n} \tag{3.57}$$

and

$$\dot{\boldsymbol{\alpha}}_b = \left[K_2 \mathbf{n} + \Delta K_{p1} \left(\mathbf{n} - \frac{\boldsymbol{\delta}}{\boldsymbol{\delta} \cdot \mathbf{n}} \right) \right] \dot{\gamma} \tag{3.58}$$

where

$$\Delta K_{p1} = K_3 \left[\frac{\boldsymbol{\delta} \cdot \mathbf{n}}{(\boldsymbol{\delta}_{in} - \boldsymbol{\delta}) \cdot \mathbf{n}} \right] \tag{3.59}$$

and $\boldsymbol{\delta}$ and $\boldsymbol{\delta}_{in}$ are defined as before, except with a dependence on $\mathbf{F}_1$ instead of the total force:

$$\boldsymbol{\delta} = \hat{\mathbf{F}} - \mathbf{F}_1 \tag{3.60}$$

The stiffening component of the force, $\mathbf{F}_2$, is defined by a bounding surface model in plastic displacement space. Unlike a traditional bounding surface model, the tangent stiffness must increase with increasing plastic displacement to describe the stiffening behaviour of HDR bearings. This is difficult to attain in a force space formulation, and necessitates the use of a displacement space framework. A vector $\boldsymbol{\varepsilon}$, which measures the normalised distance from the origin in plastic displacement space, is defined:

$$\boldsymbol{\varepsilon} = \frac{\mathbf{U}^p - \boldsymbol{\beta}_s}{r_s} \tag{3.61}$$

where $\boldsymbol{\beta}_s$ and r_s are, respectively, the centre and the radius, of a circular bounding surface in plastic displacement space.

For general hardening of the bounding surface, $\boldsymbol{\beta}_s$ and r_s evolve with kinematic and isotropic hardening laws, respectively. Furthermore, because an additional degree of freedom has been introduced to the problem in Eq. (3.56), the evolution of the stiffening component of the force, $\mathbf{F}_2$, must also be defined through a rate equation. In plastic displacement space, the following expression is analogous to Eq. (3.35):

$$\dot{\mathbf{U}}^p = \frac{1}{K_4} + \left(\frac{1 - \boldsymbol{\varepsilon}.\mathbf{n}}{\boldsymbol{\varepsilon}.\mathbf{n}} \right)^{\eta_2} \dot{\mathbf{F}}_2 \tag{3.62}$$

Substituting for $\dot{\mathbf{U}}^p$ from Eq. (3.16), and solving for $\dot{\mathbf{F}}_2$, gives:

$$\dot{\mathbf{F}}_2 = \Delta K_{p2} \dot{\gamma} \mathbf{n} \tag{3.63}$$

where

$$\Delta K_{p2} = \frac{1}{\frac{1}{K_4} + \left(\frac{1-\boldsymbol{\varepsilon}.\mathbf{n}}{\boldsymbol{\varepsilon}.\mathbf{n}}\right)^{\eta_2}} \tag{3.64}$$

Finally, the evolution of the bounding surface in plastic displacement space is represented by rate equations for $\boldsymbol{\beta}_s$ and r_s. The relative proportion of kinematic and isotropic hardening of the surface is described by an additional material parameter, $0 < \phi_{kh} < 1$, defined as the fraction of hardening which is kinematic. Similarly, $(1 - \phi_{kh})$ gives the fraction of isotropic hardening. Therefore, the following rate equations hold:

$$\dot{\boldsymbol{\beta}}_s = \frac{\phi_{kh}}{K_4}\dot{\mathbf{F}}_2 = \phi_{kh}\frac{\Delta K_{p2}}{K_4}\dot{\gamma}\mathbf{n} \tag{3.65}$$

and

$$\dot{r}_s = \frac{(1-\phi_{kh})}{K_4}\dot{\|\mathbf{F}_2\|} = (1-\phi_{kh})\frac{\Delta K_{p2}}{K_4}\frac{\mathbf{F}_2 \cdot \mathbf{n}}{\|\mathbf{F}_2\|}\dot{\gamma} \tag{3.66}$$

Because the two components of the model are coupled by the plastic displacement, they must be solved together. The following section describes the time discretisation and integration algorithm.

The unidirectional response of the stiffening surface component of the model is illustrated in Fig. 3.6(b). The total force is obtained by adding the bounding surface component of force, from Fig. 3.6(a), to the stiffening surface force. As with the bounding surface, the force is plotted as a function of plastic displacement. The stiffening surface is given by a pair of lines with a slope K_4, and the force approaches the surface from an initial plastic modulus of zero. Figure 3.6(b) also illustrates a potential problem with the stiffening surface approach: upon unloading, the plastic modulus returns to zero, and negative energy is dissipated in each cycle. When the $\mathbf{F}_2$ component is added to the $\mathbf{F}_1$ component, the total energy dissipation may be confined to positive values by the selection of appropriate model parameters. However, this may not be representative of the real cyclic response of HDR bearings, as will be shown later in this section.

3.2.3.2 Integration algorithm. Using the backward Euler scheme, the time discretisation is carried out in the same manner as before. An additional step is added by recognising that:

$$\mathbf{F}_1 = \mathbf{F} - \mathbf{F}_2 = [K_1(\mathbf{U} - \mathbf{U}_n^p)] - [F_{2,n} + (K_1 + \Delta K_{p2})\lambda\mathbf{n}] \tag{3.67}$$

This allows the following trial state to be defined:

$$\begin{cases} \mathbf{U}^{p,tr} = \mathbf{U}_n^p \\ \mathbf{F}^{tr} = K_1(\mathbf{U} - \mathbf{U}_n^p) \\ \mathbf{F}_2^{tr} = \mathbf{F}_{2,n} \\ \mathbf{F}_1^{tr} = K_1(\mathbf{U} - \mathbf{U}_n^p) - \mathbf{F}_{2,n} \\ \boldsymbol{\alpha}_y^{tr} = \boldsymbol{\alpha}_{y,n} \\ \boldsymbol{\alpha}_b^{tr} = \boldsymbol{\alpha}_{b,n} \\ \boldsymbol{\beta}_s^{tr} = \boldsymbol{\beta}_{s,n} \\ r_s^{tr} = r_{s,n} \\ f_y^{tr} = \|\mathbf{F}_1^{tr} - \boldsymbol{\alpha}_y^{tr}\| - R_y \end{cases} \tag{3.68}$$

Unloading is checked based on the bounding surface force component, $\mathbf{F}_1$. Similarly, the trial yield function, f_y^{tr}, is calculated, and if it is less than zero, a plastic correction must be performed:

$$\begin{cases} \mathbf{U}^p = \mathbf{U}^{p,tr} + \lambda\mathbf{n} \\ \mathbf{F} = \mathbf{F}^{tr} - K_1\lambda\mathbf{n} \\ \mathbf{F}_2 = \mathbf{F}_2^{tr} + \Delta K_{p2}\lambda\mathbf{n} \\ \mathbf{F}_1 = \mathbf{F}_1^{tr} - (K_1 + \Delta K_{p2})\lambda\mathbf{n} \\ \boldsymbol{\alpha}_y = \boldsymbol{\alpha}_y^{tr} + (K_2 + \Delta K_{p1})\lambda\mathbf{n} \\ \boldsymbol{\alpha}_b = \boldsymbol{\alpha}_b^{tr} + (K_2 + \Delta K_{p1})\lambda\mathbf{n} - \Delta K_p\lambda\dfrac{\boldsymbol{\delta}}{\boldsymbol{\delta}\cdot\mathbf{n}} \\ \boldsymbol{\beta}_s = \boldsymbol{\beta}_s^{tr} + \phi_{kh}\dfrac{\Delta K_{p2}}{K_4}\lambda\mathbf{n} \\ r_s = r_s^{tr} + (1-\phi_{kh})\dfrac{\Delta K_{p2}}{K_4}\dfrac{\mathbf{F}_2\cdot\mathbf{n}}{\|\mathbf{F}_2\|}\lambda \end{cases} \tag{3.69}$$

As before, $\mathbf{n} = \mathbf{n}^{tr}$, and:

$$\lambda = \frac{f_y^{tr}}{K_1 + K_2 + \Delta K_{p1} + \Delta K_{p2}} \tag{3.70}$$

Again, Eq. (3.70) gives an implicit expression for λ, as both ΔK_{p1} and ΔK_{p2} are implicit functions of λ. As before, this is resolved by evaluating the bounding surface distance parameters, $\boldsymbol{\delta}$ and $\boldsymbol{\varepsilon}$, and taking their dot products with $\mathbf{n}$, to give:

$$\boldsymbol{\delta}\cdot\mathbf{n} = (\hat{\mathbf{F}}^{tr} - \mathbf{F}_1^{tr})\cdot\mathbf{n} + (K_1 + K_2 + \Delta K_{p2})\lambda \tag{3.71}$$

and

$$\boldsymbol{\varepsilon}\cdot\mathbf{n}=\frac{1}{r_s}\left[\left(\mathbf{U}^{p,tr}-\boldsymbol{\beta}_s^{tr}\right)\cdot\mathbf{n}+\left(1-\frac{\phi_{kh}\Delta K_{p2}}{K_4}\right)\lambda\right] \tag{3.72}$$

where

$$r_s=\frac{(1-\phi_{kh})(\mathbf{F}_2^{tr}\cdot\mathbf{n}+\Delta K_{p2}\lambda)\Delta K_{p2}\lambda}{K_4\|\mathbf{F}_2^{tr}+\Delta K_{p2}\lambda\mathbf{n}\|} \tag{3.73}$$

from Eq. (3.69).

Substituting into Eqs. (3.59) and (3.64) for λ, $\boldsymbol{\delta}\cdot\mathbf{n}$, $\boldsymbol{\varepsilon}\cdot\mathbf{n}$ and r_s from Eqs. (3.70), (3.71), (3.72) and (3.73), respectively, gives two simultaneous equations for ΔK_{p1} and ΔK_{p2}, which are solved using a Newton–Raphson approach. The following vector of residuals is defined:

$$\mathbf{g}(\mathbf{\Delta K_p})=\begin{Bmatrix}g_1\\g_2\end{Bmatrix}=\begin{Bmatrix}K_3\left[\frac{\boldsymbol{\delta}\cdot\mathbf{n}}{(\boldsymbol{\delta}_{in}-\boldsymbol{\delta})\cdot\mathbf{n}}\right]^{\eta_1}-\Delta K_{p1}\\\left[\frac{1}{K_4}+\left(\frac{1-\boldsymbol{\varepsilon}\cdot\mathbf{n}}{\boldsymbol{\varepsilon}\cdot\mathbf{n}}\right)^{\eta_2}\right]^{-1}-\Delta K_{p2}\end{Bmatrix} \tag{3.74}$$

where the vector of unknowns, $\mathbf{\Delta K_p}$, is:

$$\mathbf{\Delta K_p}=\begin{Bmatrix}\Delta K_{p1}\\\Delta K_{p2}\end{Bmatrix} \tag{3.75}$$

The gradient of the residuals is a matrix, derived by taking the partial derivative of each component of $\mathbf{g}$ with respect to each component of $\mathbf{\Delta K_p}$. To calculate this gradient, the expressions for λ, $(\boldsymbol{\delta}\cdot\mathbf{n})$, $(\boldsymbol{\varepsilon}\cdot\mathbf{n})$ and r_s must first be differentiated:

$$\begin{cases}\dfrac{\partial\lambda}{\partial\mathbf{\Delta K_p}}=-\dfrac{f_y^{tr}}{(K_1+K_2+\Delta K_{p1}+\Delta K_{p2})^2}\begin{Bmatrix}1\\1\end{Bmatrix}\\[2ex]\dfrac{\partial r_s}{\partial\mathbf{\Delta K_p}}=\dfrac{(1-\phi_{kh})}{K_4\|\mathbf{F}_2\|}\mathbf{n}\cdot\left[\mathbf{F}_2\otimes\left(\lambda\begin{Bmatrix}0\\1\end{Bmatrix}+\Delta K_{p2}\dfrac{\partial\lambda}{\partial\mathbf{\Delta K_p}}\right)\right.\\\qquad\qquad\left.+\Delta K_{p2}\lambda\left(\mathbb{I}-\dfrac{\mathbf{F}_2\otimes\mathbf{F}_2}{\|\mathbf{F}_2\|^2}\right)\right]\\[2ex]\dfrac{\partial(\boldsymbol{\delta}\cdot\mathbf{n})}{\partial\mathbf{\Delta K_p}}=-\dfrac{f_y^{tr}}{(K_1+K_2+\Delta K_{p1}+\Delta K_{p2})^2}\begin{Bmatrix}K_1+K_2+\Delta K_{p2}\\-\Delta K_{p1}\end{Bmatrix}\\[2ex]\dfrac{\partial(\boldsymbol{\varepsilon}\cdot\mathbf{n})}{\partial\mathbf{\Delta K_p}}=\dfrac{1}{r_s}\left[\left(\dfrac{\partial\lambda}{\partial\mathbf{\Delta K_p}}\left(1-\dfrac{\phi_{kh}\Delta K_{p2}}{K_4}\right)-\dfrac{\lambda\phi_{kh}}{K_4}\begin{Bmatrix}0\\1\end{Bmatrix}\right)-\dfrac{\partial r_s}{\partial\mathbf{\Delta K_p}}(\boldsymbol{\varepsilon}\cdot\mathbf{n})\right]\end{cases} \tag{3.76}$$

Finally, the gradient of $\mathbf{g}$ is:

$$\begin{cases} \dfrac{\partial g_1}{\partial \Delta \mathbf{K_p}} = \begin{Bmatrix} -1 \\ 0 \end{Bmatrix} + \dfrac{\eta_1 K_3 (\boldsymbol{\delta} \cdot \mathbf{n})^{\eta_1 - 1} (\boldsymbol{\delta}_{in} \cdot \mathbf{n})}{(\boldsymbol{\delta}_{in} \cdot \mathbf{n} - \boldsymbol{\delta} \cdot \mathbf{n})^{\eta_1 + 1}} \dfrac{\partial (\boldsymbol{\delta} \cdot \mathbf{n})}{\partial \Delta \mathbf{K_p}} \\ \dfrac{\partial g_2}{\partial \Delta \mathbf{K_p}} = \begin{Bmatrix} 0 \\ -1 \end{Bmatrix} + \dfrac{\eta_2 (1 - \boldsymbol{\varepsilon} \cdot \mathbf{n})^{\eta_2 - 1}}{(\boldsymbol{\varepsilon} \cdot \mathbf{n})^{\eta_2 + 1}} \left[\dfrac{1}{K_4} + \left(\dfrac{1 - \boldsymbol{\varepsilon} \cdot \mathbf{n}}{\boldsymbol{\varepsilon} \cdot \mathbf{n}} \right)^{\eta_2} \right]^{-2} \dfrac{\partial (\boldsymbol{\varepsilon} \cdot \mathbf{n})}{\partial \Delta \mathbf{K_p}} \end{cases} \tag{3.77}$$

The Newton–Raphson algorithm used here is the same as that used in Section 3.2.2, extended to two unknown variables. The $(k+1)^{\text{th}}$ iterate of $\Delta \mathbf{K_p}$ is obtained from the k^{th} using the following expression:

$$\Delta \mathbf{K}_{\mathbf{p}}^{(k+1)} = \Delta \mathbf{K}_{\mathbf{p}}^{(k)} - \left[\frac{\partial \mathbf{g}}{\partial \Delta \mathbf{K}_{\mathbf{p}}^{(k)}} \right]^{-1} \mathbf{g} \left(\Delta \mathbf{K}_{\mathbf{p}}^{(k)} \right) \tag{3.78}$$

and convergence may be considered to be achieved when the norm of the residual function is less than the machine tolerance:

$$\| \mathbf{g} (\Delta \mathbf{K_p}) \| < TOL \tag{3.79}$$

3.2.3.3 Model application. To assess the high-strain behaviour of the stiffening surface model, the model response was compared with the experimental data from test 24 (orbit 2, 250% strain). Model parameters corresponding to the bounding surface component of loading were retained from the bounding surface model discussed in Section 3.2.2, except for K_2 which was reduced to account for the force in the stiffening component. The parameters of the stiffening surface component were selected to fit the first unidirectional, monotonic loading portion of the test cycle. The model parameters that were selected are shown in Table 3.2.

Table 3.2. Material parameters for bounding and stiffening surfaces model.

K_1	K_2	K_3	K_4	R_y	R_b	η_1	η_2	ϕ_{kh}
3.29 kip/in	0.7 kip/in	0.35 kip/in	8 kip/in	0.7 kip	2.8 kip	1	1	1

The response of the stiffening surface model is compared with the experimental behaviour in Fig. 3.8. Only the initial unidirectional loading portion of the load history (γ_x increasing to 250%, $\gamma_x = 0$) is described well by the model. When the loading direction changes, the stiffening surface model is unable to capture the bidirectional coupling of the bearing response, and the bearing force is grossly underestimated. Finally, under load reversals, the model results in negative energy dissipation, which clearly does not describe real bearing behaviour, nor satisfy Ilyushin's plasticity postulate [Lubliner, 1990].

Although it is possible that a plasticity based approach may be adopted to describe the behaviour

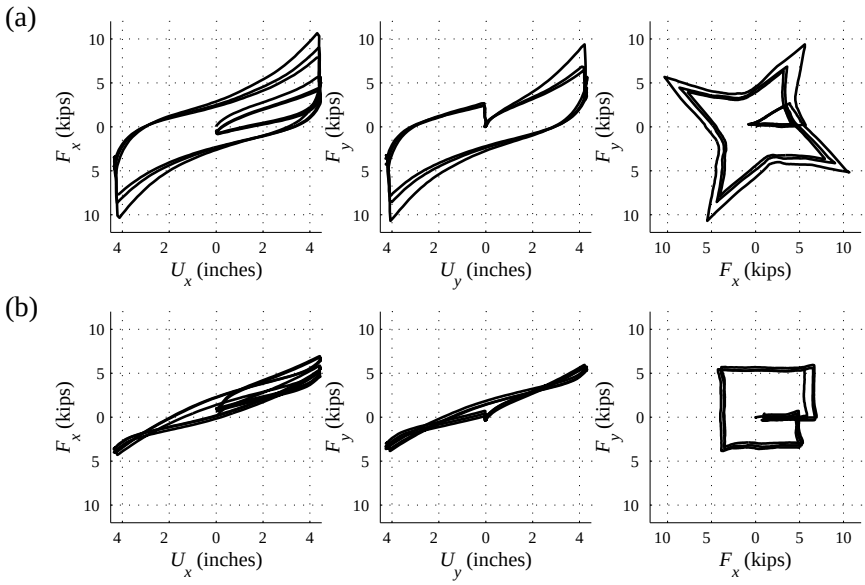

Figure 3.8. (a) Experimental response and (b) stiffening surface model response for test 24: orbit 2, $\gamma_x = \gamma_y = 250\%$, slow strain rate.

of HDR bearings, it is apparent that the approach described in this section is not sufficient for this purpose.

4. PROPOSED BIDIRECTIONAL MODEL

To address the limitations of the unidirectional phenomenological and bidirectional plasticity models described in the previous chapter, a new rate-independent bidirectional model is developed in this section. Although the behaviour of HDR bearings is recognised to have some strain-rate and time-dependent effects [Morgan, 2000], there is little experimental data available about relaxation and creep needed to characterise the rate-dependent behaviour. This limitation notwithstanding, a viscoelastic term is added to the rate-independent model, in common with other models for the viscous behaviour of elastomers. The proposed model addresses the goal of representing the effects of bidirectional loading and stiffness and damping degradation.

4.1 TIME CONTINUOUS MODEL DEVELOPMENT

As in Section 3.2, the model is expressed in terms of vector quantities $\mathbf{F}$ and $\mathbf{U}$. In addition, the unit direction of velocity vector, $\mathbf{n}$, is defined:

$$\mathbf{n} = \frac{\dot{\mathbf{U}}}{\|\dot{\mathbf{U}}\|} \tag{4.1}$$

Results from the bidirectional test programme discussed in Section 2.2 suggest that, at changes in loading direction, the force vector, $\mathbf{F} = \mathbf{F}_1 + \mathbf{F}_2$, can be decomposed into a component parallel to the displacement vector, $\mathbf{F}_1$, and a component parallel to the velocity vector, $\mathbf{F}_2$. As a demonstration of the resisting force decomposition, Fig. 4.1 shows the force vectors for the box orbit displacement history in part (a). At the circled point in the displacement orbit, for which $U_x = U_y$, the displacement vector is oriented at $45°$ to the axes, and the velocity vector is parallel to the y-axis. The two force vectors in the first cycle of loading are shown superimposed on the force loci in Fig. 4.1(b), and the second cycle is illustrated in part Fig. 4.1(c).

It is interesting to note from Fig. 4.1 that both vectors, $\mathbf{F}_1$ and $\mathbf{F}_2$, reduce in magnitude from the first to the second cycle, but within a cycle the peak magnitudes are essentially unchanged. Comparing this observation with the response for the cruciform orbit (Fig. 2.3), it may be concluded that scragging occurs when the bearing is fully unloaded to zero displacement, but does not occur when

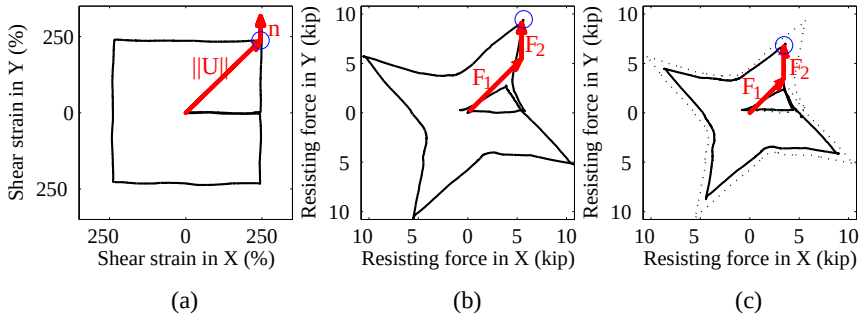

Figure 4.1. Example of decomposition of bearing force resisting force into two vectors. (a) Displacement-controlled 'box' orbit, (b) first cycle force locus, and (c) second cycle force locus.

one direction is unloaded while maintaining the other direction. This suggests that for a bearing to be considered degraded for a peak displacement value, it must be completely unloaded through the origin. This observation will be used in the definition of degradation due to scragging, as described in Section 4.1.3.

The $\mathbf{F}_1$ force component in the direction of the displacement may be expressed as a continuous, isotropic function of the displacement vector, with degradation occurring as a function of the cyclic path. This behaviour may be described by a hyperelastic force–displacement relation, modified by a scalar damage parameter. The $\mathbf{F}_2$ component is representative of hysteretic response in the bearing, and may also be defined in terms of the magnitude of the displacement vector. The hysteretic force evolves towards the direction of the velocity vector, such that, even under a sudden change in loading direction, the change in $\mathbf{F}_2$ is smooth. Hysteretic rules are required to describe the behaviour under arbitrary, bidirectional loading histories.

Using the decomposition of resisting force, $\mathbf{F}$ is defined as:

$$\mathbf{F}(\mathbf{U}, \mathbf{n}, D_S, D_M) = \mathbf{F}_1(\mathbf{U}, D_S, D_M) + \mathbf{F}_2(\mathbf{U}, \mathbf{n}, D_S) \tag{4.2}$$

where D_S and D_M are scalar history variables that account for the degradation of stiffness and damping in the first and subsequent cycles. Equation (4.2) may be considered a bidirectional generalisation of the unidirectional models discussed in Section 3.1, in which the total force is composed of an elastic force in the direction of U, and a hysteretic force in the direction of $\text{sgn}(\dot{U})$. For the bidirectional model the following subsections present the approaches for the force components and degradation history variables.

4.1.1 Elastic Component

Constitutive models of elastomers commonly consider a hyperelastic stress–strain relation, derived

from an isotropic strain energy function. The viscoplastic model of Haupt and Sedlan [2001], for example, considers a generalisation of the Mooney–Rivlin strain energy function, with five elasticity constants:

$$\Psi(\mathbf{C}) = d_1(I_1 - 3) + d_2(I_2 - 3) + d_3(I_1 - 3)(I_2 - 3) + d_4(I_2 - 3)^2 + d_5(I_1 - 3)^3 \quad (4.3)$$

where d_1 to d_5 are material parameters. The tensor $\mathbf{C}$ is the right Cauchy-Green strain tensor, and I_1 and I_2 are its first two invariants:

$$I_1 = \mathrm{tr}\,\mathbf{C} \quad ; \qquad I_2 = \frac{1}{2}\left[(\mathrm{tr}\,\mathbf{C})^2 - \mathrm{tr}\,(\mathbf{C})^2\right] \quad (4.4)$$

If it is assumed that the simple shearing of an entire bearing may be represented by a single state of stress and plane strain, the deformation gradient, $\mathbf{F}$, and right Cauchy-Green tensor for this deformation are given by:

$$\mathbf{F} = \begin{bmatrix} 1 & \gamma & 0 \\ 0 & 1 & 0 \\ 0 & 0 & 1 \end{bmatrix} \qquad \mathbf{C} = \mathbf{F}^T\mathbf{F} = \begin{bmatrix} 1 & \gamma & 0 \\ \gamma & 1+\gamma^2 & 0 \\ 0 & 0 & 1 \end{bmatrix} \quad (4.5)$$

where γ is the shear strain. This assumption is equivalent to representing the entire bearing by a single Gauss integration point, and does not take into account localised effects caused by bearing boundary conditions. For this prescribed deformation, Eq. (4.4) reduces to:

$$I_1 = I_2 = \gamma^2 + 3 \quad (4.6)$$

For a hyperelastic material, the second Piola–Kirchhoff stress tensor may be derived by differentiating the free energy equation with respect to the conjugate strain tensor. The following expression applies [Bonet and Wood, 1997]:

$$\mathbf{S} = 2\Psi_1\mathbf{1} + 4\Psi_2\mathbf{C} + 2J^2\Psi_3\mathbf{C}^{-1} \quad (4.7)$$

where $J = 1$ is the Jacobian of the transformation, and the Ψ_i terms are the derivatives of the free energy with respect to the strain invariants.

The Cauchy stress tensor is of more importance for engineering applications, and is obtained from the second Piola–Kirchoff stress tensor by transforming to the 'spatial description' of solid mechanics, through the following relationship:

$$\boldsymbol{\sigma} = J^{-1}\mathbf{F}\mathbf{S}\mathbf{F}^T \quad (4.8)$$

After some calculation, the form for the Cauchy stress tensor is obtained:

$$\boldsymbol{\sigma} = \begin{bmatrix} E(\gamma^6) & O(\gamma^5) & 0 \\ O(\gamma^5) & E'(\gamma^4) & 0 \\ 0 & 0 & E''(\gamma^4) \end{bmatrix} \quad (4.9)$$

where the terms $O(\gamma^n)$ and $E(\gamma^n)$ are odd and even polynomials of the nth order of the shear strain, γ, and the apostrophes signify that the functions are different for each component, although the matrix is symmetric. The coefficients of each polynomial are given by factors of the material parameters d_1 to d_5. For example, the shear component of Eq. (4.9) is given by:

$$\sigma_{12} = O(\gamma^5) = (2d_1 + 8d_2)\gamma + (4d_2 + 2d_3)\gamma^3 + (12d_3 + 8d_4 + 22d_5)\gamma^5 \tag{4.10}$$

Because the shear stress ($\sigma_{12} = \sigma_{21}$) components are the only concern in the bearing model, this result motivates the use of a fifth-order odd polynomial function of displacement for the elastic component of the force. Allowing for degradation with cyclic loading, the following expression for $\mathbf{F}_1$ is defined:

$$\mathbf{F}_1 = K_{S1} K_M \left[a_1 + a_2 \|\mathbf{U}\|^2 + a_3 \|\mathbf{U}\|^4 \right] \mathbf{U} \tag{4.11}$$

where a_1 to a_3 are material parameters, and K_{S1} and K_M are reduction factors to represent the effects of scragging and Mullins' effect, respectively. The reduction factors are initially equal to unity, and their evolution with cyclic loading is described in Section 4.1.3.

4.1.2 Hysteretic Damping Component

The second term in Eq. (4.2), $\mathbf{F}_2$, represents the hysteretic behaviour of the bearing. An approach similar to bounding surface plasticity [Dafalias and Popov, 1975] is used for $\mathbf{F}_2$ under general cyclic loading. Unlike the Hwang *et al.* [2002] model, the new approach provides a continuous response under load reversals, without restrictions to a harmonic loading history. It also avoids the dependence on a previous maximum load cycle in defining the hysteretic behaviour, as in the Kikuchi and Aiken [1997] model.

A bounding surface in force space, with radius $R(\|\mathbf{U}\|)$, is defined by the following expression:

$$\mathcal{B}(\mathbf{U}) = \|\mathbf{F}_2\| - R(\|\mathbf{U}\|) = 0 \tag{4.12}$$

Considering only rate-independent, isotropic behaviour, a quadratic expression is used for the dependence of the radius, R, on the current displacement vector, $\mathbf{U}$. The quadratic function is primarily motivated by experimental data, although may be considered a rate-independent simplification of the model of Hwang *et al.* [2002] under monotonic loading. The quadratic term is degraded under cyclic loading, while the constant term representing the radius of the bounding surface for $\|\mathbf{U}\| = 0$, is unchanged. These considerations lead to the following expression for the radius of the bounding surface:

$$R = b_1 + K_{S2}\, b_2 \|\mathbf{U}\|^2 \tag{4.13}$$

where b_1 and b_2 are material parameters, and K_{S2} is a reduction factor described in Section 4.1.3.

The position of the force vector relative to the bounding surface is described by a scalar distance variable, δ, and a unit direction vector along which the distance is measured, $\boldsymbol{\mu}$. Both terms are derived from the "image force", $\hat{\mathbf{F}}$, which performs a role analogous to the "image stress" in bounding surface plasticity [Dafalias and Popov, 1975]. The image force is defined by projecting the unit direction of velocity vector, $\mathbf{n}$, from the origin onto the bounding surface:

$$\hat{\mathbf{F}} = R\mathbf{n} \tag{4.14}$$

The parameters δ and $\boldsymbol{\mu}$ are then taken as the magnitude and unit direction of the vector pointing from the current force point to the image force:

$$\delta = \left\| \hat{\mathbf{F}} - \mathbf{F}_2 \right\| \quad ; \qquad \boldsymbol{\mu} = \frac{\hat{\mathbf{F}} - \mathbf{F}_2}{\left\| \hat{\mathbf{F}} - \mathbf{F}_2 \right\|} \tag{4.15}$$

Finally, an evolutionary relationship for $\mathbf{F}_2$ is required, to describe both the direction and magnitude of the rate of change of hysteretic force, $\dot{\mathbf{F}}_2$. The hysteretic force is assumed to move towards the image force in $\mathbf{F}_2$ space, such that:

$$\frac{\dot{\mathbf{F}}_2}{\|\dot{\mathbf{F}}_2\|} = \boldsymbol{\mu} \tag{4.16}$$

The magnitude of the change is given implicitly in terms of a scalar evolutionary equation for δ:

$$\dot{\delta} = -b_3 \delta \|\dot{\mathbf{U}}\| \tag{4.17}$$

which describes a smooth transition from high to low values of δ, with a rate dictated by the material parameter, b_3. Although Eq. (4.17) is expressed in rate form, the appearance of time derivatives on both sides of the equation results in a rate-independent model. Also note that a sudden change of load direction changes the direction and magnitude of the vector $\delta\boldsymbol{\mu}$, according to the definition, Eq. (4.15). However, this formulation does not suffer from the "overshooting" phenomenon of conventional bounding surface plasticity (Section 3.2.2). In this approach, the plastic modulus is controlled by the absolute value of δ, rather than a ratio of δ to an initial value, δ_{in}. This implies that after a small perturbation in the displacement history, the value of δ is essentially unchanged.

Equations (4.14) and (4.15) can be rearranged to obtain the following expression for the hysteretic force:

$$\mathbf{F}_2 = R\mathbf{n} - \delta\boldsymbol{\mu} \tag{4.18}$$

The evolution of $\mathbf{F}_2$ is summarised in Fig. 4.2. The smooth transition described by the scalar equation, (4.17), is illustrated for unidirectional loading in Fig. 4.2(a). For a given value of $\|\mathbf{U}\|$,

the values of R and δ are determined, and from these, $\mathbf{F}_2$ is calculated. For bidirectional loading, Fig. 4.2(b) shows the definition of the image force, and vectors $R\mathbf{n}$ and $\delta\boldsymbol{\mu}$, which are used to determine $\mathbf{F}_2$ from Eq. (4.18).

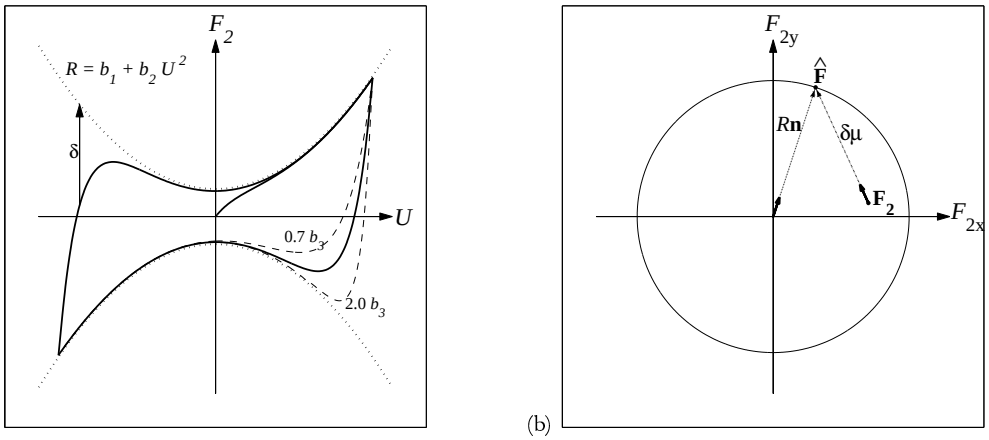

Figure 4.2. Evolution of hysteretic force, (a) Unidirectional and (b) bidirectional evolution of hysteretic component of force.

Although the hysteretic model described in this section is in some respects similar to conventional bounding surface plasticity, there are several important differences:

1. The model described here refers only to the hysteretic part of the force, which is added in parallel to an elastic component. Bounding surface plasticity is an extension of classical plasticity, in which the elastic and plastic parts of the displacement vector (or strain tensor) are added in series.

2. The image force is projected parallel to the velocity vector, and not homologously with the force point (as described in Section 3.2.2) or radially from a centre of homology (as in the radial mapping formulation; for example [Dafalias, 1986]).

3. The rate of convergence to the bounding surface is defined by the amplitude of a distance parameter in force space, and not by a ratio of current to initial distance. This not only provides a better fit of experimental data for HDR bearings, but also minimises storage requirements, and it does not require unloading checks or suffer from the overshooting problem.

4. The radius of the bounding surface is defined as a function of the current displacement vector and a damage parameter, and does not harden, either isotropically or kinematically, in the classical plasticity sense.

4.1.3 Degradation

The bidirectional experimental data presented in Section 2.2 show that, under cyclic loading conditions, the stiffness and damping of HDR bearings decrease. In general, a virgin bearing will exhibit higher stiffness and damping in the first cycle of loading at a given amplitude than on subsequent cycles. With continued cyclic loading, additional degradation accumulates, but the effect is less significant.

The distinction between scragging and Mullins' effect was discussed from a phenomenological and micromechanical point-of-view in Section 2.3. The term "scragging" is used to describe the first cycle degradation related to the maximum displacement reached, while "Mullins' effect" refers to degradation over the course of the loading process related to work done in the bearing. It is then assumed that the distinction of Clark *et al.* [1997] applies to the recovery of this damage. That is, the first cycle degradation corresponds to long-term scragging, while the accumulated degradation over all cycles corresponds to short-term Mullins' effect. Recovery of damage parameters is important when the bearing model is calibrated over a series of tests, as will be presented in Chapter 5, and is essential for accurately describing the bearing behaviour of a wide range of cyclic loading.

The model includes the following approaches for defining the reduction factors in Eqs. (4.11) and (4.13).

4.1.3.1 Scragging. The reduction factors K_{S1} and K_{S2}, represent the effects of scragging on the bearing stiffness and hysteretic forces, respectively. Exponential degradation of the two forces is considered, based on a damage parameter, D_S, which represents the state of scragging in the bearing.

Although some bidirectional effects are exhibited at higher strain levels [Morgan, 2000], the experimental data considered in Section 2.2 indicate that the scragging effect may be approximately modelled as an isotropic softening process. This suggests that the scragging damage parameter should increase when the displacement norm, $\|\mathbf{U}\|$, exceeds the previous maximum. The observations from Fig. 4.1, however, suggest that scragging does not fully take effect until the bearing is unloaded below a threshold level. Furthermore, if D_S evolves continuously while a maximum cycle is applied, then the maximum force reached will be governed by Eqs. (4.11) and (4.13), and subsequent cycles will reach the same level of force. This means that the damage parameter must be modified after some amount of unloading from a maximum.

To incorporate this observation for general cyclic loading, two damage thresholds, D_S^+ and D_S^- are defined to govern the evolution of D_S. The first parameter represents the maximum value of $\|\mathbf{U}\|$ reached, and is updated continuously with the applied displacement history. When unloading takes place from $\|\mathbf{U}\| = D_S^+$, the second parameter, D_S^- is reduced with $\|\mathbf{U}\|$, and represents the extent

of unloading, while the current scragging parameter, D_S is increased at the same rate. Load reversals within the upper and lower bounds will have no effect on D_S. When D_S^- reaches zero, the current value of D_S reaches D_S^+, and the scragging process is complete. In a continuous time setting, the rate equations of the various scragging parameters are summarised below:

$$\begin{cases} \text{if} \quad \|\mathbf{U}\| = D_S^+ \text{ and } \dot{\overline{\|\mathbf{U}\|}} > 0 \\ \qquad\qquad \dot{D}_S^+ = \dot{D}_S^- = \dot{\overline{\|\mathbf{U}\|}} \\ \qquad\qquad \dot{D}_S = 0 \\ \text{if} \quad \|\mathbf{U}\| = D_S^- \text{ and } \dot{\overline{\|\mathbf{U}\|}} < 0 \\ \qquad\qquad \dot{D}_S^+ = 0 \\ \qquad\qquad \dot{D}_S^- = \dot{\overline{\|\mathbf{U}\|}} \\ \qquad\qquad \dot{D}_S = -\dot{\overline{\|\mathbf{U}\|}} \end{cases} \tag{4.19}$$

Figure 4.3 illustrates the evolution of the scragging parameter and thresholds with initial values $D_{S,0} = D_{S,0}^+$ and $D_{S,0}^-$, under an arbitrary displacement history shown in Fig. 4.3(a). In Fig. 4.3(a), the upper and lower scragging thresholds increase from time t_1 to t_2, when the displacement norm exceeds $D_{S,0}^+$. Upon load reversal, when the displacement reaches the lower threshold (t_3 to t_4), D_S^- decreases, and the scragging parameter in Fig. 4.3(b) increases according to Eq. (4.19). A small displacement cycle between the current thresholds (t_4 to t_6) does not affect any of the parameters, and finally when the displacement returns to zero (t_6 to t_7) the scragging parameter reaches the upper threshold.

Finally, it is necessary to define the reduction factor for each component of the force vector as a function of the scalar scragging parameter. An exponential expression for each reduction factor is considered in terms of the cube of the scragging parameter. The cube of D_S is considered appropriate because this is approximately proportional to the work done by the quadratic hysteretic force defined in Eq. (4.18). The work done by the hysteretic force is representative of the energy dissipated in the bearing under virgin displacement excursions, which may be expected to give a measure of the degradation in these scragging cycles. Comparisons with experimental data in Section 5 also suggest that this assumption is reasonable. For example, the percentage degradation observed on a virgin displacement cycle to 250% strain magnitude is less than that observed on a subsequent displacement cycle to 350% strain magnitude. An exponential reduction in terms of D_S alone would predict that it takes a 500% strain to degrade the bearing the same amount. Therefore, the following expressions apply for the reduction factors:

$$K_{S1} = \exp(-c_1 D_S^3) \quad ; \qquad K_{S2} = \exp(-c_2 D_S^3) \tag{4.20}$$

where c_1 and c_2 are material parameters which govern the rate of degradation of $\mathbf{F}_1$ and $\mathbf{F}_2$, respectively.

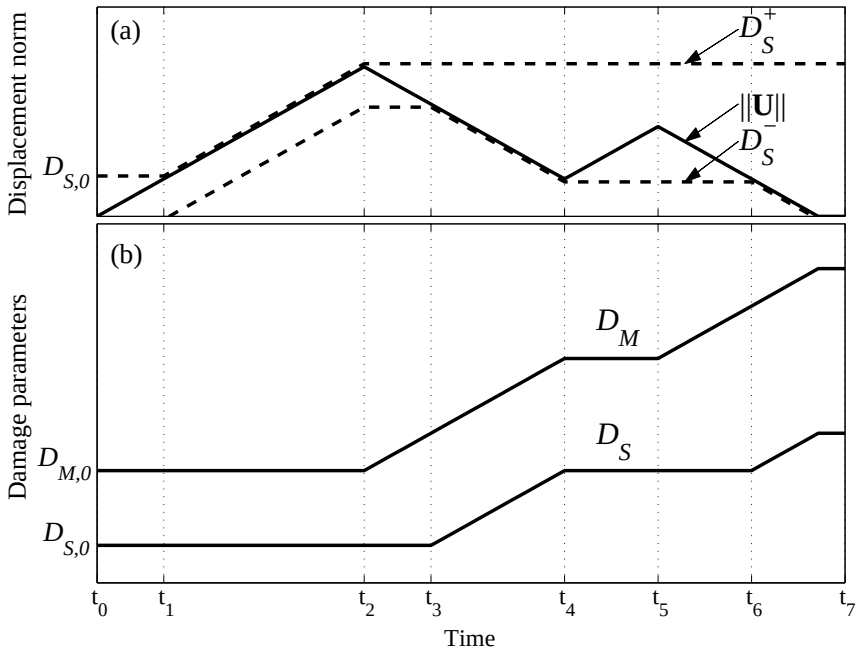

Figure 4.3. (a) Arbitrary history of displacement norm, $\|\mathbf{U}\|$, and scragging parameter upper and lower thresholds, D_S^+ and D_S^-, and (b) evolution of scragging and Mullins' effect damage parameters, D_S and D_M

4.1.3.2 Mullins' effect. Mullins' effect is accounted for in the model by the reduction factor K_M. For consistency with the scragging damage parameter, a strictly increasing, displacement-based parameter, D_M, is adopted. Unlike the scragging effect, however, Mullins' effect degradation occurs over successive cycles of loading, regardless of previous peak cycles. As with scragging though, it is desirable for Mullins' effect to be applied when the displacement norm decreases. To represent this behaviour, the rate of increase of D_M is given by the rate of decrease of the displacement norm, $\|\mathbf{U}\|$. The rate equations are summarised below, while the evolution of D_M from an initial value of $D_{M,0}$, under the general displacement history considered earlier is shown in Fig. 4.3(b). The difference between the behaviour of D_S and D_M is that the Mullins' effect parameter increases whenever the displacement is decreasing (t_2 to t_4 and t_6 to t_7), and not just when it decreases below a certain threshold.

$$\begin{cases} \text{if} \quad \overline{\|\dot{\mathbf{U}}\|} > 0, & \dot{D}_M = 0 \\ \text{if} \quad \overline{\|\dot{\mathbf{U}}\|} < 0, & \dot{D}_M = -\overline{\|\dot{\mathbf{U}}\|} \end{cases} \tag{4.21}$$

The degradation of response due to Mullins' effect is smaller than the degradation due to scragging, and tends to become insignificant after several cycles. For this reason, exponential degradation is

defined to a residual limit, with the following expression appropriate for the reduction factor:

$$K_M = c_3 + (1 - c_3)\exp(-c_4 D_M^3) \tag{4.22}$$

where c_3 and c_4 are material parameters. This expression describes a reduction factor that evolves from an initial value of 1.0 to a residual value of c_3 as D_M is increased.

The Mullins' effect reduction factor is only applied to the elastic skeleton, and not to the hysteretic force. Experimental data, such as those shown in Fig. 2.4, suggest that the reduction of the hysteretic force is small compared with the elastic force, and does not justify the inclusion of further material parameters in the model.

4.2 Time Discretisation and Integration Algorithm

The time discretisation and solution algorithm for the continuous model discussed in the previous section is relatively simple compared with the return mapping algorithm used with classical plasticity approaches (Section 3.2). Initially, Eqs. (4.1) and (4.17) are integrated using backward Euler integration to give:

$$\mathbf{n} = \frac{\mathbf{U} - \mathbf{U}_n}{\|\mathbf{U} - \mathbf{U}_n\|} \tag{4.23}$$

and

$$\delta = \frac{\delta_n}{1 + b_3\|\mathbf{U} - \mathbf{U}_n\|} \tag{4.24}$$

It must be realised that Eq. (4.24) applies along displacement paths with no sudden change of direction, as discussed in the previous section. This means that an effective value of $\delta_n = \delta_n^*$ must be defined at the start of the time step based on the current value of $\mathbf{n}$, and values of R and $\mathbf{F}_2$ at time step n. Storage requirements can also be minimised by recalculating R_n by substituting values of $\mathbf{U}_n$ and D_{Mn} (which must be stored for other steps in the algorithm) into Eq. (4.13). The effective δ_n is then given by:

$$\delta_n^* = \|R(\mathbf{U}_n, D_{Sn})\mathbf{n} - \mathbf{F}_{2n}\| \tag{4.25}$$

The unit vector, $\boldsymbol{\mu}$, can be obtained by integrating Eq. (4.16):

$$\boldsymbol{\mu} = \frac{\mathbf{F}_2 - \mathbf{F}_{2,n}}{\|\mathbf{F}_2 - \mathbf{F}_{2,n}\|} \tag{4.26}$$

From Eq. (4.15)$_2$, the vector given by $(\hat{\mathbf{F}} - \mathbf{F}_2)$ is parallel to $\boldsymbol{\mu}$, and adding and subtracting $\mathbf{F}_{2,n}$, the following result is obtained:

$$\left[(\hat{\mathbf{F}} - \mathbf{F}_{2,n}) + (\mathbf{F}_2 - \mathbf{F}_{2,n})\right] \quad \| \quad \boldsymbol{\mu} \tag{4.27}$$

The second expression in parentheses is parallel to $\boldsymbol{\mu}$ from Eq. (4.26), which shows that the first expression in parentheses is also parallel to $\boldsymbol{\mu}$. Because $\boldsymbol{\mu}$ is a unit vector, the following equation is obtained:

$$\boldsymbol{\mu} = \frac{\hat{\mathbf{F}} - \mathbf{F}_{2,n}}{\|\hat{\mathbf{F}} - \mathbf{F}_{2,n}\|} \tag{4.28}$$

which does not require the current value of the damping force vector, $\mathbf{F}_2$.

For the damage parameters, Eqs. (4.19) and (4.21) are replaced with their equivalents in a discrete time regime:

$$\begin{cases} \text{if} \quad \|\mathbf{U}\| > D_{Sn}^{+} \\ \qquad\qquad D_S^{+} = \|\mathbf{U}\| \\ \qquad\qquad D_S^{-} = D_{Sn}^{-} + (D_S^{+} - D_{Sn}^{+}) \\ \qquad\qquad D_S = D_{Sn} \\ \text{if} \quad \|\mathbf{U}\| < D_{Sn}^{-} \\ \qquad\qquad D_S^{+} = D_{Sn}^{+} \\ \qquad\qquad D_S^{-} = \|\mathbf{U}\| \\ \qquad\qquad D_S = D_{Sn} - (D_S^{-} - D_{Sn}^{-}) \\ \text{if} \quad \|\mathbf{U}\| < \|\mathbf{U}_n\| \\ \qquad\qquad D_M = D_{Mn} + \|\mathbf{U}_n\| - \|\mathbf{U}\| \end{cases} \tag{4.29}$$

The time discrete expressions in Eq. (4.29) are motivated by the desired response under arbitrary time histories, such as in Fig. 4.3, and are not obtained by directly integrating the time continuous equations. Note that the proposed form eliminates the need to consider the "crossing point" at which the inequalities are first satisfied, although it will not correctly identify the accumulation of damage for displacement histories that cross the origin in displacement space. In the implementation of the model it is necessary to provide a check of the signs of U_x and U_y, and divide the time step into unloading and reloading phases when this occurs.

The algorithm used to obtain the force for a given displacement at time t_{n+1} is summarised as follows:

1. Update damage variables, D_S and D_M, and scragging thresholds, D_S^{+} and D_S^{-}, based on the current displacement vector norm, using Eq. (4.29).
2. Calculate reduction factors, K_{S1}, K_{S2} and K_M, based on new damage variables from Eqs. (4.20) and (4.22).
3. Calculate the elastic force, $\mathbf{F}_1(\mathbf{U}, K_{S1}, K_M)$, from Eq. (4.11).

4. Calculate bounding surface radius, $R(\|\mathbf{U}\|, K_{S2})$, from Eq. (4.13).
5. Calculate direction of velocity vector, $\mathbf{n}$, from Eq. (4.23), and hence $\hat{\mathbf{F}}$ from Eq. (4.14).
6. Use Eq. (4.25) to calculate equivalent distance to bounding surface at start of time step, δ_n^*, and update distance for time $n+1$ from Eq. (4.24).
7. Calculate direction of change in hysteretic force, $\boldsymbol{\mu}$, from Eq. (4.28), and hence update hysteretic force, $\mathbf{F}_2$ using Eq. (4.18).
8. Calculate the updated force vector from Eq. (4.2), and store $\mathbf{U}$, $\mathbf{F}_2$ and $\{D_S, D_S^+, D_S^-, D_M\}$ for next time step.

For force-controlled problems, an iterative Newton–Raphson approach is used to calculate the displacement vector for a given force. For quadratic convergence of the algorithm, a consistent tangent matrix must be derived by differentiating the time discrete equations presented in this section with respect to the displacement vector. The derivation is detailed in Appendix A.

4.3 Parameter Sensitivity Study

Using the time discrete version of the model presented in the previous section, a series of sensitivity studies was carried out to examine how changes in the model parameters affect the response results. The initial parameter set is presented in Table 4.1, and displacement orbit 2 (box orbit) at 200% maximum strain were chosen for the sensitivity study. The parameter set was adapted from the model calibration presented in Chapter 5, to represent realistic bearing behaviour. The force–deformation response and force loci for the sensitivity studies are presented in Figs. 4.4–4.13. In Figs. 4.4–4.9, parameters a_1 to a_3, describing elastic response, and b_1 to b_3, describing hysteresis, were varied by factors of 0.5 and 2.0, while fixing the parameters describing degradation, c_1 to c_4 at zero. Clearly, from Eq. (4.11), increasing parameters a_1 and a_3 is expected to increase the shear force carried by the bearing, while the opposite applies for a_2, which is negative. Increasing the linear term, a_1, increases the stiffness across the range of displacements, while the higher order terms, a_2 and a_3, have an increasing effect at the higher strain levels. This is particularly evident in the third part of each figure, where the higher order terms clearly account for the "spiky" nature of the force loci.

Increasing both b_1 and b_2 can also be observed to increase the force response. Doubling the constant term, b_1, has a very small effect on the overall response (Fig. 4.7), whereas doubling the quadratic term, b_2, significantly increases the hysteretic force acting in the direction of loading (Fig. 4.8).

Figures. 4.10 and 4.11, illustrate the effect of varying scragging parameters c_1 and c_2, while holding Mullins' effect parameters c_3 and c_4 at zero. In these cases, the first cycle behaviour is the same for each analysis, but the second cycle response is degraded. The material parameters c_1 and c_2

affect the elastic and hysteretic component of force, respectively. Finally, Figs. 4.12 and 4.13 show the response for varying the Mullins' effect parameters, holding scragging parameters at zero. This case is similar to the scragging parameter study, as only two cycles on a virgin bearing are shown here, and the distinction between Mullins' effect and scragging is not observed until later cycles. The difference between the two is that the former is bounded by a minimum (represented by the factor c_3) while the latter is not. Varying this minimum (Fig. 4.12) clearly reduces the residual response after several cycles. It is evident from Fig. 4.13, however, that changing c_4 does not affect the response significantly. This is primarily because c_3 is relatively close to unity, so that the residual response under Mullins' effect degradation is not significantly different from the first cycle response.

Table 4.1. Material parameters used in sensitivity study

a_1	a_2	a_3	b_1	b_2
1.0 kip/in	-0.03 kip/in^3	0.002 kip/in^5	0.5 kip	0.1 kip/in^2
b_3	c_1	c_2	c_3	c_4
1.0 /in	0.002 /in^3	0.006 /in^3	0.8	0.02 /in^3

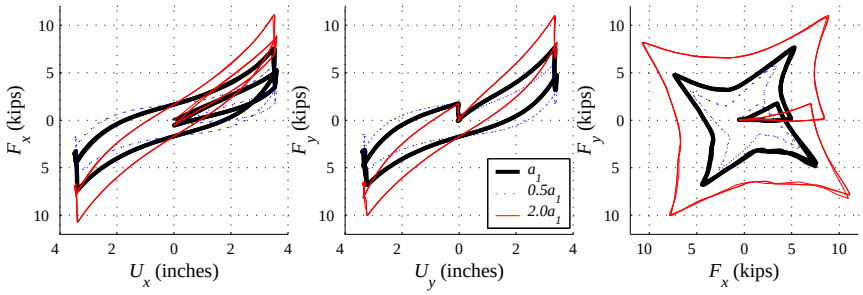

Figure 4.4. Model response under variation of a_1. Degradation parameters $c_1 = c_2 = c_3 = c_4 = 0$; other parameters defined by Table 4.1.

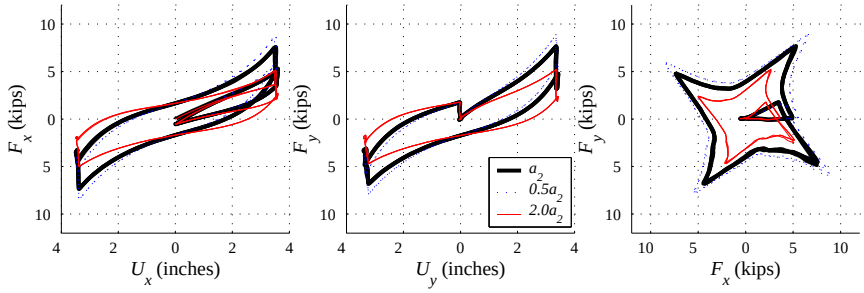

Figure 4.5. Model response under variation of a_2. Degradation parameters $c_1 = c_2 = c_3 = c_4 = 0$; other parameters defined by Table 4.1.

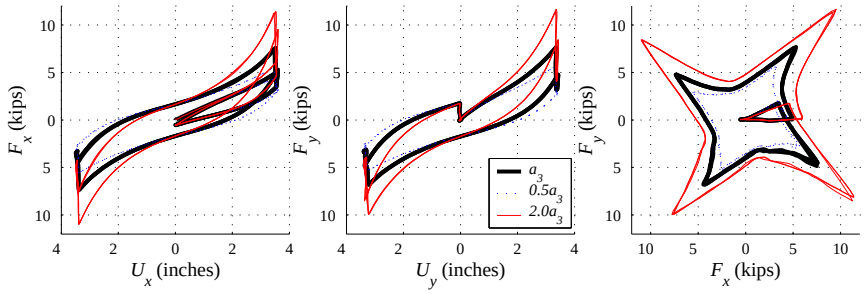

Figure 4.6. Model response under variation of a_3. Degradation parameters $c_1 = c_2 = c_3 = c_4 = 0$; other parameters defined by Table 4.1.

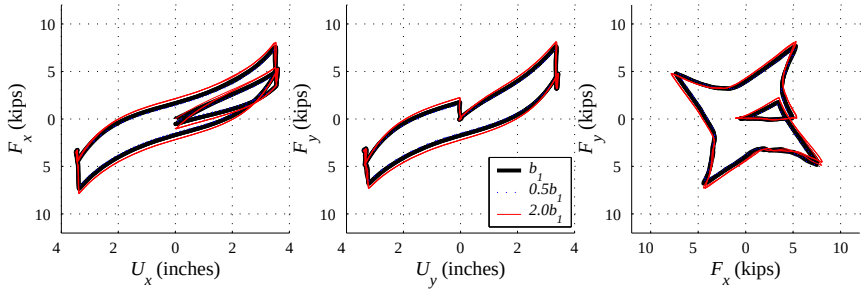

Figure 4.7. Model response under variation of b_1. Degradation parameters $c_1 = c_2 = c_3 = c_4 = 0$; other parameters defined by Table 4.1.

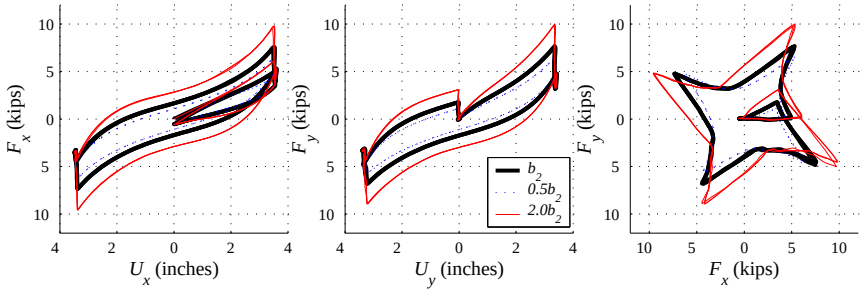

Figure 4.8. Model response under variation of b_2. Degradation parameters $c_1 = c_2 = c_3 = c_4 = 0$; other parameters defined by Table 4.1.

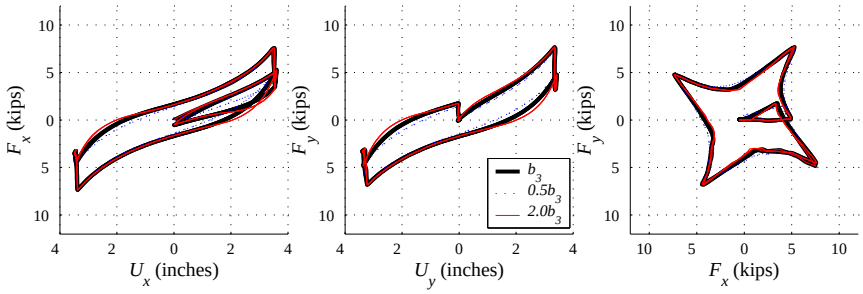

Figure 4.9. Model response under variation of b_3. Degradation parameters $c_1 = c_2 = c_3 = c_4 = 0$; other parameters defined by Table 4.1.

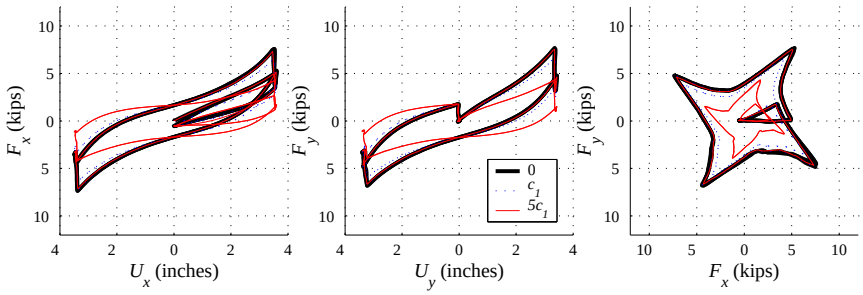

Figure 4.10. Model response under variation of c_1. Parameter $c_2 = 0$ and Mullins' effect parameters $c_3 = c_4 = 0$; other parameters defined by Table 4.1.

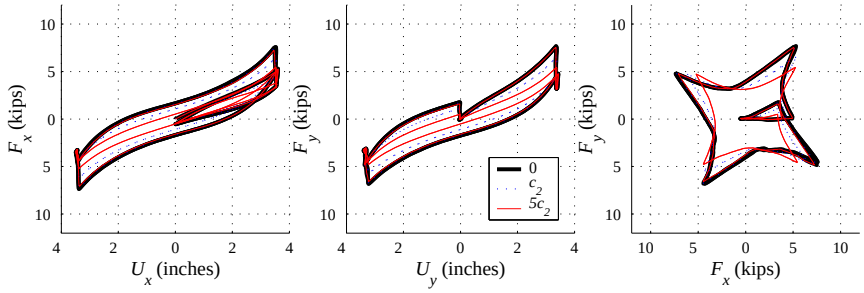

Figure 4.11. Model response under variation of c_2. Parameter $c_1 = 0$ and Mullins' effect parameters $c_3 = c_4 = 0$; other parameters defined by Table 4.1.

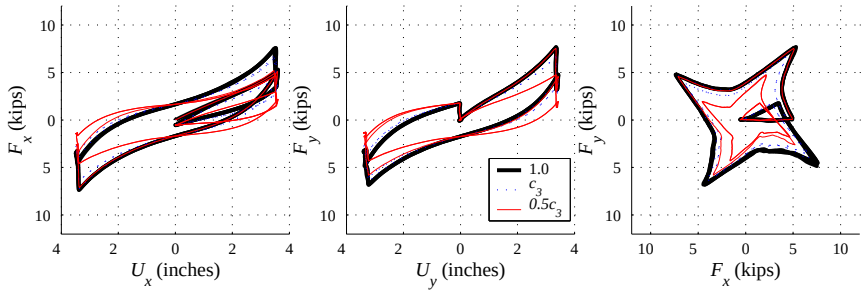

Figure 4.12. Model response under variation of c_3. Scragging parameters $c_1 = c_2 = 0$; other parameters defined by Table 4.1.

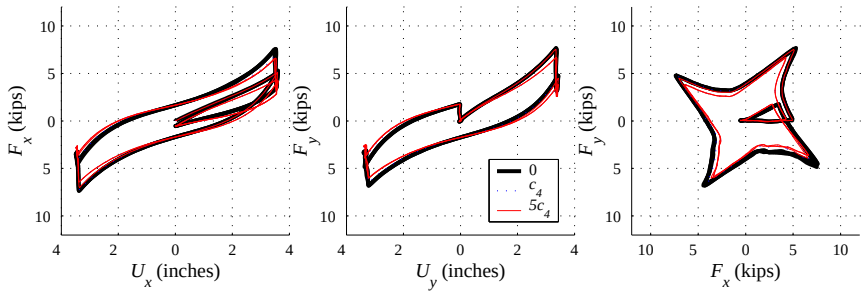

Figure 4.13. Model response under variation of c_4. Scragging parameters $c_1 = c_2 = 0$; other parameters defined by Table 4.1.

4.4 Extension of Model to Rate-Dependence

The model described in the previous sections is able to provide a good match of HDR bearing response under bidirectional load paths at a fixed strain rate (see Chapter 5). It is well known, however, that the behaviour of HDR bearings is strain rate-dependent under unidirectional and bidirectional loading [Clark *et al.*, 1997; Morgan, 2000; Huang, 2002]. As discussed earlier, the proposed model is unable to describe this rate-dependence, and it must therefore be calibrated for strain rates appropriate for earthquake loading.

As discussed in the previous chapter, existing phenomenological models of unidirectional bearing response are either rate-independent, or, if rate-dependence is included in the model, they are calibrated separately for every set of experimental data. There appears, however, to be little practical value in including rate-dependent terms in a model if the calibrated parameter set cannot be used to describe bearing response at a strain rate that differs from the experiment. In addition, the rate-dependent terms adopted in the Huang [2002] (Eqs. (3.1)–(3.3)) and Tsai *et al.* [2003] (Eqs. (3.7)–(3.8)) models are inadequate for non-harmonic, bidirectional loading, and are therefore inappropriate for the proposed model described above.

Three-dimensional constitutive models of elastomers [Govindjee and Simo, 1992; Miehe and Keck, 2000; Haupt and Sedlan, 2001] typically describe rate-dependence and relaxation effects within the framework of viscoelasticity. These models add a rate-dependent term in parallel with a rate-independent term, with the latter comprising either an elastic [Govindjee and Simo, 1992], or an elasto-plastic [Miehe and Keck, 2000; Haupt and Sedlan, 2001] model. Rheologically, the rate-dependent portion of these models can be represented by a number of Maxwell elements (illustrated in Fig. 4.14) in parallel, with linear or nonlinear spring stiffness, K_i, and dashpot viscosity, η_i. Adopting this approach to the current model, the bearing force can be redefined:

$$\mathbf{F}(\mathbf{U}, \mathbf{n}, D_S, D_M) = \mathbf{F}_1(\mathbf{U}, D_S, D_M) + \mathbf{F}_2(\mathbf{U}, \mathbf{n}, D_S) + \sum_i^n \mathbf{F}_{3,i}(\dot{\mathbf{F}}_1) \tag{4.30}$$

where $\mathbf{F}_1$ and $\mathbf{F}_2$ are defined as before, and each of the n rate-dependent force terms are obtained from the following evolutionary equation:

$$\dot{\mathbf{F}}_{3,i} = K_i \left(\dot{\mathbf{U}} - \frac{\mathbf{F}_3}{\eta_i} \right) \tag{4.31}$$

The time discretisation and solution algorithm for the enhanced model fits into the same scheme described above, with $\mathbf{F}_1$ and $\mathbf{F}_2$ obtained as in Section 4.2. Equation (4.31) is discretised according to the backward Euler scheme, and solved for each $i = 1$ to n:

$$\mathbf{F}_{3,i} = \frac{\mathbf{F}_{3,in} + K_i(\mathbf{U} - \mathbf{U}_n)}{1 - \Delta t K_i/\eta_i} \tag{4.32}$$

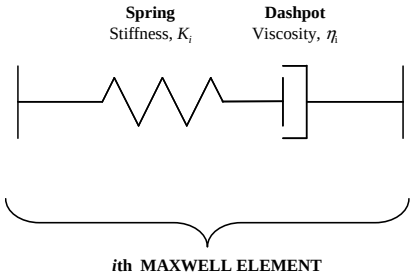

Figure 4.14. Maxwell element – one-dimensional rheological model of viscoelasticity.

where subscript n and no subscript represent the previous and present time step, respectively, and Δt is the time step.

Unlike Eq. (4.17), the mixture of vectors and their time derivatives in Eq. (4.31) ensures that the resulting force term is rate-dependent – this is especially evident from the presence of the time step in Eq. (4.32).

5. VALIDATION OF PROPOSED MODEL

5.1 BIDIRECTIONAL CALIBRATION OF RATE-INDEPENDENT PARAMETERS

The bidirectional model described in the previous chapter uses ten material parameters to describe the rate-independent response. An appropriate identification procedure must be used to determine these parameters for a given bearing. In many studies of bearing models, a separate identification procedure is carried out for each of a series of tests to show that a model can represent both scragged and non-scragged response. For example, Hwang *et al.* [2002] determine parameter values for a bearing in the virgin state, followed by a separate parameter identification for a subsequent test. Although good agreement is found between the measured and predicted hysteresis loops, there are significant changes in the values of the parameters, including those parameters that describe components that are not expected to degrade with cyclic loading. Because the degradation depends on the history of loading, a better approach is to identify a set of parameters for a bearing that represents the cyclic degradation over a series of loads.

In the bidirectional models defined in the previous section, the two damage parameters, D_S and D_M, represent semi-permanent scragging and relatively short-term Mullins' effect, respectively. Experimental evidence suggests that the former degradation is recovered over a period of several years, while the latter is fully recovered in approximately one day, although partial recovery occurs over a shorter period [Thompson *et al.*, 2000]. In the experimental programme described in Section 2.1, the tests were separated by time periods ranging from 5 minutes to 24 hours. To represent recovery of bearing stiffness between tests, the damage parameter, D_M, was set to zero, while D_S was retained between tests.

The complete test programme of the HDR bearings is summarised in Table 5.1. The orbit number (from Fig. 2.2) is given, as well as the maximum shear strain in the x- and y-directions (γ_x and γ_y, respectively), and testing rate. Note that the data for tests 13, 17 and 21 were not available nor included in the subsequent analyses.

The parameter identification for the bidirectional model is carried out for the test series by using the downhill simplex algorithm [Nelder and Mead, 1965]. The algorithm only requires evaluation of the

Table 5.1. Tests of HDR bearings and weights and residuals from model calibration[a]

Test	Orbit	Rate (Hz)	$\gamma_x(\%)$	$\gamma_y(\%)$	$w_{i,1}$	$w_{i,2}$	$\theta_{i,2}$	$w_{i,3}$	$w_{i,4}$	$\theta_{i,4}$
(1)	1s	0.01	25	25	—	—	1.1733	—	—	1.0402
(2)	1s	0.01	250	250	**0.4**	**0.5**	**0.2247**	**0.4**	**0.5**	**0.2088**
(3)	1s	0.01	25	25	—	—	0.7888	—	—	0.7324
(4)	1s	0.01	100	100	—	—	0.4896	**0.2**	**0.0**	**0.4299**
(5)	1s	0.01	200	200	—	—	0.4095	**0.2**	**0.0**	**0.3658**
(6)	2s	0.01	25	25	—	—	0.3323	—	—	0.4079
(7)	3s	0.01	25	25	—	—	0.4638	—	—	0.6072
(8)	4s	0.01	25	25	—	—	0.4762	—	—	0.5859
(9)	2s	0.01	25	100	—	—	0.3707	—	—	0.4448
(10)	3s	0.01	25	100	—	—	0.5695	—	—	0.7707
(11)	4s	0.01	25	100	—	—	0.4936	—	—	0.6796
(12)	2s	0.01	100	100	**0.2**	**0.0**	**0.3453**	—	—	0.3830
(13)	3s	0.01	100	100	—	—	—	—	—	—
(14)	4s	0.01	100	100	—	—	0.5329	—	—	0.5981
(15)	4r	0.50	100	100	—	—	0.3191	—	—	0.2134
(16)	2s	0.01	100	200	—	—	0.3361	—	—	0.3110
(17)	3s	0.01	100	200	—	—	—	—	—	—
(18)	4s	0.01	100	200	—	—	0.6258	—	—	0.6064
(19)	4r	0.50	100	200	—	—	0.2203	—	—	0.1770
(20)	2s	0.01	200	200	—	—	0.1987	—	—	0.1764
(21)	3s	0.01	200	200	—	—	—	—	—	—
(22)	4s	0.01	200	200	—	—	0.5777	—	—	0.5375
(23)	4r	0.50	200	200	—	—	0.2290	—	—	0.1964
(24)	2s	0.01	250	250	**0.2**	**0.0**	**0.2334**	—	—	0.4311
(25)	3s	0.01	250	250	—	—	0.3224	—	—	0.6541
(26)	4s	0.01	250	250	—	—	0.2276	—	—	0.4851
(27)	1s	0.01	25	25	—	—	0.5154	—	—	0.6644
(28)	1s	0.01	250	250	**0.2**	**0.5**	**0.2409**	**0.2**	**0.5**	**0.2218**

[a]Bold lines are tests used in model calibration.

objective function (not gradients), and it is computationally efficient. The function to be minimised is the weighted sum of the residuals from a subset of the tests in the experimental programme, in which the residual from test i is defined as:

$$\theta_i(\mathbf{a}) = \frac{\int \left| \left(\mathbf{F}_{i,e} - \mathbf{F}_{i,m}(\mathbf{a})\right)^T d\mathbf{U}_i \right|}{\int \left| \mathbf{F}_{i,e}^T \, d\mathbf{U}_i \right|} \tag{5.1}$$

where $\mathbf{U}_i$ and $\mathbf{F}_{i,e}$ are the experimental force and displacement from test i, and $\mathbf{F}_{i,m}(\mathbf{a})$ is the resisting force determined by the model with parameters given in vector $\mathbf{a}$. The residual is

normalised with respect to the total work done in the test. Each residual is weighted by a scalar, w_i, with $\sum w_i = 1$, so that the total residual is given by:

$$\Theta = \sum_{i=1}^{\text{no. tests}} \left(w_i \theta_i\right) \tag{5.2}$$

This form of the residual function allows flexibility in the identification algorithm. To assess the predictive capabilities of the model, the weights for certain tests can be set to zero to remove this data from the parameter optimisation. Note, however, that the change in the scragging parameter must still be considered over the entire test regime for an appropriate determination of material parameters.

Data for calibration are selected to be representative of the bearing response under different load paths and strain levels. In this case, tests 2, 12, 24 and 28 were selected for the calibration. The first two represent the high strain, unidirectional behaviour of the bearing under displacement orbit 1. These give an indication of the bearing response in both the virgin state of the bearing and in the fully degraded state. The latter two tests are representative of bidirectional response, under displacement orbit 2, at both medium and high strain levels with total shear strain magnitudes of 140% and 350%, respectively. Orbits 3 and 4 were not considered in the calibration, to give an indication of the predictive power of the model. Furthermore, low strain tests were also ignored, as they are less critical for earthquake engineering applications.

The calibration is carried out in two stages to separate the degradation into scragging and Mullins' effect components. Of the tests included in the calibration, both tests 2 and 24 are expected to induce scragging degradation, because they represent the highest strain for the bearing. In the first stage of the calibration, only first half-cycle data are considered, and the minimisation is carried out on material parameters $(a_1, a_2, a_3, b_1, b_2, b_3, c_1, c_2)$, ignoring the degradation due to Mullins' effect $(c_3 = 1, c_4 = 0)$. In the second stage, all cycles are used, and material parameters (c_1, c_3, c_4) are re-calibrated, holding the other parameters fixed. The parameter c_1 is included in the second calibration to separate the scragging and Mullins' effects. The weights from each stage of the calibration, $w_{i,1}$ and $w_{i,2}$, are shown in Table 5.1.

The evolution of the degradation parameters, D_S and D_M, over the course of the experimental programme, is shown in Fig. 5.1. The scragging parameter increases when the displacement vector reaches a new peak value, whereas the Mullins' parameter increases during each test, but is recovered between tests. The material parameters obtained in the calibration procedure are shown in Table 5.2.

The experimental data from the tests included in the calibration are compared with the model response in Figs. 5.2, 5.3 and 5.4, and the residuals are given in Table 5.1. The model response shows an excellent fit of the orbit 1, unidirectional behaviour (Fig. 5.2), capturing both the strain stiffening

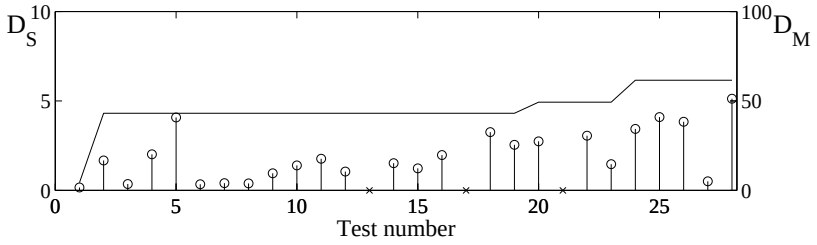

Figure 5.1. Evolution of D_S (continuous line) and D_M (discrete points) over test programme.

Table 5.2. Material parameters from displacement-controlled tests, calibrated for orbit 1 and 2 test data.

a_1	a_2	a_3	b_1	b_2
1.3387 kip/in	-0.0170 kip/in^3	0.0006 kip/in^5	0.7436 kip	0.2022 kip/in^2
b_3	c_1	c_2	c_3	c_4
1.9431 /in	0.0018 /in^3	0.0059 /in^3	0.8847	0.0003 /in^3

and degradation at the beginning and end of the test regime. The model response for the box orbit 2 also provides an accurate representation of medium strain level (Fig. 5.3) bidirectional behaviour, in terms of both magnitude and direction of the force vector in the first cycle. The high strain level (Fig. 5.4) response is also captured qualitatively, although degradation is slightly overestimated in the second cycle response. It is interesting to note that the second, third and fourth 'corners' of the orbit 2 experimental force locus are greater in magnitude than the first excursion, particularly for the second and subsequent cycles. This unusual behaviour observed in tests may be caused by anisotropy in the bearing at very large strain levels.

To assess the predictive capability of the model, the response for tests not included in the calibration (although included in the calculation of D_S) can be examined. Representative comparisons of experimental data and model response are presented in Figs. 5.5 to 5.8. The residuals for each test, as defined in Eq. (5.1), are also given in Table 5.1. It can be observed that the residuals of the tests not included in the calibration routine are greater, although not significantly, than for the tests included in the calibration (shown in boldface). The exceptions are the residuals for the low strain level orbits, tests 1, 3, 6, 7, 8 and 27, which are generally greater than the residuals from other tests. For these tests, relatively small deviations from experimental behaviour in the model response represent a large percentage of the total work done in the test, which leads to a large normalised residual. In most cases, the medium to high strain behaviour is of more interest for design. The model response for orbits 1 and 2 is particularly accurate, probably because other tests under these displacement orbits had been included in the calibration. The model response for orbit 3 is also accurately described, but bearing forces under orbit 4 are slightly overestimated by the calibrated model, particularly for the

high strain test (corresponding to a maximum shear strain vector magnitude of 310%). However, the direction of the force vector is still obtained accurately in these tests.

Finally, the results from the orbit 4, high strain rate tests are presented in Fig. 5.9, and compared with the model response using material parameters calibrated for slow test data. The experimental results (top half of Fig. 5.9) may also be compared with the slow tests (Fig. 5.8) to assess the strain-rate dependence directly. For the maximum strain levels and strain rates considered, the 0.5 Hz tests result in resisting force levels up to 30% greater than those observed in the 0.01 Hz tests. Consequently, the rate-independent model response for a bearing calibrated to the slow rate tests underestimates the forces in faster tests. In this case, however, where the slow rate forces have been overestimated initially, the model provides a good fit of the data for the 100% and 200% strain tests.

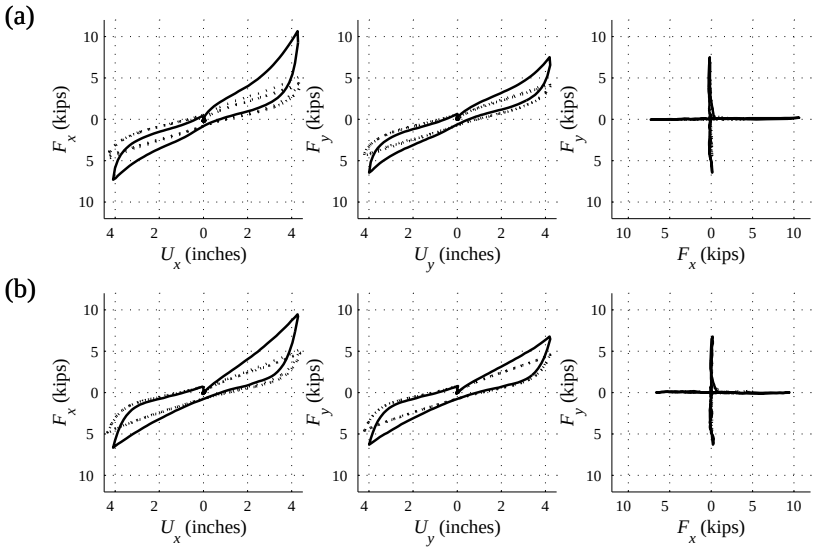

Figure 5.2. (a) Experimental response and (b) model response with parameters in Table 5.2, for tests 2 (solid line) and 28 (dotted line): orbit 1, $\gamma_x = \gamma_y = 250\%$.

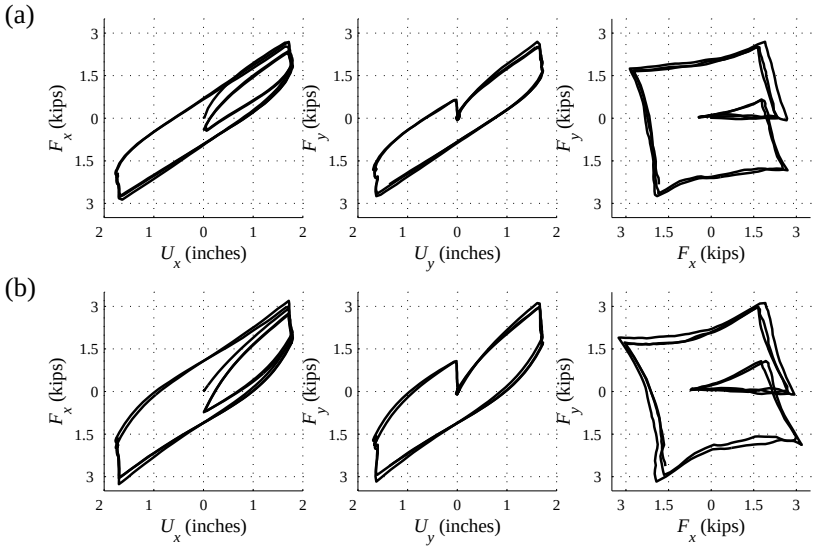

Figure 5.3. (a) Experimental response and (b) model response with parameters in Table 5.2, for test 12: orbit 2, $\gamma_x = \gamma_y = 100\%$.

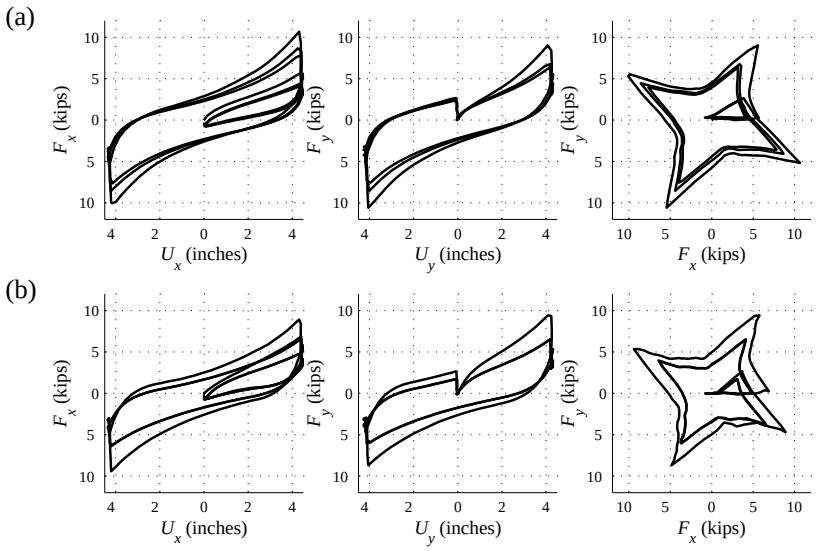

Figure 5.4. (a) Experimental response and (b) model response with parameters in Table 5.2, for test 24: orbit 2, $\gamma_x = \gamma_y = 250\%$.

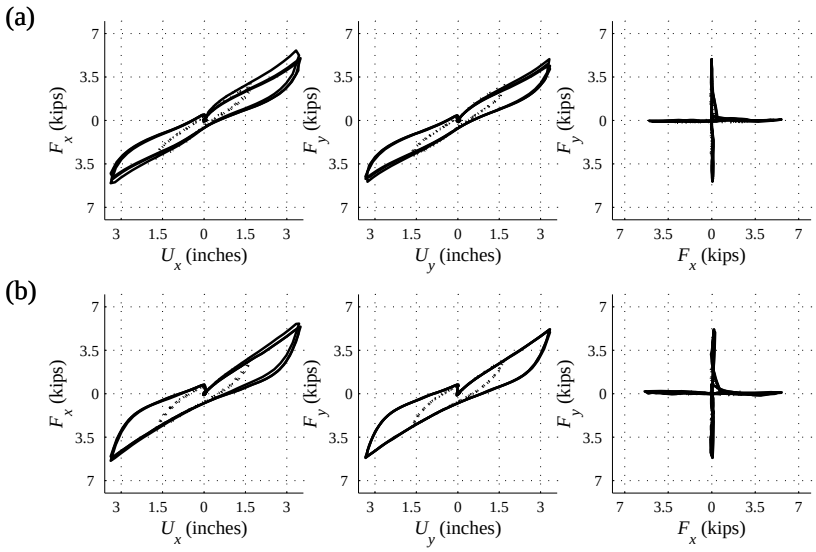

Figure 5.5. (a) Experimental response and (b) model response with parameters in Table 5.2, for tests 4 (dotted line) and 5 (solid line): orbit 1, $\gamma_x = \gamma_y = 100\%$ and $\gamma_x = \gamma_y = 200\%$. Tests not included in model calibration.

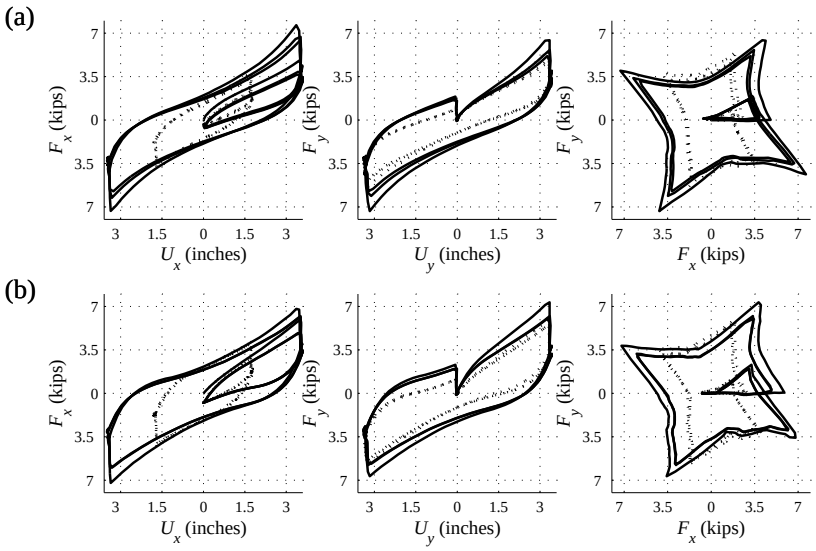

Figure 5.6. (a) Experimental response and (b) model response with parameters in Table 5.2, for tests 16 (dotted line) and 20 (solid line): orbit 2, $\gamma_x = \gamma_y = 100\%$ and $\gamma_x = \gamma_y = 200\%$. Tests not included in model calibration.

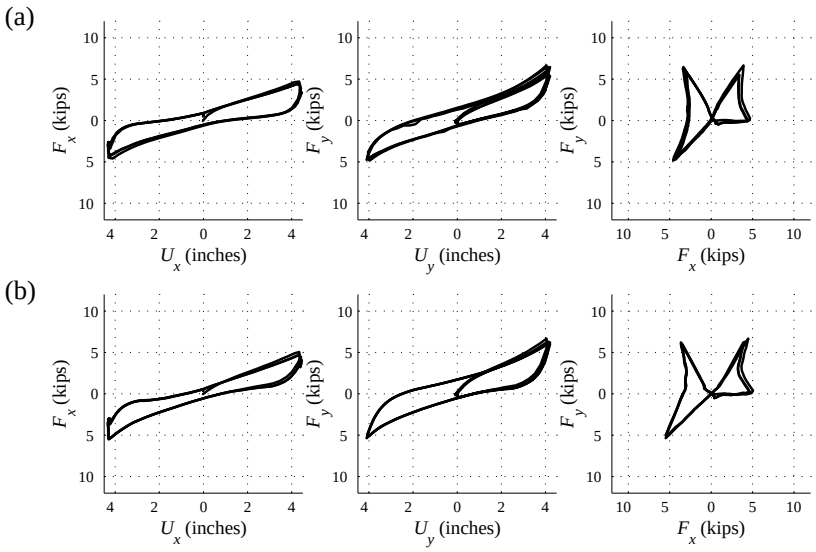

Figure 5.7. (a) Experimental response and (b) model response with parameters in Table 5.2, for test 25: orbit 3, $\gamma_x = \gamma_y = 250\%$. Test not included in model calibration.

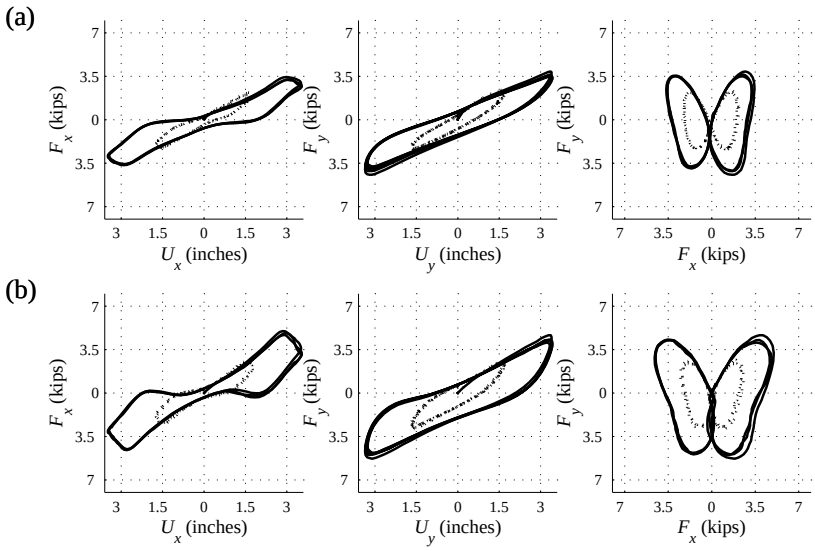

Figure 5.8. (a) Experimental response and (b) model response with parameters in Table 5.2, for tests 14 (dotted line) and 22 (solid line): orbit 4, $\gamma_x = \gamma_y = 100\%$ and $\gamma_x = \gamma_y = 200\%$, slow strain rate. Tests not included in model calibration.

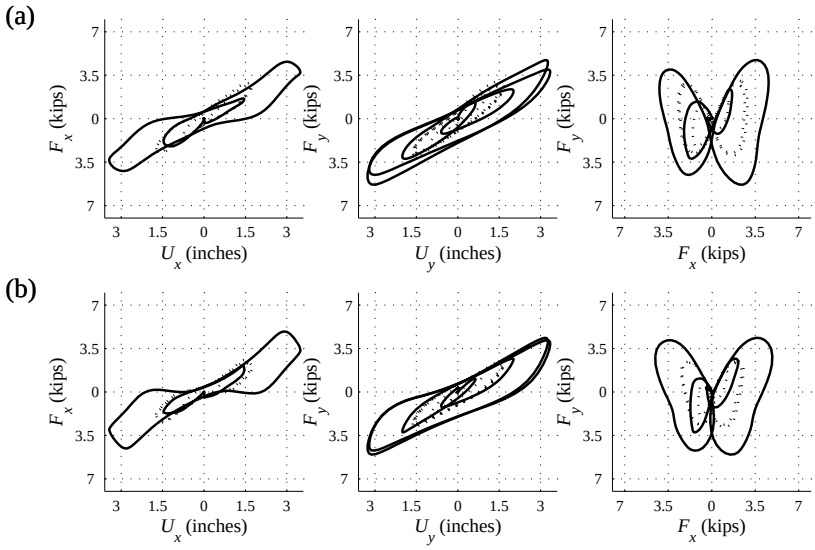

Figure 5.9. (a) Experimental response and (b) model response with parameters in Table 5.2, for tests 15 (dotted line) and 23 (solid line): orbit 1, $\gamma_x = \gamma_y = 100\%$ and $\gamma_x = \gamma_y = 200\%$, rapid strain rate. Tests not included in model calibration.

5.2 UNIDIRECTIONAL CALIBRATION OF RATE-INDEPENDENT PARAMETERS

For practical use of the model for design, it would be preferable to calibrate material parameters based only on unidirectional tests. Because of the vector summation involved in the model, it could be expected that there may be difficulties using unidirectional calibrated parameters for bidirectional analyses.

To examine this issue, the two-step calibration described in the previous section was repeated with the weights, $w_{i,3}$ and $w_{i,4}$, given in Table 5.1. Note that only orbit 1 tests carry a non-zero weighting in the two calibration phases, although the other tests are included in the analysis process for a proper account of scragged and unscragged behaviour. Orbit 1, the cruciform orbit, includes loading in both directions, but the two directions are loaded consecutively rather than simultaneously. This means that the first half-cycle data used in the first phase of the calibration are unidirectional, and the full data used in the second phase are equivalent to two full unidirectional cycles, if the assumption of isotropic damage is valid. The tests included in the calibration represent a range of strain levels from 100% to 250%, and virgin and scragged response.

The parameters obtained in this calibration are shown in Table 5.3. Comparing with Table 5.2, and considering the sensitivity studies of Section 4.3, it can be observed that the only significant changes from the first calibration are in the elastic component, governed by parameters a_1, a_2 and a_3. The residuals from this calibration routine, $\theta_{i,4}$, are also presented in Table 5.1. In general, the residuals are less than for the previous calibration for orbit 1 tests across the full range of strains (tests 1–5, 28; exception test 27). For the orbits 2–4, low strain level tests (tests 6–14) the residuals are 11%–38% greater than for the first calibration, whereas at a medium to high strain level (tests 16–23) the residuals are 3%–20% less. At the highest strain levels (tests 24–26), the residuals from the unidirectional calibration are again greater than for the bidirectional calibration. Finally, the rapid tests (tests 15, 19 and 23) have lower residuals for the second calibration, although as discussed above, without accounting for strain-rate dependence in the model, this has little significance.

Table 5.3. Material parameters from pseudo-static displacement tests, calibrated for orbit 1 test data only.

a_1	a_2	a_3	b_1	b_2
1.5818 kip/in	-0.0665 kip/in^3	0.0029 kip/in^5	0.7930 kip	0.2007 kip/in^2
b_3	c_1	c_2	c_3	c_4
1.9081 /in	0.0018 /in^3	0.0069 /in^3	0.8652	0.0004 /in^3

Figures 5.10–5.17 compare the experimental and model behaviour for selected tests from Table 5.1. Comparing Figs. 5.2 and 5.10, it is apparent that, although the differences are slight, the unidirectional

calibration captures the stiffening behaviour exhibited in tests 2 and 28 more accurately. For the tests shown in Figs. 5.11, 5.13 and 5.14, the unidirectional calibration performs similarly to the bidirectional data. However, Figs. 5.12 and 5.15, show that the model response for the second calibration greatly overestimates the observed behaviour for these high strain level tests. As discussed earlier, the parameters obtained from both calibrations suggest that, of the two components of force, only the elastic skeleton is changed significantly. This observation can also be made from Figs. 5.12 and 5.15, by decomposing the force vector into its components.

From the comparisons between unidirectional and bidirectional calibrations, it is apparent that neither procedure provides uniform accuracy across the full range of strain levels and displacement orbits. In particular, it is not true that a calibration procedure that includes bidirectional test data is better suited for calibrating the proposed bidirectional model for all load paths. From the test residuals, it seems that the principal difference between the two procedures was in the range of strains, and not the displacement orbits, covered in the calibrated tests. The first calibration included a range of peak strain magnitudes from 140% (test 12) to 350% (test 24), whereas the second calibration included a range from 100% (test 4) to 250% (tests 2 and 28). Accordingly, the second calibration performed worse for the tests at strain levels beyond this range. If unidirectional tests were available up to strain levels of 350%, it may be possible to effectively calibrate the model across a larger range using only unidirectional tests.

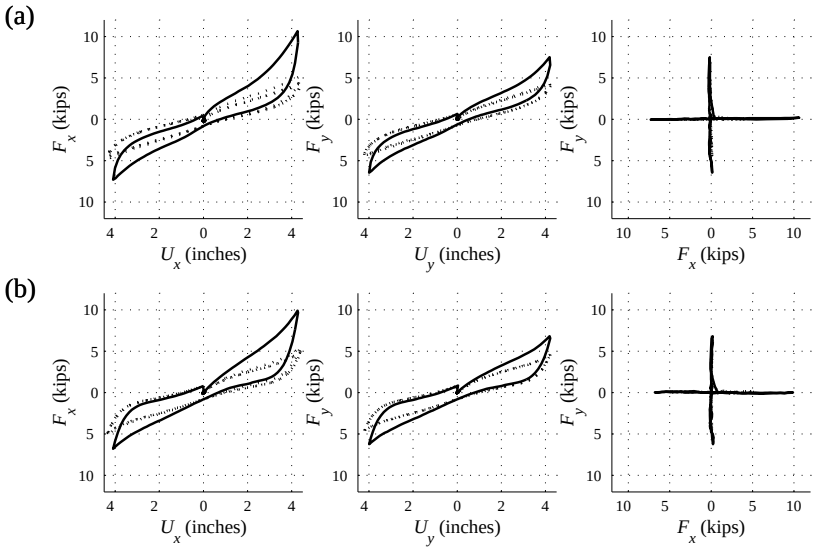

Figure 5.10. (a) Experimental response and (b) model response with parameters in Table 5.3, for tests 2 (solid line) and 28 (dotted line): orbit 1, $\gamma_x = \gamma_y = 250\%$.

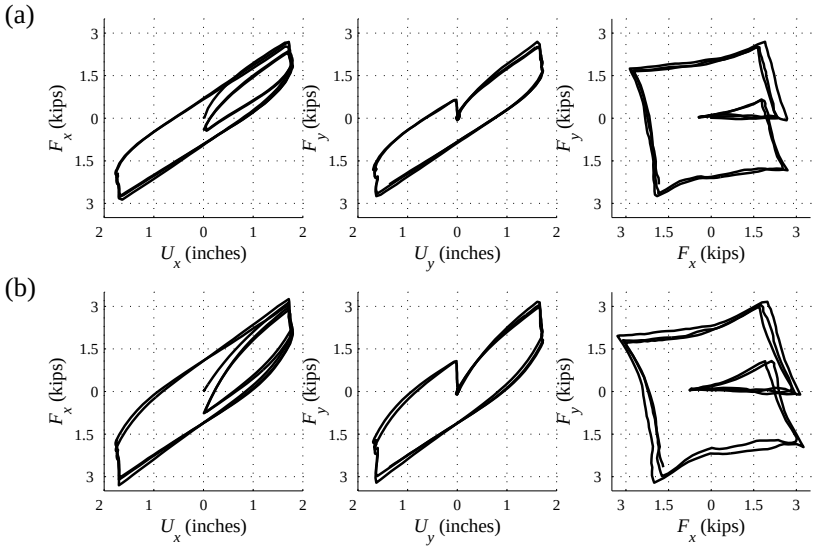

Figure 5.11. (a) Experimental response and (b) model response with parameters in Table 5.3, for test 12: orbit 2, $\gamma_x = \gamma_y = 100\%$. Test not included in model calibration.

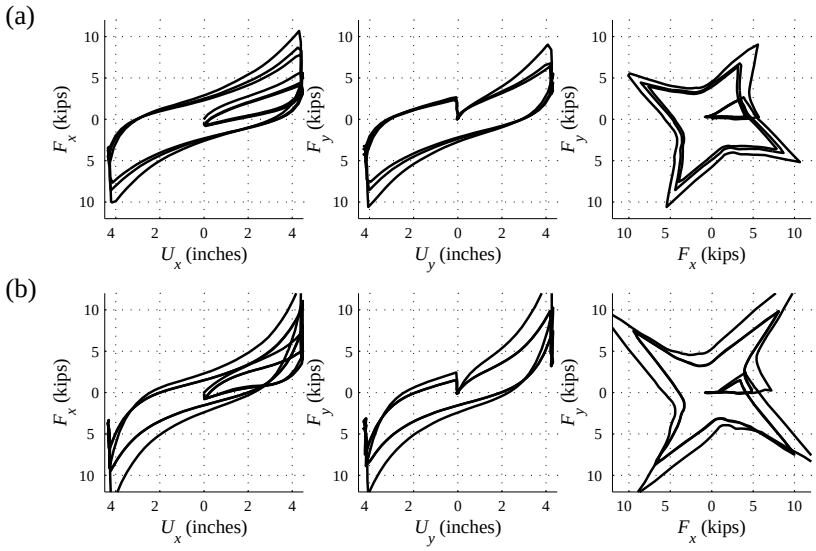

Figure 5.12. (a) Experimental response and (b) model response with parameters in Table 5.3, for test 24: orbit 2, $\gamma_x = \gamma_y = 250\%$. Test not included in model calibration.

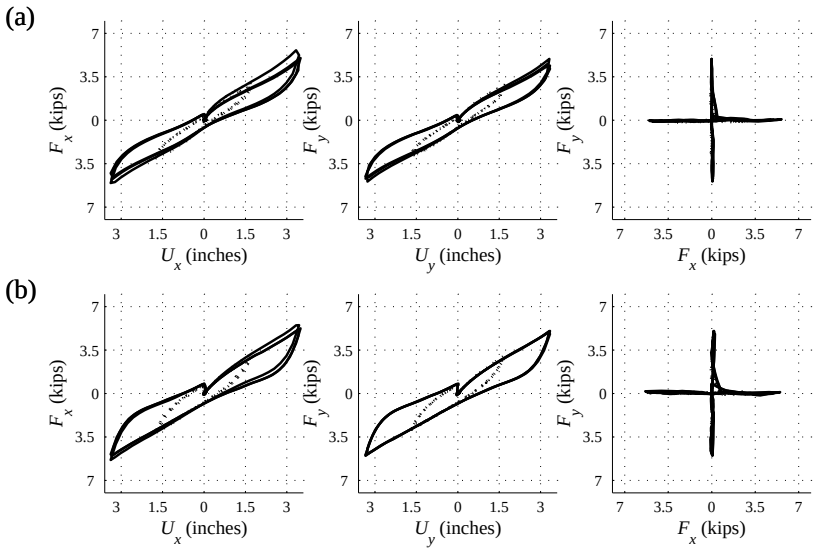

Figure 5.13. (a) Experimental response and (b) model response with parameters in Table 5.3, for tests 4 (dotted line) and 5 (solid line): orbit 1, $\gamma_x = \gamma_y = 100\%$ and $\gamma_x = \gamma_y = 200\%$.

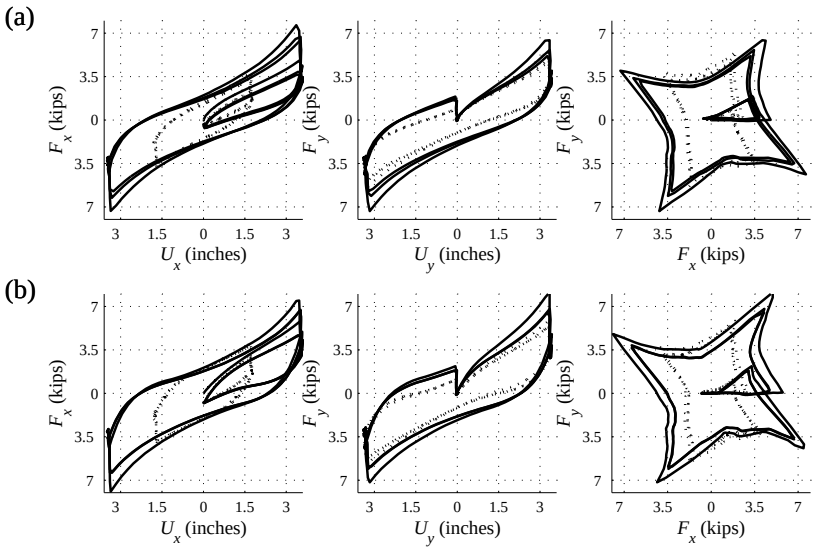

Figure 5.14. (a) Experimental response and (b) model response with parameters in Table 5.3, for tests 16 (dotted line) and 20 (solid line): orbit 2, $\gamma_x = \gamma_y = 100\%$ and $\gamma_x = \gamma_y = 200\%$. Tests not included in model calibration.

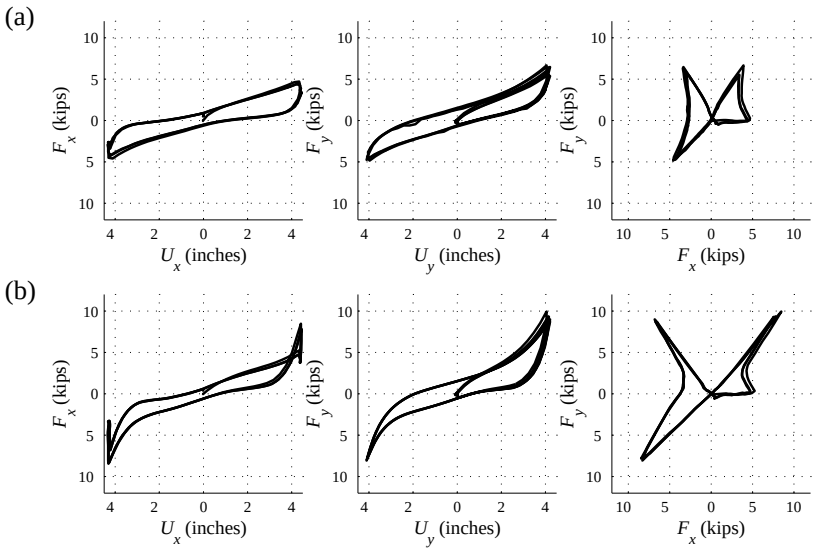

Figure 5.15. (a) Experimental response and (b) model response with parameters in Table 5.3, for test 25: orbit 3, $\gamma_x = \gamma_y = 250\%$. Test not included in model calibration.

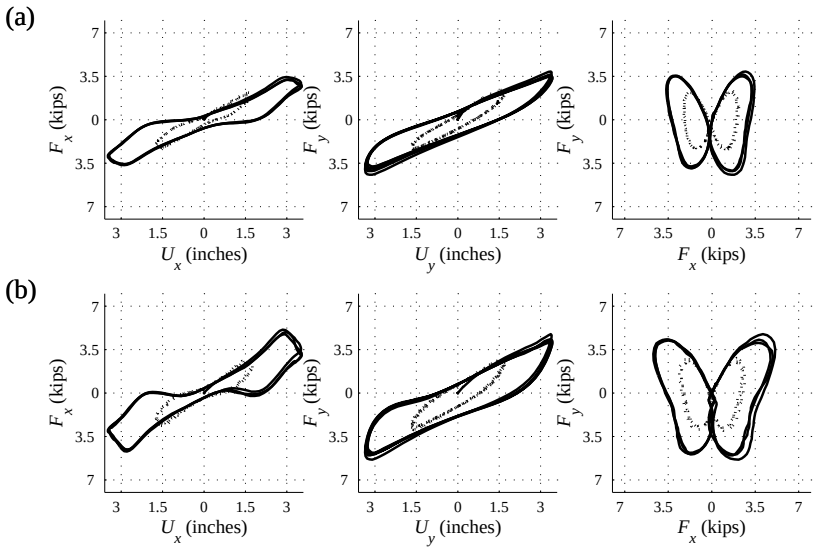

Figure 5.16. (a) Experimental response and (b) model response with parameters in Table 5.3, for tests 14 (dotted line) and 22 (solid line): orbit 4, $\gamma_x = \gamma_y = 100\%$ and $\gamma_x = \gamma_y = 200\%$, slow strain rate. Tests not included in model calibration.

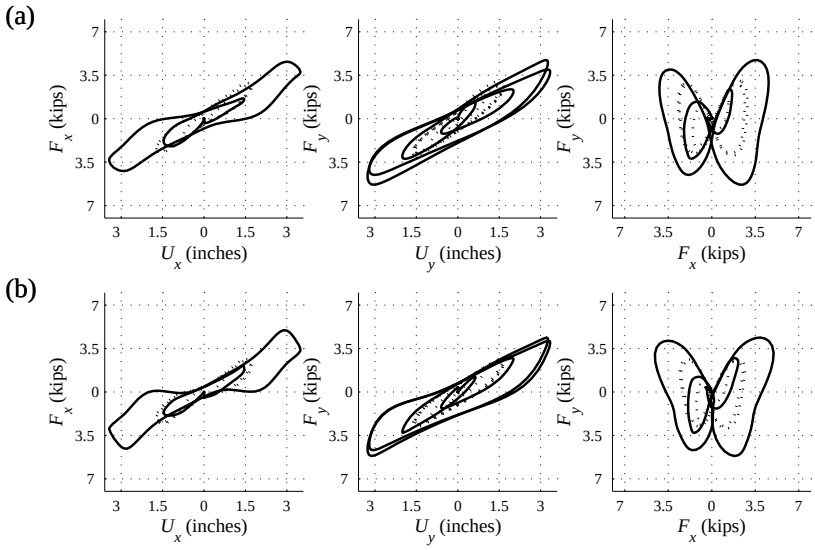

Figure 5.17. (a) Experimental response and (b) model response with parameters in Table 5.3, for tests 15 (dotted line) and 23 (solid line): orbit 1, $\gamma_x = \gamma_y = 100\%$ and $\gamma_x = \gamma_y = 200\%$, rapid strain rate. Tests not included in model calibration.

5.3 Rate-Dependent Parameter Calibration

Ideally, the parameters describing rate-dependence of the proposed model, K_i and η_i for $i = 1$ to n, could be calibrated in a third step, after parameters a_1–c_4 are obtained for rate-independent response. The rate-dependent calibration fits into the same scheme described above, by fixing rate-independent parameters at the values obtained above, assigning a non-zero weighting to the residuals from high strain-rate tests, and carrying out the downhill simplex algorithm on the weighted residual. The number of Maxwell springs, n, adopted in the calibration would depend on the desired accuracy, although one spring should be sufficient to describe behaviour at two strain-rates: pseudo-static rates and those typical of earthquake excitation. This procedure assumes that the parameters obtained for pseudo-static data do not already include a rate-dependent component, which is a reasonable assumption for the slow strain-rate used in the testing programme described here.

Although conceptually simple, this rate-dependent parameter calibration was not carried out in this work. The experimental programme contained only three tests at a strain-rate appropriate for earthquake ground motion, and, for practical reasons, these tests were only performed with displacement orbit 4. It would be difficult to calibrate three material parameters for this limited test data. More importantly, however, the proposed model calibrated for bidirectional (orbits 1 and 2) or unidirectional (orbit 1) data overestimate the slow strain-rate orbit 4 response (Figs. 5.8 and 5.16), and calibrating the rate-dependent parameters for the rapid strain-rate tests would be meaningless. If unidirectional test data at rapid strain-rates were available, the parameters d_1–d_3 could be determined with more confidence.

5.4 Sensitivity of Calibration Procedure to Initial Parameter Set

The form of the objective function used in the parameter calibrations in the previous sections, Eq. (5.1), does not permit analytical differentiation, and the evaluation of a gradient would require numerical differentiation with respect to the model parameters. This procedure is computationally demanding, because it requires multiple objective function evaluations for every trial parameter set. For this reason, in Sections 5.1–5.3, the downhill simplex algorithm was used, which is a computationally efficient procedure that does not require gradient evaluations.

As with other minimisation routines, the downhill simplex algorithm determines a local minimum of the objective function in the neighbourhood of an initial trial point. For the objective function used here, Eq. (5.1), multiple local minima exist, and it is important to determine an initial point in the vicinity of the global minimum of the function. For a model with ten or more parameters, however, this is difficult to determine *a priori*. The validation described in Section 5.1 reduces this difficulty slightly, by separating the original parameter set into two smaller subsets. The issue of determining an appropriate initial trial set, however, remains a problem.

In Section 5.1, a trial parameter set was selected based on visual inspection of bidirectional test data. When bidirectional data are available, the decomposition illustrated in Fig. 4.1 reduces the problem dimension further, by separating elastic and hysteretic damping components of the force vector, and the corresponding parameter subsets. It is also important to take into account the sensitivity of the model to the individual parameters, as evaluated in Section 4.3. Using this information, the effort in determining an initial parameter set may be focussed on those parameters which affect the model response most significantly.

In the unidirectional validation described in Section 5.2, the bidirectional parameter set in Table 5.2 was used as an initial trial, except for parameters c_3 and c_4 which were set as 1.0 and 0, respectively. This was appropriate for determining the sensitivity of the calibration to the weightings assumed in the objective function ($w_{i,1}$–$w_{i,4}$ in Table 5.1), but it makes use of information about the bidirectional data that would not usually be available in a set of unidirectional test data. For unidirectional calibration, it is more difficult to visually separate the elastic and hysteretic damping components of the force vector, and it is therefore more difficult to determine an appropriate initial parameter set.

Because of the difficulties in determining a set of trial parameters with which to begin the simplex algorithm, it is important to evaluate the sensitivity of the proposed calibration procedure to the model parameters. A systematic, quantitative evaluation of the sensitivity would require the evaluation of objective function gradients, and higher order gradients would also allow the separation of local and global minima. Due to the difficulties in determining these gradients, however, a qualitative sensitivity study was carried out, by varying the trial parameter set and investigating the changes in the converged parameters and test residuals. The initial parameter sets were selected based on variations of the parameters in Table 5.2, and residual weightings were as for the two-step bidirectional calibration in Table 5.1. The results from the sensitivity study are summarised in Table 5.4, which shows the converged parameters, residuals from the tests included in the calibration (test numbers 2, 12, 24 and 28), and the weighted residual from each calibration step, Θ_1 and Θ_2.

The weighted residuals shown in Table 5.4 correspond to local minima of the objective function determined by the downhill simplex algorithm. Although there is some variation in the converged parameter sets, the variation in the weighted residuals is relatively small. The final calibration, with an initial parameter set corresponding to half the elastic component and twice the damping component, converges to a local minimum nearly identical to that obtained in Section 5.1. The other three calibrations converge to slightly different local minima of the objective function, with some variations in the final parameters. Comparing the residuals for both individual tests and weighted sums, however, it is clear that the differences in response of the converged parameter sets is small. For engineering applications, any of the calibrations shown in Table 5.4 will adequately describe bearing behaviour.

Table 5.4. Converged parameters and residuals for different initial parameter sets.

	Table 5.2, a_1–c_4	$2.0 \times (a_1$–$b_3)$, $c_1 = c_2 = c_4 = 0, c_3 = 1$	$0.5 \times (a_1$–$b_3)$, $c_1 = c_2 = c_4 = 0, c_3 = 1$	$2.0 \times (a_1$–$a_3)$, $0.5 \times (b_1$–$b_3)$, $c_1 = c_2 = c_4 = 0, c_3 = 1$	$0.5 \times (a_1$–$a_3)$, $2.0 \times (b_1$–$b_3)$, $c_1 = c_2 = c_4 = 0, c_3 = 1$
a_1	1.3387	1.5516	1.2484	1.2233	1.3417
a_2	−0.0170	−0.0568	0.0042	0.0151	−0.0186
a_3	0.0006	0.0019	0.0000	−0.0003	0.0007
b_1	0.7436	0.7800	0.6871	0.6860	0.7467
b_2	0.2022	0.1732	0.1984	0.1771	0.2023
b_3	1.9431	1.8688	2.1518	2.6385	1.9184
c_1	0.0018	0.0019	0.0020	0.0020	0.0018
c_2	0.0059	0.0042	0.0061	0.0057	0.0059
c_3	0.8847	0.8300	0.9061	0.9101	0.8823
c_4	0.0003	0.0002	0.0003	0.0003	0.0004
$\theta_{2,2}$	0.2247	0.2331	0.2349	0.2376	0.2247
$\theta_{12,2}$	0.3453	0.3889	0.2952	0.2967	0.3461
$\theta_{24,2}$	0.2334	0.2034	0.2691	0.2961	0.2314
$\theta_{28,2}$	0.2409	0.2967	0.2453	0.2737	0.2406
Θ_1	0.1620	0.1940	0.1678	0.1759	0.1621
Θ_2	0.2328	0.2649	0.2401	0.2557	0.2326

To further illustrate this point, selected test results for the calibration shown in the second column of Table 5.4 are presented in Figs. 5.18–5.21. This calibration corresponded to an initial parameter set with double the elastic and damping parameters of Section 5.1, and the weighted residuals from each stage of the calibration are the worst of those considered in Table 5.4. The plots show a similar match of experimental data to the corresponding figures in Section 5.1 (Figs. 5.2, 5.6, 5.7, 5.8), although the original calibration describes the high-strain test data more accurately (Figs. 5.7 and 5.20).

Table 5.4 and Figs. 5.18–5.21 suggest that, from initial parameters within the range of 50%–200% of the values corresponding to the global minimum, a converged parameter set adequate for engineering purposes may be obtained. Clearly, the values obtained in Section 5.1 may not correspond to a global minimum of the objective function, but Figs. 5.2–5.8 show that the match of experimental behaviour for this set of parameters is excellent. Although not a rigorous assessment of the robustness of the calibration procedure, these results suggest that the validation protocol described in Sections 5.1 and 5.2 may be used to calibrate the proposed model in design applications.

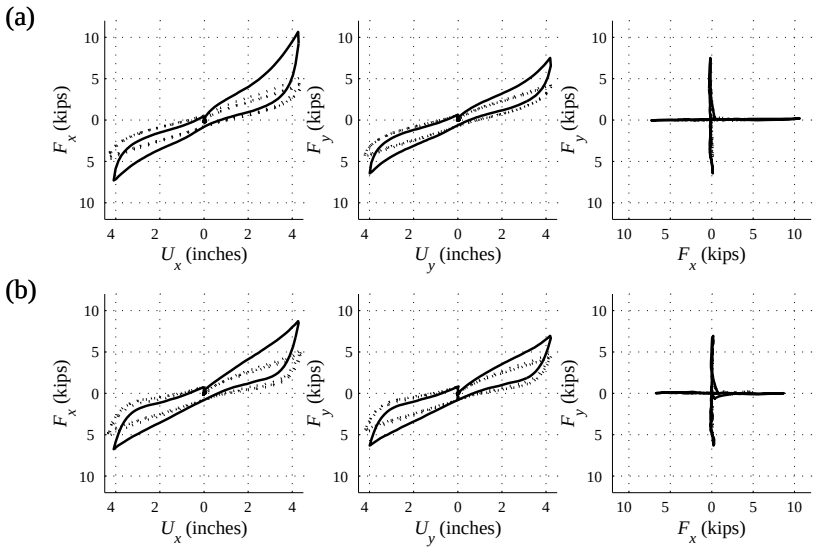

Figure 5.18. (a) Experimental response and (b) model response with parameters in second column of Table 5.4, for tests 2 (solid line) and 28 (dotted line): orbit 1, $\gamma_x = \gamma_y = 250\%$.

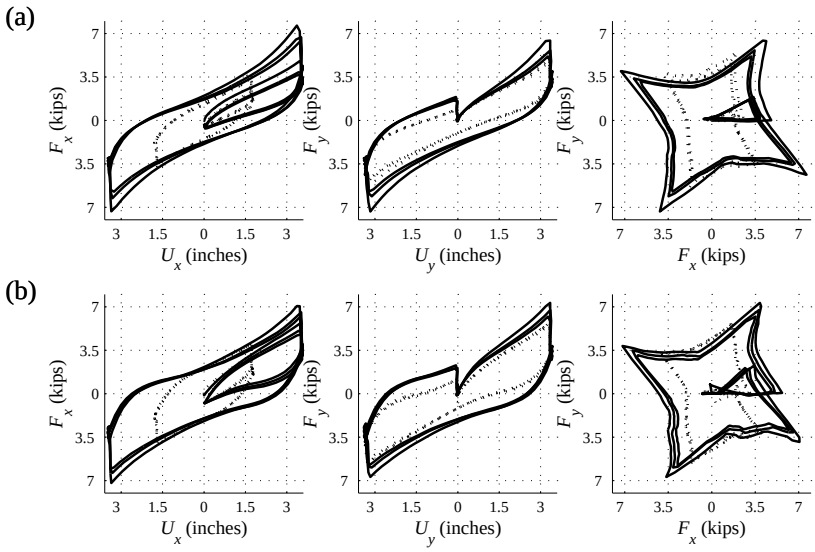

Figure 5.19. (a) Experimental response and (b) model response with parameters in second column of Table 5.4, for tests 16 (dotted line) and 20 (solid line): orbit 2, $\gamma_x = \gamma_y = 100\%$ and $\gamma_x = \gamma_y = 200\%$. Tests not included in model calibration.

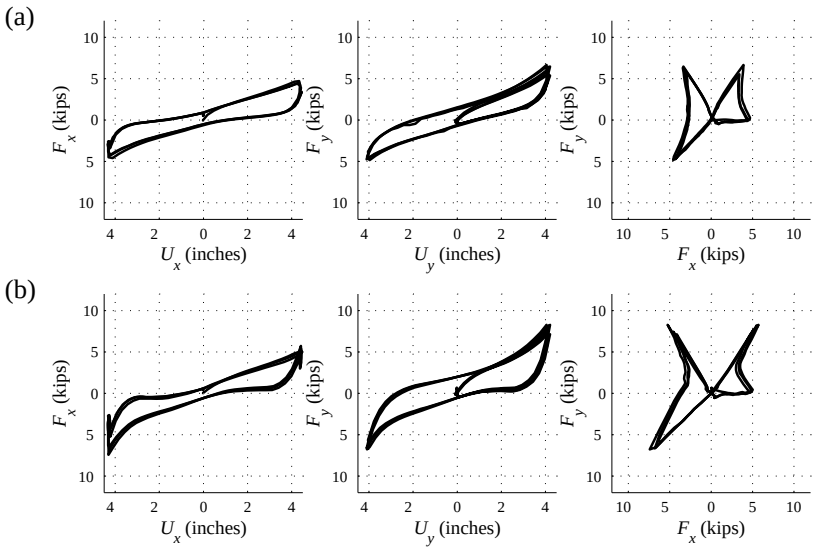

Figure 5.20. (a) Experimental response and (b) model response with parameters in second column of Table 5.4, for test 25: orbit 3, $\gamma_x = \gamma_y = 250\%$. Test not included in model calibration.

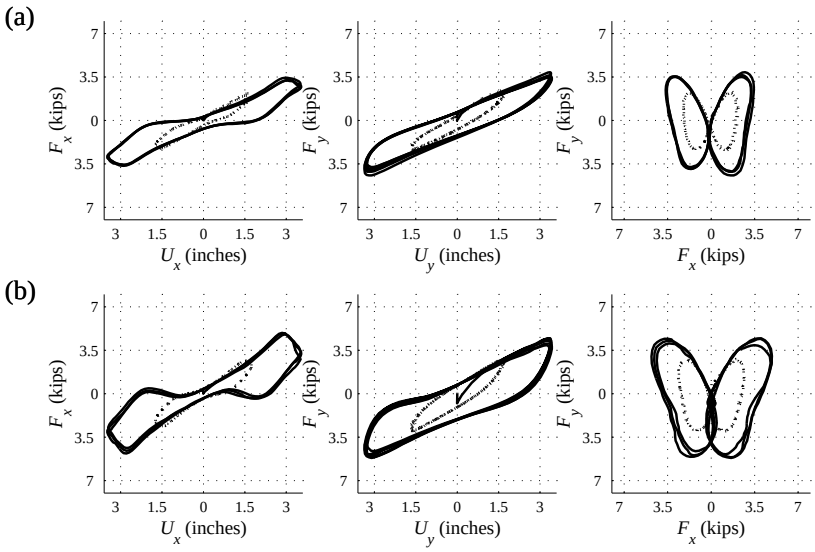

Figure 5.21. (a) Experimental response and (b) model response with parameters in second column of Table 5.4, for tests 14 (dotted line) and 22 (solid line): orbit 4, $\gamma_x = \gamma_y = 100\%$ and $\gamma_x = \gamma_y = 200\%$, slow strain rate. Tests not included in model calibration.

5.5 Experimental Calibration Protocol for Proposed Model

The mathematical model for bidirectional behavior of HDR bearings developed in Chapter 4 provides a good representation of experimental data. Clearly, in an experimental programme specifically designed for calibrating the model, 28 bidirectional tests would not be carried out. This section discusses some minimum requirements of a series of experiments for effective calibration of the bidirectional model.

A practical calibration protocol for the model would require, as a minimum, unidirectional testing at different strain levels, to assess the stiffness and damping properties of the bearing. It was suggested in Section 5.2 that unidirectional testing may be sufficient for calibrating bidirectional properties. If unidirectional tests are used, it is necessary to include tests at strain levels higher than the maximum strain expected in dynamic analysis. Because the stiffness and degradation properties of model and actual bearing response are dependent on the magnitude of the displacement vector, the maximum strain should be calculated based on a vector norm, and not a maximum x- or y-direction component.

For assessment of the material parameters representing degradation, the timing of the test series must be controlled. Because the proposed model describes both the temporary Mullins' effect, and semi-permanent scragging, these effects should be carefully distinguished in the testing protocol. In the calibration performed here, it is likely that some of the degradation included in the scragging parameter was more appropriately described as short-term Mullins' degradation. Although this did not affect the accuracy of the model in this case, it would be useful to distinguish these effects for analysis of the earthquake response of a bearing after the Mullins' effect has recovered, and at various stages of scragging recovery. For the purpose, it would be ideal to leave at least a full hour in between testing at each strain level, so that the bearing can be considered completely recovered from Mullins' effect ($D_M = 0$), while still 'scragged' ($D_{S,i} = D_{S,i-1}$).

Finally, the strain-rate dependence of the bearing must be considered. In the current model, this factor has not been adequately investigated, and the model should be calibrated at strain rates typical of earthquake ground motion before it can be used for time history analyses. Alternatively, if the extension of the model to include rate-dependent behaviour proposed in Section 4.4 is investigated further, it is possible that fewer dynamic tests may be required.

Based on the above considerations, it is suggested that a standard unidirectional test programme, with the following components can be used to define the material parameters for the proposed bidirectional model:

- Cyclic loading at 100%, 200%, 250% and 350% maximum strain to describe behaviour across a range of strains.

- Three cycles at each strain level, to assess first-cycle degradation, and additional degradation, if appropriate.
- At least one hour in between each strain level to allow for Mullins' effect recovery.
- At least one dynamic test to assess rate-dependence.

The effects of temperature and axial load must be defined *a priori*, by calibrating the model for a range of temperatures and axial loads, and defining appropriate limits of applicability.

Aside from the dependence on temperature and axial load, and the addition of rate-dependence to the model, several other factors need to be verified before this standard programme can be used for the calibration of full-scale HDR bearings. The isotropic scragging parameter, although appropriate for the Bridgestone KL301 bearings considered here, may not be appropriate for other elastomeric compounds [Thompson *et al.*, 2000]. Additionally, the use of unidirectional calibration for high shear strain bidirectional behaviour has not been conclusively validated. Finally, the bidirectional tests carried out on scaled bearings in this thesis should be compared with prototype bearing behaviour.

6. ANALYSIS AND DESIGN OF SEISMICALLY ISOLATED BRIDGES

As discussed in Chapter 1, HDR bearings are commonly used in the seismic protection of bridges. The models for bearing response considered in the previous chapters are combined with appropriate models for pier and superstructure response to obtain an accurate representation of global structural behaviour for analysis and design. Because of the unique structural form of seismically-isolated bridges, particularly in the distribution of structural stiffness and damping, their analysis and design requires considerations in addition to those made in a ductile, non-isolated pier seismic design philosophy. Some aspects of the design process are simplified, however, as isolation in some respects leads to a more regular structural response, dominated by the fundamental mode of vibration.

In this chapter, existing design and analysis procedures for seismically-isolated bridges are summarised, with emphasis on those features that are of particular relevance to HDR bearings. All of the design methods described here are based on an equivalent linearisation of the bearing response, as discussed in Section 3.1.1. Although elastic pier behaviour is typically assumed in both design and analysis of isolated bridges, the possibility of explicitly designing for pier ductility limits at higher earthquake intensity levels is also considered.

6.1 Time-history Analysis of Seismically Isolated Bridges

This section summarises some of the most important considerations for the time-history analysis of bridges, particularly those that are most relevant for bridges protected with seismic isolation. The four components of the equation of motion – mass, stiffness, damping and input motion – are considered individually.

The modelling of movement joints, flexible or yielding abutments, and foundation flexibility are important for describing the response of real bridges. These aspects are beyond the scope of this thesis, however, and are not discussed here. Priestley *et al.* [1996] provide a more detailed discussion of time history analysis, including these features.

6.1.1 Mass of Structural Elements

Most of the inertial mass in bridge systems is concentrated in the superstructure. It is for this reason that isolation devices placed between the substructure and superstructure are effective at protecting piers from excessive seismic demand. In the case of a rigid superstructure, the rotational moment of inertia of the deck can be calculated for rotations about a vertical axis, and the mass can be lumped at the centre-of-mass. For a flexible superstructure, tributary mass may be lumped above each isolation device.

The consideration of substructure mass is particularly important for isolated bridge systems. For relatively stiff piers, it will generally be adequate to consider a lumped mass at the top of the pier, below the isolation system. Priestley *et al.* [1996] express the generalised mass of the substructure as:

$$m^* = M_1 + \frac{\bar{m}_c H_c}{3} \tag{6.1}$$

where M_1 is the tributary mass of the superstructure, and $\bar{m}_c$ and H_c are the mass per unit height and clear height of the pier, respectively. In isolated piers, it will be appropriate to separate the two terms in Eq. 6.1 into two lumped masses, separated by the isolation system. For more slender piers, where higher modes can influence the response, multiple lumped masses may be considered, distributed over the height of the pier.

6.1.2 Substructure and Superstructure Modelling

The substructure and superstructure of isolated bridges are generally designed to behave elastically under design level excitation. This can simplify time history analysis considerably, as all structural nonlinearity is concentrated in the isolation devices. Furthermore, it can be expected that isolated bridge response will be relatively insensitive to substructure stiffness, within an order of magnitude, as the flexibility of the isolators dominates the response. This hypothesis is investigated in the parametric studies in Chapter 7.

For reinforced concrete structures, even the appropriate determination of elastic stiffness properties is not entirely straightforward. It is common in design and analysis to assume a cracked section stiffness as a function of gross section moment of inertia and Young's modulus, and to detail reinforcing steel to accommodate the seismic demand in terms of forces. This procedure, however, assumes that the amount of longitudinal steel does not influence the section stiffness, an assumption that does not accurately describe reinforced concrete response [Priestley, 2003]. A more rational approach based on this result is to assign elastic stiffness to reinforced concrete members as the ratio of yield strength and yield deformation of the idealised bilinear force–deformation response.

The above discussion is of less significance for isolated bridges, in which the flexibility of the

isolation bearings is expected to dominate the response of the system. For the purposes of time history analysis, traditional methods based on a fixed proportion of the gross section stiffness should be adequate. Because the more rational approach fits readily into a displacement-based design procedure, at least for substructure response, this representation of elastic stiffness is adopted in the design recommendations in Sections 6.2.3 and 6.2.4.

For ground motion intensities exceeding the design level, it may be necessary to allow for pier nonlinearity in the structural model. In the case of reinforced concrete piers under uniaxial bending, the modified Takeda hysteresis rule [Otani and Sozen, 1972] is commonly used to describe the nonlinear behaviour. The modified Takeda hysteresis rule is a bilinear version of the original trilinear Takeda model [Takeda *et al.*, 1970], and includes degradation of loading and unloading stiffness under cyclic loading. The bilinear version includes four model parameters; the first three are the same as for the classical plasticity bilinear model (Fig. 6.1(a)), while the fourth parameter, α controls the ductility-dependent unloading stiffness. The unloading stiffness, K_u is given by:

$$K_u = K\mu^{-\alpha} \tag{6.2}$$

where μ is the maximum ductility previously obtained in the same direction ($\mu \geq 1$).

On reloading, the hysteretic response is directed towards the previous maximum force–displacement point. The behaviour of the bilinear Takeda rule under simple loading cycles is illustrated in Fig. 6.1(b). For small loading and unloading cycles, several additional rules control the hysteretic behaviour. Subsequent applications [Carr, 2004] have added an additional parameter, β, to modify the reloading stiffness of the model, and to increase the size of hysteresis loops.

The parameters corresponding to the bilinear skeleton curve of the modified Takeda hysteresis rule may be determined by a moment–curvature analysis of the section that is being modelled. This curve may be replaced by a bilinear approximation using appropriate definitions of yield curvature and yield force [Priestley, 2003], and the curve defined by its three parameters: initial stiffness, yield force and post-yield stiffness. Section analyses do not describe cyclic unloading and reloading as accurately as monotonic loading, and the unloading parameter, α (and if appropriate, the reloading parameter, β) should be calibrated against experimental data. For bridge piers, α values from 0.5 to 0.7 are appropriate, depending on the level of axial load, while β is generally taken as zero [Priestley *et al.*, 1996].

The modified Takeda model, if calibrated correctly, generally describes the uniaxial loading of reinforced concrete members accurately. However, under real ground motion, axial loads may vary in bridge piers due to vertical excitation or pier geometry, and piers may be loaded under biaxial bending moments. It is possible to extend the Takeda framework to include the effect of axial load on the yield force under uniaxial loading [Carr, 2004]; it is more difficult to extend the model to allow

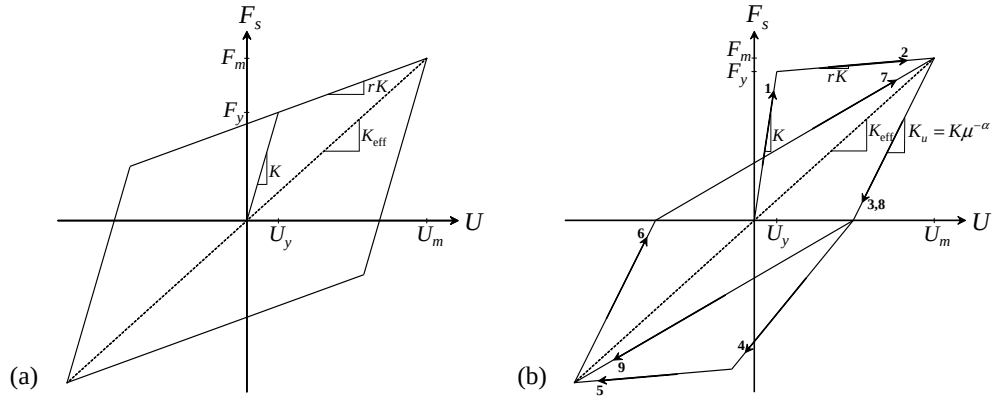

Figure 6.1. Hysteretic force–displacement response. (a) Bilinear model, and (b) modified Takeda model.

for biaxial bending.

One option for describing the biaxial bending of reinforced concrete piers (although neglecting axial load dependence) is to represent pier inelasticity with a bilinear coupled plasticity model (Section 3.1.1, and Fig. 6.1(a)). This may provide a more accurate description of the yield force under simple biaxial load paths, such as the first two branches of the box orbit in Fig. 2.2. The unloading behaviour of the bilinear model will be significantly different from the Takeda model, however, and consequently energy dissipation in cyclic loading will also differ. The bilinear classical plasticity model may be able to give some indication of the importance of bidirectional earthquake motion in an isolated bridge model, but it will probably not be adequate to describe pier inelastic response.

To more accurately model the axial load–bending moment interaction, and biaxial loading of reinforced concrete sections, several alternative models have been suggested. Saiidi *et al.* [1989] suggested that the response of a rectangular section may be represented by five uniaxial springs, with hysteretic behaviour calibrated correctly to model section response. One spring in each of the four corners represents the combined behaviour of concrete and reinforcing steel in that quadrant, including bar slip. A fifth spring in the centre of the section models the central portion of concrete. Lai *et al.* [1984] separated the corner springs into separate concrete and steel springs, resulting in a nine-spring model. Other authors [Li *et al.*, 1987] have introduced a more generalised multi-spring (MS) model with an arbitrary number of springs used to define concrete response, and one steel spring per reinforcing bar. Models consisting entirely of axial springs in parallel generally do not include the effect of shear deformations on member response.

The original five and nine-spring models were elegant in their simplicity, and provided a reasonable

match of reinforced concrete column biaxial bending and axial force interaction. The more springs that are added to such a model, however, the closer it resembles a fiber model. In the latter, a section integration is carried out over the section, with a certain integration rule and an arbitrary number of integration points. If the midpoint integration rule is used, the "fiber" name is most apt, referring to each section integration point integrated over the length of the member. This is the main difference between MS and fiber models – in the former, the element inelasticity is restricted to pre-determined sections, generally at member ends, while in the latter, the inelasticity is integrated over the member length.

The element integration can be carried out in a stiffness or flexibility formulation [Spacone *et al.*, 1996]. In the former, shape functions are assigned to the member deformation, generally based on elastic, prismatic deflected shapes. The deformed shape of an inelastic or non-prismatic member will not be described accurately by these shape functions, and several elements will be required per member. In the flexibility formulation interpolation functions describe the force and moment distribution along the member, which can be derived exactly from the end moments based on equilibrium. This formulation will give a much more accurate deformed shape and an exact member force profile, at the expense of increased computational effort.

6.1.3 Bearing Modelling

The unidirectional response of HDR bearings can be described using any of the mathematical models described in Chapters 3 and 4. For time-history analysis, both the viscoelastic and bilinear models (Section 3.1.1) will require iteration to determine strain-dependent properties. Some of the more complicated models may not be able to describe bearing response *a priori*, for reasons discussed in Sections 3.1.2–3.1.4. In this case, it may be necessary to adopt an iterative approach to determine model parameters appropriate for the level of shear strain, axial load, and strain rate experienced in the bearing during the time history analysis.

The model proposed in Chapter 4 is the only one capable of describing the bidirectional response of HDR bearings for a range of strain levels. The model can be calibrated for a given bearing using the procedure described in Chapter 5. Axial load and temperature dependence have not been considered however, and it will be necessary to calibrate the model for the appropriate level prior to the analysis.

6.1.4 Viscous Damping

In nonlinear time history analysis of multiple degree-of-freedom (MDOF) structural models, the mass and stiffness matrices ($\mathbf{M}$ and $\mathbf{K}$, respectively) are generally assembled from simple element models, based on known material properties. It is, however, impractical to assemble the damping matrix ($\mathbf{C}$) in the same manner, from material and element dissipative properties. This difficulty

is partly due to the fact that viscous damping is used in the equation of motion as a mathematical convenience, and is used to represent energy dissipation in the structure from a number of sources. It is not used to describe energy dissipation due to structural element hysteresis, which should be accounted for in a hysteretic model (Sections 6.1.2 and 6.1.3). For this reason, a simplified model is generally used to determine the viscous damping matrix for time history analysis.

Although more complicated expressions are sometimes suggested [Caughey, 1960; Wilson and Penzien, 1972], the following equations represent some commonly-used models for the damping matrix:

$$\mathbf{C} = a_0\mathbf{M} \tag{6.3}$$

$$\mathbf{C} = a_1\mathbf{K} \tag{6.4}$$

$$\mathbf{C} = a_0\mathbf{M} + a_1\mathbf{K} \tag{6.5}$$

The damping models expressed in Eqs. (6.3)–(6.5) are referred to as *mass proportional damping*, *stiffness proportional damping* and *Rayleigh damping*, respectively [Rayleigh, Lord, 1945; Chopra, 2001].

In Eqs. (6.4) and (6.5), the initial stiffness matrix of the structural model, or the tangent stiffness matrix may be used for $\mathbf{K}$. The former assumption results in a damping matrix that does not change as the structure undergoes inelastic deformation. The latter assumption implies a damping matrix which reduces in magnitude with structural nonlinearity. Clearly, the choice of viscous damping model should best represent energy dissipation in the real structure under a range of loading conditions.

Analysts often assume that the choice of viscous damping model will have little significance on the maximum response of a nonlinear system. Priestley and Grant [2005], however, show that for a nonlinear single degree-of-freedom (SDOF) system with a fraction of critical damping of 5%, the damping model can have a large influence on the peak displacement. They suggest that the tangent stiffness proportional damping model is the most justified physically, and recommend its use for nonlinear time history analysis.

The tangent stiffness proportional model is potentially problematic when applied to a stiffening system, such as the proposed HDR bearing model (Chapter 4). For low bearing strain levels, the damping will decrease with increasing deformation, while at higher levels, the damping will increase. Provided that the bearing deformation is not too far into the stiffening range, however, this increase in damping coefficient will occur when the relative velocity is low, and the damping force should not be affected significantly. The proposed model includes energy dissipation in hysteresis and in small load reversals, and ideally no viscous damping would be assigned to the bearing deformation. However, this would imply the use of a non-classical damping matrix, which increases the computational effort significantly. If the bilinear model is used for bearing response (Section 3.1.1), then tangent stiffness

proportional damping is less problematic.

6.1.5 Ground Motion

To carry out time history analysis, at least one input ground motion is required. In fact, for the verification of a structural design, design provisions [AASHTO, 1999] frequently specify that a suite comprising a minimum of three or seven records is used – for three records, the maximum of all the peak values of a given response quantity for all analyses should be designed for, while for seven records, the average may be taken. The selection and, if appropriate, modification, of ground motion records for time history analysis will have a significant outcome on the design response quantities obtained.

Typically, input ground motions are selected from a database of real earthquake accelerograms. To provide an appropriate input energy content to the structural model, it is usually considered important to select recordings of earthquakes with a similar magnitude and fault mechanism, and recorded at a similar distance from the fault rupture, as the earthquake scenario that forms the primary contribution to the seismic hazard at the site. This can be determined from a knowledge of faults in the area, or from a deaggregation of a probabilistic seismic hazard assessment (PSHA). The latter option will be necessary when many possible scenarios contribute to the seismic hazard. It should also be recognised that different scenarios may dominate the hazard for different intensity measures, such as peak ground acceleration, velocity and displacement. Bommer and Acevedo [2004] suggest that the earthquake magnitude is the most important parameter, and that less consideration should be given to the distance and fault mechanism in the selection of real records for time history analysis.

For unidirectional time history analysis, it is generally permitted to scale ground motion records in amplitude by multiplying by a constant scaling factor. Frequency scaling is also sometimes allowed, although this may lead to ground motions with unrealistic frequency contents. According to Vanmarcke [1979], factors in the range of 0.5–2.0 lead to physically realistic ground motions for inelastic analysis – outside this range, the energy output of the record may not be compatible with its duration. Bommer and Acevedo [2004] suggest that the upper limit of 2.0 may be difficult to maintain for records that are scaled to a code design spectrum that has been determined from a PSHA that includes the effect of scatter. In this case, code spectral ordinates will be representative of hazard levels of a number of standard deviations above the median, and to obtain real records compatible with this degree of scatter, in addition to seismological parameters such as magnitude and distance, would require an extremely large ground motion database.

In any case, provided that the scaling factor is not too extreme, the record can be adjusted such that the error with respect to some design spectrum is minimised across a range of periods, or at a period

corresponding to the fundamental period (or isolated period) of the structural model. The latter approach may be more appropriate, as uniform-hazard design spectra contain the aggregation of different sources of hazard, and it may be difficult to provide a good match of the design spectrum across a range of periods. On the other hand, if only one modal period is considered, the demand on higher modes may not be hazard-consistent. Numerical studies of isolation systems [e.g. Ryan and Chopra, 2004] sometimes use the peak ground velocity as a parameter to which to scale records, as it is representative of the ground motion demand at typical vibration periods of isolated structures.

Artificially-generated records are also often used for time history analysis. The advantage of artificial records is that they can be generated directly for a given design spectrum, and are representative of a code hazard-consistent demand level across a large range of periods. Design spectra, however, are unlikely to be realistic for a single real earthquake recording, as they are an amalgamation of several records and sources of seismicity. For this reason, artificial records are often criticised for containing an unrealistic frequency and energy content, that may not be appropriate for inelastic time history analysis.

Bidirectional time history analyses require two horizontal components of ground motion. Two individual artificial records will not exhibit the degree of correlation required for a realistic ground motion pair; similarly, two real records from different events or different sites cannot, in general, be combined to form a realistic bidirectional ground motion. The general approach in this case is to use two ground motions recorded in orthogonal horizontal directions from the same instrument and same event. If vertical input is also considered, a three component real ground motion pair will provide the best representation of tridirectional demand.

An alternative approach to the specification of appropriately-correlated ground motion pairs is to represent the bidirectional seismic demand in terms of principal directions, according to the definition of Penzien and Watabe [1975]. In this model, the ground motion pair is rotated in a horizontal plane, such that the two horizontal components are statistically uncorrelated. It is further assumed that the vertical component is uncorrelated, and represents a third principal direction of the ground motion. In this case, it is feasible that two artificial records, two real records from different earthquake events, or a combination of a real and artificial record could be used to represent the principal horizontal components. In the case of real events, it would be important to consider records with approximately the same magnitude, duration and energy characteristics, as otherwise the combined motion would not be physically realistic. The use of artificial records in this manner does not remove the problems associated with frequency and energy input, discussed earlier with respect to unidirectional seismic demand. Furthermore, when the ground motions have been specified in terms of principal directions, it is unclear how these should be oriented with respect to the structural axes.

Assuming the first approach is used, in which matching ground motion recordings are used, it will

be necessary to scale the components to match the seismic hazard appropriate for the site. Ground motions measured in orthogonal directions will, in general, have different response spectral shapes and intensity. If each record in a pair is scaled by a different factor, then the resulting bidirectional ground motion may not be representative of a realistically attainable earthquake recording. For this reason, generally a single scaling factor is used to amplify both horizontal components, and, if appropriate, the vertical component, to match a design level hazard.

The scaling factor to use should take into account the way in which the design spectrum has been defined, and what component of ground motion it is supposed to represent. Generally, code spectra are defined by a PSHA, for which the principal ground motion intensity prediction is carried out using attenuation relationships. Attenuation relationships are derived from a regression based on a number of real ground motions, to determine the expected intensity of motion at a site based on magnitude, distance (epicentral, or other measure), and other parameters of a hypothetical event. Generally, either the maximum of two orthogonal horizontal, or their geometric mean is used in the regression, with the latter case presumably representing a random direction of demand. Therefore, it appears that design code spectra should also be representative of either peak or random directions of ground motion, and pairs or triples of records should be scaled accordingly. For example, the Eurocode 8 [CEN, 2003] design spectrum is considered to be representative of the peak ground motion [Bommer and Acevedo, 2004].

It is clear, however, that if two components of ground motion are applied to a regular structural model, the peak response of the structure will be governed neither by the geometric mean of two randomly selected orthogonal components, nor by their peak, but by some "worst" component. This will be generally be greater than both the average and "peak" demands, by an amount that will depend on the earthquake and site characteristics. For near-fault motions, fault normal (FN) and fault parallel (FP) components will differ greatly in terms of demand, and the response spectrum determined from average or peak of two random components is a poor measure of design demand. Even when near-fault effects are not important, a design spectrum that gives a measure of peak bidirectional demand seems to be a useful design tool.

The 1999 AASHTO Guide Specifications for Seismic Isolation Design [AASHTO, 1999] state that the square-root-sum-of-squares (SRSS) combination of the two component response spectra should be scaled to match the design spectrum. Assuming that the intent of the SRSS combination is to determine the peak bidirectional demand, it is clear from the discussion above that the code spectrum is considered to represent the peak rather than the average demand. This is an important consideration for the representation of bidirectional seismic demand for design (Section 6.2.1). In the context of the current discussion, however, it will be interesting to determine if the SRSS combination of two components of ground motion provides a good scaling measure for bidirectional time history

analyses.

For elastic time history analysis of regular structures, a bidirectional response spectrum can be determined in the same manner as a unidirectional response spectrum. Recall that the latter may be derived in the time domain by carrying out a series of elastic time history analyses of a SDOF system for a range of structural periods, and determining the peak response in each case. Similarly, time history analyses may be carried out on an uncoupled 2-DOF system, with the same period in each direction. The vector demand is calculated at each time step, and the peak bidirectional response is plotted against period. This bidirectional response spectrum gives a direct measure of the elastic bidirectional demand for a regular structure.

Different representations of bidirectional spectral demand are compared in Fig. 6.2. The elastic displacement spectrum is used, as it forms the basis of current displacement-based design methods, as discussed in Section 6.2.1, and a viscous damping ratio of 5% is assumed. Figures 6.2(a) and (b) show the spectra calculated for ground motion pairs LA11–12 and LA17–18, respectively, from the FEMA/SAC database [SAC, 1997], discussed in Section 7.1.4. In addition to the unidirectional displacement spectrum for each component, the geometric mean (generally considered in the derivation of attenuation relationships), the SRSS combination and the bidirectional spectrum are shown.

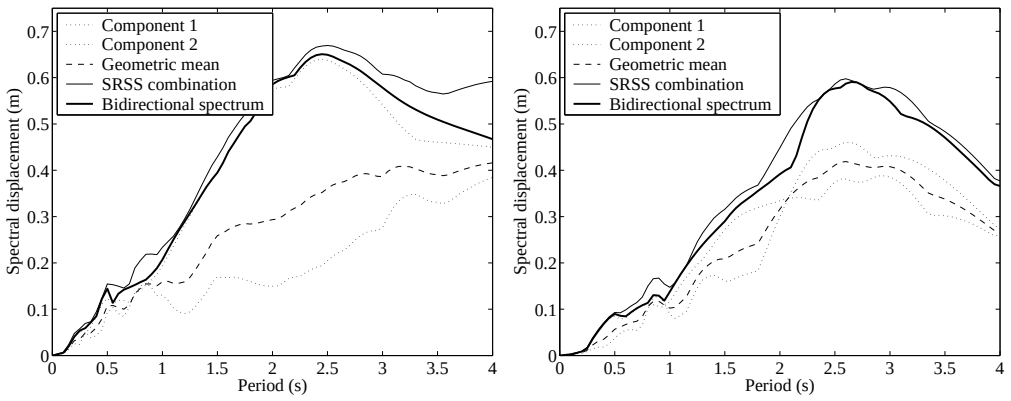

Figure 6.2. Unidirectional elastic displacement response spectra, and various representations of bidirectional spectral response. (a) LA11–12, and (b) LA17–18 ground motion pairs. Refer to Table 7.2, but note that only the SAC scaling factor has been applied here.

The ground motion pairs used in Figs. 6.2(a) and (b) were selected from the LA ground motion suite to demonstrate extremes in the representation of bidirectional demand. Figure 6.2(a) shows the spectral demand of a ground motion pair for which the spectral intensity of the two components are very different. For this pair of records, the maximum of the two unidirectional spectra is a good measure of the bidirectional demand, while the geometric (or arithmetic) mean is a poor measure.

Figure 6.2(b), however, is for a ground motion pair for which the unidirectional spectra are similar. In this case, the bidirectional spectrum is greater than both individual components, but is closer to the mean response. The other ground motion pairs in the LA suite exhibited behaviour in between these two extremes.

Two important conclusions can be drawn from Fig. 6.2. The first conclusion is that the SRSS combination rule provides a good, conservative measure of the bidirectional demand on regular structures. This observation was generally valid for the other ground motions considered, although not all were as close to the bidirectional response spectrum as those shown in Figs. 6.2(a) and (b). The second conclusion is that, even though these records had been scaled to the same level of average demand (see Section 7.1.4 for a description of the scaling process used in the preparation of the FEMA/SAC database), the bidirectional demand is different. Comparing the geometric means in Figs. 6.2(a) and (b), it is apparent that for periods less than 3.0 seconds, the displacement demand is approximately the same. The bidirectional demand, represented through either the SRSS combination or bidirectional response spectrum, is higher across the entire period range in Fig. 6.2(a). For near-fault recordings, the variability between the mean and bidirectional peak response could be expected to be greater.

Although the bidirectional response spectrum is not difficult to derive, it is only applicable for regular structures with the same period in all directions. It should be observed, however, that this is also a limitation of the SRSS combination rule. Taking the square-root-sum-of-squares at each vibration period only has any significance for structures with that period in both directions. To determine the SRSS response of an irregular structure, with different periods in each direction, it would be necessary to take the SRSS of spectral ordinates for each of the two periods. Similarly, the bidirectional spectrum concept could be extended to irregular structures by deriving peak spectra for combinations of different periods in each direction. Either of these representations of bidirectional demand for irregular structures could possibly be presented in a three-dimensional plot or on several two-dimensional plots for different ratios of periods. In any case, the bidirectional elastic response spectra derived in this manner may not have the same applicability to inelastic design that the unidirectional spectrum is assumed to have in current design methods (see Sections 6.2.1 and 6.2.2). Furthermore, for application to MDOF time history analysis, where a number of modal vibration periods may be of importance, either the SRSS or bidirectional spectrum approaches may be used as an indication of bidirectional seismic demand.

Finally, the ground motion pairs or triples are used as the input in a time history analysis. Codes typically specify that the worst orientation of the ground motion should be considered for design, without giving guidelines on how this should be determined. Many studies of bidirectional response of structures [e.g. Huang, 2002] rotate the input motion about a number of directions, and consider

the maximum values of each response quantity of interest. Design ground motion combination rules, such as the CQC3 rule and its derivatives, provide more guidance about how this worst case direction should be obtained, and are discussed in more depth in Section 6.2.1.

6.2 Design of Seismically Isolated Bridges

Confidence in current design methods for seismically-isolated bridges has developed to such an extent that modern design codes, such as the 1999 AASHTO Guide Specifications for Seismic Isolation Design [AASHTO, 1999], only require time history analysis under certain circumstances. However, there remain some unknown or controversial aspects in any of these design methodologies, especially in the areas of the determination of maximum response quantities under bidirectional loading, and the equivalent linearisation of nonlinear bearing and pier behaviour. Furthermore, there is a lack of consistency in the specification of response modification factors, R, which determine the seismic demand on piers when the full design load in isolation bearings is developed.

This section provides a summary of some of these design aspects, with particular reference to the design methods of Priestley *et al.* [1996] and the AASHTO guide [AASHTO, 1999]. In addition, an explicit method for determining appropriate pier design strengths is developed by considering performance goals at more than one level of seismic hazard.

6.2.1 Representation of Bidirectional Seismic Demand

Traditionally, seismic demand has been represented by an elastic acceleration design spectrum, evaluated for 2–5% viscous damping. Relationships between elastic and inelastic response that approximately hold over a certain period range, such as the "equal displacement rule" [Veletsos and Newmark, 1960], are used to determine the acceleration demand on an inelastic structure. This spectral demand can be applied in an equivalent static analysis, or a multiple mode response spectrum analysis.

In the last decade, several design methods based directly on peak structural displacements instead of forces have been proposed. Sullivan *et al.* [2003] provide a summary of a number of these methods, and assess their performance at meeting design objectives. One of the methods, known as "direct displacement-based design", has been particularly well-developed for bridge applications [Kowalsky *et al.*, 1994; Priestley *et al.*, 1996; Alvarez-Botero, 2004]. This method uses a 5%-damped, elastic displacement design spectrum, and adjustment factors to reduce the spectral ordinate for higher values of damping. Effective structural period and damping are calculated from linearised structural properties (Section 6.2.2). Similarly, the AASHTO [1999] Uniform Load Method, gives design guidelines for peak bearing displacement, in addition to the elastic seismic coefficient (equivalent to spectral acceleration). These methods allow the deformation of isolation bearings and other

structural elements to be controlled directly.

The elastic displacement spectrum specified for displacement-based seismic design is given in several different forms in the literature. A displacement spectrum derived directly from a design acceleration response spectrum will increase linearly in the range of periods for which acceleration decreases with the square of the period – the "equal velocity" region of the spectrum. The minimum period for which this is applicable depends on soil type, and dominant magnitude considered in the seismic hazard assessment for a region, but is typically around 0.5 seconds. Eurocode 8 [CEN, 2003], however, introduces a limiting period, T_D, above which displacement spectral ordinates are constant. The period T_D is specified as 1.2 seconds or 2.0 seconds, for low and high magnitude earthquake spectral shapes, respectively. Faccioli *et al.* [2004], however, suggest that the displacement response spectrum may continue increasing linearly up to periods in the range of 10 seconds, for high magnitude earthquake recordings. This suggests that in regions for which the seismic hazard is governed by large magnitude earthquake events, the Eurocode 8 design spectrum corner period could be increased significantly for displacement-based design applications.

The elastic displacement design spectrum must be adjusted for equivalent viscous damping values (Section 6.2.2) other than 5%. AASHTO [1999] provides adjustment factors, B, as a function of the equivalent fraction of critical damping for the structure. Damping values in excess of 30% provide no further reduction, unless a time-history analysis is carried out with an appropriate hysteresis model for the bearing. For linearly viscoelastic systems, however, the reduction values may be extended to a maximum of 50% damping.

Eurocode 8 [CEN, 2003] specifies the following reduction factor for the elastic design spectrum:

$$\eta = \sqrt{\frac{0.1}{0.05 + \xi}} \geq 0.55 \tag{6.6}$$

where ξ, the fraction of critical damping, is specified as a decimal. Reduction factors from AASHTO [1999] and Eurocode 8 [CEN, 2003] are compared in Fig. 6.3. Note that in AASHTO, the 5% spectrum is divided by B, whereas in Eurocode 8, it is multiplied by η. Therefore, the AASHTO values are inverted in Fig. 6.3. It is evident from Fig. 6.3 that the reduction of design spectra for damping is similar in both codes for all damping values of practical interest.

The seismic demand at longer return periods must also be assessed when different performance levels are considered. The AASHTO Guide Specifications for Seismic Isolation Design [AASHTO, 1999] state that design is for a 475-year return period, although it specifies limits on displacements for vertical stability requirements based on a 2400-year "maximum credible event" (MCE). The demand for the MCE, represented in terms of peak ground acceleration (PGA), is generally 5–50% higher than the design level for high seismicity zones, and up to 170% higher for zones of

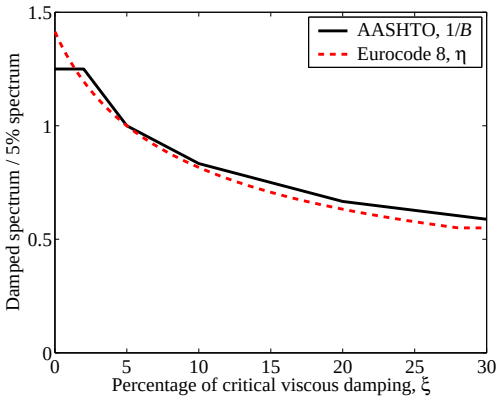

Figure 6.3. Reduction factor for damped displacement design spectrum.

lower seismicity [Reaveley and Nordenson, 1992]. Isolated systems may be particularly vulnerable to increased seismic demand, and it is important that bearings are able to withstand safely the MCE. This issue is investigated thoroughly for isolated bridges in Chapter 7.

When unidirectional seismic demand is represented by a design spectrum, either in terms of accelerations or displacements, the effect of loading by two or three ground motion components is taken into account in statistical combination rules. Typically, percentage rules, such as the "30%-rule" or "40%-rule", are specified for combining response quantities determined for each component. In these methods, the two horizontal components are applied to the structure, using static procedures, response spectrum modal analyses or unidirectional linear time history analyses. The total bidirectional response quantities are calculated by adding 100% of the response calculated for the most demanding component and a reduced percentage for the other horizontal component. For example, the International Building Code [ICC, 2000] and Eurocode 8 [CEN, 2003], among others, use a reduction factor of 30% for response spectrum modal analysis, although do not require the consideration of bidirectional loading for the equivalent static analysis procedure. The latter specification also allows for a vertical component of seismic input in the 30%-rule, if vertical effects are considered to be important.

As an alternative to simplified percentage combination rules, a square-root-sum-of-squares (SRSS) or complete quadratic combination (CQC) may be performed to combine response quantities due to orthogonal horizontal maxima. Based on the ground motion model of Penzien and Watabe [1975], Smeby and Der Kiureghian [1985] developed the "CQC3 rule" to calculate the expected maximum of a response quantity, r, for three orthogonal components of ground motion. In the original method, the two horizontal components of ground motion must have identical spectral shapes (differing by a constant factor, γ), and be polarised into principal directions. The following expression is obtained

for the expected maximum value of the response quantity (using the notation of López *et al.* [2000]):

$$r(\theta) = \left\{ \left[r_x^2 + (\gamma r_y)^2\right] \cos^2\theta + \left[(\gamma r_x)^2 + r_y^2\right] \sin^2\theta + 2(1-\gamma^2) r_{xy} \sin\theta\cos\theta + r_z^2 \right\}^{1/2} \tag{6.7}$$

where θ is the angle of incidence of the major principal direction of ground motion with respect to the structural axes, r_k ($k = x, y, z$) is the peak response to each of the three components of ground motion, determined from a response spectrum modal analysis and the original CQC modal combination rule [Wilson *et al.*, 1981], and r_{xy} is the cross-correlation of modal responses.

By differentiating Eq. (6.7), it can be shown [Smeby and Der Kiureghian, 1985] that the angle of incidence that gives the maximum value of r is given by:

$$\theta_{cr} = \frac{1}{2} \tan^{-1}\left[\frac{2r_{xy}}{r_x^2 - r_y^2}\right] \tag{6.8}$$

The "critical" value of r is then given by [Anastassiadis *et al.*, 1998; López *et al.*, 2000]:

$$r_{cr} = \left\{ (1+\gamma^2)\left(\frac{r_x^2 + r_y^2}{2}\right) + (1-\gamma^2)\sqrt{\left(\frac{r_x^2 - r_y^2}{2}\right)^2 + r_{xy}^2} + r_z^2 \right\}^{1/2} \tag{6.9}$$

The maximum response quantity for all angles of incidence of ground motion has some intuitive appeal as a conservative value for design purposes. Except in near-fault regions, the orientation of principal ground motion components is difficult or impossible to assess at the design stage, and rotating the potential seismic demand through 360° ensures that the most demanding direction of seismic input is accounted for. It could be argued, however, that this design criterion is inconsistent with the concept of risk, and implies a much greater seismic hazard at the site than really exists. Considering a uniform hazard design spectrum corresponding to a return period of 475 years, for example, it is expected that the spectral ordinate will be obtained once every 475 years, on average. The return period of an event with principal components rotated to the worst angle of incidence for a given structure is much longer (infinitely long if the value of r_{cr} is obtained for a single, discrete value of $\theta = \theta_{cr}$). For this reason, the expected value for all θ may be a more appropriate measure of design level demand:

$$E(r) = \frac{1}{2\pi} \int_0^{2\pi} r(\theta)\, \mathrm{d}\theta \tag{6.10}$$

Equation (6.10) is impossible to solve in closed form for the $r(\theta)$ given by Eq. (6.7). It is relatively straightforward, however, to numerically integrate, by evaluating $r(\theta)$ for a number of different θ values, and calculating the mean value. For structures that are regular in plan, the difference between the mean and maximum values should be relatively small.

It should be noted that in the original presentation of the CQC3 rule [Smeby and Der Kiureghian, 1985], it was suggested that a random variable approach could be used to determine response

quantities for a given statistical distribution of θ. This could be appropriate, for example, when a known fault with well-defined geometry governs the seismic hazard in a region. In the more usual case where the distribution of incidence angle is unknown, a uniform probabilistic distribution, with $0° \leq \theta < 360°$, is appropriate, and Eq. (6.10) may be used to determine the expected value. Smeby and Der Kiureghian [1985], however, give the root-mean-square (RMS) for a known distribution of θ, which may be determined in closed-form from Eq. (6.7). Although the closed-form solution makes the RMS value of r appealing from a mathematical and practical point-of-view, the expected value given in Eq. (6.10) is consistent with the probabilistic definition of the hazard, and should therefore be used in design applications.

Note that the problem of determining maximum response quantities for the worst case direction of earthquake attack is different from the determination of bidirectional demand, considered in Section 6.1.5. In that case, the peak demand was determined for a given orientation of the ground motion components, based on the response of a regular structure. The determination of the worst-case θ, however, considers the peak demand for an irregular structure with the ground motion components rotated through 360°. As discussed in Section 6.1.5 and above, the former is consistent with the hazard defined at the site, while the latter assumes a level of hazard greater than stated in the code design spectrum.

6.2.2 Linearisation of Bearing and Pier Properties

Existing normative guidelines [BSSC, 1997; AASHTO, 1999] and other design methods [Priestley *et al.*, 1996] typically recommend the use of an equivalent linear viscoelastic model for bearing design in isolated structures. Isolated piers are designed elastically, and sufficient reserve capacity is provided to ensure linear behaviour under design level excitation. In this chapter, however, the possibility of pier yielding at higher intensities is also considered, to assess the interaction of inelastic pier response with the effectiveness of seismic isolation. In this case, pier nonlinearity is also represented by an equivalent linear viscoelastic model, as assumed in design methods for non-isolated bridges [Priestley *et al.*, 1996] based on the "substitute structure" approach [Shibata and Sozen, 1976]. A consistent approach to the modelling of bearing and pier nonlinearity allows the interaction between structural elements and isolation devices to be studied at various performance levels in a rational manner.

Jacobsen [1930] first proposed using the energy dissipated in one cycle of harmonic response for the equivalent linear representation of a nonlinear viscous damping term. The same author later applied a similar approach to nonlinear hysteretic systems [Jacobsen, 1960], although in this reference, the "equivalent viscous damping ratio" calculated was used for the quantitative evaluation of energy dissipation only, and no corresponding stiffness value was assigned for predicting nonlinear response.

Jacobsen used the following expression for the equivalent viscous damping:

$$\xi_{eff} = \frac{1}{2\pi}\left(\frac{\text{Work done in half a cycle}}{\text{Work area under skeleton curve}}\right) \tag{6.11}$$

where the skeleton curve considered in the reference is an imaginary curve that traces out the centre of the hysteresis loop. As noted by Jacobsen,"this definition introduces an element of artistic judgment because in many practical cases the skeleton is not known ... [and] can be conjectured only" [Jacobsen, 1960, p. 1032].

Rosenblueth and Herrera [1964] modified the approach of Jacobsen, by equating the energy dissipated in a cycle of harmonic hysteresis with the same quantity for a linear viscoelastic system at resonance. The linear system was assigned an "effective stiffness" equal to the secant stiffness to the point of maximum displacement on the hysteresis loop. The value of equivalent viscous damping obtained by this method is only the same as Eq. (6.11) if the skeleton curve is considered to be a straight line connecting the origin to the point of maximum displacement on the hysteresis loop. Assigning the effective stiffness and damping properties to a linear viscoelastic system allows the nonlinear response to be estimated by solving the linear equation of motion.

The approach of Rosenblueth and Herrera [1964] has been widely adopted in design methods [e.g. Shibata and Sozen, 1976; Priestley *et al.*, 1996] and forms the basis of several code design procedures [AASHTO, 1999]. Some authors [Dwairi and Kowalsky, 2004; Blandon, 2004] refer to this method as "Jacobsen's approach", although from the discussion above, it is evident that this may not be appropriate. Following Jennings [1968], Rosenblueth and Herrera's equivalent linearisation approach is referred to as the "geometric stiffness method" herein.

Aside from the dependence of material properties on the displacement, other variations in bearing behaviour must be taken into account in design. In the AASHTO Guide Specifications for Seismic Isolation Design [AASHTO, 1999], bearing response is first expressed in terms of a bilinear force–displacement model, and then converted to effective stiffness and equivalent viscous damping parameters. For high-damping rubber bearings, property modification factors [Thompson *et al.*, 2000] are applied independently to the yield force and post-yield stiffness, to adjust material properties for the effects of temperature, ageing, velocity, wear caused by travelling, and cyclic degradation caused by Mullins' effect and scragging. The original specifications of the modification factors for elastomeric bearings were based on limited experimental data, and one of the primary goals of the Caltrans Protective Systems Project, described in Section 2.1, was the reevaluation of these factors [Thompson *et al.*, 2000]. Minimum and maximum adjustment factors are given for the post-yield stiffness and zero displacement force intercept (equivalent to the yield force in Chapter 3), and are used to calculate minimum and maximum effective linear properties.

For an individual isolation bearing, or a number of bearings in parallel, the equivalent viscous damping is calculated by equating the energy dissipated in a single cycle of hysteretic response and a linear viscoelastic system with stiffness K_{eff}. Using the geometric stiffness method, discussed above, the following equation is obtained for the bilinear parameters shown in Fig. 6.1(a):

$$\xi_{eff,h} = \frac{2(\mu-1)(1-r)}{\pi\mu(1+r\mu-r)} \tag{6.12}$$

where μ is the bearing design ductility, U_d/U_y, and the subscript h refers to the hysteretic component of energy dissipation. Considering minimum and maximum adjustment factors in turn, the linearised viscoelastic model can then be used to provide expected upper and lower bounds for the maximum displacement and force in the bearing in a given earthquake.

It is also possible to apply the geometric stiffness method to the model proposed in Chapter 4. The following expressions for effective stiffness and equivalent viscous damping are derived in Appendix B:

$$K_{eff} = c_3\left(a_1 + a_2U_d^2 + a_3U_d^4\right)\exp\left(-c_1D_{S,0}^3\right) + \left(\frac{b_1}{U_d} + b_2U_d\right)\exp\left(-c_2D_{S,0}^3\right) \tag{6.13}$$

$$\xi_{eff,h} = \frac{1}{2\pi K_{eff,b}U_d^2}\left[4b_1\left(U_d - \frac{1}{b_3}\right) + \frac{4}{3}K_{S,2}\,b_2U_d^2\left(U_d - \frac{3}{b_3}\right)\right] \tag{6.14}$$

where U_d is the design displacement of the bearing, $D_{S,0}$ is the level of prescragging, and all other parameters are defined in Chapter 4. Equations (6.13) and (6.14) may used in the place of Eq. (6.12) for HDR bearings that have been calibrated using the procedure outlined in Chapter 5. If K_{eff} and ξ_{eff} are calculated for multiple values of $D_{S,0}$, this could replace the property modification factor concept, at least for modification of bearing properties due to scragging [Thompson *et al.*, 2000]. The accuracy of the equivalent viscoelastic model defined by Eqs. (6.13) and (6.14) is investigated in Chapter 7.

The equivalent viscous damping for a hysteretic element, such as a bridge pier loaded into the inelastic range, may be evaluated in a similar manner. Calculating the energy dissipated for the modified Takeda hysteresis rule with a specified design ductility, assuming degraded response (cycle 6-7-8-9 in Fig. 6.1(b)), gives the following expression for hysteretic damping:

$$\xi_{eff,h} = \frac{1}{\pi}\left[1 - \mu^{\alpha-1}(1+r\mu-r)\right] \tag{6.15}$$

where α is a Takeda model parameter that controls the unloading stiffness. The equivalent viscous damping for an equivalent linearisation of the Takeda model was calculated this way by Kowalsky *et al.* [1994], although other authors such as Otani [1981] have used this expression as a measure of energy dissipation in the modified Takeda model in the past.

The calculation of equivalent viscous damping from Eqs. (6.12) and (6.15), for bilinear or modified Takeda hysteresis, respectively, is conceptually appealing for its simplicity, and has been incorporated into several design methods [e.g. Priestley *et al.*, 1996; Priestley, 2003] and codes [e.g. AASHTO, 1999] for bridge piers, seismic isolators, and other structural elements. However, the use of energy dissipation in a full cycle of harmonic loading at the basis of the geometric stiffness method may not give an adequate representation of response in some cases. In particular, Eqs. (6.12) and (6.15) assume that both the hysteretic oscillator and the equivalent viscoelastic model respond harmonically at a frequency given by the fundamental frequency of the structure. It is readily apparent from typical displacement histories for ground motion input that these conditions are met for neither linear nor nonlinear structural response.

For these reasons, researchers [Hwang *et al.*, 1996; Franchin *et al.*, 2001; Miranda and Jorge, 2002; Blandon, 2004; Dwairi and Kowalsky, 2004] have investigated the accuracy of the geometric stiffness approach for bilinear and modified Takeda hysteresis models. The results suggest that Eq. (6.12) tends to lead to significantly lower peak displacements than the nonlinear analysis with bilinear hysteresis (i.e. viscoelastic model overdamps), for a range of post-yield stiffness values. Equation (6.15) leads to consistently higher peak displacements than analyses with modified Takeda hysteresis (i.e. viscoelastic model underdamps), although for an elastic period greater than 1.0 seconds and target ductilities less than 4.0, the error is within 10% [Miranda and Jorge, 2002]. The results of Miranda and Jorge [2002] should be interpreted with caution, however: the viscous component of the equivalent damping, $\xi_{eff,v} = 5\%$, was not adjusted for ductility, using the corrections discussed below. This point is revisited at the end of this section.

Other approaches have been proposed to derive equivalent linearised properties for bilinear and modified Takeda hysteresis models. Jennings [1968] and Iwan and Gates [1979] evaluated a number of these methods, based primarily on the response of elastoplastic systems, and, in the latter reference, a degrading model more representative of reinforced concrete response. Franchin *et al.* [2001] and Miranda and Jorge [2002] compare some of the recent alternatives for linearising bilinear hysteresis, while Blandon [2004] and Dwairi and Kowalsky [2004] investigate correction factors for Eq. (6.15) at low periods.

Design methods that use the equivalent linearisation approach provide guidelines for determining equivalent linear properties for the entire structure from the properties of individual elements. For a series system, such as a simple pier-isolator with superstructure mass, design methods [e.g. Priestley *et al.*, 1996] specify that the effective stiffness may be taken as the series combination of the effective stiffness of each element. The damping is determined from the ratio of total energy dissipated to the energy dissipated by the substitute structure, as for an individual element. To take into account other sources of energy dissipation in the structure, and for consistency with time history analysis,

the total viscous damping is usually given by an expression of the following form:

$$\xi_{eff,v} = \xi_{eff,v} + \xi_{eff,h} \tag{6.16}$$

where $\xi_{eff,v}$ and $\xi_{eff,h}$ represent the total energy dissipation due to viscous damping and element hysteresis, respectively.

Of the two components of Eq. (6.16), the dependence of the hysteretic term on ductility is more evident, and has been discussed above. The viscous damping component of Eq. (6.16), however, has received less attention in the literature. In the original applications [Gulkan and Sozen, 1974; Shibata and Sozen, 1976] of the substitute structure approach, a value of 2% was assumed as representative of a limit to the effective damping as the ductility tends to unity. Subsequent applications [Priestley, 2003] have used a fraction of critical damping of 5%, presumably to coincide with the value typically assumed in nonlinear time history analyses. However, as with the choice of hysteretic model, the damping model assumed in analysis has a significant effect on the appropriate amount of equivalent viscous damping to specify in Eq. (6.16). In the nonlinear model, damping is typically assigned with respect to initial structural properties (mass or initial stiffness), or instantaneous properties (tangent stiffness), and not secant stiffness as specified in the substitute structure approach. Clearly, the dependence on damping model is neglected when a constant value of $\xi_{eff,v}$ is assumed for all applications.

For this reason, a study was conducted on the appropriate dependence of the viscous component on the damping model, hysteresis model and design ductility, for SDOF systems. Although a constant damping coefficient is typically assumed in time history analysis, results for the models discussed for MDOF systems in Section 6.1.4 were considered, for consistency with MDOF analysis. The substitute structure method is based on the representation of nonlinear MDOF systems with equivalent linear SDOF systems, and therefore the direct application of the SDOF results is applicable. The details of this study are discussed more thoroughly elsewhere [Grant *et al.*, 2004; Priestley and Grant, 2005]; the results are summarised below.

Using a similar approach to Rosenblueth and Herrera [1964] for the viscous damping force, viscous damping corrections for the three damping models given by Eqs. (6.3)–(6.5) were derived, based on SDOF harmonic steady-state response. Damping was defined by either a constant damping coefficient, or one that varies with the tangent stiffness. The modified Takeda and bilinear hysteresis rules were used for the nonlinear behaviour.

For a constant damping coefficient, (Eq. (6.3), or Eqs. (6.4)–(6.5) with the initial stiffness matrix), the viscous component of the equivalent viscous damping is given by:

$$\xi_{eff,v} = \lambda_1 \, \xi_v \tag{6.17}$$

where ξ_v is the fraction of critical damping specified in the time history analysis, and λ_1 is a correction factor:

$$\lambda_1 = \sqrt{\frac{K}{K_{eff}}} \tag{6.18}$$

for both the bilinear and modified Takeda hysteresis rules. The dependence of λ_1 on both ductility and the model parameter r is shown in Fig. 6.4.

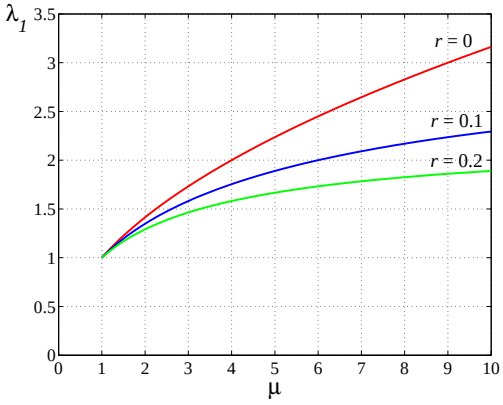

Figure 6.4. λ_1 **correction factor for bilinear and modified Takeda models.**

For "pure" tangent stiffness proportional damping (Eq. (6.4) using the tangent stiffness matrix for $\mathbf{K}$), the correction factor depends on the hysteresis model. For either model, the viscous damping is given by:

$$\xi_{eff,v} = \lambda_1 \lambda_2 \, \xi_v \tag{6.19}$$

where λ_1 is obtained from Eq. (6.18). For bilinear and Takeda hysteresis, the correction factor λ_2 is shown in Figs. 6.5(a) and (b), respectively. Figure 6.5(b) assumes that α is equal to 0.5, although the dependence of λ_2 on this parameter is small. It can be observed from Figs. 6.4 and 6.5 that for all values of ductility and post-yield stiffness, the total correction factor, $\lambda_1 \lambda_2$, is less than unity.

For tangent stiffness proportional Rayleigh damping (Eq. (6.5) using the tangent stiffness matrix for $\mathbf{K}$), the resultant correction factor is a combination of the two models discussed above. The post-yield stiffness, r, must be replaced with an effective value, r^*, which represents the ratio of the inelastic to the elastic damping coefficient. For a bilinear SDOF system, this value is given by:

$$r^* = \frac{a_0 m + a_1 r k}{a_0 m + a_1 k} \tag{6.20}$$

where a_0 and a_1 are the Rayleigh damping coefficients from Eq. (6.5), and m and k are the mass and elastic stiffness, respectively. The effective post-yield stiffness from Eq. (6.20) may be used with

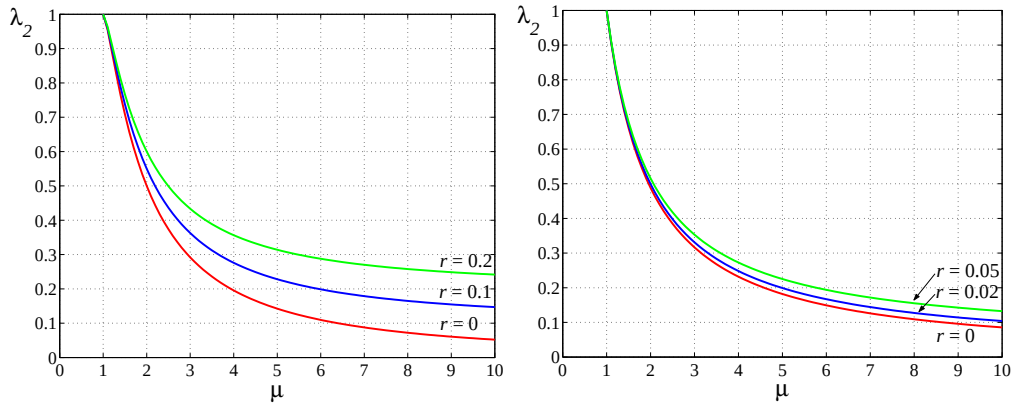

Figure 6.5. λ_2 **correction factor. (a) Bilinear model, and (b) modified Takeda model.**

Fig. 6.5(a) for bilinear hysteresis to determine the appropriate correction factor for tangent stiffness proportional Rayleigh damping. For modified Takeda hysteresis, Fig. 6.5(b) and Eq. (6.20), with some modification, may be used to determine λ_2.

The appropriate value of $\xi_{eff,v}$ to use for design depends on which of the damping models discussed above best represents the real structural response. If "pure" tangent stiffness proportional damping is specified, as recommended in Section 6.1.4, with modified Takeda hysteresis to a target ductility of 4.0, and $r = 5\%$, then, from Figs. 6.4 and 6.5(b), $\lambda_1 = 1.87$ and $\lambda_2 = 0.28$. For $\xi_v = 2\%$, this results in a design viscous damping value of $\xi_{eff,v} = 1.0\%$, while for $\xi_v = 5\%$, $\xi_{eff,v} = 2.6\%$ should be specified in Eq. (6.16). Although this correction will not make a large difference to the response in the former case, it could be more significant for the higher damping value. In either case, the correction is required for a consistent representation of viscous damping in analysis and design.

Taking into account the viscous damping correction, the results of Miranda and Jorge [2002] can be reinterpreted. Miranda and Jorge performed a series of analyses to assess the performance of Eq. (6.15), in addition to other models, by comparing the peak displacement response for nonlinear and linearised viscoelastic hysteresis. As reported earlier, they found that Kowalsky's equation tended to underdamp the response, compared with nonlinear response under the modified Takeda model. The viscous component of the fraction of critical damping was taken as equal for both nonlinear and linearised analyses, $\xi_v = \xi_{eff,v} = 5\%$, and the viscous component of the damping coefficient was not modified with structural yielding. A range of target ductility values from 1.5 to 6.0 was considered, and the post-yield stiffness coefficient $r = 0$.

For this set of parameters, a range of λ_1 correction factors may be obtained from Fig. 6.4: for $\mu = 1.5$,

$\lambda_1 = 1.2$, and for $\mu = 6$, $\lambda_1 = 2.4$. From Eq. (6.17), values of $\xi_{eff,v}$ between 6% and 12% should have been used in Eq. (6.16), rather than a constant value of 5%. This would explain the tendency of the equivalent linear model to consistently underdamp the structural response. The results of Blandon [2004], in which a similar series of analyses was carried out with $\xi_v = \xi_{eff,v} = 0\%$, albeit for a smaller number of ground motions, support this explanation, although correction factors to the hysteretic component of the equivalent viscous damping were still required to match the nonlinear response. In both studies the prediction of Eq. (6.16) was consistently poor for low periods.

The λ_1 correction factor, shown in Fig. 6.4, is derived from an exact relationship between viscous damping specified based on initial stiffness (ξ_v) and viscous damping specified in terms of secant stiffness ($\xi_{eff,v}$). The λ_2 factor, shown in Fig. 6.5(a) and (b), is based on the same assumptions as Eqs. (6.12) and (6.15) for the hysteretic component, and therefore requires validation. A numerical validation procedure, described in more detail elsewhere [Grant *et al.*, 2004], shows that the analytical values of λ_2 are consistently, although not significantly, low across a range of ductility values, periods and other model parameters. A simplified equation for the total correction factor for bilinear hysteresis is suggested:

$$\lambda_1\lambda_2 = 1 - 0.11(\mu - 1)(1 - r) \tag{6.21}$$

and for modified Takeda hysteresis:

$$\lambda_1\lambda_2 = 1 - 0.095(\mu - 1)(1 - r) \tag{6.22}$$

Equations (6.21) and (6.22) are recommended for values of μ between 1.0 and 6.0, and a maximum post-yield stiffness of 0.2 and 0.05, respectively. They can be used in place of Figs. 6.4 and 6.5(a) or (b) to give an appropriate adjustment to the viscous damping value for use with "pure" tangent stiffness proportional damping.

These results have been derived for SDOF systems, and it is not immediately evident how they will apply to MDOF systems, in which different hysteresis models describe the response of each element, and a given structural ductility corresponds to individual values of element ductility. For classically-damped systems (Section 6.1.4), the viscous damping matrix is representative of energy dissipation in the whole structure, and it is generally not possible to associate a level of viscous damping with an individual bearing, superstructure or substructure element. It may, however, be appropriate to use an expression like Eq. (6.16) for the pier response alone, and ignore viscous damping in the bearings. If this is the case, then the correction factor given by Eq. (6.22) would apply. This approach, and the application of these correction factors to MDOF structures in general, requires further investigation.

6.2.3 Displacement-Based Design of Isolated Bridges

The replacement of pier and bearing nonlinearity with equivalent viscoelastic models allows a rational design methodology based directly on displacements to be developed. Priestley *et al.* [1996] gives

a summary of the approach for a simple isolated bridge pier model, in which a target system displacement and bearing ductility level are assumed, and the corresponding pier displacement and bearing yield displacement are calculated from the effective stiffness ratios. They also suggest that a regular bridge response, for which the effective stiffness of each pier-isolator system is equal, will give the most efficient design, an assumption which allows each isolated pier and abutment to be designed independently. Calvi and Pavese [1998] have suggested criteria for the optimal design of an isolation system for the retrofit of existing bridges – an approach that also aims to regularise the response of the bridge as much as possible. The Uniform Load Method in the Guide Specifications for Seismic Isolation Demand [AASHTO, 1999] gives seismic demand in terms of an equivalent seismic force, although because this is derived from the secant stiffness and spectral displacement of the structure, it is equivalent to a displacement-based approach.

Because the limitation of bearing displacements is the primary design goal, and the equivalent linearisation of bearing properties is carried out with respect to the design displacement level, it appears more rational to target the bearing displacement directly in the design process. Essentially this is equivalent to the methods of Priestley *et al.* [1996] and AASHTO [1999], although it removes the need to assume a bearing yield ductility, which has little meaning for HDR bearings. In this section, the approach of Priestley *et al.* [1996] is restated in this form, for a single isolated pier system. The design method is presented specifically for elastomeric bearings for which the relationship between shear modulus and strain is known, and the total bearing displacement, U_b, is given by:

$$U_b = \gamma_b t_r \tag{6.23}$$

where γ_b is the shear strain in the bearing, and t_r is the effective rubber thickness.

The range of effective periods expected for isolated bridges suggests that a linearly increasing displacement spectrum will generally be appropriate for design in regions where high magnitude earthquakes govern the probabilistic seismic demand. Effective isolation periods will typically be in the "constant velocity" portion of the response spectrum, provided that the recommendations of Faccioli *et al.* [2004] for extending the upper corner period for high magnitude spectral shapes are adopted (see Section 6.2.1). This linear spectrum may be parameterised in terms of a single spectral ordinate for 5% damping at a given period. The assumed design spectrum is illustrated in Fig. 6.6, in which T_C and T_D are the lower and upper bounds to the "constant velocity" range, and U_C and U_D are the corresponding spectral displacements. For periods outside this range, the dotted line portions of Fig. 6.6 are more appropriate for design, although in the following it will be assumed that the solid line holds for all periods. For these parameters and assumptions, the 5% displacement spectral ordinate is given by:

$$U(T, 5\%) = U_D \left(\frac{T}{T_D} \right) \tag{6.24}$$

For lower magnitude events, or long isolated periods, it may be possible to assume that the effective system period is greater than T_D, in which case $U(T, 5\%) = U_D$ will be a more appropriate expression for the spectral response. In the following, Eq. (6.24) will be assumed, although it will be necessary to check this assumption at the conclusion of the design, and, if necessary, adjust the spectral demand accordingly.

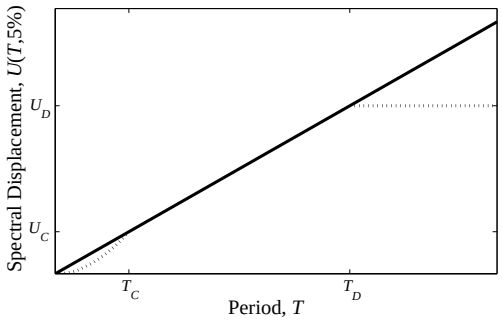

Figure 6.6. Assumed design displacement spectrum. Bold line assumes linear with period; dotted line is consistent with EC8 [CEN, 2003] acceleration spectral shape.

The Eurocode [CEN, 2003] damping adjustment factor, Eq. (6.6) will be assumed, giving the following displacement spectral ordinate as a function of effective period and equivalent viscous damping:

$$U(T, \xi) = \eta \cdot U(T, 5\%) = U_D \sqrt{\frac{0.1}{0.05 + \xi}} \left(\frac{T}{T_D} \right) \tag{6.25}$$

The proposed design methodology, therefore, aims to determine the effective rubber thickness, t_r, for a number of high-damping rubber bearings in parallel, with a total cross-sectional area of A_b, while maintaining the following performance objectives at the design intensity level:

D1. Rubber shear strain in the HDR bearing, U_b/t_r, is equal to the assumed design shear strain, γ_{bd}.

D2. Pier remains elastic, with a specified margin of safety.

To satisfy the second requirement, and to determine the elastic pier stiffness, it must be recognised that pier stiffness is dependent on strength. In the traditional force-based design approach, a reasonable pier stiffness is assumed for design before the required strength is determined. This would theoretically require iteration – once the pier strength has been determined, the pier stiffness should be adjusted – but this is seldom performed in practice. For isolated systems, in which the response is dominated by the flexibility of the isolation device, iteration may be unnecessary.

Nonetheless, it is more consistent within a displacement-based design framework to express the pier stiffness in terms of strength:

$$K_{pd} = \frac{F_{py}}{U_{py}} \tag{6.26}$$

where F_{py} and U_{py} are the pier yield force and yield displacement, respectively.

The yield displacement may be determined from the yield curvature, ϕ_{py} ; for zero moment at the top of the pier, it is given by:

$$U_{py} = \frac{\phi_{py} H^2}{3} \tag{6.27}$$

where H is the pier height.

Priestley [2003] reports that the yield curvature for circular bridge piers may be determined from:

$$\phi_{py} = \frac{2.25\varepsilon_y}{D} \tag{6.28}$$

where D is the pier diameter, and ε_y is the longitudinal reinforcement yield strain. For rectangular columns:

$$\phi_{py} = \frac{2.10\varepsilon_y}{h} \tag{6.29}$$

where h is the pier depth. Equations (6.28) and (6.29) are correct to approximately 10% accuracy.

To satisfy design performance goal number D2, to ensure that the piers remain elastic, it will be necessary to design for a pier yield force greater than or equal to the design force in the bearing. Priestley *et al.* [1996] note that the maximum expected variation in bearing design force should be around 10%, based on code requirements for isolation devices, and therefore suggest that the following equation should be adequate to ensure elastic pier behaviour:

$$F_{py} = \frac{F_{bd}}{0.85} = 1.18 F_{bd} \tag{6.30}$$

AASHTO [1999] specify response modification factors, R, that are 50% of the value used for non-isolated piers, but not less than 1.5. This value is dependent on the pier bent configuration: for single columns, the unadjusted R-factor is 3.0, while for multiple column bents, $R = 5$. Therefore, the values appropriate for these bent configurations in an isolated bridge are $R = 1.5$ and $R = 2.5$, respectively. The pier yield force is given by:

$$F_{py} = \frac{F_{bd}}{R} \tag{6.31}$$

The commentary [AASHTO, 1999] states that the intention of these response modification factors is to target elastic substructure behaviour at design intensity (with a target pier ductility of unity), while

allowing for an increase in pier capacity due to material overstrength and structural redundancy. It notes that the yield force in Eq. (6.31) "represents an average value, which may be exceeded given the inherent variability in the characteristics of the design-basis earthquake" [AASHTO, 1999, p. 23]. The value from Eq. (6.31) is the design value for the yield force, but the expected value is 50% higher (for single piers), and is equal to the bearing design force.

The AASHTO [1999] method and the method of Priestley *et al.* [1996] represent very different design philosophies. Although both methods target elastic pier behaviour at design level intensity, the former method specifies an *expected* pier ductility of 1.0, while the latter method specifies a *design* pier ductility of 0.85. If the expected strength is 50% or 150% higher than the design strength (for single and multiple pier bents, respectively), then AASHTO [1999] proposes R values 1.8 and 3.0 times those implied by the suggestion of Priestley *et al.* [1996]. This difference could possibly be explained by an increase in confidence in the use of seismic isolation for bridges between the dates of publication of the two methods, and consequently less conservatism in the design approach. In any case, the bridge piers will require ductile detailing in conjunction with capacity design principles, and it is not likely that bridges designed according to AASHTO [1999] will collapse under design level excitation. The major difference in behaviour may be expected at higher levels of excitation in an extreme earthquake; this possibility is explored from a design point-of-view in the next section, and numerically in a series of parametric studies in Chapter 7.

Assuming that the shear modulus of the elastomer, $G(\gamma_b)$, is a known function of the bearing shear strain, γ_b, the bearing design shear force is:

$$F_{bd} = G(\gamma_{bd}) A_b \gamma_{bd} \tag{6.32}$$

and the effective bearing stiffness is:

$$K_{bd} = \frac{F_{bd}}{U_{bd}} = \frac{G(\gamma_{bd}) A_b}{t_r} \tag{6.33}$$

Alternatively, Eq. (6.13), or an appropriately calibrated bilinear model, may be used to determine the bearing stiffness at the design level.

For an individual pier-isolator system, the total flexibility is equal to the sum of the pier and bearing flexibilities. Inversely, the equivalent system design stiffness is given by:

$$K_{sd} = \frac{K_{pd} K_{bd}}{K_{pd} + K_{bd}} \tag{6.34}$$

Assuming inertial forces on the pier are much smaller than on the superstructure, the system period is therefore:

$$T_{sd} = 2\pi \sqrt{\frac{M_1}{K_{sd}}} \tag{6.35}$$

where M_1 is the tributary mass of the superstructure, as before.

The equivalent viscous damping of the system is weighted in proportion to displacements:

$$\xi_{sd} = \frac{\xi_{bd} K_{pd} + \xi_{pd} K_{bd}}{K_{bd} + K_{pd}} = \frac{K_{sd}}{K_{bd}} \xi_{bd} \tag{6.36}$$

where it has been assumed that the viscous damping in the substructure and superstructure is zero, and that all energy dissipation occurs in the bearings. The equivalent viscous damping of an individual bearing is independent of its thickness, as the critical damping level scales with the bearing, and may be obtained from a known relationship of damping in terms of rubber strain, or from Eqs. (6.12) or (6.14), for the bilinear or proposed model, respectively.

From Eqs. (6.32), (6.34) and (6.23), the total system design displacement may be expressed as:

$$U_{sd} = \gamma_{bd} t_r \left(1 + \frac{K_{bd}}{K_{pd}}\right) \tag{6.37}$$

Finally, the design condition that the system displacement at the design strain in the bearing is equal to the spectral displacement for the linearised system may be enforced. Equating Eqs. (6.25) and (6.37), and solving Eqs. (6.26) and (6.31)–(6.36), the following effective rubber thickness is obtained:

$$t_r = \frac{0.1}{0.05 + \xi_{bd}} \left[\frac{M_1}{G(\gamma_{bd}) A_b} \left(\frac{2\pi U_D}{\gamma_{bd} T_D} \right)^2 - \frac{2RU_{py}}{\gamma_{bd}} \right] \tag{6.38}$$

where $R = 0.85$ if the recommendations of Priestley *et al.* [1996] are followed. The pier force design level may be obtained from Eqs. (6.31) and (6.32).

Although the design methodology outlined in this section was developed only for a simple pier-isolator system, it is possible to extend the method to the design of bridges including variable length isolated piers and isolated abutments. In this case, the assumption of single degree-of-freedom response, inherent in the displacement-based design procedure, may not describe the real bridge response accurately; the degree of coupling between the piers will be influenced by the superstructure stiffness. If pier lengths are not too irregular, it should be possible to follow the design philosophy of Priestley *et al.* [1996], by setting the design displacements of each pier-isolator subsystem as equal, and solving the system of design equations for each bearing rubber thickness. Equal design displacement at each pier suggests that effective stiffness should be assigned in proportion to tributary mass. Alvarez-Botero [2004] has investigated appropriate representations of continuous superstructure, non-isolated bridge decks, and it is possible that these results may be extended to isolated bridges.

The equivalent viscous damping for the system may be evaluated using the same principles as before. In AASHTO [1999], it is calculated from the total energy dissipated in all piers, normalised with

respect to a linear viscoelastic system, as in Section 6.2.2. Priestley *et al.* [1996] evaluates the equivalent viscous damping by weighting the individual pier-isolator subsystem with the corresponding tributary mass, normalised by the total superstructure mass. The evaluation of effective stiffness and equivalent viscous damping for the whole structure allows the computation of the displacement spectral ordinate, and, consequently, the effective rubber thickness for each bearing. In the case that bent heights are very irregular, it may be necessary to specify a different cross-sectional area of isolation bearings for each bent, to obtain a physically realisable design solution. In extreme cases, it may not be possible to ensure regular response, and more sophisticated design procedures may be necessary.

The design procedure discussed here also readily permits the inclusion of foundation flexibility. Provided that the flexibility can be quantified in terms of an equivalent linear viscoelastic rotational spring, this extra term can be added in series in Eq. (6.34), and the extra energy dissipation taken into account in Eq. (6.36). Each foundation-pier-isolator subsystem can then be designed for regular response, as before.

6.2.4 Design for Multiple Performance Levels

The design methodology summarised in the previous section allows a simple calculation of bearing rubber thickness and pier yield force, based on some simplifying assumptions about seismic demand, material properties, and pier overstrength requirements. The method does not, however, give any indication of the behaviour of the system for higher intensity earthquakes. As discussed in Section 6.2.1, this can be particularly important for regions of low to medium seismicity, for which the maximum credible earthquake (MCE) is significantly higher in intensity than the design level event. A measure of the performance under greater-than-design level intensity is also of particular interest for bridges isolated with HDR bearings, for which the stiffness may increase for displacements exceeding the design displacement, and lead to higher moment demands in piers. An explicit consideration of demand corresponding to a longer return period earthquake is required.

In this section, the same simple isolator-pier system will be considered, with the possibility of extending the methodology to include multiple piers and foundation flexibility, as discussed in the previous section. Two performance levels will be identified, in a general sense, and design goals for each level will be determined. The system of equations may be solved to determine the rubber thickness and pier yield force (or, equivalently, the response modification factor, R) that satisfies all of these goals.

The spectral demand given by Eq. (6.25) is extended to allow multiple levels of intensity:

$$U(T,\xi,I) = I \cdot U_D \sqrt{\frac{0.1}{0.05+\xi}} \left(\frac{T}{T_D}\right) \tag{6.39}$$

where I is a factor which represents the increased demand at the intensity level being considered. In general, U_D and T_D are specified for the design intensity level, for which $I_d = 1.0$. For higher values of I, the effective period and equivalent viscous damping of the system are also changing, and the demand spectral ordinate will increase by a factor:

$$\frac{U(T,\xi,I)}{U(T_{sd},\xi_{sd},I_d)} = \left(\frac{I}{I_d}\right)\sqrt{\frac{0.05+\xi_{sd}}{0.05+\xi}}\left(\frac{T}{T_{sd}}\right) \tag{6.40}$$

which, in general, is not equal to I.

Clearly, it will not be necessary to enforce elastic pier behaviour for $I > I_d$. For inelastic pier response, the pier ductility is defined by:

$$\mu_p = \frac{U_p}{U_{py}} \tag{6.41}$$

Assuming the modified Takeda model (Section 6.1.2) is representative of concrete pier response, the pier effective stiffness for $\mu_p > 1$ is given by:

$$K_p = K_{pd}\mu_p^{-1}\left(1 + r\mu_p - r\right) \approx \frac{F_{bd}}{U_{py}R\mu_p} \tag{6.42}$$

from Eqs. (6.26) and (6.31), as r, the post-yield stiffness ratio (see Fig. 6.1), is approximately zero for reinforced concrete piers. The equivalent viscous damping ratio for $\mu_p > 1$ is determined from Eq. (6.15), which depends only on the pier ductility and post-yield stiffness ratio, and not on the elastic stiffness or yield force of the pier.

With the definitions given in Eqs. (6.39)–(6.42), it is possible to define a set of performance goals for the isolated bridge response. The aim is to determine the effective rubber thickness, t_r, and pier yield force, F_{py}, such that:

D1. For $I = I_d = 1$, rubber shear strain in the HDR bearing, U_b/t_r, is equal to the assumed design shear strain, γ_{bd}.

D2. For $I = I_d = 1$, pier remains elastic.

M1. For $I = I_m$, rubber shear strain, γ_{bm}, does not exceed $\gamma_{b,max}$, determined from bearing stability, or elastomer strength requirements.

M2. For $I = I_m$, pier ductility does not exceed μ_{pm}, a predefined limit.

Note that performance goals D1 and D2 correspond to design level intensity, and M1 and M2 are defined with respect to intensity I_m, which could represent the maximum credible event, or another

level of seismic hazard. The following procedure assumes that goals D1 and M2 govern at their respective intensity levels; goals D2 and M1 must be checked for the final design.

Equations (6.30) and (6.31) are not used in the design for multiple performance levels, as the pier yield force is now a design variable. The other equations of the previous section, Eqs. (6.26)–(6.29) and (6.32)–(6.37) are applied directly to the $I = I_d$ intensity level. For $I = I_m$, the linearised pier properties are determined from Eqs. (6.15) and (6.42), and the following equations are also defined:

$$\begin{cases} F_{bm} = G(\gamma_{bm}) A_b \gamma_{bm} \\ K_{bm} = \dfrac{F_{bm}}{U_{bm}} = \dfrac{G(\gamma_{bm}) A_b}{t_r} \\ K_{sm} = \dfrac{K_{pm} K_{bm}}{K_{pm} + K_{bm}} \\ T_{sm} = 2\pi \sqrt{\dfrac{M_1}{K_{sm}}} \\ \xi_{sm} = \dfrac{\xi_{bm} K_{pm} + \xi_{pm} K_{bm}}{K_{bm} + K_{pm}} \\ U_{sm} = \mu_{pm} U_{py} \left(1 + \dfrac{K_{pm}}{K_{bm}} \right) \end{cases} \tag{6.43}$$

For general relations for elastomer stiffness, Eq. (6.32), and equivalent viscous damping in terms of bearing strain, the system of equations defined above cannot be solved explicitly for t_r and F_{py}. The following quadratic equation for the pier yield force can, however, be determined to satisfy performance goal M2:

$$(0.05 + \xi_{bm}) F_{py}^2 + (0.05 + \xi_{pm}) K_{bm} \mu_{pm} U_{py} F_{py} - 0.1 M_1 K_{bm} \left(\frac{2\pi I_m U_D}{T_D} \right)^2 = 0 \tag{6.44}$$

This suggests the following iterative procedure to determine F_{py} and t_r:

1. Determine ξ_{pm} from Eq. (6.15).
2. Initially, assume that the shear stiffness and damping for the bearing at $I = I_m$ are equal to the known design values, K_{bd} and ξ_{bd}, respectively.
3. Solve Eq. (6.44) for F_{py} using the quadratic formula.
4. Calculate R from Eq. (6.32), and the effective rubber thickness from Eq. (6.38).

5. For the assumption of zero post-yield stiffness, $r \approx 0$, $F_{pm} = F_{py} = F_{bm}$, and therefore:

$$\gamma_{bm} = \frac{F_{py}}{K_{bm} t_r} \tag{6.45}$$

   Update values of K_{bm} and ξ_{bm}, and iterate from step 3.

6. Check that $F_{pd} < F_{py}$ (to satisfy requirement D2), and $F_{bm} < F_{b,max}$ (to satisfy M1).

The procedure is implemented in a simplified form in the next chapter, and compared with the results from time history analyses.

7. PARAMETRIC STUDIES OF ISOLATED BRIDGE RESPONSE

7.1 INTRODUCTION

In this chapter, the proposed bearing model is used in a series of parametric studies to investigate the bidirectional response of bridges isolated with HDR bearings. Huang [2002] carried out a similar study for softening bearing types using a bilinear coupled plasticity model (as in Section 3.2.1), but did not investigate the dependence of the response on the input intensity of the ground motion. This is of particular importance for isolation with HDR bearings, for which the stiffening effect is likely to be influential beyond design level ground motion intensity. Other factors, such as pier inelasticity and superstructure flexibility, are also considered in this study. The main objectives of the parametric studies were:

1. To investigate the sensitivity of the response of isolated bridge systems to ground motion intensity, particularly if seismic demand exceeds design level.
2. To compare the effectiveness of common types of isolation devices with that of HDR bearings.
3. To test the robustness and applicability of the proposed bearing model and integration algorithm.
4. To assess the displacement-based design procedure, particularly for multiple performance levels, developed in the previous chapter.
5. Finally, to study the sensitivity of the peak system response to various modelling assumptions, including the treatment of scragging and scragging recovery, the elastic pier period, the choice of ground motion suite, and superstructure flexibility.

7.1.1 Bridge Configurations

The parametric studies were carried out on three bridge configurations, illustrated in Fig. 7.1. Configuration 1 (Fig. 7.1(a)) is a simple pier and bearing model, with one lumped mass representing the superstructure, and another for the mass of the substructure. The model can represent the

behaviour of a bridge with all piers identical in stiffness, and free abutments. Alternatively, if bearings have been designed to regularise the response of each (foundation)-pier-isolator subsystem, then their response may be effectively decoupled, as in Configuration 1. Each lumped mass has one degree-of-freedom (DOF) in each orthogonal horizontal direction, and therefore the total number of DOFs is four. Tributary lumped weights of 10 MN for the superstructure and 1 MN for the substructure are used.

Figure 7.1(b) is an elevation of bridge Configurations 2 and 3. Both models comprise a single, central pier-isolator system, and isolated abutments at each end. In Configuration 2, the superstructure is considered rigid, and the response is thus described by five DOFs – the four from Configuration 1, and a superstructure rotational DOF about the vertical axis. The fifth DOF is not excited in the symmetric analyses considered here, however. In Configuration 3, the superstructure is considered flexible, with a single generalised DOF [Chopra, 2001] used to describe its flexural deformation. With x and L as defined in the plan view, Fig. 7.1(c), the deformation is described by a cosine function:

$$U_{ss}(x) = U_6 \cos(\frac{\pi x}{2L}) \tag{7.1}$$

The equivalent mass ($\tilde{m}$) and stiffness ($\tilde{k}$) of the superstructure may be determined [Chopra, 2001]:

$$\tilde{m} = \overline{m}L \tag{7.2}$$

and

$$\tilde{k} = EI\left(\frac{2\pi}{L}\right)^4 \cdot L \tag{7.3}$$

where $\overline{m}$ is the superstructure mass per unit length, and EI is the flexural stiffness of the superstructure. Similarly, the equivalent ground motion influence scalar in the direction of U_6 is given by:

$$\tilde{L} = \frac{4\overline{m}L}{\pi} \tag{7.4}$$

The use of an equivalent DOF for the response of the bridge simplifies the analysis considerably. For a larger bridge model, however, it would be an oversimplified representation of the deck response, as it removes the influence of the higher modes of the superstructure on the overall response of the bridge. Alvarez-Botero [2004] conducted parametric studies of non-isolated bridges with flexible abutments, and found that the sinusoidal deflected shape is a particularly poor representation of superstructure deformation when central piers are stiff relative to the abutments.

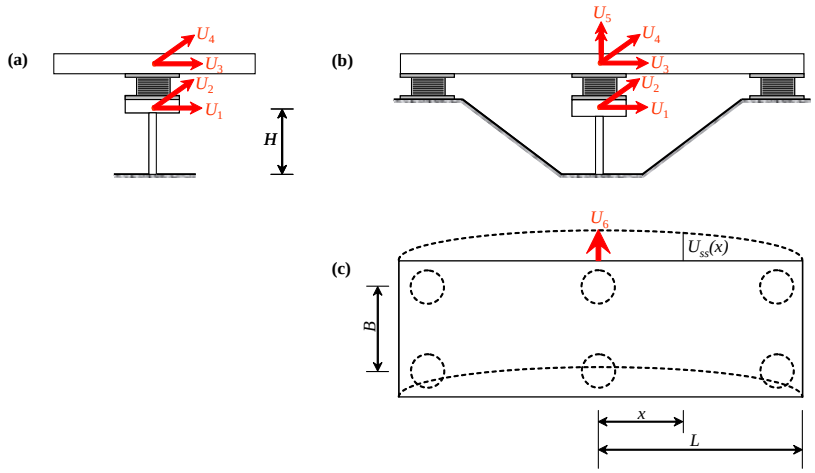

Figure 7.1. Bridge configurations for parametric studies. (a) Elevation for Configuration 1, (b) elevation for Configurations 2 & 3, and (c) plan for Configuration 3.

7.1.2 Superstructure and Substructure Modelling

Pier behaviour was represented by a linear elastic model, with the same stiffness in each direction. An initial pier stiffness of 71.5 MN/m is assigned, to give an elastic non-isolated pier period of 0.75 seconds, ignoring pier weight. This value was also varied for each configuration to assess the sensitivity of the response to the pier stiffness.

Although piers are usually designed to remain elastic in isolated bridges, it is important to understand how the effects of seismic isolation and pier yielding may interact for high seismic demand. To investigate the effects of pier inelasticity, various inelastic models were adopted for the piers. Although it is recognised that the initial stiffness of reinforced concrete (RC) elements varies with strength Priestley [2003], in this study a constant initial stiffness equal to 71.5 MN/m was adopted, for simplicity. Because there are no simple models for the biaxial bending of RC piers, an uncoupled modified Takeda model was used to represent pier response in each direction (Section 6.1.2). Parameters of $\alpha = 0.5$ and $\beta = 0$ were used, with a post-yield stiffness ratio of 5%.

To assess the sensitivity of response to bidirectional loading, two further plasticity models – coupled and uncoupled bilinear – were also used. Although neither of these models is particularly appropriate for RC piers, a comparison between the results of the two may give some indication of the error in using an uncoupled Takeda model as the primary description of biaxial pier bending. In each case, 5% post-yield stiffness was assumed.

7.1.3 Bearing Modelling

In all configurations, bidirectional bearing behaviour is represented by the model from Chapter 4. Due to the fact that no full-scale, bidirectional test results were available for HDR bearings, data from the scaled Bridgestone KL301 bearing calibration, described in Chapter 5 were used. As discussed earlier, these bearings were originally specified as 2.5 scale bearings for building seismic isolation, with a diameter of 175 mm, and total rubber thickness (t_r) of 45 mm. However, bearings scaled by a factor of 4.0 are more appropriate for bridge applications.

The virgin parameter set in Table 5.2 was used as a basis for parameters a_1–b_3, while the parameters accounting for stiffness and damping degradation were set to zero (with $c_3 = 1$). To represent the effects of pre-scragging of 250%, the virgin material parameter set was adjusted for an initial $D_S = 2.5t_r$. This initial scragging accounts for the fact that bearings are typically provided by the manufacturer in a degraded state, and subsequent hysteretic behaviour within this limit may be considered stable. The parameters were further adjusted to describe the total bearing system behaviour of four bearings per pier, and converted to SI units. Finally, the scaling factor to convert from scaled to prototype bearings, η was used as a variable in the bearing design process described below. Parameters were scaled by assuming that shear stress-shear strain properties of the elastomer remain constant; forces were multiplied by η^2 and displacements were multiplied by η. Scaling the bearing size in all directions allows the first and second shape factors, S_1 and S_2, to be maintained. These are defined as [Clark *et al.*, 1997]:

$$S_1 = \frac{\phi}{4t} \quad ; \qquad S_2 = \frac{\phi}{t_r} \tag{7.5}$$

where ϕ is the diameter of the steel shim, t is the thickness of each rubber layer, and t_r is the total rubber thickness, as defined earlier. For the Bridgestone bearings considered here, $S_1 = 20$ and $S_2 = 4$.

Sensitivity studies were also carried out on the HDR bearing model for three additional cases. In the first, the scragged bearing properties corresponding to 250% prescragging were retained, but the degradation parameters were not set to zero. Clearly, because of the isotropic damage model adopted in Section 4.1.3, this will only affect the response for intensity levels for which 250% strain is exceeded in the bearing. The other two sensitivity studies considered virgin bearing parameters, with scragging turned on and off in the model. As discussed previously, experimental evidence [Thompson *et al.*, 2000] suggests that virgin parameters are recovered over a time frame well within the design life of bridges. For this reason, it is important to consider this in the parametric studies.

To compare the effectiveness of HDR isolation systems with LR and FPS systems, another set of analyses was carried out with a kinematic hardening, coupled plasticity model for the bearings (Section 3.2.1). This model has been shown to describe bidirectional response of FPS bearings

[Mosqueda *et al.*, 2004] effectively, and is also commonly applied to LR bearings. In the latter case, model parameters are strain-dependent, at least for the lead core dimensions considered by Huang [2002]. Furthermore, the bidirectional behaviour of LR bearings is not completely described by the classical kinematic hardening approach for all load paths. These limitations notwithstanding, the bilinear model was adopted to contrast the behaviour of softening isolation devices such as FPS and LR bearings, with the stiffening behaviour of HDR bearings at high strains.

Because the LR bearing parameters are strain-dependent, two base sets of parameters were considered, from the calibrations of Huang [2002]. The two parameter sets correspond to bearing response for maximum strain levels of 100% and 150% – the former level represents the design strain assumed for the bearings in Section 7.1.5, while the latter is appropriate for the bearing demand at higher intensities. Although it would be more accurate to use a model that described the transition between these two representations, as well as LR bearing response at other strain levels, these two parameter sets should provide some information about LR bearing response at least two levels of seismic demand.

FPS bearing response is dependent on the level of axial load on the bearing – which can vary during a single event – in addition to the friction coefficient of the bearing surface, μ, and the bearing radius, R. Simple bilinear representations of response based on these parameters, although crude, provide a useful approximation to actual bearing response [Mosqueda *et al.*, 2004]. A pseudo-yield displacement of 0.01 inches (0.25 mm) was utilised for computational convenience, as recommended by Constantinou *et al.* [1993]. Two parameter sets, corresponding to low friction ($\mu = 0.06$) and high friction ($\mu = 0.12$), were derived using the design process discussed in Section 7.1.5, with a design displacement given by $R/8$. Priestley *et al.* [1996] recommend an absolute limit of $R/5$ for FPS bearings, and a reduction factor of $5/8$ for design purposes seems appropriate. In any case, it would be possible to adapt the multiple-performance-level design process described in Section 6.2.4 to FPS bearings, and the $R/5$ recommendation may be an appropriate performance goal for the MCE intensity level.

7.1.4 Ground Motions

A set of ground motion records was selected from the FEMA/SAC database SAC [1997] to use as input for the time history analyses. The database contains several suites of ground motion, scaled to the 1997 United States Geological Survey (USGS) hazard maps for various seismic hazard zones and the 1997 NEHRP spectral shape. The records are provided in orthogonal pairs, and are rotated into fault normal (FN) and fault parallel (FP) components, which can influence the intensity for near-fault recordings. The ground motions correspond to magnitude–distance pairs that are characteristic of each area, as determined from deaggregations of the probabilistic seismic hazard assessment (PSHA). Each pair of records is subsequently scaled by a single scaling factor to

minimise the squared error between the USGS target spectrum and the average response spectrum of the time histories at periods of 0.3, 1.0, 2.0 and 4.0 seconds, with weighting factors of 0.1, 0.3, 0.3 and 0.3, respectively. The spectral ordinate for 4.0 seconds was determined from a separate (PSHA), conducted by Abrahamson [SAC, 1997] – the target acceleration spectral ordinates, and corresponding displacement ordinates, are shown in Table 7.1.

Table 7.1. Target spectral ordinates for SAC [1997] ground motion scaling.

Period, T (sec)	0.3	1.0	2.0	4.0
$Sa(T, 5\%)$ (g)	1.07	0.68	0.33	0.123
$Sd(T, 5\%)$ (m)	0.02	0.17	0.33	0.49

A suite of earthquake recordings corresponding to a 10% exceedance-in-50-year hazard for firm soil sites in the Los Angeles (LA) area was selected for the time history analyses. A summary of the LA suite, including a description of each record, magnitude and distance information, and the scaling factor applied in preparation of the database, is presented in Table 7.2. Because the regression to determine the scaling factor for each record is carried out on the acceleration spectrum for a range of periods, the displacement spectrum for longer effective periods appropriate for isolated structures exhibit a large degree of scatter. For this reason, a second scaling factor has been applied here such that the average displacement response spectral ordinate for each pair for a period of 3.0 seconds is equal to the average of the 2.0 second and 4.0 second displacement ordinate from Table 7.1. Although it would be more consistent with the design procedure (discussed below) to use the bidirectional spectral ordinate rather than the average, it is consistent with the use of random ground motion components in the PSHA determination of hazard to use the average of the two. The second scaling factor, and the product of the two factors, is shown in Table 7.2.

Table 7.2. Los Angeles (LA) ground motion suite, and scaling factors for analyses.

SAC Name	Record	SAC Scaling Factor	2nd Scaling Factor	Total Scaling Factor
LA01–LA02	Imperial Valley, 1940, El Centro	2.01	0.78	1.56
LA03–LA04	Imperial Valley, 1979, Array #05	1.01	0.50	0.51
LA05–LA06	Imperial Valley, 1979, Array #06	0.84	0.55	0.46
LA07–LA08	Landers, 1992, Barstow	3.20	0.73	2.34
LA09–LA10	Landers, 1992, Yermo	2.17	0.84	1.83
LA11–LA12	Loma Prieta, 1989, Gilroy	1.79	1.10	1.96
LA13–LA14	Northridge, 1994, Newhall	1.03	1.07	1.10
LA15–LA16	Northridge, 1994, Rinaldi RS	0.79	1.05	0.83
LA17–LA18	Northridge, 1994, Sylmar	0.99	0.61	0.61
LA19–LA20	North Palm Springs, 1986	2.97	1.26	3.75

Note that the total scaling factors in Table 7.2 range from 0.46–3.75. As discussed in Section 6.1.5, factors in the range of 0.5–2.0 may be more likely to lead to physically realistic ground motions for inelastic analysis. It could also be argued that the deaggregation of the PSHA would give different results (in terms of magnitude–distance pairs) for different spectral ordinates, and therefore the records selected for the LA suite may not be specifically appropriate for the long periods of interest here. Nevertheless, it is assumed in this study, for both the reference level ground motion in Table 7.2 and subsequent scaling to represent different hazard levels, that accelerograms scaled by a constant factor are representative of physically realisable ground motion. In any case, the scaling factors in Table 7.2 generally lie within the recommended range, with three exceptions, and the ground motion pairs obtained by such a scaling will be more physically realistic than spectrum-compatible, artificial records. The maximum applied scaling factor (3.75) is also less than the upper limit of 4.0 proposed by other authors [Krinitzsky and Chang, 1977].

The displacement response spectra for each of the 20 scaled records, derived for a viscous damping ratio of 5% are shown in pairs in Fig. 7.2. The dotted line in each plot is the bidirectional response spectrum, described in Section 6.1.5, and the dashed line is the displacement response spectrum represented by the ordinates in Table 7.1. It is evident that the mean for each pair provides a good representation of design level demand for the range of periods applicable to isolation design ($T > 2.0$ seconds). As observed in Section 6.1.5, the maximum demand from spectrum compatible earthquakes will be greater than the unidirectional design demand, however, and the bidirectional response spectrum will govern the maximum response under these ground motions. This represents a greater level of seismic demand, as is apparent in each of the plots, and for this reason, the mean of all ten bidirectional spectra is used for the bearing design described in Section 7.1.5.

To study the sensitivity of the analysis results and design procedure (discussed below), sets of ground motions from a suite corresponding to a 10% exceedance-in-50-year hazard for Seattle (SE), and a suite of unscaled near-fault (NF) recordings were also used. The SE suite was rescaled according to the procedure described above for the LA suite, while the NF recordings were left unscaled. A description of each ground motion considered in the analyses, and the scaling factors applied is provided in Tables 7.3 and 7.4, for the SE and NF suites, respectively. More details of the ground motions in each suite may be found in the SAC [1997] report.

As discussed below, the ground motions described by Table 7.2 and Fig. 7.2, in addition to the scaled SE and unscaled NF suites of ground motion, are representative of design level hazard. Each ground motion pair has been scaled to a comparable hazard level, and the displacement spectra are used directly for the bearing and pier design (see Section 7.1.5). To investigate the response of the isolated bridge models to intensities different from that considered in design, a third scaling factor is applied to the ground motion pairs. For each bridge configuration, bearing type, ground

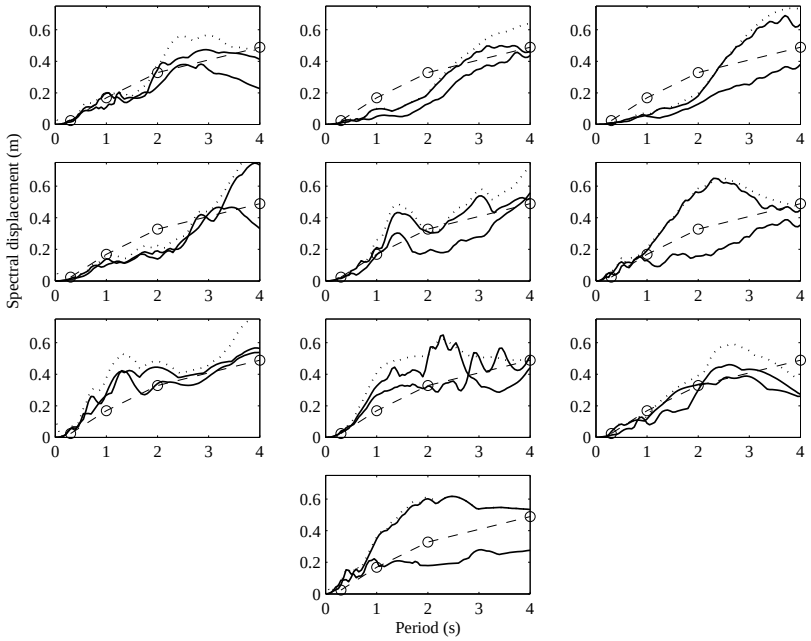

Figure 7.2. LA ground motion suite, displacement response spectra for each pair, $\xi = 5\%$ (solid lines), target spectrum for scaling (dashed) and bidirectional spectrum for pair (dotted).

Table 7.3. Seattle (SE) ground motion suite, and scaling factors for analyses.

SAC Name	Record	SAC Scaling Factor	2nd Scaling Factor	Total Scaling Factor
SE01–SE02	Long Beach, Vernon CMD Bldg.	0.49	0.54	0.27
SE03–SE04	Morgan Hill, 1984, Gilroy	2.84	1.02	2.91
SE05–SE06	West Wa., Olympia, 1949	1.86	0.66	1.23
SE07–SE08	West Wa., Seattle Army Base, 1949	5.34	1.61	8.58
SE09–SE10	North Palm Springs, 1986	1.71	1.25	2.13
SE11–SE12	Puget Sound, Wa., Olympia, 1965	4.30	1.19	5.12
SE13–SE14	Puget Sound, Wa., Federal OFC, 1965	5.28	1.33	7.04
SE15–SE16	Western Wa., Tacoma County, 1965	8.68	1.04	8.99
SE17–SE18	Llolleo, Chile 1985	1.24	1.08	1.33
SE19–SE20	Vinadel Mar, Chile, 1985	1.69	1.76	2.97

motion suite, and other sensitivity studies considered, analyses are carried out for ground motion scaling factors of 0.1–2.0, in increments of 0.1. The higher scaling factors are of particular interest, resulting in ground motions in excess of design levels. As discussed in Section 6.2.1, a factor of 2.0

Table 7.4. Near-fault (NF) ground motion suite, and scaling factors for analyses.

SAC Name	Record	SAC Scaling Factor	2nd Scaling Factor	Total Scaling Factor
NF01–NF02	Tabas, 1978	1.00	1.00	1.00
NF03–NF04	Loma Prieta, 1989, Los Gatos	1.00	1.00	1.00
NF05–NF06	Loma Prieta, 1989, Lex. Dam	1.00	1.00	1.00
NF07–NF08	C. Mendocino, 1992, Petrolia	1.00	1.00	1.00
NF09–NF10	Erzincan, 1992	1.00	1.00	1.00
NF11–NF12	Landers, 1992	1.00	1.00	1.00
NF13–NF14	Nothridge, 1994, Rinaldi	1.00	1.00	1.00
NF15–NF16	Nothridge, 1994, Olive View	1.00	1.00	1.00
NF17–NF18	Kobe, 1995	1.00	1.00	1.00
NF19–NF20	Kobe, 1995, Takatori	1.00	1.00	1.00

above design intensity, or sometimes greater, may be representative of the "maximum considered" hazard of 2% exceedance-in-50-years for low or moderate seismic intensity. Although the LA area is certainly a high seismic zone, the results are nevertheless of interest, as bearings will in any case be smaller in zones of lower seismicity, and the results will be qualitatively comparable.

7.1.5 Design of Bearings and Piers

To investigate the accuracy of the displacement-based design method discussed in Section 6.2, each bridge configuration was designed to meet the appropriate performance goals under the suite of input ground motions. The design approach was simplified slightly by assuming that the initial stiffness of each pier, whether elastic or inelastic, was independent of its strength. Furthermore, the use of scaled bearing parameters described in Section 7.1.3 suggested the use of the bearing scaling factor, η, as the primary design parameter. For the inelastic pier analyses, the yield strength of the pier, F_{py}, was used as a secondary design parameter, with the intention of satisfying performance goals D2 and M2, from Section 6.2.4.

The AASHTO specifications for isolation design [AASHTO, 1999] prescribe a lateral displacement limit for elastomeric bearings of $2.5t_r$, in addition to limits for the total shear strain due to vertical loads, rotation and lateral displacement. Stanton [1998] recommends a displacement limit of $2.0t_r$ to prevent delamination of the elastomer from the steel plates. To limit strains below this level for design level ground motion, a bearing design displacement corresponding to 150% design strain was considered in this study. As the scale bearing rubber thickness (45mm) scales with the scaling factor, η, the bearing design displacement is given by:

$$U_d = (150\%)(45\text{mm}) \times \eta \tag{7.6}$$

from Eq. (6.23).

The effective stiffness of the bearing at the design level, K_{bd}, is calculated from the unscaled bearing parameters obtained earlier, and also increases in proportion to the scaling factor. The equivalent viscous damping, ξ_{bd}, is found from Eq. (6.14), and is independent of scaling factor; a value of $\xi_{bd} = 10.4\%$ was calculated for the model parameters used here. The system effective stiffness, effective period and equivalent viscous damping are determined by considering the pier and isolator in series, as in Eqs. (6.34)–(6.36).

The average of the bidirectional ground motion spectra, derived for the equivalent viscous damping of the system, was used as the design displacement spectrum. Although this is not consistent with the use of any specific design code, it allows this approximation to be removed from the comparison of analysis results with design goals, and obviates the need for bidirectional combination rules. A trial scaling factor was assumed, and the structural period corresponding to a displacement of U_{sd} was found from the design spectrum. The scaling factor was adjusted until the period was approximately equal to the effective period of the system, T_{sd}. The above procedure converged for a scaling factor of $\eta = 5.6$, which corresponds to a prototype bearing diameter of 975 mm and rubber thickness of 250 mm.

The design spectrum for $\xi_{sd} = 9.5\%$, along with each of the individual bidirectional spectra for the same damping level, is shown in Fig. 7.3. The figure also shows the converged design point at $T_{sd} = 2.61$ seconds, and $U_{sd} = 0.42$ metres. It can be observed that even at a period of 3.0 seconds, for which the average response spectrum for each pair was normalised to a single value, there is some scatter about the mean. This scatter is due to the variability of the effects of damping – transforming the spectra from 5% to 9.5% – and the variation in the bidirectional demand for a given average displacement spectrum, as already observed in Fig. 7.2. For the design period of 2.61 seconds, the scatter is even greater, and some scatter in the analysis results can be expected. However, the mean over all ten analyses should provide a good measure of design performance.

The design procedure was also carried out for the bidirectional bearing models, representing the behaviour of LR and FPS bearings. For the LR bearing parameter set, calibrated parameters from 100% strain unidirectional loading tests by Huang [2002] were used, and scaled in the same way as for the HDR bearings. The bearings were originally 180 mm in diameter, with a total rubber thickness of 87 mm. An isolation system of four bearings, with a scaling factor of 4.3, was used to obtain a design point for the LA suite averaged displacement response spectrum, corresponding to a design displacement of $U_{sd} = (100\%)t_r = 375$mm. Parameters from the 150% strain unidirectional tests were also used; these parameters were scaled by the same factor (4.3), as they were intended not to represent a conscious design choice, but to account for reduced bearing stiffness for bearings greater than design level displacement demand. Two parameter sets were derived for the FPS bearings,

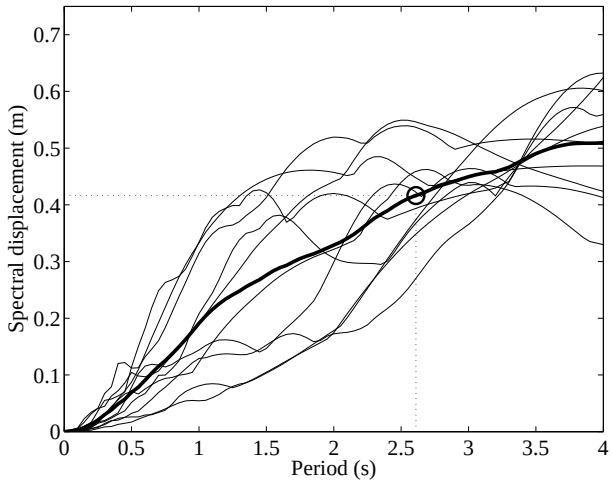

Figure 7.3. LA ground motion suite bidirectional displacement response spectra for 9.5% damping, and averaged spectrum (bold), with displacement-based bearing design point (circled).

corresponding to friction coefficients of $\mu = 0.06$ and $\mu = 0.12$. Assuming a bearing design displacement of one eighth of the bearing radius, design radiuses of 2.3 metres and 1.5 metres were obtained.

Sensitivity studies on ground motion input and representation of bidirectional demand were also carried out. The SE and NF ground motion suites were used, as described earlier, and the bearing scaling factor was determined accordingly. Furthermore, a design spectrum corresponding to the average of all twenty spectra from the LA suite, instead of the ten bidirectional pairs, was also used. This last assumption corresponds to normal design practice, in which unidirectional design is carried out with a design spectrum that corresponds to a random ground motion direction, instead of the worst direction which will govern the response of a regular structure. In regular design, however, bidirectional combination rules are used to account for this. A sensitivity study was also carried out on designing the HDR bearings for a strain level of 200%.

In addition to these elastic pier design cases, piers were also designed inelastically using the procedure discussed in Section 6.2.4. The methodology was adapted to the design parameters defined earlier, and values of $I_m/I_d = 1.5$ and 2.0, and $\mu_{pm} = 4$ were used. Performance goal M2 was ignored so that the goal of reaching target pier ductilities could be highlighted. Because the elastic pier stiffness is assumed to be constant here, the bearing scaling factor is identical to the elastic pier design. Pier yield forces of $0.77F_{bd}$ and $1.05F_{bd}$ were found for $I_m/I_d = 1.5$ and 2.0, respectively.

Finally, the designs were repeated for Configurations 2 and 3. In each case, two bearings were

used at the abutments, and four at the central pier, in proportion to the tributary weight of the superstructure. In Configuration 2, the central pier flexibility implies that the abutment bearings will govern the bearing design, provided that the same scaling factor is used for each bearing. The multiple performance level design methodology is difficult to adopt in closed form to the more complicated bridge geometries, so the inelastic pier designs from Configuration 1 were used. It was also impossible to design Configuration 3 without iteration on the deck displacement, so bearing designs from Configuration 2 were used for every case. This design procedure could be improved for more complicated bridge geometries by considering superstructure shape functions, such as that proposed by Alfawakhiri and Bruneau [2000] for non-isolated bridges with flexible abutments, and representing the abutment bearing and central pier-bearing ensemble by equivalent linear springs. The parametric studies of Alvarez-Botero [2004], that considered an iterative procedure to determine deflected shapes appropriate for displacement-based design, may also be applicable in this case.

The bearing scaling factors for each design case (or bearing radius for the FPS bearings) can be found in the captions to the figures found at the end of Sections 7.2–7.4.

7.1.6 Analysis Parameters

Newmark's method [Newmark, 1959] with parameters $\beta = 0.25$ and $\gamma = 0.5$ was used for the solution of the equation of motion, and the nonlinear state determination was carried out with Newton–Raphson iteration. The tangent stiffness matrix for the bearing model is derived in Appendix A. For coupled plasticity modelling of the inelastic behaviour of piers, the tangent matrix can be obtained by differentiating the governing equations in Section 3.2.1. For uncoupled models the tangent matrix is trivial to determine, as the off-diagonal components are zero, and the diagonals are obtained from the scalar stiffness in each direction.

Due to uncertainties in the application of viscous damping models for stiffening systems (Section 6.2.2), no viscous damping is used in the analyses or design.

7.2 Configuration 1: Identical Piers, Rigid Superstructure

For each bidirectional analysis, the peak bearing displacement and pier force were determined from the vector magnitudes at each time step. These maxima were normalised with the bearing design displacement, U_d, and design force, $F_d = K_{bd}U_d$, and are shown over the range of intensities in Fig. 7.4. The mean of the maxima across the whole ground motion suite is shown in bold in each plot. Although there is scatter in the individual ground motion results, it is comparable with the scatter in the bidirectional displacement spectra (Fig. 7.3) that correspond to the actual level of demand on the structure. Some general trends can be observed: at the design intensity level ($I/I_d = 1$), the peak displacements and forces are scattered about the design values (U_{bd} and F_{bd}), and the mean value

shows a good match of the target values. This observation validates the displacement-based design procedure outlined above, and suggests that a nonlinear response spectrum that gives the maximum response in any direction would be a useful design aid [Huang, 2002].

Figure 7.4 also illustrates the effect that the HDR bearing strain-stiffening phenomenon has on seismic isolation. For displacement levels in excess of the design displacement, Fig. 7.4a shows that the bearing deformation does not increase in direct proportion to the intensity, although the curvature of the mean line is not large. However, Fig. 7.4b illustrates the trade-off of limiting the displacement; the pier forces are increased significantly for the higher intensity levels. These observations will be more evident when the strain-stiffening HDR model is compared with a bilinear model typical of other bearing types.

To compare the effectiveness of HDR isolation systems with LR and FPS systems, another set of analyses was carried out with a bilinear force–displacement model for the bearings. The average maxima over all records are shown in Fig. 7.5. The response quantities from each bearing model are normalised with the design displacement and design force of each bearing so that the results can be compared. The exception is the LR model with parameters corresponding to 150% strain ("ultimate"), which represents the ultimate level properties of the "design" LR bearing, and is therefore normalised with respect to the corresponding design properties. The bearing models have been designed for the design intensity individually, and the displacement and force response is approximately the same at the design level of the bearing ($U/U_d = F/F_d = 1$). The displacements for the FPS model with high friction are slightly underestimated – for this model, the yield force is high relative to the post-yield stiffness, and the equivalent linearisation is less applicable.

For intensity levels above I_d, the difference between stiffening and bilinear response continues to diverge. The maximum displacement of the LR model exceeds 150% strain ($1.5U_d$) for a normalised intensity of 1.3, and therefore the "ultimate" properties may be considered representative of real LR bearing softening behaviour at this data point. This suggests that at a normalised intensity of 2.0, the normalised peak force may be even less than the 1.5 obtained here, and in any case will be significantly less than the HDR bearing. The difference in the peak displacements at the highest intensity values is not that significant, which suggests that the use of a bilinear model with one set of model parameters may be appropriate for analysis where only peak displacement is of interest. The differences among the three bearing types at high intensities again illustrates the trade-off discussed earlier – the stiffening behaviour of HDR bearings limits the maximum displacements for high strain levels, at the cost of higher forces developing in the piers.

A second sensitivity study was carried out on the inclusion of the scragging phenomenon in the bearing model. The parameters corresponding to scragging in the proposed model were retained from the calibration (Table 5.2), although the parameters corresponding to Mullins' effect were not

($c_3 = 1$, $c_4 = 0$). The parameters were converted to SI units, scaled for four bearings, and further modified for a scaling factor, η. Furthermore, another two sets of analyses were carried out with virgin material properties, including and excluding scragging effects, to investigate the effect on bridge response if the original bearing properties are recovered.

The results from this set of analyses are summarised in Fig. 7.6. It can be observed that the introduction of further scragging to the model does not affect the response until the prescragging level of 250% strain ($U = 5/3U_d$) is exceeded, due to the isotropic softening model used for the degradation, and even for these levels the peak forces are identical for $I/I_d \leq 2$. This justifies the use of no scragging in the other parametric studies in this chapter. The virgin parameter set results in a slightly stiffer model, and this is reflected in the lower displacements in Fig. 7.6a and higher forces in Fig. 7.6b. For the case of virgin parameters and scragging included, the peak force is probably observed before the peak displacement, as the former cycle softens the bearing for subsequent cycles. This is dependent on the properties of the ground motion, but it is reflected in Fig. 7.6, as the forces are higher for the scragging model with virgin parameters at higher intensities, but the displacements converge to the same value as the prescragged model.

The use of a different ground motion set for the bearing design and time history analyses was also investigated. Ten pairs of near-fault (NF) ground motion records from the FEMA/SAC database were used, and the bearing was redesigned for the mean bidirectional displacement spectrum of all ten ground motion pairs. Near-fault ground motions are considered to be particularly demanding for isolated systems, due to the high spectral response at long periods, and high amplitude velocity pulses. The NF recordings in the FEMA/SAC database are not scaled to a design spectrum, and consequently there is significantly more scatter in the response spectra. The bridge model was also redesigned for the scaled Seattle (SE) ground motion, as discussed in Section 7.1.4, to represent a region of more moderate seismicity.

The displacement and force response, normalised separately with respect to the values for each bearing design, are shown in Fig. 7.7. Even if NF motions are more demanding for an isolated system, it can be observed that this additional demand is included in the bidirectional demand spectrum, and was therefore included in the design procedure. The design for the SE ground motion suite led to a slight underestimation of the design displacement and force, and this discrepancy was magnified at the high intensity levels. This is particularly noteworthy, in that the factor of $I/I_d = 2.0$ is of more relevance for regions of moderate seismicity, and a ground motion corresponding to 2.0 times design intensity may be approximately representative of a 2%-exceedance-in-50-year hazard in these areas. This hazard level is adopted as the "maximum considered event" in several design codes [AASHTO, 1999].

Figures 7.8 and 7.9 consider the sensitivity of results to two assumptions in the design process. The

first assumption (Fig. 7.8) deals with the representation of bidirectional demand by way of a response spectrum calculated for a random ground motion component. Clearly, the actual peak bidirectional response of a structure will be governed by the "worst component" of the earthquake motion. This is not identical to taking the worst case angle of incidence of ground motion, θ, which, as discussed in Section 6.2.1, is inconsistent with the design hazard level. In the former case, the hazard-consistent ground motion and the structure are fixed in space, and the peak response is governed by the peak displacement demand in a vector sense. In the latter, the given ground motion is rotated to determine the maximum of all peak vector displacement values, for $0 < \theta < 360°$. Figure 7.8 shows that the design demand is largely underestimated by the unidirectional spectrum, by around 40% for peak bearing displacements and forces. This also leads to corresponding differences in the demand curves for intensity levels below and above the design intensity.

The second design assumption considered is the design strain specified for the HDR bearing. A design strain of 200% was considered, following the upper limit recommended by Stanton [1998], to contrast the value of 150% used in the main designs. Changing this value moves the design point with respect to the stiffening range of the Bridgestone bearings, and could be expected to affect the results particularly for $I > I_d$. Figure 7.9 shows that the displacement demand is not significantly different across the whole intensity range, although the forces for the 200% design strain case are higher for higher intensity level. The demand levels reached in these analyses represent the maximum range of applicability of the bearing parameters used here, which were calibrated for vector strain levels up to 350% (Chapter 5).

Related to the issue of how to account for bidirectional seismic ground motion input is how to determine bidirectional structural response from unidirectional analyses. Bidirectional analyses require extra modelling and computational effort on the part of the analyst. Ground motions are typically applied in orthogonal directions in independent, unidirectional analyses, and the maximum response, or some combination of response quantities from each analysis, are considered for design. To determine if the maximum value is able to accurately capture the real peak response, the analyses were repeated with ground motion pairs from the LA suite, applied independently. The maximum displacement and force were calculated for each pair of records, and averaged over the suite. In addition, the mean of all 20 unidirectional analyses was computed for each response quantity, to investigate the difference between mean and peak input in the design approach that was discussed earlier.

The results from this study are summarised in Fig. 7.10. The maximum displacements, averaged over all ground motion pairs, do not significantly underestimate the bidirectional displacements and forces across the range of intensities. The peak force for the maximum unidirectional case describes the bidirectional force demand very well. These observations suggest that unidirectional

analyses could be adequate for isolated bridge design. The bridge model used here, however, is an idealisation of real bridges, and this may not apply for bridges with different stiffness in transverse and longitudinal directions. The mean value of each pair of unidirectional analyses underestimates the peak bidirectional demand by an amount consistent with the difference observed between the two curves in Fig. 7.8.

The remaining parametric studies in this section are concerned with pier modelling, for both elastic and inelastic behaviour. The first such sensitivity study was carried out considering different values of elastic pier stiffness. Non-isolated pier periods of 0.75, 1.0 and 1.5 seconds were used, corresponding to pier stiffness values of 702, 394 and 175 MN/m, respectively, considering only the superstructure mass in the calculation. Figure 7.11 shows that the series system behaviour is relatively insensitive to the pier stiffness, as the flexibility of the bearing dominates the response. Of more interest for flexible bridges is how effective seismic isolation can be at reducing the demand. The data in Fig. 7.11 could be compared with a non-isolated, elastic pier analysis, although this would require a more realistic representation of damping in the pier.

Figures 7.12 and 7.13 show the bearing displacements and forces, and pier ductility for different hysteresis models of nonlinear pier behaviour. A response modification factor of 1.0 was used, such that the pier yield strength was equal to the bearing design force, $F_{py} = F_{bd}$. The modified Takeda model is representative of unidirectional reinforced concrete response, but response in orthogonal directions is uncoupled, which may not describe biaxial pier response accurately. The bilinear models have "fatter" hysteresis loops, and are expected to dissipate more energy in analyses for which the demand exceeds the yield level. Comparing the two uncoupled pier models in Figs. 7.12 and 7.13, the bilinear model exhibits lower demand in terms of bearing displacements and forces, and pier forces.

The coupled bilinear model gives results that are similar to the modified Takeda model, and greater than the uncoupled bilinear model, for all response quantities. The implication of this is that analyses using two uncoupled modified Takeda model in orthogonal directions may underestimate the real bidirectional demand slightly. Although it is not possible to extend the Takeda model to bidirectional action, it would be possible to conduct a series of analyses with the ground motion input rotated through a angles, $0 < \theta < 360°$. This is not the same approach as calculating the worst case direction for the CQC3 method, discussed earlier, as here it is used to make up for modelling limitations rather than to account for different directions of possible earthquake attack. This approach would only be appropriate for regular structures, as otherwise the orientation of the ground motion with respect to structural axes will affect the response. In any case, the difference between the coupled and uncoupled bilinear results in Figs. 7.12 and 7.13 is not large, and qualitative conclusions can still be drawn from the uncoupled Takeda analyses.

Of more significance are the large pier ductilities observed for ground motions exceeding design level

intensity, regardless of hysteresis model. For seismic demand greater than approximately 1.2 times design demand, the pier ductility increases rapidly. As observed in the commentary of the AASHTO design provisions [AASHTO, 1999], if the post-yield stiffness of the pier is significantly less than the tangent stiffness of the bearing, then after pier yielding, most of the subsequent seismic demand will be carried in the piers. Allowing pier ductility at design level will eliminate the benefit derived from isolation, and require ductile detailing of piers. It should be noted that the response modification factor of 1.5 or 2.5 specified in AASHTO (and discussed in Section 6.2.3) allows the possibility of some pier yielding at design level, while Priestley *et al.* [1996] use a capacity design approach to ensure that this is not likely. Figure 7.13 shows that the latter approach may be prudent for safe design if greater hazard levels are not considered explicitly in the design process.

The performance-based design approach discussed in Section 6.2.4 aims to directly control pier yielding by designing for multiple performance levels. In addition to the normal design requirements, the performance goals chosen to demonstrate this procedure were a target pier ductility of 4.0 at 1.5 and 2.0 times the design level hazard. This resulted in pier forces of $F_{py} = F_{bd} = 0.77$ and $F_{bd} = 1.05$, respectively.

The results from the analyses using these designs are shown in Figs. 7.14 and 7.15. Figure 7.14 shows the predictable result that allowing for more pier ductility at design level limits bearing demand at design intensity and beyond. Figure 7.15 shows that the designs attain the target ductility levels well, except that the $F_{bd} = 1.05$ obviously allow for some pier yielding at design level which may not be allowable. Both designs were slightly unconservative, and it will be necessary to increase these levels for safe design. To be consistent with the design philosophy of Priestley *et al.* [1996], an additional factor of 1.15 would also be appropriate, allowing for up to 15% variation in bearing properties. It is also possible that pier ductilities in excess of 4.0 will be allowable for ultimate level design – any variation of performance goals can be taken into account explicitly in the design process.

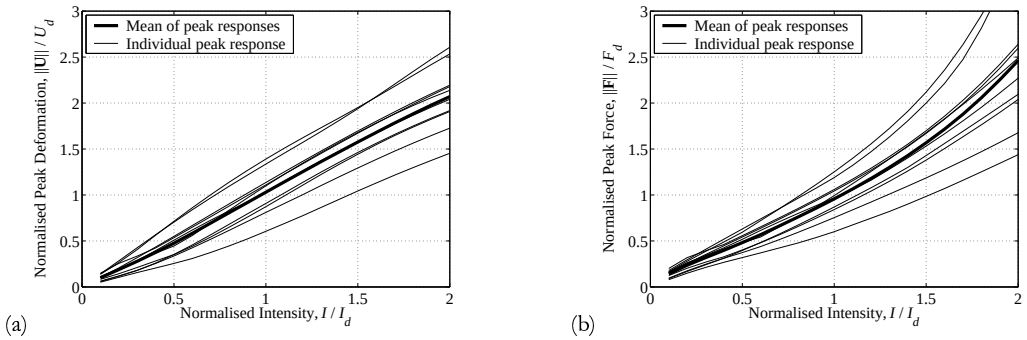

Figure 7.4. Configuration 1: Peak bearing response, all records and mean. (a) Peak displacement, and (b) peak force. $\eta = 5.6$.

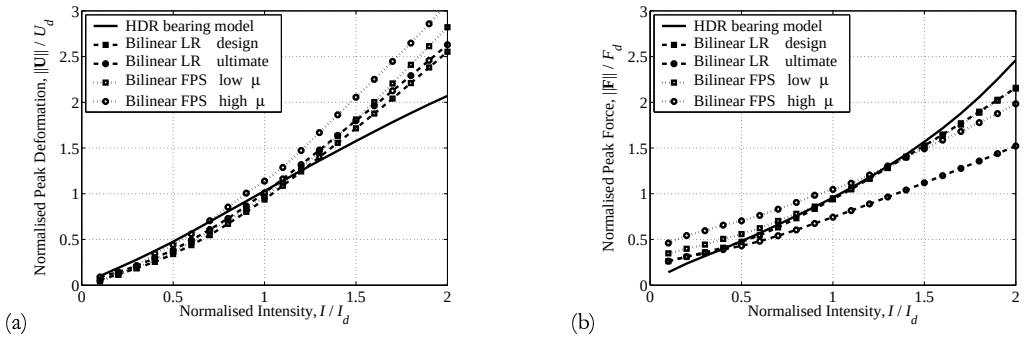

Figure 7.5. Configuration 1: Peak bearing response, different bearing models. (a) Peak displacement, and (b) peak force. $\eta = 5.6$ (HDR), $\eta = 4.3$ (LR), and $R = 2.3$ and 1.5m (FPS, low and high friction).

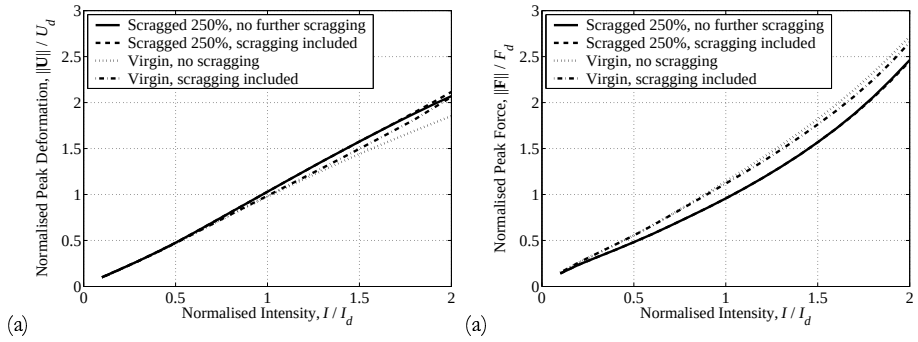

Figure 7.6. Configuration 1: Peak bearing response, different models of scragging. (a) Peak displacement, and (b) peak force. $\eta = 5.6$.

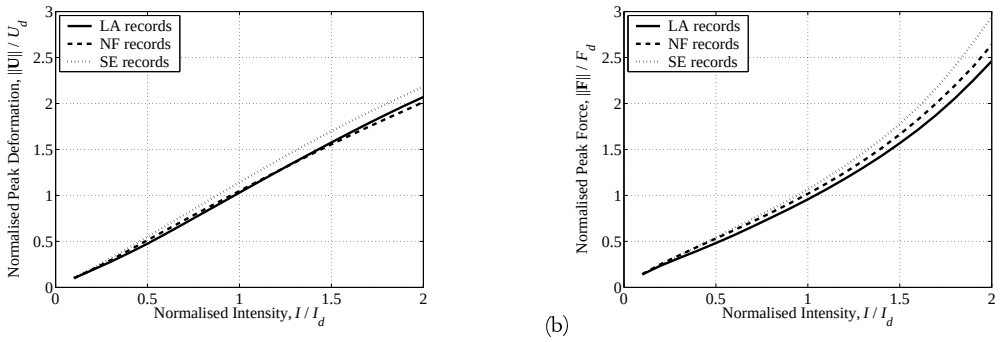

Figure 7.7. Configuration 1: Peak bearing response, different ground motion suites. (a) Peak displacement, and (b) peak force. $\eta = 5.6$ **(LA),** $\eta = 3.7$ **(SE),** $\eta = 8.8$.

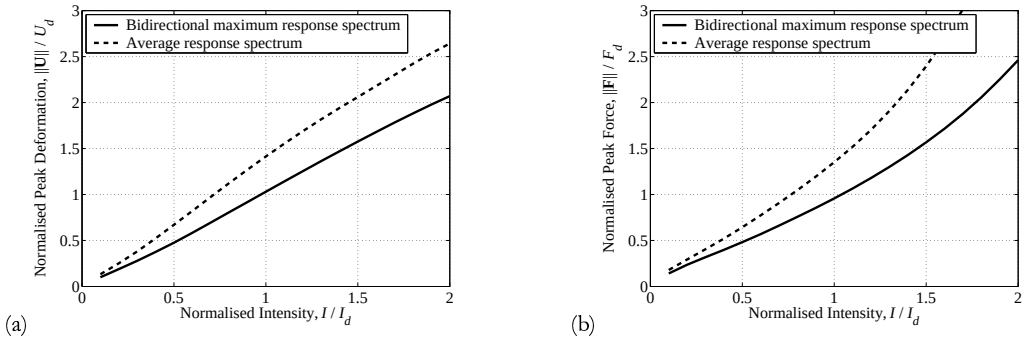

Figure 7.8. Configuration 1: Peak bearing response, different types of design spectra. (a) Peak displacement, and (b) peak force. $\eta = 5.6$ (bidirectional) and $\eta = 4.5$ (average).

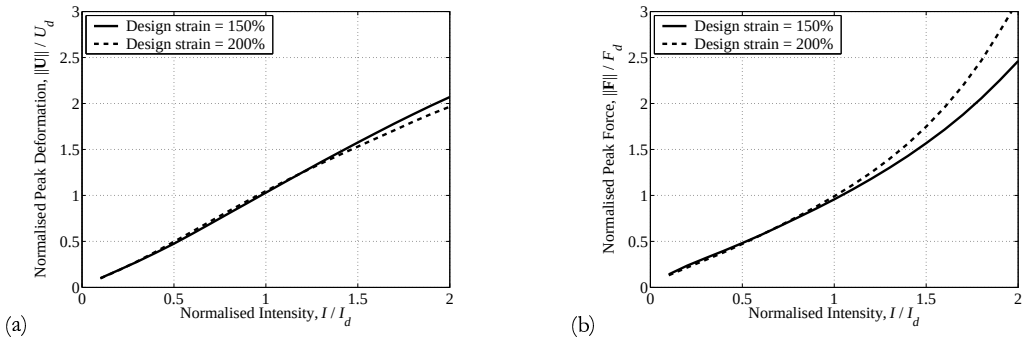

Figure 7.9. Configuration 1: Peak bearing response, different design strains. (a) Peak displacement, and (b) peak force. $\eta = 5.6$ (150%) and $\eta = 4.5$ (200%)

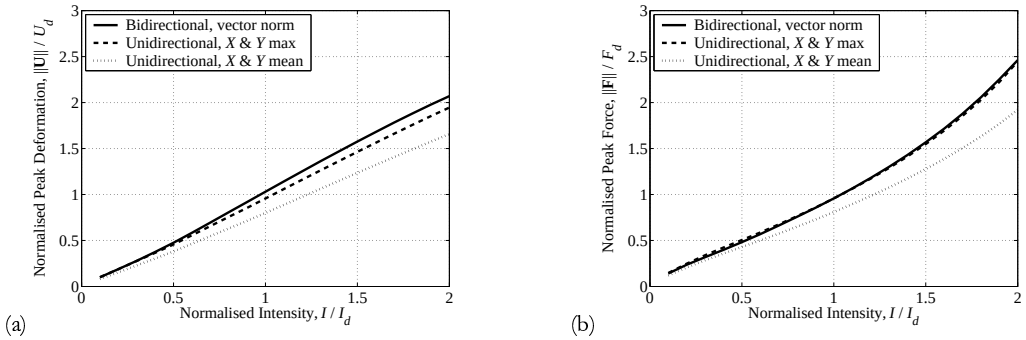

Figure 7.10. Configuration 1: Peak bearing response, different bidirectional ground motion combination rules. (a) Peak displacement, and (b) peak force. $\eta = 5.6$.

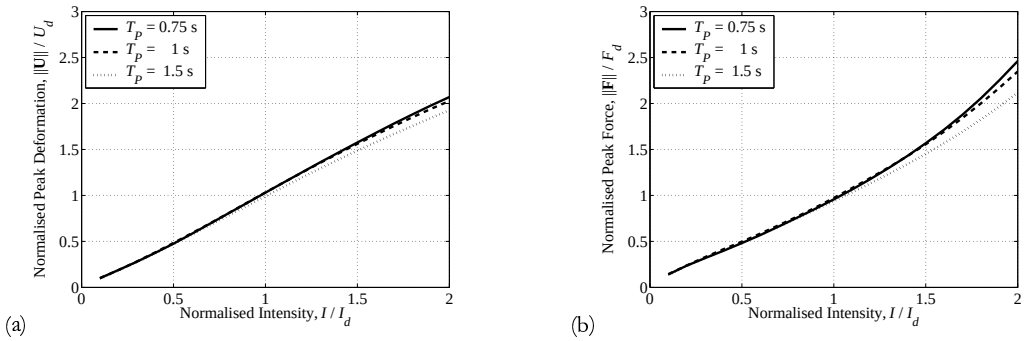

Figure 7.11. Configuration 1: Peak bearing response, different unisolated pier periods. (a) Peak displacement, and (b) peak force. $\eta = 5.6$.

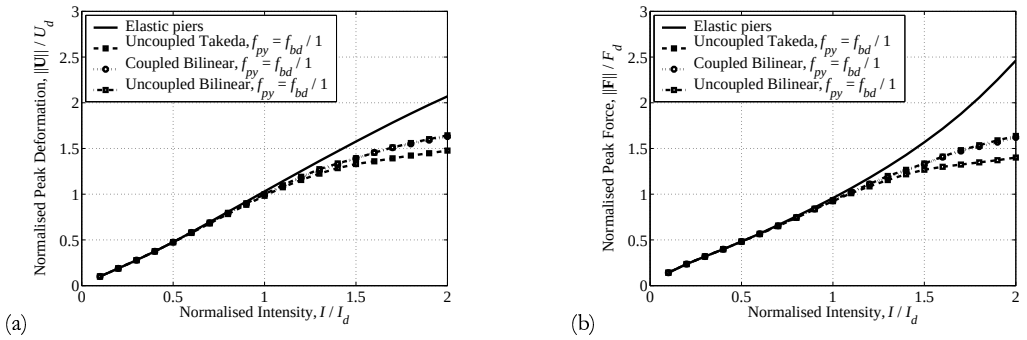

Figure 7.12. Configuration 1: Peak bearing response, different nonlinear pier models. (a) Peak displacement, and (b) peak force. $\eta = 5.6$.

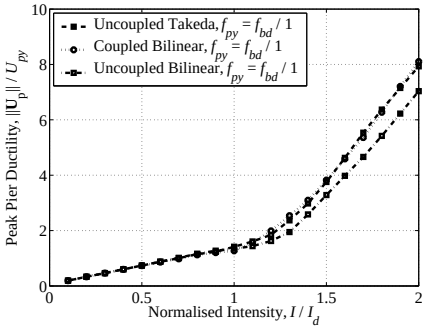

Figure 7.13. Configuration 1: Peak pier ductility, different nonlinear pier models. $\eta = 5.6$.

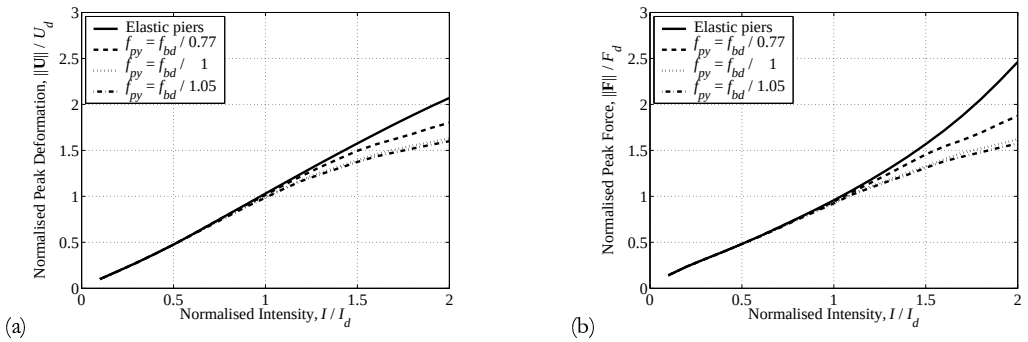

Figure 7.14. Configuration 1: Peak bearing response, different pier yield forces. (a) Peak displacement, and (b) peak force. $\eta = 5.6$.

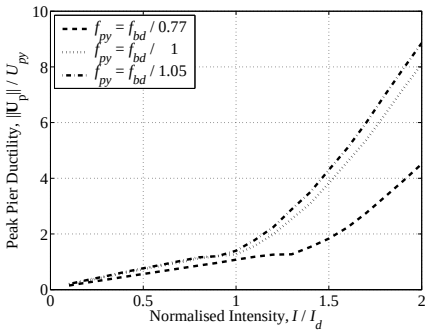

Figure 7.15. Configuration 1: Peak pier ductility, different pier yield forces. $\eta = 5.6$.

7.3 Configuration 2: Isolated Pier and Abutments, Rigid Superstructure

The same parametric studies described above were carried out for a bridge model of Configuration 2 (Fig. 7.1), with span length, $L = 10$ m. The normalisations in the figures in this section are carried out with respect to the individual design displacement and design force for each bearing. Because the abutment bearings govern the design, the design values for those bearings are known. The design values for the central bearings are calculated such that the stiffness of the pier-isolator system are the same as the abutment bearing. This requires iteration, as the bearing properties are dependent on the displacement, but the process converges in only a few steps.

Figures 7.16 and 7.17 show the abutment and central bearing demands for all of the Configuration 2 analyses. Comparing with Fig. 7.4, the superstructure behaviour does not significantly affect the peak bearing response. The degree of scatter and the mean of the normalised peak bearing displacement for the central bearing are slightly larger than for the abutment bearing. These results show that the design procedure provides adequate designs for meeting the performance goals, even for slightly more complicated bridge geometries.

Figures 7.18–7.31 show the results for the elastic pier designs of Configuration 2, corresponding to the Configuration 1 results in Figures 7.5–7.13. The same general observations made in Section 7.2 can be made here. Figure 7.29, however, shows that the central bearing response is more sensitive to the use of bidirectional or unidirectional analyses. The maximum of two orthogonal unidirectional analyses underestimates the bidirectional demand on the bearing, particularly in terms of normalised bearing force. For irregular, or more complicated bridge designs, it is expected that this underestimation would be further emphasised. The 30%-rule, or more complicated combination rules, could be assessed here.

For inelastic pier designs (Figs. 7.32–7.37), the response of Configuration 2 is clearly different from Configuration 1 (Figs. 7.12–7.15). The abutment bearing demand is not reduced significantly by pier yielding, as the total displacement demand on the central bearing-pier system must be carried by the abutment bearing alone, coupled by a rigid superstructure. For real abutment bearing design, this suggests that either larger bearings will be necessary, or the foundation may also be designed to yield. The latter option is more difficult than it is for piers, for which the behaviour can be more readily controlled.

The central bearing demand and pier ductility demand for $F_{py} = F_{bd}$ is approximately the same as for Configuration 1 which suggests that the uncoupled modified Takeda model is again adequate for representing bidirectional structural demand. In addition, the multiple performance level design meets the objectives to an acceptable degree of accuracy (Fig. 7.37), although it can be observed that a pier yield force of $F_{py} = F_{bd}/1.0$ results in a better match of the target pier ductility of 4.0 at an

intensity of $1.5I_d$ than $F_{py} = F_{bd}/1.05$.

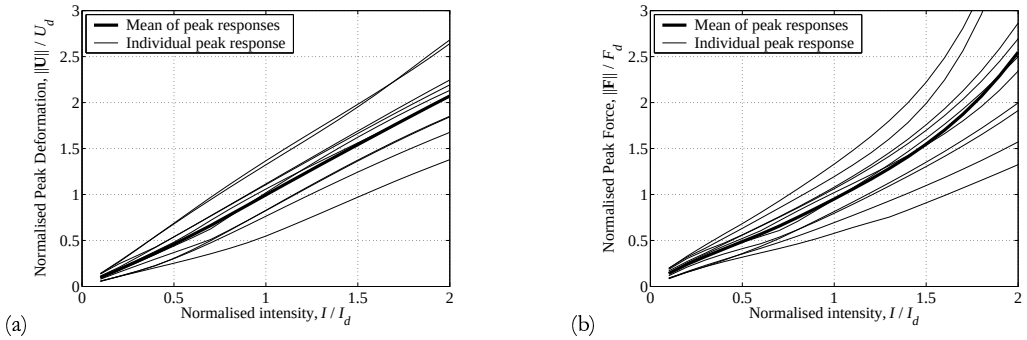

Figure 7.16. Configuration 2: Peak abutment bearing response, all records and mean. (a) Peak displacement, and (b) peak force. $\eta = 5.8$.

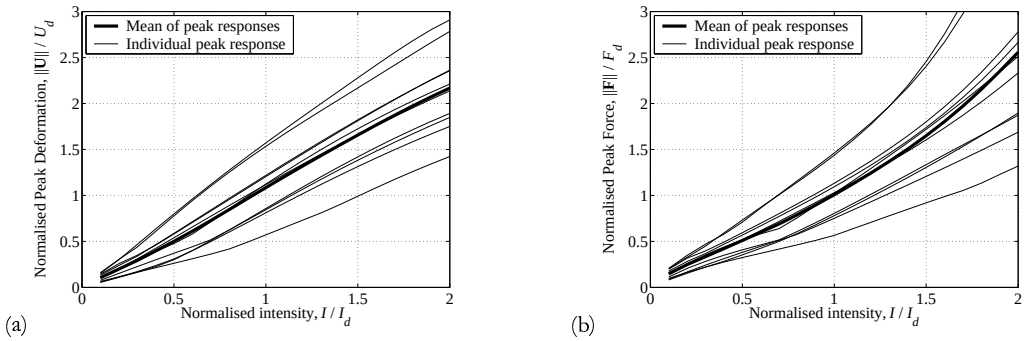

Figure 7.17. Configuration 2: Peak central bearing response, all records and mean. (a) Peak displacement, and (b) peak force. $\eta = 5.8$.

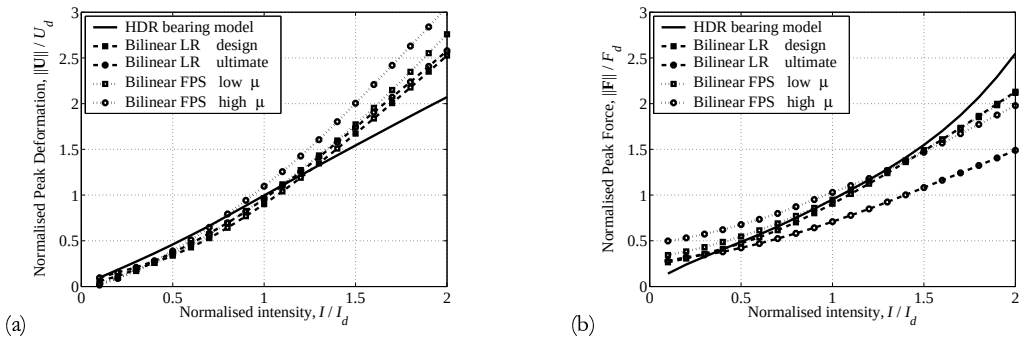

Figure 7.18. Configuration 2: Peak abutment bearing response, different bearing models. (a) Peak displacement, and (b) peak force. $\eta = 5.8$ (HDR), $\eta = 4.4$ (LR), $R = 2.4$ and 1.6m (FPS, low and high friction).

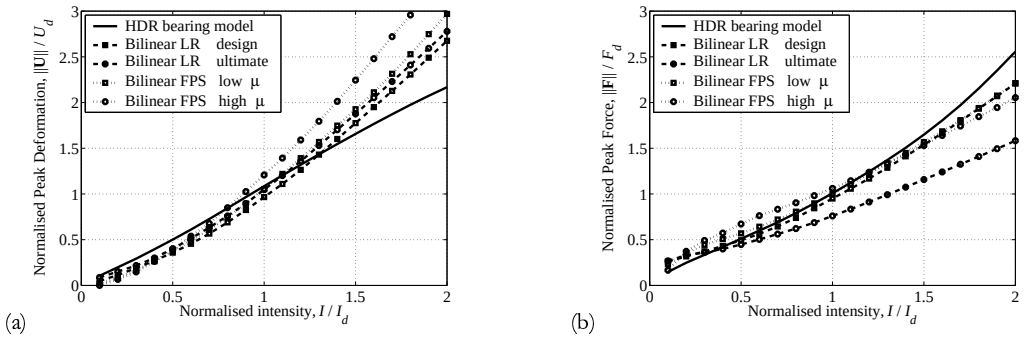

Figure 7.19. Configuration 2: Peak central bearing response, different bearing models. (a) Peak displacement, and (b) peak force. $\eta = 5.8$ (HDR), $\eta = 4.4$ (LR), $R = 2.4$ and 1.6m (FPS, low and high friction).

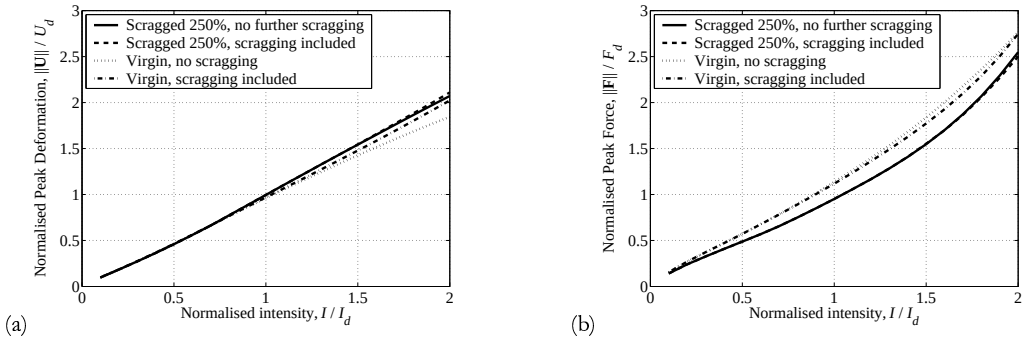

Figure 7.20. Configuration 2: Peak abutment bearing response, different models of scragging. (a) Peak displacement, and (b) peak force. $\eta = 5.8$.

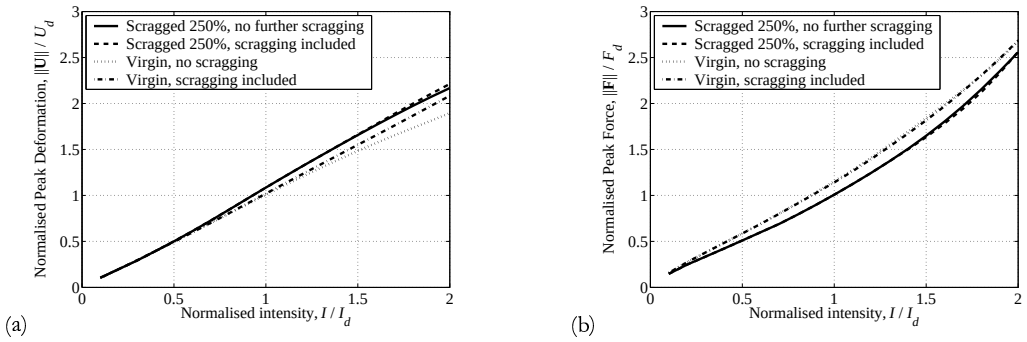

Figure 7.21. Configuration 2: Peak central bearing response, different models of scragging. (a) Peak displacement, and (b) peak force. $\eta = 5.8$.

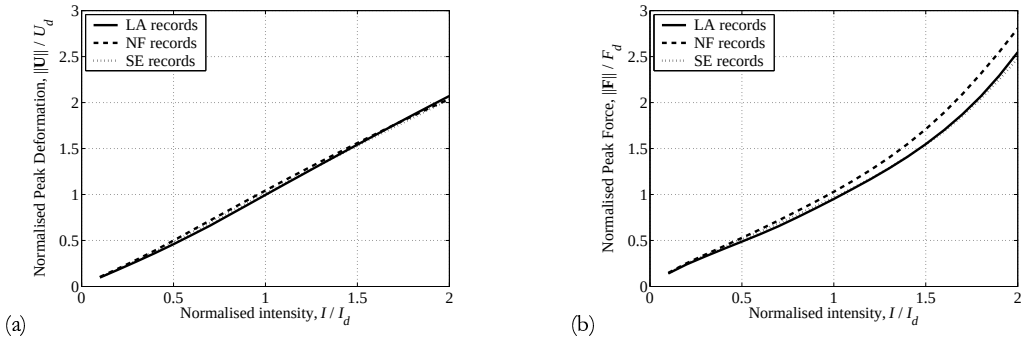

Figure 7.22. Configuration 2: Peak abutment bearing response, different ground motion suites. (a) Peak displacement, and (b) peak force. $\eta = 5.8$ (LA), $\eta = 3.8$ (SE), $\eta = 9.4$ (NF).

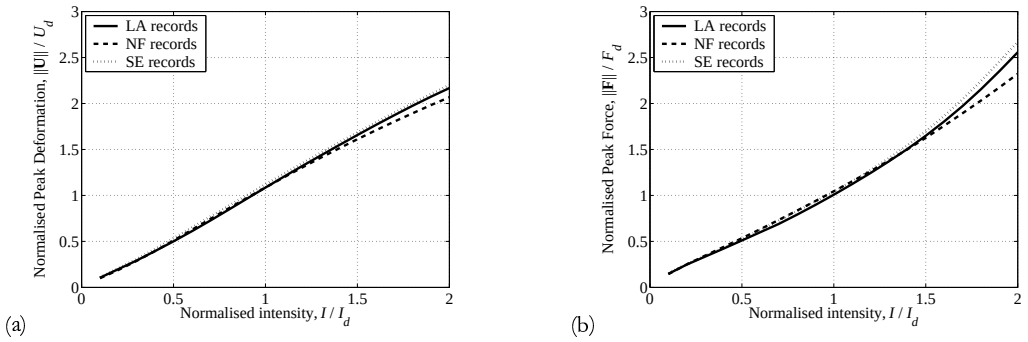

Figure 7.23. Configuration 2: Peak central bearing response, different ground motion suites. (a) Peak displacement, and (b) peak force. $\eta = 5.8$ (LA), $\eta = 3.8$ (SE), $\eta = 9.4$ (NF).

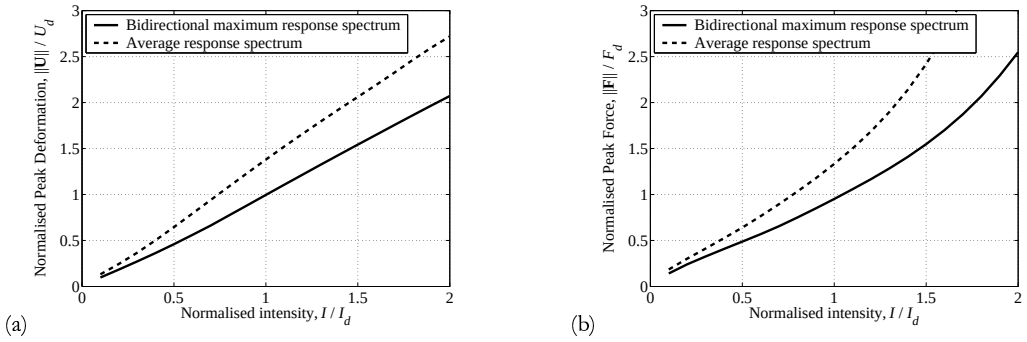

Figure 7.24. Configuration 2: Peak abutment bearing response, different types of design spectra. (a) Peak displacement, and (b) peak force. $\eta = 5.8$ (bidirectional), $\eta = 4.6$ (average).

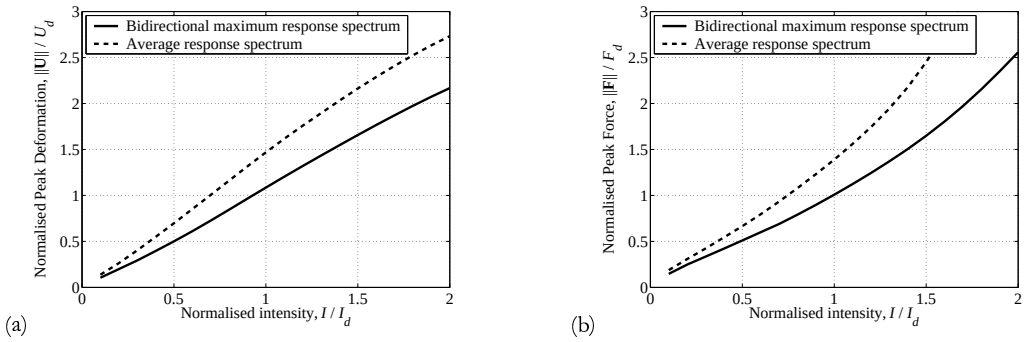

Figure 7.25. Configuration 2: Peak central bearing response, different types of design spectra. (a) Peak displacement, and (b) peak force. $\eta = 5.8$ (bidirectional), $\eta = 4.6$ (average).

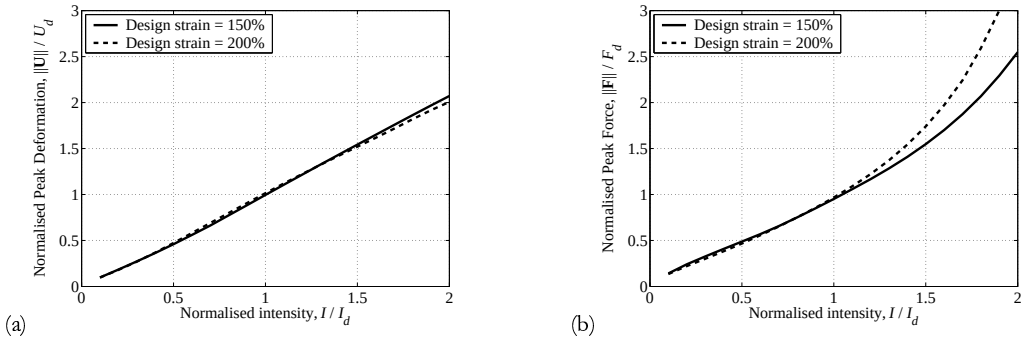

Figure 7.26. Configuration 2: Peak abutment bearing response, different design strains. (a) Peak displacement, and (b) peak force. $\eta = 5.8$ (150%), $\eta = 4.7$ (200%).

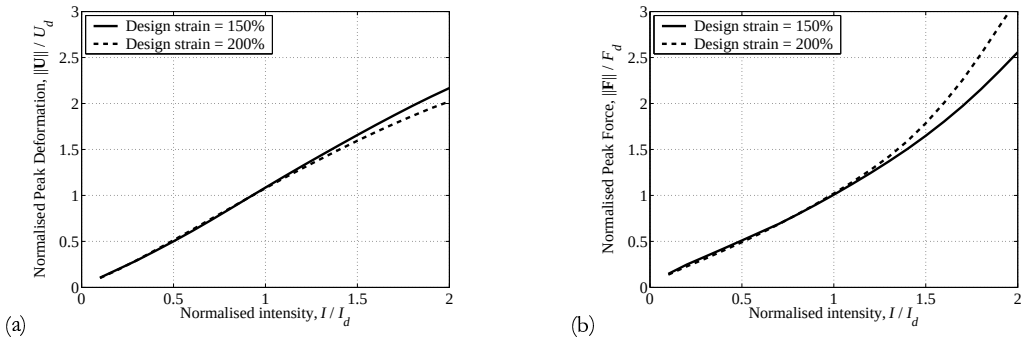

Figure 7.27. Configuration 2: Peak central bearing response, different design strains. (a) Peak displacement, and (b) peak force. $\eta = 5.8$ (150%), $\eta = 4.7$ (200%).

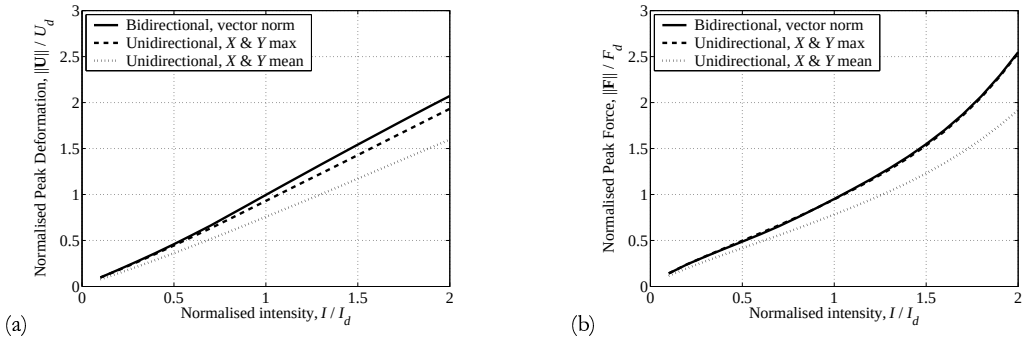

Figure 7.28. Configuration 2: Peak abutment bearing response, different bidirectional ground motion combination rules. (a) Peak displacement, and (b) peak force. $\eta = 5.8$.

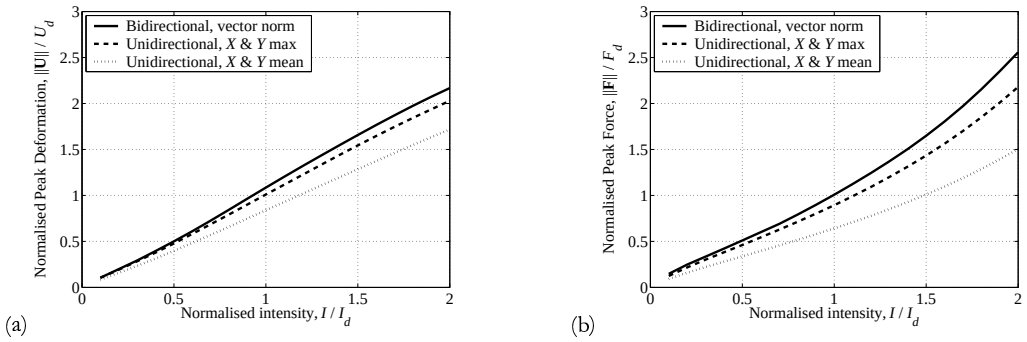

Figure 7.29. Configuration 2: Peak central bearing response, different bidirectional ground motion combination rules. (a) Peak displacement, and (b) peak force. $\eta = 5.8$.

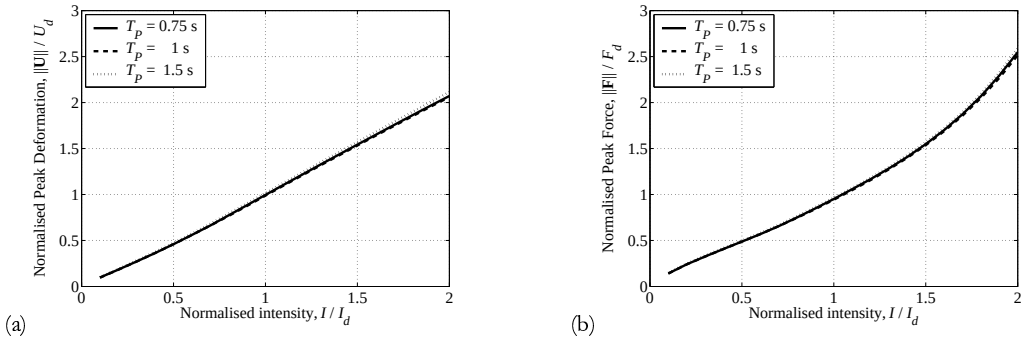

Figure 7.30. Configuration 2: Peak abutment bearing response, different unisolated pier periods. (a) Peak displacement, and (b) peak force. $\eta = 5.8$.

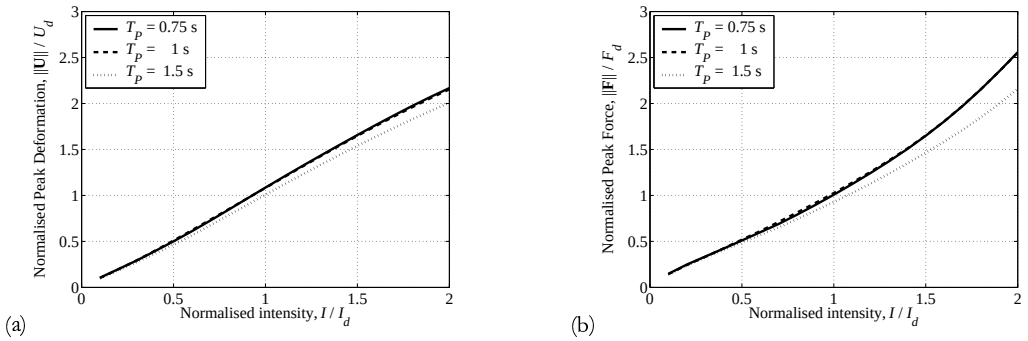

Figure 7.31. Configuration 2: Peak central bearing response, different unisolated pier periods. (a) Peak displacement, and (b) peak force. $\eta = 5.8$.

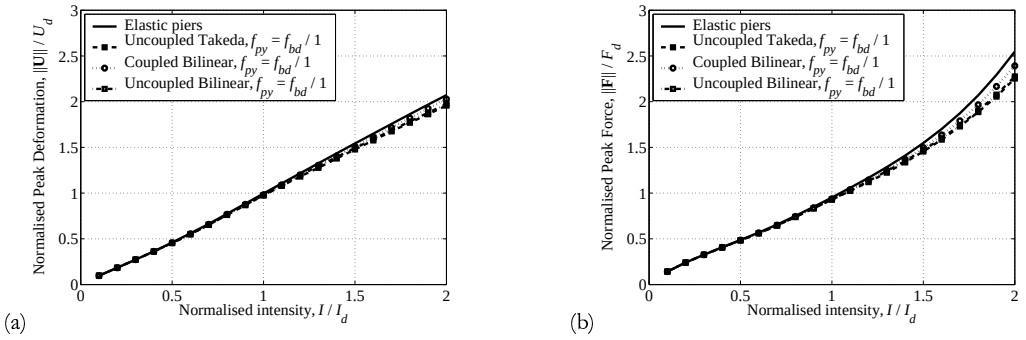

Figure 7.32. Configuration 2: Peak abutment bearing response, different nonlinear pier models. (a) Peak displacement, and (b) peak force. $\eta = 5.8$.

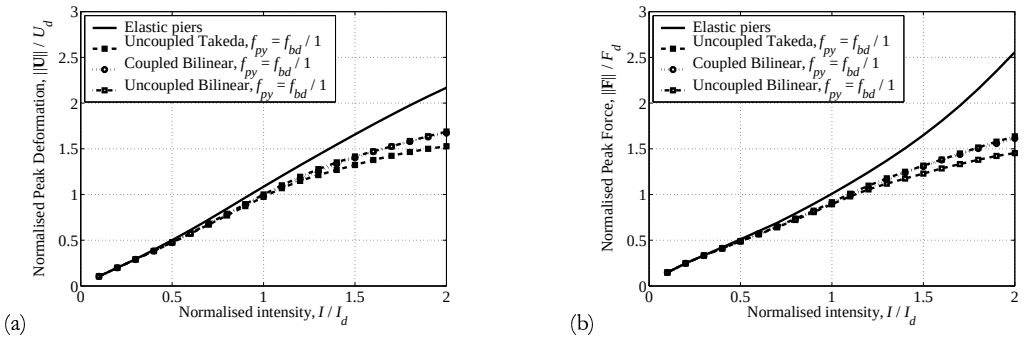

Figure 7.33. Configuration 2: Peak central bearing response, different nonlinear pier models. (a) Peak displacement, and (b) peak force. $\eta = 5.8$.

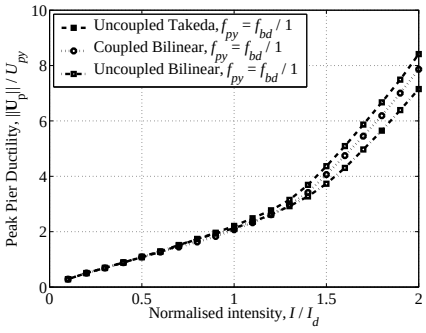

Figure 7.34. Configuration 2: Peak pier ductility, different nonlinear pier models. $\eta = 5.8$.

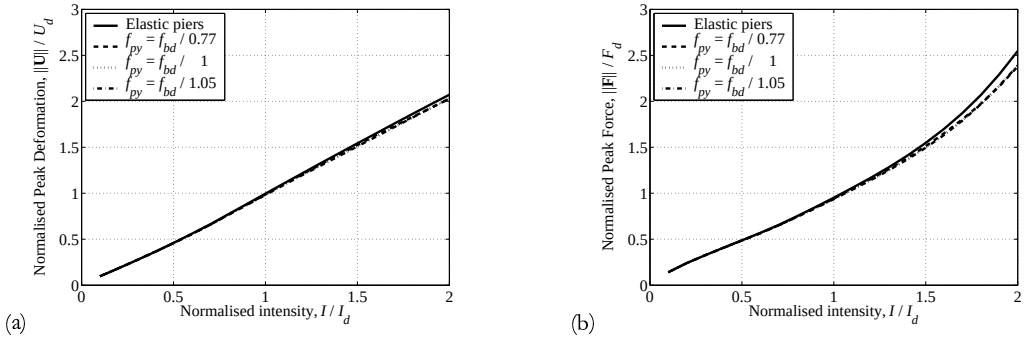

Figure 7.35. Configuration 2: Peak abutment bearing response, different pier yield forces. (a) Peak displacement, and (b) peak force. $\eta = 5.8$.

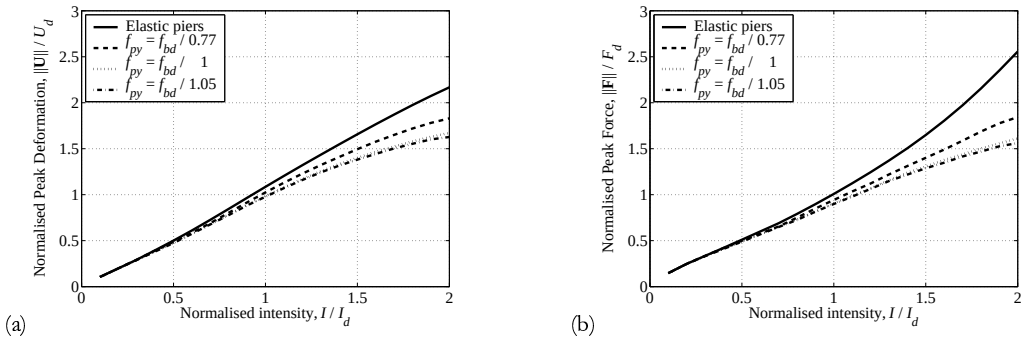

Figure 7.36. Configuration 2: Peak central bearing response, different pier yield forces. (a) Peak displacement, and (b) peak force. $\eta = 5.8$.

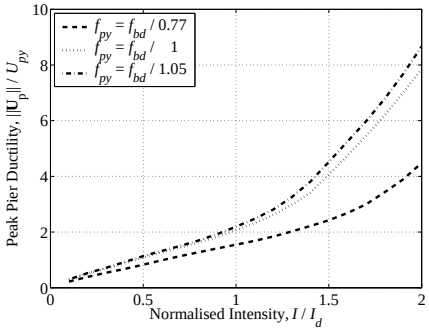

Figure 7.37. Configuration 2: Peak pier ductility, different pier yield forces. $\eta = 5.8$.

7.4 Configuration 3: Isolated Pier and Abutments, Flexible Superstructure

The parametric studies from the previous section were repeated for a bridge of Configuration 3, with a superstructure flexural stiffness, $EI_{ss} = 2 \times 10^7$ kNm^2, and span length, $L = 10$ m. This value is of the approximate order of magnitude for box girder bridge decks, although slab decks may be significantly more flexible. For a relatively stiff bridge deck, it may be possible to neglect the superstructure deformation and design for the same displacement in each abutment-isolator and pier-isolator system. This has been carried out in this section, by using exactly the same bearing and pier designs as in Section 7.3.

Figures 7.38 and 7.39 demonstrate that this design assumption is appropriate in this case. The normalised mean demand quantities for the abutment and central bearings are both approximately equal to 1.0 at the design level intensity. Furthermore, the results for other intensity levels are similar to Configurations 1 and 2, with slightly more scatter in the central pier force values at high intensities. Clearly, the superstructure deformation does not have a significant effect on bridge response for the stiffness value selected.

This observation also holds for the other parametric studies (Figs. 7.40–7.66). In addition to the bearing and pier demand quantities, average peak superstructure deformations for each set of analyses, normalised with respect to the abutment bearing design displacement, are shown (Figs. 7.42, 7.45, 7.48, 7.51, 7.54, 7.57, 7.60, 7.63(b), 7.66(b)). The superstructure deformation is equal to the total transverse displacement of the central deck, minus the transverse displacement of the deck at the displacements (i.e. rigid body displacement removed).

The response of different bearing types in terms of these response quantities is shown in Figs. 7.40–7.42. It can be observed that the difference between the HDR model and other bearing types is even more pronounced than in Configurations 1 and 2 (Figs. 7.5, 7.18 and 7.19). The HDR model behaviour is similar among the three configurations, but the bilinear models exhibit higher displacement and force demand in Configuration 3, particularly in the central bearing. In particular, the designs for the low friction FPS model and LR model with ultimate parameters are unconservative, and the central bearings are subjected to extreme normalised peak displacements at higher intensities. The reason for this extra demand can be observed in Fig. 7.42. For these bearing types, the superstructure displacement is higher than the other designs across the range of intensities, which implies greater deformation in the pier-isolator subsystem than in the abutment isolator. In these cases, the central bearing will probably reach the design displacement level before the abutment bearing, and should govern the design process. For abutment and central bearings of different sizes, it will be possible to provide a more regular design that minimises superstructure deformation.

Another parametric study that exhibited results that were significantly different from the other configurations was the ground motion suite sensitivity study (Figs. 7.46–7.48). Unlike Configurations 1 and 2, for which the response was relatively unaffected by the choice of ground motion suite, the difference in deck displacements observed among the three cases (Fig. 7.48) leads to significantly different demand on the central bearing. Specifically, the NF and SE suites result in lower and higher normalised superstructure displacements, respectively, with the corresponding effect on central bearing demand. Because response quantities are normalised by the respective demand values, this corresponds to conservatism and unconservatism in the design process for these suites, respectively. The results for the SE suite, for which the higher intensity values are representative of MCE demand, are particularly alarming, and it is apparent that the superstructure flexibility needs to be included in the structural model and equivalent linearisation, even for simple bridges of this nature. In this case, it is possible that the response spectra for the SE suite are of such a shape that a change in structural period due to the addition of superstructure flexibility leads to a significant increase in demand.

Figures 7.55–7.57 compare the results using unidirectional maximum or mean values to approximate the bidirectional demand. The maximum unidirectional value significantly underestimates the bidirectional response in this case, more so than the discrepancy observed for Configuration 2. Figure 7.57 shows that this is not due to a difference in superstructure deformation. In any case, this observation helps to confirm the hypothesis that the unidirectional maximum becomes increasingly inappropriate as the bridge configuration becomes more complex or irregular.

The introduction of inelasticity into pier response has a large effect on bearing and pier response quantities (Figs. 7.61–7.66). The central bearings experience an increased displacement and force demand compared to Configuration 2, especially for $I > I_d$ (Fig. 7.62). The effect of the hysteretic rule is approximately unchanged, but the normalised displacements and forces are up to around $0.15U_d$ and $0.35F_d$ greater than for the rigid deck case at an intensity of $I/I_d = 2$. Neither the abutment bearing response for all intensity levels, nor the central bearings for $I < I_d$ are affected significantly (Fig. 7.61–7.62).

The most significant difference between Configurations 2 and 3 with inelastic piers can be observed in Fig. 7.63(a) (cf. Fig. 7.34). The pier ductility demands for each hysteretic model are between 25% and 100% greater than the corresponding values from Configuration 2 at $I/I_d = 1$, and at least 35% greater at $I/I_d = 2$. Clearly, the increased demand in the central pier-isolator system due to the introduction of superstructure flexibility (Fig. 7.63(b)) is accommodated entirely in inelastic deformation of the pier. This is consistent with the observation of the AASHTO provisions [AASHTO, 1999] that, for low post-yield stiffness of the pier, additional deformation beyond pier yielding will be carried almost entirely in the pier. This highlights the need to restrict pier yielding at design level, and suggests that the reduction factors adopted by the code [AASHTO, 1999] may be

too low if higher performance levels are not specifically addressed.

Similar observations can be made from Figs. 7.64–7.66, which show the results for different response modification factors, as for the previous configurations. Central bearing (Fig. 7.65) and pier demands (Fig. 7.66(a)) are increased by the introduction of superstructure flexibility (Fig. 7.66(b)), while abutment bearing demand is not increased significantly (Fig. 7.64). It can be observed that the multiple performance level design process, which did not take into account superstructure flexibility, was unconservative for the pier ductility target of 4.0 at $I/I_d = 1.5$ and 2.0. The ductility performance targets were exceeded by approximately 90% in each case, while for Configuration 2 the overestimation was less than 10%. It is apparent that the inclusion of superstructure flexibility in the design process is essential, at least for the superstructure stiffness considered here.

To investigate the dependence of response quantities on the superstructure stiffness, a further sensitivity study was conducted with EI_{ss} values one order of magnitude above, and up to two orders of magnitude below, the original value selected. Elastic pier behaviour, with the same properties used earlier, was assumed. The results from these studies are shown in Figs. 7.67–7.69. It is interesting to observe that, although the superstructure deformation reduced significantly by decreasing EI_{ss} from 2×10^7 to 2×10^8 kNm^2, the bearing response quantities are not affected significantly. This suggests that stiffness of this magnitude may be considered essentially rigid for elastic pier response. The observations of the previous paragraphs, however, suggest that this is not the case with inelastic piers.

Decreasing the stiffness of the superstructure, the abutment bearing demand reduces, and central bearing demand increases. For a value of around $EI_{ss} = 2 \times 10^5$ kNm^2, the bearing responses are essentially uncoupled, and the assumption of an infinitely flexible superstructure is not unwarranted. Note that because the response quantities are normalised with respect to the rigid deck design values, the lines on Figs. 7.67 and 7.68 do not converge to the same value – instead the ratio of the latter to the former is given by the ratio of design displacements for the abutment and central bearings. In this case, the ratio is approximately 1.7.

From the superstructure sensitivity study, two further observations can be made. Firstly, the difference in behaviour from 2×10^6 to 2×10^7 kNm^2 flexural stiffness is particularly marked, which represents a transition from flexible to stiff deck behaviour. Secondly, the stiffness values used here must also be related to the span length of 10 m, and conclusions will only be appropriate for other spans by adjusting for the effective stiffness of the deck in Eq. (7.3).

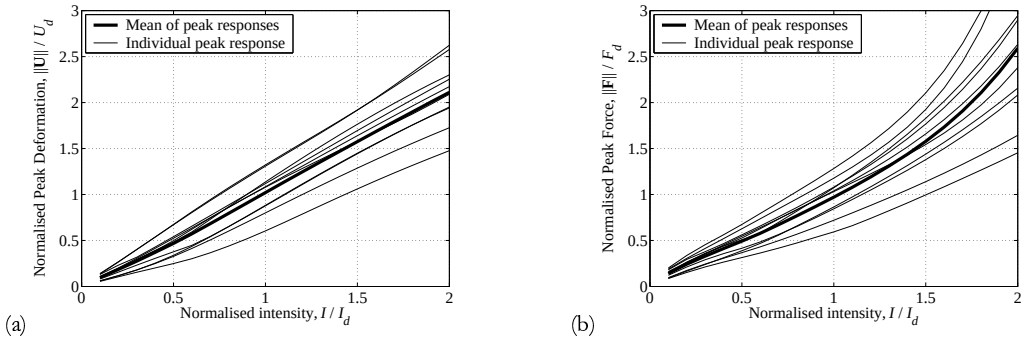

Figure 7.38. Configuration 3: Peak abutment bearing response, all records and mean. (a) Peak displacement, and (b) peak force. $\eta = 5.8$.

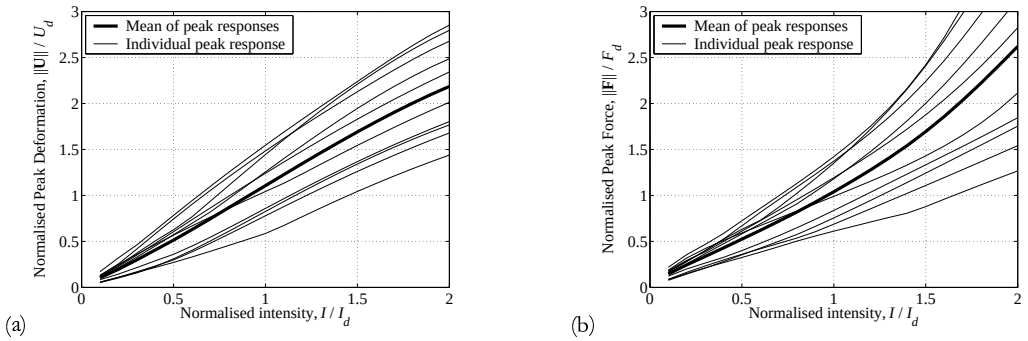

Figure 7.39. Configuration 3: Peak central bearing response, all records and mean. (a) Peak displacement, and (b) peak force. $\eta = 5.8$.

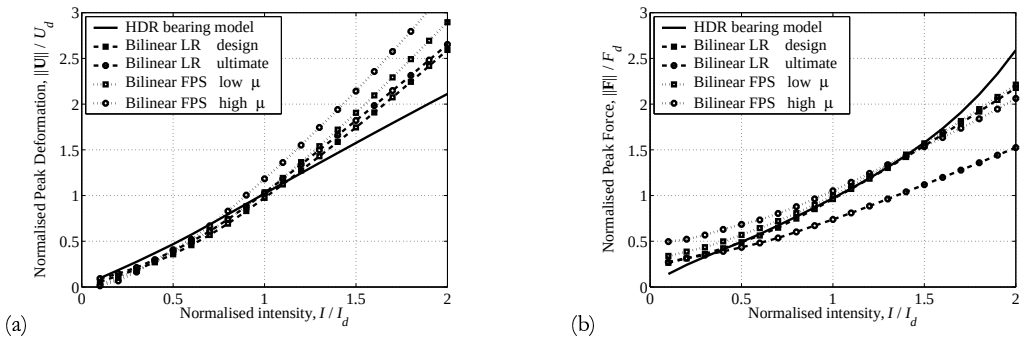

Figure 7.40. Configuration 3: Peak abutment bearing response, different bearing models. (a) Peak displacement, and (b) peak force. $\eta = 5.8$ (HDR), $\eta = 4.4$ (LR), $R = 2.4$ and 1.6m (FPS, low and high friction).

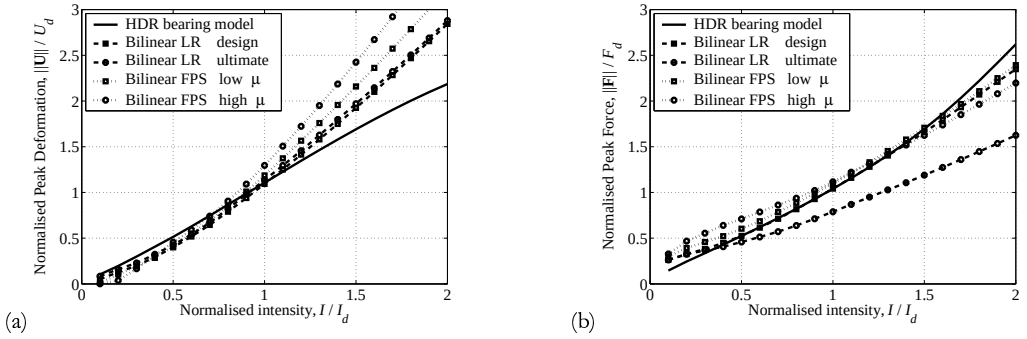

Figure 7.41. Configuration 3: Peak central bearing response, different bearing models. (a) Peak displacement, and (b) peak force. $\eta = 5.8$ (HDR), $\eta = 4.4$ (LR), $R = 2.4$ and 1.6m (FPS, low and high friction).

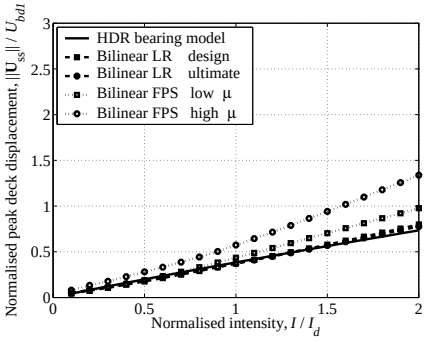

Figure 7.42. Configuration 3: Peak superstructural deformation, different bearing models. $\eta = 5.8$ (HDR), $\eta = 4.4$ (LR), $R = 2.4$ and 1.6m (FPS, low and high friction).

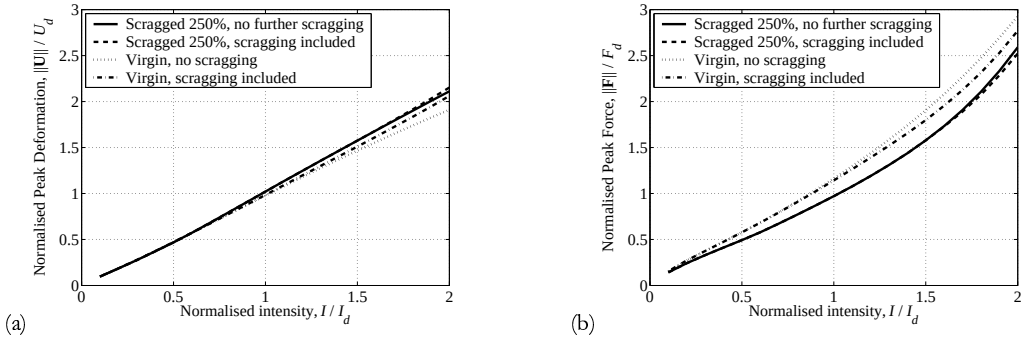

Figure 7.43. Configuration 3: Peak abutment bearing response, different models of scragging. (a) Peak displacement, and (b) peak force. $\eta = 5.8$.

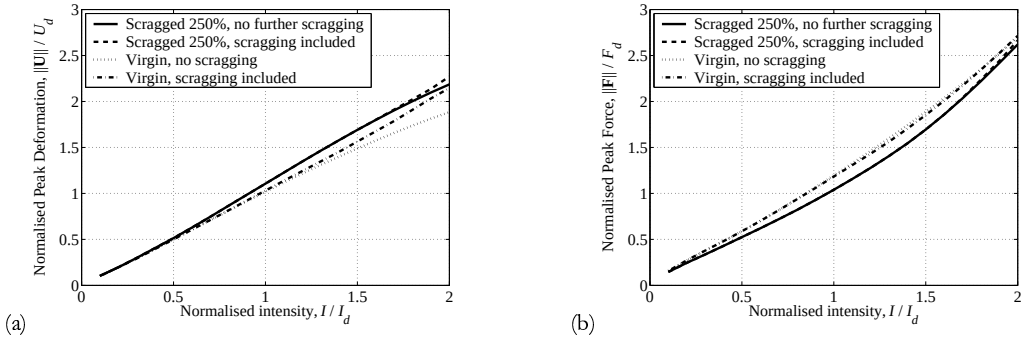

Figure 7.44. Configuration 3: Peak central bearing response, different models of scragging. (a) Peak displacement, and (b) peak force. $\eta = 5.8$.

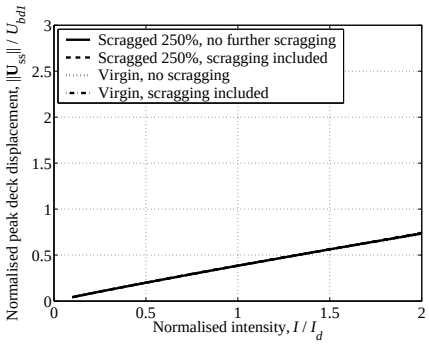

Figure 7.45. Configuration 3: Peak superstructural deformation, different models of scragging. $\eta = 5.8$.

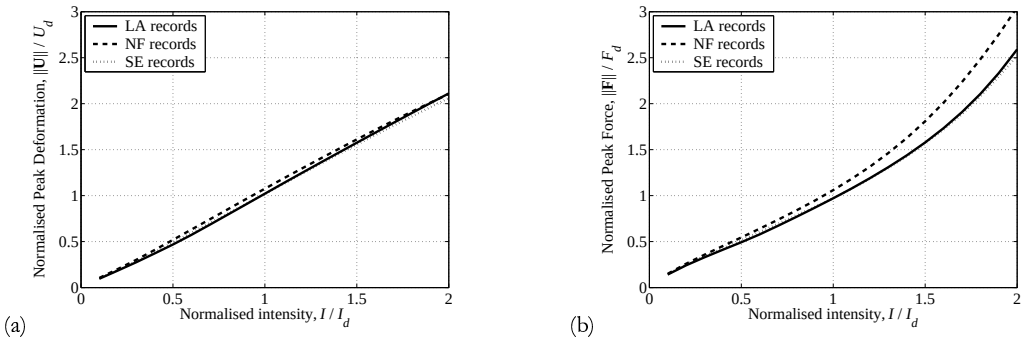

Figure 7.46. Configuration 3: Peak abutment bearing response, different ground motion suites. (a) Peak displacement, and (b) peak force. $\eta = 5.8$ (LA), $\eta = 3.8$ (SE), $\eta = 9.4$ (NF).

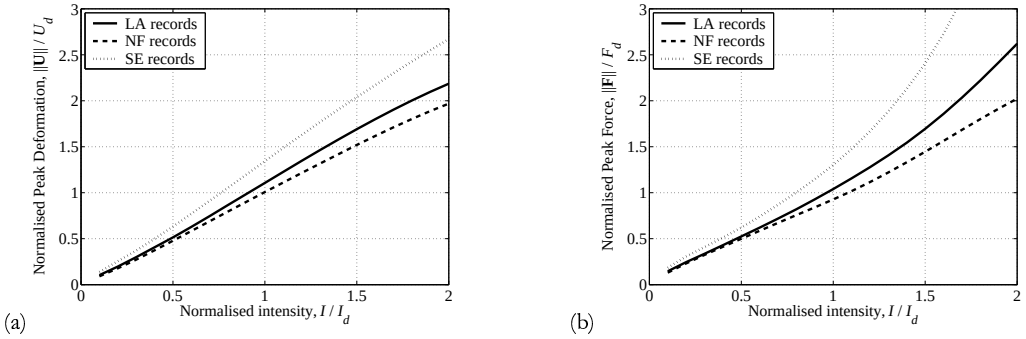

Figure 7.47. Configuration 3: Peak central bearing response, different ground motion suites. (a) Peak displacement, and (b) peak force. $\eta = 5.8$ (LA), $\eta = 3.8$ (SE), $\eta = 9.4$ (NF).

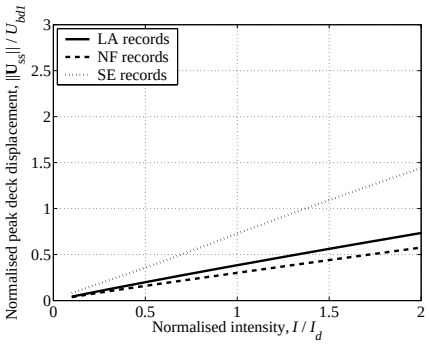

Figure 7.48. Configuration 3: Peak superstructural deformation, different ground motion suites. $\eta = 5.8$ (LA), $\eta = 3.8$ (SE), $\eta = 9.4$ (NF).

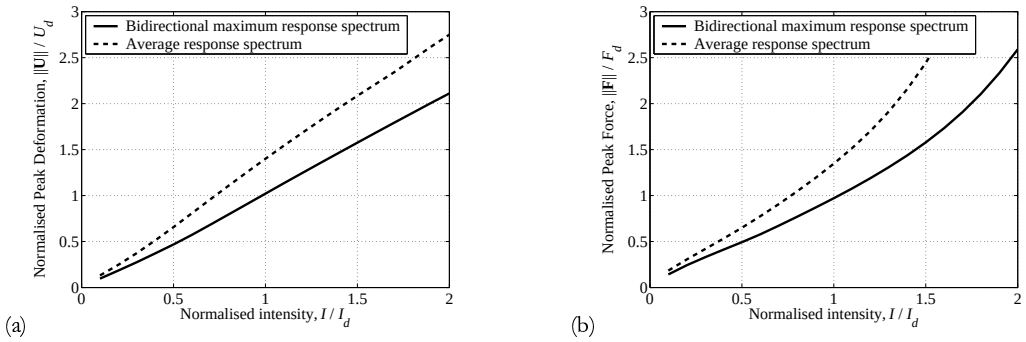

Figure 7.49. Configuration 3: Peak abutment bearing response, different types of design spectra. (a) Peak displacement, and (b) peak force. $\eta = 5.8$ (bidirectional), $\eta = 4.6$ (average)..

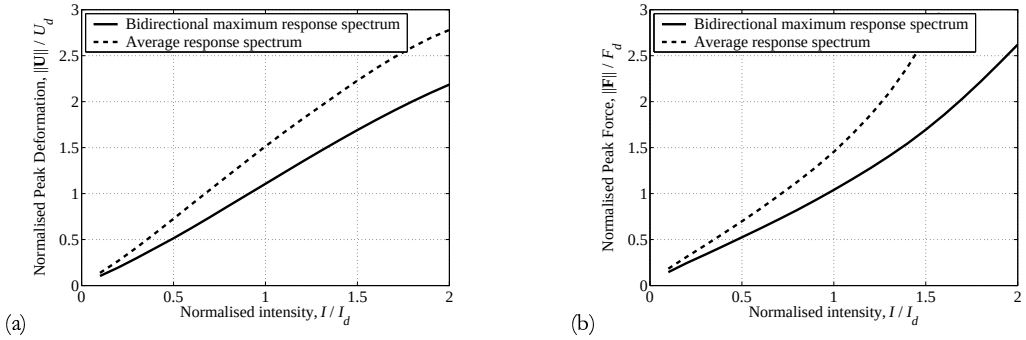

Figure 7.50. Configuration 3: Peak central bearing response, different types of design spectra. (a) Peak displacement, and (b) peak force. $\eta = 5.8$ (bidirectional), $\eta = 4.6$ (average).

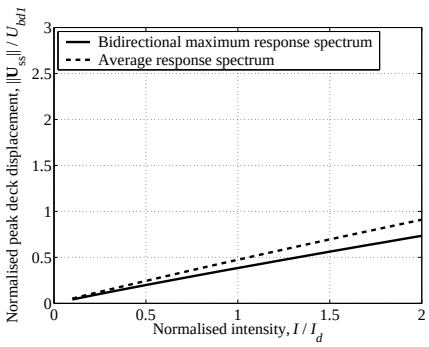

Figure 7.51. Configuration 3: Peak superstructural deformation, different types of design spectra. $\eta = 5.8$ (bidirectional), $\eta = 4.6$ (average).

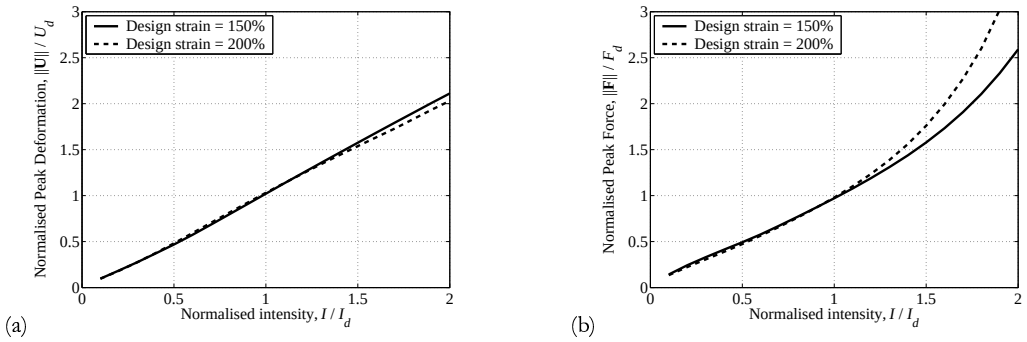

Figure 7.52. Configuration 3: Peak abutment bearing response, different design strains. (a) Peak displacement, and (b) peak force. $\eta = 5.8$ (150%), $\eta = 4.7$ (200%).

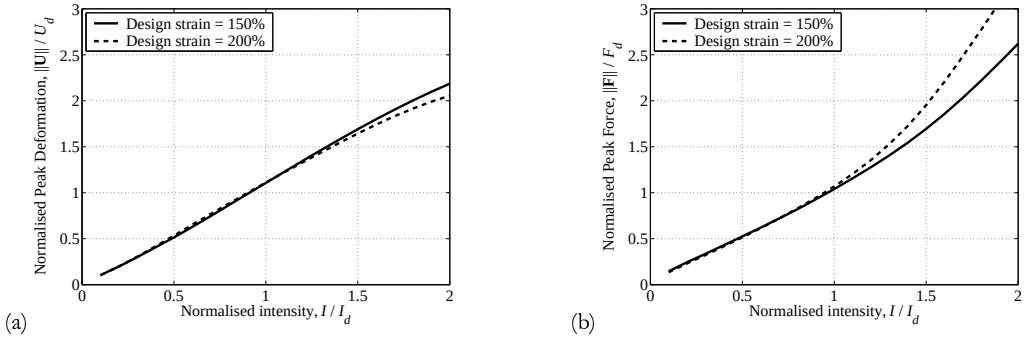

Figure 7.53. Configuration 3: Peak central bearing response, different design strains. (a) Peak displacement, and (b) peak force. $\eta = 5.8$ (150%), $\eta = 4.7$ (200%).

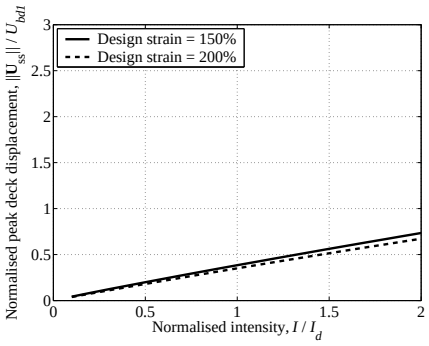

Figure 7.54. Configuration 3: Peak superstructural deformation, different design strains. $\eta = 5.8$ (150%), $\eta = 4.7$ (200%).

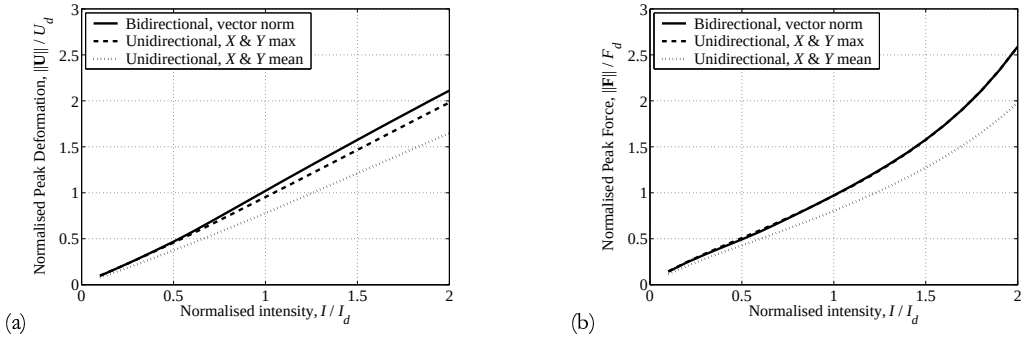

Figure 7.55. Configuration 3: Peak abutment bearing response, different bidirectional ground motion combination rules. (a) Peak displacement, and (b) peak force. $\eta = 5.8$.

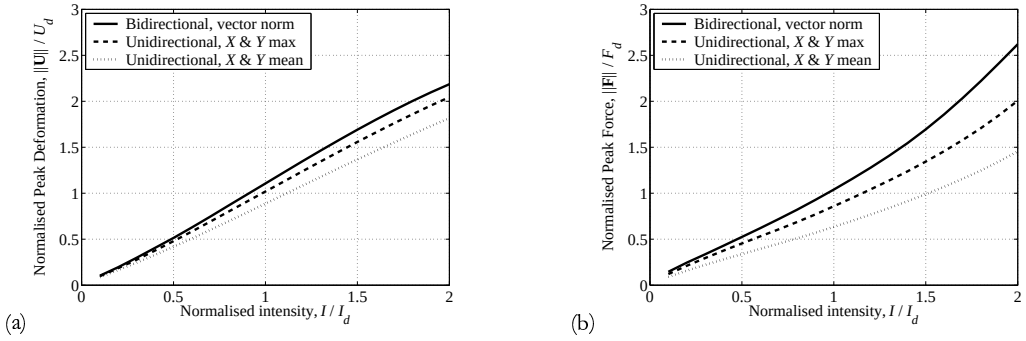

Figure 7.56. Configuration 3: Peak central bearing response, different bidirectional ground motion combination rules. (a) Peak displacement, and (b) peak force. $\eta = 5.8$.

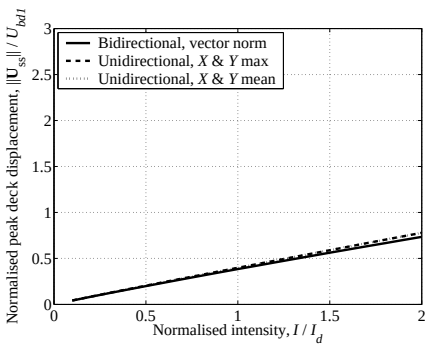

Figure 7.57. Configuration 3: Peak superstructural deformation, bidirectional ground motion combination rules. $\eta = 5.8$.

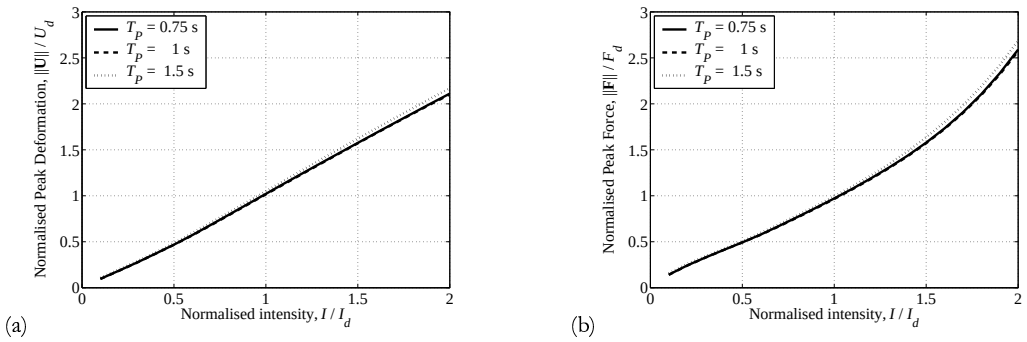

Figure 7.58. Configuration 3: Peak abutment bearing response, different unisolated pier periods. (a) Peak displacement, and (b) peak force. $\eta = 5.8$.

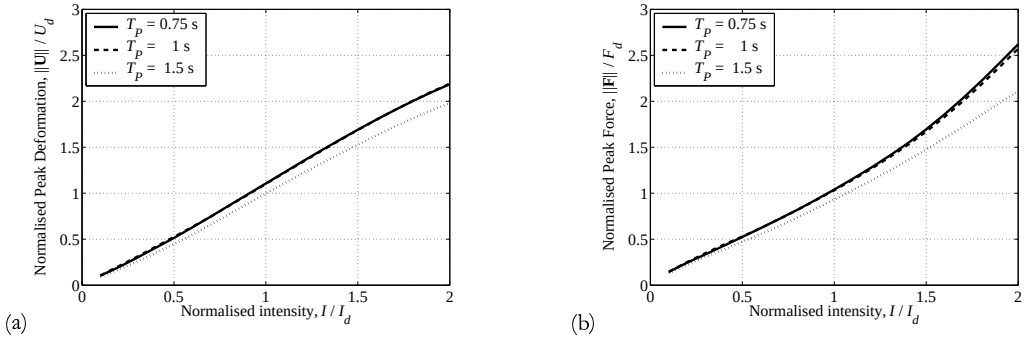

Figure 7.59. Configuration 3: Peak central bearing response, different unisolated pier periods. (a) Peak displacement, and (b) peak force. $\eta = 5.8$.

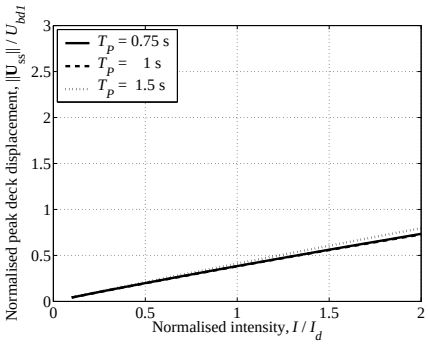

Figure 7.60. Configuration 3: Peak superstructural deformation, different unisolated pier periods. $\eta = 5.8$.

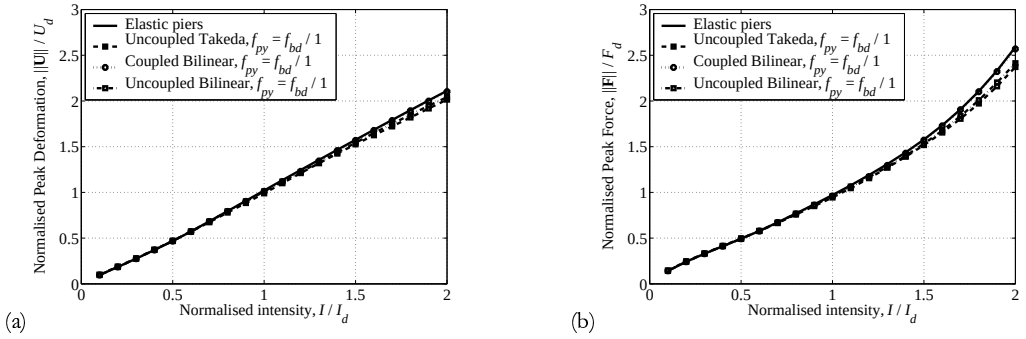

Figure 7.61. Configuration 3: Peak abutment bearing response, different nonlinear pier models. (a) Peak displacement, and (b) peak force. $\eta = 5.8$.

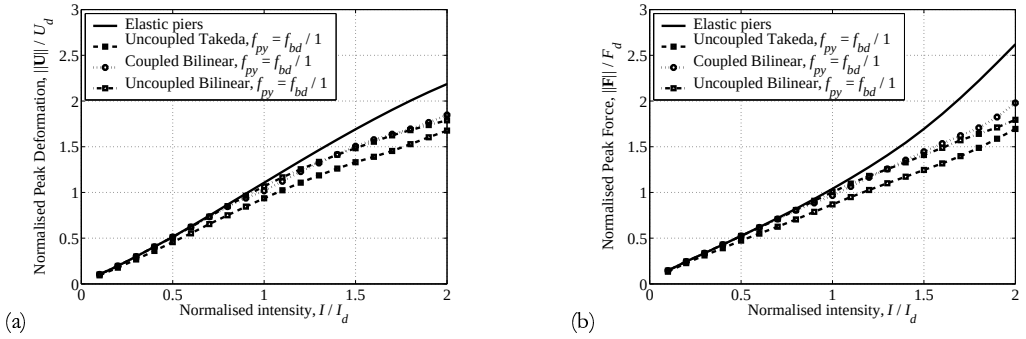

Figure 7.62. Configuration 3: Peak central bearing response, different nonlinear pier models. (a) Peak displacement, and (b) peak force. $\eta = 5.8$.

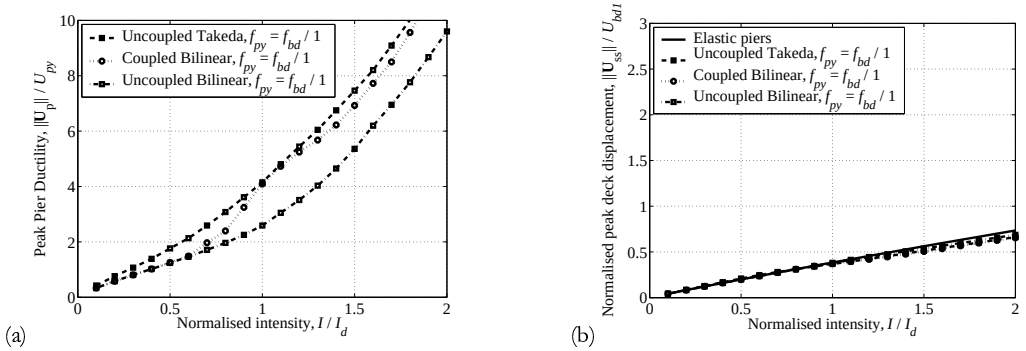

Figure 7.63. Configuration 3: (a) Peak pier ductility, and (b) peak superstructural deformation; different nonlinear pier models. $\eta = 5.8$.

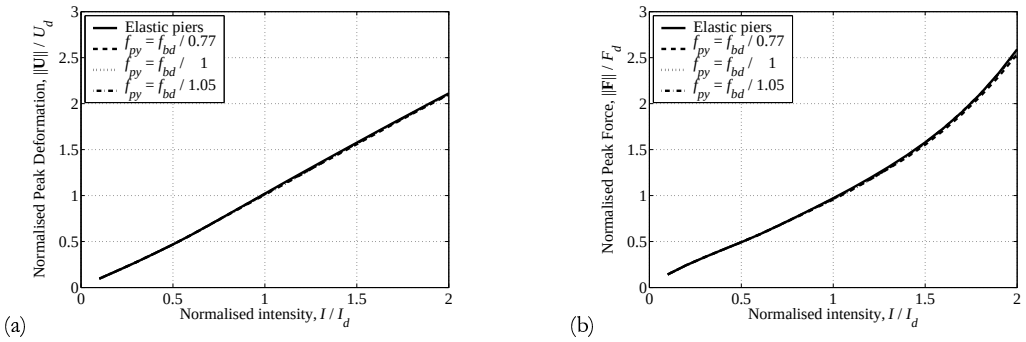

Figure 7.64. Configuration 3: Peak abutment bearing response, different pier yield forces. (a) Peak displacement, and (b) peak force. $\eta = 5.8$.

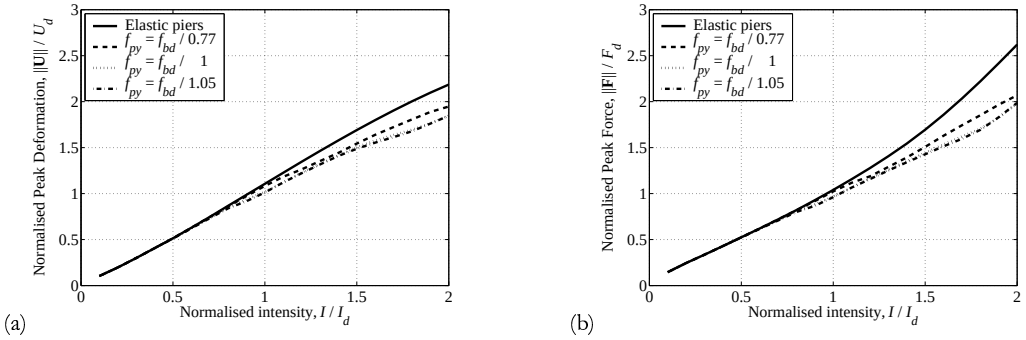

Figure 7.65. Configuration 3: Peak central bearing response, different pier yield forces. (a) Peak displacement, and (b) peak force. $\eta = 5.8$.

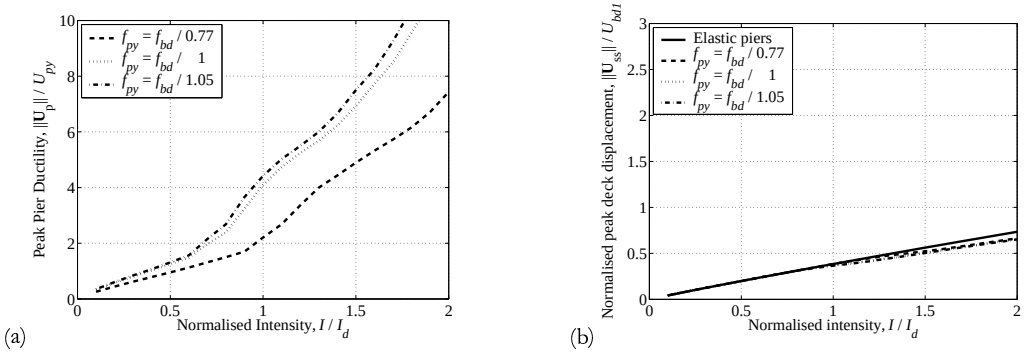

Figure 7.66. Configuration 3: (a) Peak pier ductility, and (b) peak superstructural deformation; different pier yield forces. $\eta = 5.8$.

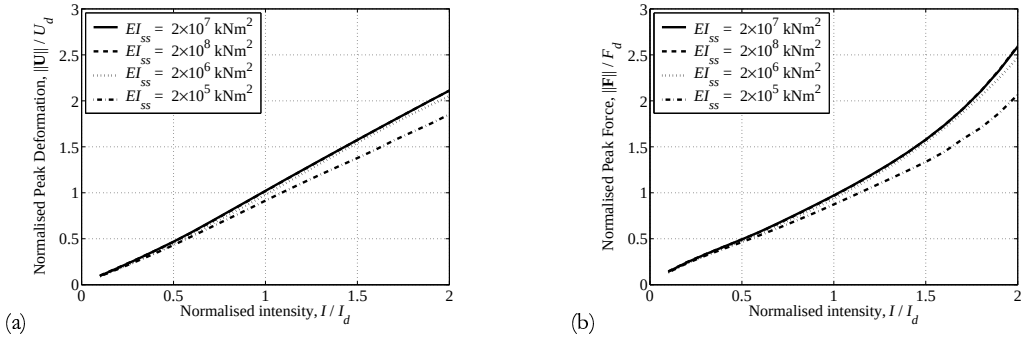

Figure 7.67. Configuration 3: Peak abutment bearing response, different superstructure stiffness. (a) Peak displacement, and (b) peak force. $\eta = 5.8$.

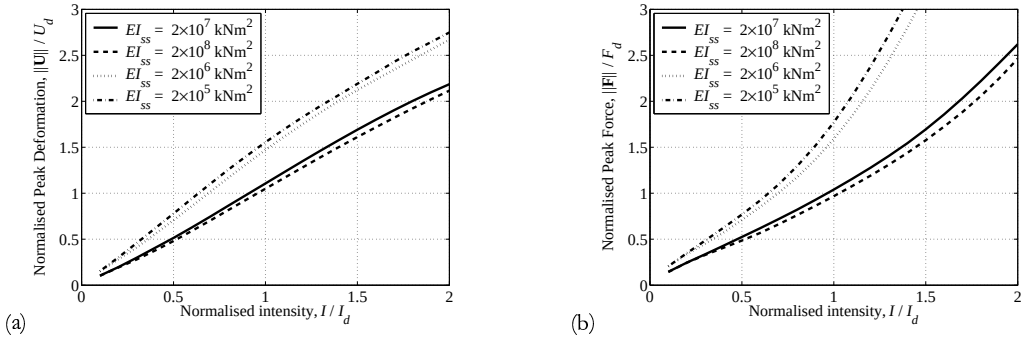

Figure 7.68. Configuration 3: Peak central bearing response, different superstructure stiffness. (a) Peak displacement, and (b) peak force. $\eta = 5.8$.

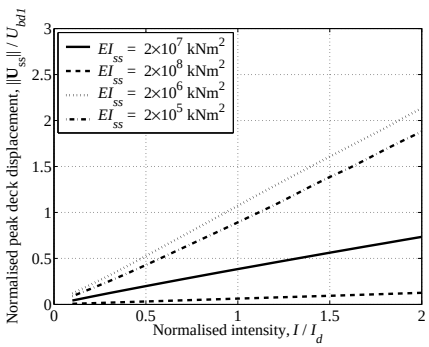

Figure 7.69. Configuration 3: Peak superstructural deformation, different superstructure stiffness. $\eta = 5.8$.

8. CONCLUSIONS

8.1 Modelling of Bidirectional Response of High-damping Rubber Bearings

The behaviour of high-damping rubber bearings is complex, even in a unidirectional setting. HDR bearing response is characterised by stiffening behaviour at high strain levels, nonlinear damping, and degradation of stiffness and damping over successive cycles of loading. Current models for unidirectional response suffer from several major limitations and are difficult to extend to general, bidirectional load paths. To the author's knowledge, no phenomenological models have been developed specifically for the bidirectional response of HDR bearings. Some developments based on classical plasticity theory were discussed here, although they were unable to describe the experimental response with any accuracy.

For this reason, a new phenomenological model has been developed to describe the bidirectional shear force–deformation response of HDR bearings. Key features of the model are:

- An additive decomposition of the force vector into components parallel to the displacement vector and velocity vector.
- An elastic force defined by an odd, fifth order polynomial in the shear displacement, motivated by a generalised Mooney–Rivlin free energy equation.
- A nonlinear damping envelope, with general hysteretic response defined within this envelope by an approach similar to bounding surface plasticity.
- Degradation of bearing stiffness and damping due to both long-term scragging degradation, and short-term Mullins' effect.

A calibration procedure was also developed in order to obtain a unique set of material parameters for a given bearing. Calibration of the model was carried out over a series of tests, with appropriate damage parameters retained between tests to model the degradation of the bearing over the entire

test programme. The calibrated model response provided an excellent match of stiffness, damping and degradation characteristics of the bearing behaviour for slow strain rate tests.

Although an extension of the model was proposed, the model was not able to accurately describe the rate-dependence of HDR bearings. The high strain rate tests included in the Caltrans Seismic Protective Systems Project were limited to one displacement orbit, which generally resulted in an increase of up to 30% in the total force vector over the slower tests. However, for this orbit the prediction of the model already overestimated the observed response, and the calibration of rate-dependent parameters would not be effective. Further research needs to be conducted to ascertain whether the strain-rate dependent component is able to predict the earthquake response of HDR bearings from slow strain rate tests.

In order to make use of the model in dynamic analysis of full-scale HDR bearings, a practical calibration procedure must be developed. It was suggested that unidirectional testing at various strain magnitudes, up to the peak bidirectional excursions used here (350%), would be sufficient. In any case, such a calibration protocol would need to address the possibility of axial load and temperature dependence of HDR bearing behaviour, in addition to the strain rate effects discussed above.

The proposed model effectively describes the bidirectional shear force–deformation response of a HDR bearing. The model can be used to help understand the importance of material nonlinearity, bidirectional behaviour and cyclic degradation of HDR bearings on the system response of seismically-isolated structures under strong ground motion.

8.2 Analysis and Design of Isolated Bridges

The analysis and design of isolated bridges, with particular emphasis on the consideration of bidirectional demand and response, the equivalent linearisation of structural properties, and displacement-based design methodologies were summarised. Some results and recommendations are discussed below.

The treatment of viscous damping in analysis and design is a problem not only for isolated bridges, but for all dynamic structural analysis. For design based on an equivalent linearisation of bearing and pier properties, it was shown to be important to adjust the level of viscous damping according to the assumed hysteresis and damping models, and the target ductility level. Expressions were given for the corrected viscous damping component for bilinear and modified Takeda hysteresis models, based on a some simple models for the viscous damping coefficient, consistent with those specified for multiple degree-of-freedom systems. The correction factors, however, were derived based on the response of single degree-of-freedom systems, and their use in multiple degree-of-freedom analyses

requires further investigation.

The assessment of bidirectional earthquake demand and structural response was discussed. In dynamic analysis of structures for which the bidirectional response is required, time history analysis is often carried out with the simultaneous application of a pair of ground motions in orthogonal directions. These ground motions are usually scaled to a code spectrum that is representative of hazard in a given area. In cases where the uniform hazard spectra are derived from a probabilistic seismic hazard assessment that considers a random ground motion component, it was recommended that the average of the two components should be amplitude scaled to the code spectrum, rather than the SRSS combination suggested by the AASHTO Guide Specifications for Seismic Isolation Design [AASHTO, 1999]. Alternatively, it was suggested that a bidirectional response spectrum defined by the maximum vector response of a single degree-of-freedom oscillator to two components of ground motion, could be used to give a more exact measure of seismic demand.

The evaluation of bidirectional demand in design is often carried out by combining unidirectional response quantities with an appropriately defined combination rule. Simple rules such as the "30%-rule" are often specified by design codes. More rigorously, peak response quantities resulting from three directions of simultaneous earthquake input can be obtained from the CQC3 combination rule, for a given orientation of horizontal components. It was suggested that the practice of taking the maximum of all possible orientations when using the CQC3 approach is not only overly conservative, but is also inconsistent with the level of hazard presented in the code spectrum. Instead, the expected value of a response quantity over all orientations should be used for design.

Existing design methods for isolated bridges target elastic pier response at design level hazard. This is achieved by specifying pier yield forces greater than the bearing design forces, by a factor equal to the inverse of a response modification factor, R. The design methods differ, however, in the value specified for R, and there is little consideration of bridge response for ground motion intensity in excess of the design level intensity. A design methodology was presented here as an extension of existing displacement-based design methods, that explicitly considers the performance of the structure at two hazard levels. This could be particularly important for HDR bearings, which may exhibit stiffening behaviour at strains greater than the design strain.

The design method is based on linearisation of bearing and pier properties at two different levels of response, corresponding to design and maximum credible seismic hazard. Performance goals are defined to prevent pier yielding at the design hazard level, and to limit pier ductility at the maximum credible level, while also limiting bearing strains to specified limits. A simple iterative algorithm was proposed to assign bearing and pier properties based on these design goals.

8.3 Parametric Studies of Isolated Bridges

Parametric studies of a number of simple isolated bridge configurations were presented. The studies investigated the response of isolated structures for a range of ground motion scaling factors, to represent different levels of earthquake hazard.

The first bridge configuration considered a simple pier-isolator system, to represent a bridge with no superstructure coupling. It was shown that the stiffening behaviour of HDR bearings is effective at reducing the displacement demand on bearings at high earthquake intensity levels, when compared with softening systems such as LR and FPS bearings. The trade-off is that the pier forces may be significantly higher, particularly when compared with a bilinear model calibrated for ultimate level LR bearing response. Designers of isolated bridges should be aware of the possibility of excessively large pier forces for extreme ground motions.

Although allowed for in the mathematical model, degradation of bearing properties was shown to have little impact on structural response over a range of intensity levels. Bridge response quantities were also relatively insensitive to the elastic pier stiffness, when pier inelasticity was not included in the analysis, which justified the assumption that pier stiffness was independent of yield strength. Bearing yield strain assumed in the design process also had little effect on normalised bearing displacements, but the assumption of 200% design strain was shown to lead to excessively large elastic pier forces. It was suggested that 150% strain is a more appropriate design limit, at least for the Bridgestone bearings considered in this thesis.

Pier inelasticity was also modelled in the parametric studies to more accurately describe structural response under ground motion exceeding design level. Two uncoupled Takeda models were considered in orthogonal directions, and compared with coupled and uncoupled bilinear models. The difference between the latter two models was generally less than 10–15%, which suggests that the use of an uncoupled Takeda model, which cannot be extended to bidirectional response but provides a good description of reinforced concrete behaviour in unidirectional loading, was adequate.

The yield strength of the pier was also varied, assuming two designs carried out according to the multiple performance level method described herein. It was shown that the proposed method achieved the design goals adequately, and provides an improvement over existing methods in which higher levels of earthquake hazard are not explicitly considered. The pier yield strength should also be adjusted for design purposes by a factor of 1.15 to ensure elastic pier behaviour at the design level under a 10% variation in bearing properties, in common with the capacity design philosophy of Priestley *et al.* [1996].

These conclusions did not change significantly when more complicated bridge geometries were

considered. Because identical bearings were considered at the abutments and piers, pier yielding reduced the response of the latter without affecting the response of the former significantly. For real bridge design, it will be more appropriate to design abutment bearings with the same design stiffness as the series combination of the pier and bearing stiffness. The multiple performance level design approach could also be extended to consider different bearing sizes with similar performance goals.

The introduction of superstructure flexibility to the system had a large effect on bearing and pier response. A range of superstructure stiffness values was considered, with limits corresponding to fully coupled and uncoupled bearings. The multiple performance level design procedure did not perform adequately in this case, although the design was carried out for the original bridge configuration, and did not include superstructure flexibility. The performance of the design method could be improved by extending the procedure to more complicated geometries, although the simplicity of the expressions for bearing thickness and pier yield force would be sacrificed, and more iteration would be required.

8.4 Areas for Future Research

Although the proposed model was able to describe the slow strain behaviour of HDR bearings accurately, strain rate effects were not included in the model. It would be desirable to add rate-dependence to the model, to allow the accurate dynamic analysis of bearings calibrated for slow strain data.

The multiple performance level design method did not allow for superstructure flexibility, or irregular distributions of pier and bearing stiffness. The results of studies such as Alvarez-Botero [2004], which considers appropriate deflected shapes for bridge superstructures, could be used to extend the method to include coupling of the superstructure and pier response.

Finally, the parametric studies performed in this thesis were limited to simple bridge geometries, and simple hysteresis models for nonlinear pier response. More complicated geometries, including more spans with regular or irregular distributions of pier stiffness, could be considered, along with a more accurate representation of pier nonlinearity.

REFERENCES

Alfawakhiri, F. and Bruneau, M. [2000] "Flexibility of superstructures and supports in the seismic analysis of simple bridges," *Earthquake Engineering and Structural Dynamics*, Vol. 29, pp. 711–729.

Alvarez-Botero, J. C. [2004] "Displacement-based design of continuous concrete bridges under transverse seismic excitation," Master's thesis, European School for Advanced Studies in Reduction of Seismic Risk (ROSE School), Pavia, Italy.

American Society of State Highway and Transit Officials (AASHTO) [1999] *Guide Specifications for Seismic Isolation Design*, Washington, D.C.

Anastassiadis, K., Avramidis, I. E., and Panetsos, P. K. [1998] "Earthquake resistant design of structures under three-component orthotropic seismic excitation," *Proceedings of the 11th European Conference on Earthquake Engineering*, Paris.

Arruda, E. M. and Boyce, M. C. [1993] "A three-dimensional consitutive model for the large stretch behavior of rubber elastic materials," *Journal of the Mechanics of Physics and Solids*, Vol. 41, No. 2, pp. 389–412.

Bergström, J. S. and Boyce, M. C. [1998] "Constitutive modeling of the large strain time-dependent behavior of elastomers," *Journal of the Mechanics of Physics and Solids*, Vol. 46, pp. 931–954.

Blandon, C. [2004] "Equivalent viscous damping in direct displacement-based design," Master's thesis, European School for Advanced Studies in Reduction of Seismic Risk (ROSE School), Pavia, Italy.

Bommer, J. J. and Acevedo, A. B. [2004] "The use of real earthquake accelerograms as input to dynamic analysis," *Journal of Earthquake Engineering*, Vol. 8, No. Special Issue 1, pp. 43–91.

Bonet, J. and Wood, R. [1997] *Nonlinear Continuum Mechanics for Finite Element Analysis*, Cambridge University Press.

Bouc, R. [1967] "Forced vibration of mechanical system with hysteresis," *Proceedings of Fourth Conference on Nonlinear Oscillation*, Prague, Czechoslovakia.

Bridgestone Corporation [1994] *Rubber Compound & Base Isolator Design Information.*

Bueche, F. [1960] "Molecular basis of the Mullins' effect," *Journal of Applied Polymer Science*, Vol. 4, No. 10, pp. 107–114.

Building Seismic Safety Council [1997] *FEMA 273/274: NEHRP Recommended Provisions for Seismic Regulations for New Buildings.*

Calvi, G. M. and Pavese, A. [1998] "Optimal design of isolated bridges and isolation systems for existing bridges," *Proceedings of the U.S.–Italy Workshop on Seismic Protective Systems for Bridges*, pp. 407–429, Multidisciplinary Center for Earthquake Engineering Research, State University of New York at Buffalo.

Carr, A. J. [2004] "Ruaumoko—a program for inelastic time-history analysis," Tech. rep., Department of Civil Engineering, University of Canterbury, New Zealand.

Casciati, F. [1989] "Stochastic dynamics of hysteretic media," *Structural Safety*, Vol. 6, pp. 259–269.

Caughey, T. K. [1960] "Classical normal modes in damped linear dynamic systems," *Journal of Applied Mechanics, Transactions of the ASME*, Vol. 27, pp. 269–271.

Chagnon, G., Marckmann, G., Verron, E., Gornet, L., Ostoja-Kuczynski, E., and Charrier, P. [2002] "A new modeling of Mullins' effect an viscoelasticity of elastomers based on a physical approach," *International Rubber Conference*, Prague, Czech Republic.

Chang, Y. W. and Seidensticker, R. W. [1993] "Dynamic characteristics of low shear modulus–high damping seismic isolation bearings," Report No. ANL/RE-93/7, Argonne National Laboratory, Argonne, Illinois.

Chopra, A. K. [2001] *Dynamics of Structures: Theory and Applications to Earthquake Engineering*, Prentice–Hall, Upper Saddle River, N.J., 2nd edn.

Clark, P., Aiken, I. D., and Kelly, J. M. [1997] "Experimental studies of the ultimate behavior of seismically-isolated structures," Technical Report UCB/EERC–97/18, Earthquake Engineering Research Center.

Clark, P. W. and Kelly, J. M. [1996] "Energy-based modeling of high-damping rubber isolators for dynamic analysis," *ASCE International Conference and Exposition on Natural Disaster Reduction*, Washington, D.C.

Comité Européen de Normalisation (CEN) [2003] *Eurocode 8: Design of structures for Earthquake resistance, Draft 6*, Brussels.

Constantinou, M. C., Kartoum, A., Reinhorn, A. M., and Bradford, P. [1992] "Sliding isolation system for bridges: Experimental study," *Earthquake Spectra*, Vol. 8, No. 3, pp. 321–344.

Constantinou, M. C., Tsopelas, P., Kim, Y.-S., and Okamoto, S. [1993] "NCEER–Taisei Corporation research program on sliding seismic isolation systems for bridges: experimental and analytical study

of a Friction Pendulum System (FPS)," Technical Report NCEER-93-0020, National Center for Earthquake Engineering Research, Buffalo, New York.

Dafalias, Y. F. [1986] "Bounding surface plasticity. I: Mathematical foundation and hypoplasticity," *Journal of Engineering Mechanics*, Vol. 112, No. 9, pp. 966–987.

Dafalias, Y. F. and Herrmann, L. R. [1982] "Bounding surface formulation of soil plasticity," *Soil Mechanics — Transient and Cyclic Loads*, eds. G. N. Pande and O. C. Ziekiewicz, chap. 10, pp. 253–282, Wiley, New York.

Dafalias, Y. F. and Popov, E. P. [1975] "A model for nonlinearly hardening materials for complex loading," *Acta Mechanica*, Vol. 21, No. 3, pp. 173–192.

Dafalias, Y. F. and Popov, E. P. [1976] "Plastic internal variables formalism of cyclic plasticity," *Journal of Applied Mechanics*, Vol. 43, pp. 645–651.

Dwairi, H. and Kowalsky, M. [2004] "Investigation of Jacobsen's equivalent viscous damping approach as applied to displacement-based seismic design," *Proceedings of the 13th World Conference on Earthquake Engineering*, Vancouver, Canada.

Faccioli, E., Paolucci, R., and Rey, J. [2004] "Displacement spectra for long periods," *Earthquake Spectra*, Vol. 20, No. 2, pp. 347–376.

Franchin, P., Monti, G., and Pinto, P. E. [2001] "On the accuracy of simplified methods for the analysis of isolated bridges," *Earthquake Engineering and Structural Dynamics*, Vol. 30, pp. 363–382.

Govindjee, S. and Simo, J. [1991] "A micro-mechanical based continuum damage model for carbon black filled rubbers incorporating Mullins' effect," *Journal of the Mechanics of Physics and Solids*, Vol. 39, No. 1, pp. 87–112.

Govindjee, S. and Simo, J. [1992] "Mullins' effect and the strain amplitude dependence of the storage modulus," *International Journal of Solids and Structures*, Vol. 29, No. 14, pp. 1737–1751.

Grant, D. N., Blandon, C., and Priestley, M. J. N. [2004] "Modelling inelastic response in direct displacement-based design," Tech. rep., European School for Advanced Studies in Reduction of Seismic Risk (ROSE School), Pavia, Italy, in preparation.

Gulkan, P. and Sozen, M. A. [1974] "Inelastic responses of reinforced concrete structures to earthquake motions," *Journal of the American Concrete Institute*, Vol. 71, No. 12, pp. 601–609.

Haupt, P. and Sedlan, K. [2001] "Viscoplasticity of elastomeric materials: experimental facts and constitutive modelling," *Archive of Applied Mechanics*, Vol. 71, pp. 89–109.

Huang, W.-H. [2002] "Bi-directional testing, modeling, and system response of seismically isolated bridges," Ph.D. thesis, University of California, Berkeley.

Huang, W.-H., Fenves, G. L., Whittaker, A. S., and Mahin, S. A. [2000] "Characterization of seismic isolation bearings from bidirectional testing," *Proceedings of the 12th World Conference on Earthquake Engineering*, Auckland, New Zealand.

Hwang, J. S., Lin, C. Y., Ku, S. W., and Kau, W. J. [1996] "Analysis accuracy implied by equivalent linear models of bridge isolation," *Proceedings of the 11th World Conference on Earthquake Engineering*, Acapulco, Mexico.

Hwang, J. S., Sheng, L. H., and Gates, J. H. [1994] "Practical analysis of bridges on isolation bearings with bilinear hysteresis characteristics," *Earthquake Spectra*, Vol. 10, pp. 705–727.

Hwang, J. S., Wu, J. D., Pan, T.-C., and Yang, G. [2002] "A mathematical hysteretic model for elastomeric isolation bearings," *Earthquake Engineering and Structural Dynamics*, Vol. 31, pp. 771–789.

International Code Council (ICC) [2000] *International Building Code*, Falls Church, Va.

Iwan, W. D. [1980] "Estimating inelastic response spectra from elastic spectra," *Earthquake Engineering and Structural Dynamics*, Vol. 8, pp. 375–388.

Iwan, W. D. and Gates, N. C. [1979] "Estimating earthquake response of simple hysteretic structures," *Journal of the Engineering Mechanics Division, ASCE*, Vol. 105, No. EM3, pp. 391–405.

Jacobsen, L. S. [1930] "Steady forced vibrations as influenced by damping," *Transactions ASME*, Vol. 52, pp. 169–181.

Jacobsen, L. S. [1960] "Damping in composite structures," *Proceedings of the 2nd World Conference on Earthquake Engineering*, Vol. 2, pp. 1029–1044, Tokyo and Kyoto, Japan.

Jankowski, R. [2004] "Non-linear model of high damping rubber bearing," *Proceedings of the 13th World Conference on Earthquake Engineering*, Vancouver, Canada.

Jennings, P. C. [1968] "Equivalent viscous damping for yielding structures," *Journal of the Engineering Mechanics Division, ASCE*, Vol. 94, No. EM1, pp. 103–116.

Kartoum, A., Constantinou, M. C., and Reinhorn, A. M. [1992] "Sliding isolation system for bridges: Analytical study," *Earthquake Spectra*, Vol. 8, No. 3, pp. 345–372.

Kelly, J. M. [1991] "Dynamic and failure characteristics of Bridgestone isolation bearings," Report No. UCB/EERC-91/04, Earthquake Engineering Research Center, University of California, Berkeley.

Kelly, J. M. [1996] *Earthquake-Resistant Design with Rubber*, Springer-Verlag, London, 2nd edn.

Kelly, J. M. [1998] "The analysis and design of elastomeric bearings for application in bridges," *Proceedings of the U.S.–Italy Workshop on Seismic Protective Systems for Bridges*, pp. 73–88, Multidisciplinary Center for Earthquake Engineering Research, State University of New York at Buffalo.

Kelly, J. M. and Çelebi, M. [1984] "Verification testing of prototype bearings for a base isolated building," Report No. UCB/SESM-84/01, Department of Civil Engineering, University of California, Berkeley.

Kikuchi, M. and Aiken, I. D. [1997] "An analytical hysteresis model for elastomeric seismic isolation bearings," *Earthquake Engineering and Structural Dynamics*, Vol. 26, pp. 215–231.

Kowalsky, M. J., Priestley, M. J. N., and MacRae, G. A. [1994] "Displacement-based design. A methodology for seismic design applied to single degree of freedom reinforced concrete structures," Report SSRP 94/16, University of California, San Diego.

Krieg, R. D. [1975] "A practical two surface plasticity theory," *Journal of Applied Mechanics*, Vol. 42, pp. 641–646.

Krinitzsky, E. L. and Chang, F. K. [1977] "Specifying peak motions for design earthquakes," State-of-the-art for assessing earthquake hazards in the United States, Report 7, Miscellaneous Paper S-73-1, US Army Corps of Engineers, Vicksburg, Mississippi.

Lai, S.-S., Will, G. T., and Otani, S. [1984] "Model for inelastic biaxial bending of concrete members," *Journal of Structural Engineering, ASCE*, Vol. 110, pp. 2563–2584.

Li, K.-N., Otani, S., and Aoyama, H. [1987] "Reinforced concrete columns under varying axial load and bi-direction horizontal load reversals," *Proceedings of the Pacific Conference on Earthquake Engineering*, Vol. 1, pp. 141–152, Wairakei, New Zealand.

López, O. A., Chopra, A. K., and Hernández, J. J. [2000] "Critical response of structures to multicomponent earthquake excitation," *Earthquake Engineering and Structural Dynamics*, Vol. 29, pp. 1759–1778.

Lubliner, J. [1990] *Plasticity theory*, Macmillan.

Masing, G. [1926] "Eigenspannungen und verfertigung beim messing," *Proceedings, 2nd International Conference on Applied Mechanics*, Zurich.

Miehe, C. and Keck, J. [2000] "Superimposed finite elastic-viscoelastic-plastoelastic stress response with damage in filled rubbery polymers. Experiments, modelling and algorithmic implementation," *Journal of the Mechanics of Physics and Solids*, Vol. 48, pp. 323–365.

Ministry of Public Works [1998] *Guidelines for Design, Construction and Approval of Isolated Structures*, Rome, Italy.

Miranda, E. and Jorge, R.-G. [2002] "Evaluation of appropriate methods to estimate maximum inelastic displacement demands," *Earthquake Engineering and Structural Dynamics*, Vol. 31, pp. 539–560.

Morgan, T. A. [2000] "Characterization and seismic performance of high-damping rubber isolation bearings," CE299 report, University of California, Berkeley.

Mosqueda, G., Whittaker, A. S., and Fenves, G. L. [2004] "Characterization and modeling of friction pendulum bearings subjected to multiple components of excitation," *Journal of Structural Engineering, ASCE*, Vol. 130, No. 3, pp. 433–442.

Mróz, Z. [1967] "On the description of anisotropic workhardening," *Journal of Mechanics and Physics of Solids*, Vol. 15, pp. 163–175.

Mullins, L. [1969] "Softening of rubber by deformation," *Rubber Chemistry and Technology*, Vol. 42, No. 1, pp. 339–362.

Nelder, J. A. and Mead, R. [1965] "Downhill simplex method on multi-dimensional minimization," *Computer Journal*, Vol. 7, pp. 308.

Newmark, N. M. [1959] "A method of computation for structural dynamics," *Journal of the Engineering Mechanics Division, ASCE*, Vol. 85, pp. 67–94.

Otani, S. [1981] "Hysteresis models of reinforced concrete for earthquake response analysis," *Journal of Faculty of Engineering, University of Tokyo*, Vol. XXXVI, No. 2, pp. 407–441.

Otani, S. and Sozen, M. A. [1972] "Behavior of multistory reinforced concrete frames during earthquakes," Structural Research Series 392, University of Illinois, Urbana.

Pan, T.-C. and Yang, G. [1996] "Nonlinear analysis of base-isolated MDOF structures," *Proceedings of the 11th World Conference on Earthquake Engineering*, Acapulco, Mexico.

Park, R. J., Wen, Y.-K., and Ang, A. H.-S. [1986] "Random vibration of hysteretic systems under bi-directional ground motions," *Earthquake Engineering and Structural Dynamics*, Vol. 14, pp. 543–557.

Penzien, J. and Watabe, M. [1975] "Characteristics of 3-dimensional earthquake ground motions," *Earthquake Engineering and Structural Dynamics*, Vol. 3, pp. 365–373.

Priestley, M. J. N. [2003] "Myths and fallacies in earthquake engineering, revisited," The Ninth Mallet Milne Lecture, I.U.S.S. Press, Pavia, Italy.

Priestley, M. J. N. and Grant, D. N. [2005] "Viscous damping in analysis and design," *Journal of Earthquake Engineering*, Vol. 9, No. Special Issue 1, pp. in press.

Priestley, M. J. N., Seible, F., and Calvi, G. M. [1996] *Seismic Design and Retrofit of Bridges*, John Wiley & Sons.

Rayleigh, Lord [1945] *Theory of Sound*, Vol. 1, Dover Publications, New York.

Reaveley and Nordenson [1992] "Acceptable damage in low and moderate seismic zones," *Proceedings, 4th U.S.-Japan Workshop on Improvement of Structural Design and Construction Practices, ATC-15-3 Report*, Redwood City, CA.

Rosenblueth, E. and Herrera, I. [1964] "On a kind of hysteretic damping," *Journal of the Engineering Mechanics Division, ASCE*, Vol. 90, No. EM4, pp. 37–48.

Ryan, K. L. and Chopra, A. K. [2004] "Estimation of seismic demands on isolators based on nonlinear analysis," *Journal of Structural Engineering, ASCE*, Vol. 130, No. 3, pp. 392–402.

SAC [1997] "Suites of earthquake ground motion for analysis of steel moment frame structures," Tech. Rep. SAC/BD-97/03, Woodward-Clyde Federal Services, SAC Steel Project.

Saiidi, M., Ghusn, G., and Jiang, Y. [1989] "Five-spring element for biaxially bent R/C columns," *Journal of Structural Engineering, ASCE*, Vol. 115, No. 2, pp. 398–416.

Shibata, A. and Sozen, M. A. [1976] "Substitute-structure method for seismic design in R/C," *Journal of the Structural Division, ASCE*, Vol. 102, No. 1, pp. 1–18.

Simo, J. and Hughes, T. [1998] *Computational inelasticity*, Springer-Verlag.

Smeby, W. and Der Kiureghian, A. [1985] "Modal combination rules for multicomponent earthquake excitation," *Earthquake Engineering and Structural Dynamics*, Vol. 13, pp. 1–12.

Spacone, E., Filippou, F. C., and Tauser, F. F. [1996] "Fiber beam-column model for non-linear analysis of R/C frames. 1. formulation." *Earthquake Engineering and Structural Dynamics*, Vol. 25, pp. 711–725.

Stanton, J. [1998] "The 1997 AASHTO seismic isolation guide specification," *Proceedings of the U.S.–Italy Workshop on Seismic Protective Systems for Bridges*, pp. 31–46, Multidisciplinary Center for Earthquake Engineering Research, State University of New York at Buffalo.

Sullivan, T. J., Calvi, G. M., Priestley, M. J. N., and Kowalsky, M. J. [2003] "The limitations and performances of different displacement based design methods," *Journal of Earthquake Engineering*, Vol. 7, No. Special Issue 1, pp. 201–241.

Takeda, T., Sozen, M. A., and Nielsen, N. N. [1970] "Reinforced concrete response to simulated earthquakes," *Journal of the Structural Division, ASCE*, Vol. 96, No. ST12, pp. 2557–2573.

Tarics, A. G., Way, D., and Kelly, J. M. [1984] "The implementation of base isolation for the Foothill Communities Law and Justice Center," Report to the National Science Foundation, Reid and Tarics Associates, San Francisco.

Thompson, A. C. T. [1998] "High damping rubber seismic isolation bearings — behavior and design implications," CE299 report, University of California, Berkeley.

Thompson, A. C. T., Whittaker, A. S., Fenves, G. L., and Mahin, S. A. [2000] "Property modification factors for elastomeric seismic isolation bearings," *Proceedings of the 12th World Conference on Earthquake Engineering*, Auckland, New Zealand.

Tsai, C. S., Chiang, T.-C., Chen, B.-J., and Lin, S.-B. [2003] "An advanced analytical model for high damping rubber bearings," *Earthquake Engineering and Structural Dynamics*, Vol. 32, pp. 1373–1387.

Tsopelas, P. C., Constantinou, M. C., and Reinhorn, A. M. [1994] "3D-BASIS-ME: Computer program for nonlinear dynamic analysis of seismically isolated single and multiple structures and liquid storage tanks," Technical Report NCEER-94-0010, State University of New York at Buffalo.

Tyler, R. G. and Robinson, W. H. [1984] "High-strain tests on lead–rubber bearings for earthquake loading," *Bulletin of the New Zealand National Society for Earthquake Engineering*, Vol. 18, No. 4, pp. 90–105.

Vanmarcke, E. H. [1979] "State-of-the-art for assessing earthquake hazards in the united states: representation of earthquake ground motion. scaled accelerograms and equivalent response spectra." Miscellaneous Paper S-73-1, Report 14, US Army Corps of Engineers Waterways Experiment Station, Vicksburg, Mississippi.

Veletsos, A. S. and Newmark, N. M. [1960] "Effect of inelastic behavior on the response of simple systems to earthquake motions," *Proceedings of the 2nd World Conference on Earthquake Engineering*, Vol. 2, pp. 895–912, Tokyo and Kyoto, Japan.

Wen, Y.-K. [1976] "Method for random vibration of hysteretic systems," *Journal of the Engineering Mechanics Division, ASCE*, Vol. 102, pp. 249–263.

Wilson, E. L., Der Kiureghian, A., and Bayo, E. P. [1981] "A replacement for the SRSS method in seismic analysis," *Earthquake Engineering and Structural Dynamics*, Vol. 10, pp. 187–194.

Wilson, E. L. and Penzien, J. [1972] "Evaluation of orthogonal damping matrices," *International Journal for Numerical Methods in Engineering*, Vol. 4, pp. 5–10.

Zayas, V., Low, S., and Mahin, S. [1987] "The FPS earthquake resisting system," Tech. Rep. UCB/EERC-87/01, Earthquake Engineering Research Center, University of California, Berkeley.

A. DERIVATION OF THE CONSISTENT TANGENT MATRIX FOR THE PROPOSED MODEL

The consistent tangent matrix for the integration algorithm presented in Section 4.2 is defined as:

$$\mathbb{C} = \frac{d\mathbf{F}}{d\mathbf{U}} = \frac{d\mathbf{F}_1}{d\mathbf{U}} + \frac{d\mathbf{F}_2}{d\mathbf{U}} \tag{A.1}$$

Differentiating Eq. (4.11) with respect to the displacement vector and damage parameters, the derivative of $\mathbf{F}_1$ is obtained:

$$\begin{aligned}\frac{d\mathbf{F}_1}{d\mathbf{U}} = \frac{\partial \mathbf{F}_1}{\partial \mathbf{U}} &+ \left(\frac{\partial \mathbf{F}_1}{\partial K_{S,1}}\right) \otimes \left[\left(\frac{\partial K_{S,1}}{\partial D_S}\right)\left(\frac{\partial D_S}{\partial \mathbf{U}}\right)\right] \\ &+ \left(\frac{\partial \mathbf{F}_1}{\partial K_M}\right) \otimes \left[\left(\frac{\partial K_M}{\partial D_M}\right)\left(\frac{\partial D_M}{\partial \mathbf{U}}\right)\right]\end{aligned} \tag{A.2}$$

Similarly, differentiating Eq. (4.18) gives the derivative of $\mathbf{F}_2$:

$$\begin{aligned}\frac{d\mathbf{F}_2}{d\mathbf{U}} = &\left(\frac{\partial \mathbf{F}_2}{\partial R}\right) \otimes \left(\frac{\partial R}{\partial \mathbf{U}}\right) + \left(\frac{\partial \mathbf{F}_2}{\partial \mathbf{n}}\right) \cdot \left(\frac{\partial \mathbf{n}}{\partial \mathbf{U}}\right) \\ &+ \left(\frac{\partial \mathbf{F}_2}{\partial \delta}\right) \otimes \left(\frac{\partial \delta}{\partial \mathbf{U}}\right) + \left(\frac{\partial \mathbf{F}_2}{\partial \boldsymbol{\mu}}\right) \cdot \left(\frac{\partial \boldsymbol{\mu}}{\partial \mathbf{U}}\right)\end{aligned} \tag{A.3}$$

The partial derivatives in Eqs. (A.2) and (A.3) are summarised below:

$$\begin{aligned}\frac{\partial \mathbf{F}_1}{\partial \mathbf{U}} &= K_{S,1}K_M\Big\{\left(a_1 + a_2\|\mathbf{U}\|^2 + a_3\|\mathbf{U}\|^4\right)\mathbf{I} + 2\left(a_2 + 2a_3\|\mathbf{U}\|^2\right)\mathbf{U}\otimes\mathbf{U}\Big\} \\ \frac{\partial \mathbf{F}_1}{\partial K_{S,1}} &= K_M\left(a_1 + a_2\|\mathbf{U}\|^2 + a_3\|\mathbf{U}\|^4\right)\mathbf{U} \\ \frac{\partial \mathbf{F}_1}{\partial K_M} &= K_{S,1}\left(a_1 + a_2\|\mathbf{U}\|^2 + a_3\|\mathbf{U}\|^4\right)\mathbf{U}\end{aligned}$$

$$\frac{\partial K_{S,1}}{\partial D_S} = -3c_1 D_S^2 \exp(-c_1 D_S^3)$$
$$\frac{\partial K_{S,2}}{\partial D_S} = -3c_2 D_S^2 \exp(-c_2 D_S^3)$$
$$\frac{\partial K_M}{\partial D_M} = -3c_4(1-c_3) D_M^2 \exp(-c_4 D_M^3)$$
$$\frac{\partial D_S}{\partial \mathbf{U}} = \begin{cases} -\frac{\mathbf{U}}{\|\mathbf{U}\|}, & \|\mathbf{U}\| < D_{S,n}^- \\ 0, & \|\mathbf{U}\| \geq D_{S,n}^- \end{cases}$$
$$\frac{\partial D_M}{\partial \mathbf{U}} = \begin{cases} -\frac{\mathbf{U}}{\|\mathbf{U}\|}, & \|\mathbf{U}\| < \|\mathbf{U}_n\| \\ 0, & \|\mathbf{U}\| \geq \|\mathbf{U}_n\| \end{cases}$$
$$\frac{\partial \mathbf{F}_2}{\partial R} = \mathbf{n}$$
$$\frac{\partial \mathbf{F}_2}{\partial \mathbf{n}} = R\mathbf{I}$$
$$\frac{\partial \mathbf{F}_2}{\partial \delta} = -\boldsymbol{\mu}$$
$$\frac{\partial \mathbf{F}_2}{\partial \boldsymbol{\mu}} = -\delta\mathbf{I}$$
$$\frac{\partial R}{\partial \mathbf{U}} = b_2 \left(2K_{S,2}\mathbf{U} + \|\mathbf{U}\|^2 \frac{\partial K_{S,2}}{\partial D_S} \frac{\partial D_S}{\partial \mathbf{U}} \right)$$
$$\frac{\partial \mathbf{n}}{\partial \mathbf{U}} = \frac{1}{\|\mathbf{U} - \mathbf{U}_n\|} \{\mathbf{I} - \mathbf{n} \otimes \mathbf{n}\}$$
$$\frac{\partial \delta}{\partial \mathbf{U}} = -\frac{\delta_n b_3 \mathbf{n}}{(1 + b_3\|\mathbf{U} - \mathbf{U}_n\|)^2}$$
$$\frac{\partial \boldsymbol{\mu}}{\partial \mathbf{U}} = \frac{1}{\|\hat{\mathbf{F}} - \mathbf{F}_{2,n}\|} (\mathbf{I} - \boldsymbol{\mu} \otimes \boldsymbol{\mu}) \cdot \frac{\partial \hat{\mathbf{F}}}{\partial \mathbf{U}}$$
$$\frac{\partial \hat{\mathbf{F}}}{\partial \mathbf{U}} = \mathbf{n} \otimes \frac{\partial R}{\partial \mathbf{U}} + R \frac{\partial \mathbf{n}}{\partial \mathbf{U}}$$

where $\mathbf{I}$ is the identity matrix. These expressions may be substituted into Eqs. (A.2), (A.3) and (A.1) to give the tangent matrix consistent with the linearisation.

B. DERIVATION OF EQUIVALENT LINEAR PROPERTIES FOR THE PROPOSED MODEL

For unidirectional, monotonic loading, neglecting the effects of strain-rate dependence, Eqs. (4.2), (4.1), (4.11), (4.13), (4.15), (4.16), (4.18) reduce to:

$$F(U) = F_1 + F_2 = K_{S,1}K_M\Big(a_1 + a_2U^3 + a_3U^5\Big) + K_{S,2}\Big(b_1 + b_2U^2\Big) \tag{B.1}$$

where F, F_1, F_2 and U are the unidirectional equivalents of the corresponding vectors in bidirectional loading. Equation (B.1) assumes that when $U = U_d$, $\delta = 0$, an assumption that is verified below.

As discussed in Chapter 6, in the geometric stiffness method, the effective stiffness of an equivalent linear visco-elastic model is taken as the secant stiffness to the design point, ($F(U_d)$, U_d). The Mullins' effect reduction factor, may be expressed from Eq. (4.22) as the stabilised value for large D_M, $K_M = c_3$. The scragging reduction factors are a function of the prescragging level specified by the manufacturer, or the level of scragging assumed at the start of the design process (if recovery of virgin behaviour is considered). The scragging parameter, $D_S = D_{S,0}$ is specified in units of displacement (or strain, multiplied by the rubber thickness, t_r), and $K_{S,1}$ and $K_{S,2}$ are determined from Eq. (4.20). Finally, the effective bearing stiffness at design level is found from:

$$K_{\mathit{eff},b} = \frac{F(U_d)}{U_d} \tag{B.2}$$

which gives:

$$\begin{aligned} K_{\mathit{eff},b} = c_3\left(a_1 + a_2U_d^2 + a_3U_d^4\right)\exp\left(-c_1D_{S,0}^3\right) \\ + \left(\frac{b_1}{U_d} + b_2U_d\right)\exp\left(-c_2D_{S,0}^3\right) \end{aligned} \tag{B.3}$$

The equivalent viscous damping is often calculated from the area under the hysteresis loop describing one complete stabilised cycle, A_h. This is representative of the hysteretic energy dissipated in a peak cycle, and may be equated with the energy dissipated in one cycle of an equivalent linear visco-elastic

oscillator. Assuming F_1 does not change over the period (i.e. K_M and D_S are constant), then this area may be obtained from twice the integral of F_2 between $-U_d$ and U_d:

$$A_h = 2\int_{-U_d}^{U_d} F_2(U)\,\mathrm{d}U = 2\int_{-U_d}^{U_d} \Big(R(U) - \delta(U)\Big)\,\mathrm{d}U \tag{B.4}$$

The parameter δ may be evaluated explicitly in this case, as the unidirectional displacement, U, increases monotonically from $-U_d$ to U_d. The variation of δ over this half-cycle is given by:

$$\delta(U) = C\exp(-b_3 U) \tag{B.5}$$

where C is a constant of integration. Note that Eq. (B.5) is a general solution of the unidirectional version of Eq. (4.17).

For stabilised hysteretic response:

$$\delta(U_d) = 2R(-U_d) - \delta(-U_d) \tag{B.6}$$

which specifies that the half-cycle from U_d to $-U_d$ is identical to the half-cycle from $-U_d$ to U_d, taking into account the discrete change of δ with change in load direction.

Substituting Eq. (B.5) into Eq. (B.6), and rearranging, gives the following expression for the constant of integration:

$$C = \frac{2R(-U_d)}{\exp(b_3 U_d)\Big[1 + \exp(-2b_3 U_d)\Big]} \tag{B.7}$$

For realistic values of b_3 and U_d the exponential term, $\exp(-2b_3U_d) \ll 1$. For example, with $b_3 \approx 2$ per inch from Table 5.2, and $U_d = 200\% \times 1.8$ in., the exponential term, $\exp(-2b_3U_d) = 6 \times 10^{-7}$. This suggests that the force point is almost touching the bounding surface for this level of displacement, as was assumed in the bidirectional decomposition of $\mathbf{F}$ in Section 4.1, and again above when calculating the effective stiffness at $U = U_d$. Taking into account this assumption, and substituting from Eq. (B.7) into Eq. (B.5), gives:

$$\delta = 2R(-U_d)\exp\Big(-b_3(U + U_d)\Big) \tag{B.8}$$

Finally, Eq. (B.8) is substituted back into the integral, and Eq. (B.4) is evaluated to obtain the total

hysteretic area over a full cycle:

$$\begin{aligned} A_h &= 2\int_{-U_d}^{U_d}\left[b_1 + K_{S,2}\,b_2U^2 - 2R(-U_d)\exp\Big(-b_3(U+U_d)\Big)\right]\mathrm{d}U \\ &= 2\left[b_1U + \frac{1}{3}K_{S,2}\,b_2U^3 + \frac{2}{b_3}R(-U_d)\exp\Big(-b_3(U+U_d)\Big)\right]_{-U_d}^{U_d} \\ &= 4b_1U_d + \frac{4}{3}K_{S,2}\,b_2U_d^3 + \frac{4}{b_3}R(-U_d) \\ &= 4b_1\left(U_d - \frac{1}{b_3}\right) + \frac{4}{3}K_{S,2}\,b_2U_d^2\left(U_d - \frac{3}{b_3}\right) \end{aligned} \tag{B.9}$$

The hysteretic area, A_h, is equated with the energy dissipated in a single cycle of linear viscoelastic hysteresis. This leads to the following expression, which is routinely used in calculating viscous damping from experimental data:

$$\xi_{eff,b} = \frac{A_h}{2\pi K_{eff,b}U_d^2} \tag{B.10}$$

The effective stiffness and hysteretic area may be substituted from Eqs. (B.3) and (B.9) respectively, to obtain the equivalent viscous damping for use with the HDR bearing model.

Note that the assumption that D_S does not change over the response is equivalent to assuming that the prescragging level, $D_{S,0}$ is greater than U_d. This will generally be true for prescragged bearings obtained directly from the manufacturer, and specifying reasonable levels of design displacement. However, when scragging recovery is being taken into account, the stabilised hysteresis will no longer be representative of the maximum response cycle under general earthquake excitation up to the design displacement, and Eq. (B.10) will, in general, underestimate the dissipated energy.

It should be noted that different approaches for determining the effective stiffness and equivalent viscous damping have been discussed in the literature. For isolation devices for which a bilinear hysteretic model is appropriate, Franchin *et al.* [2001] give a summary of some of the expressions that have been derived for these parameters. The equivalent visco-elastic parameters calculated in this appendix are relevant for calibrating design approaches with the proposed mathematical model, although experimental curves of effective stiffness and equivalent viscous damping versus maximum shear strain may be more appropriate for design and analysis of a real bearing.